Supramolecular Polysaccharide Composite Materials: Green And Recyclable Synthesis, Characterization, Analytical And Biomedical Applications

Simon Duri
Marquette University

SUPRAMOLECULAR POLYSACCHARIDE COMPOSITE MATERIALS: GREEN AND RECYCLABLE SYNTHESIS, CHARACTERIZATION, ANALYTICAL AND BIOMEDICAL APPLICATIONS

By

Simon Duri, BSc. (Hons.), MSc.

A dissertation submitted to the Faculty of the Graduate School,

Marquette University,

in Partial Fulfillment of the Requirements for the

Degree of Doctor of Philosophy

Milwaukee, Wisconsin, USA

August 2013

ABSTRACT

SUPRAMOLECULAR POLYSACCHARIDE COMPOSITE MATERIALS: GREEN AND RECYCLABLE SYNTHESIS, CHARACTERIZATION, ANALYTICAL AND BIOMEDICAL APPLICATIONS

Simon Duri, BSc. (Hons.), MSc.

Marquette University, 2013

A simple novel recyclable synthetic method was successfully developed for the synthesis of polysaccharide composite materials. The method involves the use of 1-butyl-3-methylimidazolium chloride [$BMIm^+Cl^-$], a simple ionic liquid, as the sole solvent. Naturally abundant and renewable materials such as cellulose (CEL) and chitosan (CS) were used for the preparation of the composite materials. CEL is the most abundant compound on earth, while CS is a product of deacetylation of chitin, which is the second most abundant material on earth. [$BMIm^+Cl^-$] is relatively non toxic, non volatile and stable over a wide range of temperature eliminating one of the major pathways to environmental contamination, making the method developed here environmentally friendly. In addition, at least 88% of the [$BMIm^+Cl^-$] used can be recovered for re-use, making the method much cheaper and green compared to methods employing traditional organic solvents. CEL and CS are attractive materials for their natural abundance, biodegradability and biocompatibility. While CEL is known for its superior mechanical properties, CS has been widely investigated and applied in adsorption of both organic and inorganic pollutants, antimicrobial, hemostasis, wound dressings and drug delivery systems. Composite materials made from CEL and CS are therefore expected to have combined advantages and qualities of both of these materials. Dissolution of both CEL and CS and successful regeneration was followed by X-ray diffraction. FT-IR, NIR and ^{13}C CP MAS NMR spectroscopy were used to characterize the chemical composition of the regenerated composite materials. The morphology of the regenerated materials was evaluated using SEM. Results of tensile strength measurements showed that indeed, addition of CEL, a material of superior mechanical strength, to CS leads to considerable improvement in the strength of the materials. Up to 5 times increase in tensile strength was achieved by adding 80% CEL to CS. Doping the materials with cyclodextrins was found to not only improve their pollutant adsorption capacity, but also impart some size selectivity to the materials. Results of antimicrobial studies showed activity against a number of both gram negative and gram positive bacteria, while the blood absorption properties of these materials are comparable to commercially available products.

ACKNOWLEDGMENTS

I would like to thank my supervisor Dr. Chieu D. Tran who has the attitude and the substance of a genius for his mentorship, guidance, patience, leadership and his depth of understanding in the subject of my research. I would also like to thank my committee members Dr. Jeanne M. Hossenlopp and Dr. Michael D. Ryan for their support and mentorship and lastly but not least my lab mates for their persistent help and support.

TABLE OF CONTENT

LIST OF TABLES

LIST OF FIGURES

LIST OF SCHEMES

Chapter 1. INTRODUCTION

1.1. Background

For a very long time, the synthetic polymer industry has offered some great benefits to society. Unfortunately, synthetic polymers come from petroleum resources and these are not unlimited. In addition, non-biodegradable plastics have become a major threat to the environment. As a result, a lot of attention is now being paid to the exploitation and exploration of natural polymers. Natural polymers possess some unique properties which make them much more attractive than synthetic polymers for a variety of applications. Some of these attractive features are listed below:

- Biodegradable – Naturally occurring polymers produced by all living organisms. They show no adverse effects on the environment or human being.
- Biocompatible and non-toxic
- Economic - They are cheaper and their production cost is less than synthetic materials.
- Safe and devoid of side effects – They are from a natural source and hence, safe and without side effects.
- Easy availability – They are abundant in nature and in many countries, they are produced in large quantities due to their application in many industries.

It is because of these unique and attractive features that natural polymers are gaining more and more attention and are even tipped to replace synthetic polymers in numerous applications. Such considerations have prompted the initiation of this study which seeks

to develop a novel synthetic procedure to prepare polysaccharide composite materials. Cellulose (CEL) was chosen not only for its natural abundance, but also because it is biocompatible and biodegradable. In addition, the superior mechanical and rheological properties of CEL will be used to improve the corresponding properties of the resultant multi-component composite materials. Another natural polymer that will be used in the composite materials is Chitosan (CS). As will be described in later sections, CS also has some unique properties that could be exploited in a variety of applications for the resultant composite materials. These include excellent adsorbent capability, wound healing, hemostasis, blood adsorption, antimicrobial activity and drug delivery.[1–11] Selectivity is a very special feature to have in any material especially if they are to be used for adsorption of small compounds. Cyclodextrins (CDs), have unique cavities that allow them to form guest-host complexes with a wide range of analytes.[12,13] Accordingly, CDs will also be incorporated into our composite materials and experiments will be designed and carried out to determine whether by doping our composites with CDs, we can confer some size and shape selectivity to our composite materials. One of the biggest limitations in the processing of natural polymers such as CEL and CS is the lack of a solvent or solvent system that can be used to dissolve such polymers under relatively mild conditions. However, the advent of ionic liquids (ILs) seems to be changing that. 1-butyl-3methylimidazolium chloride [$BMIm^+Cl^-$] is one such ionic liquid. It is made from chlorobutane and 1-methylimidazole both of which are easily available and can be easily purified by normal and vacuum distillation respectively. In addition to that, [$BMIm^+Cl^-$] can dissolve both CEL and CS allowing the use of a single solvent to dissolve both

polymers.[14–17] A brief description of the chemistry and some selected properties of CEL, CS, CDs and ILs is given in the following sections.

1.2. Cellulose

Cellulose (CEL) is the principal structural component of cell walls of plants as illustrated in Figure 1.1. It is a natural polysaccharide and the most abundant renewable bio-organic substance on earth. It is non-toxic, renewable, modifiable, biocompatible and biodegradable, which make it one of the most promising feedstock for industry in the future [18–20]. Cellulose has a number of traditional applications including its use in furniture, clothing and medical products. Chemically, cellulose structure consists of β-(1→4)-linked glucose residues leading to the formation of polydisperse linear polymer chains which form hydrogen-bonded structures. An example of such a structure is depicted in Scheme 1.1.

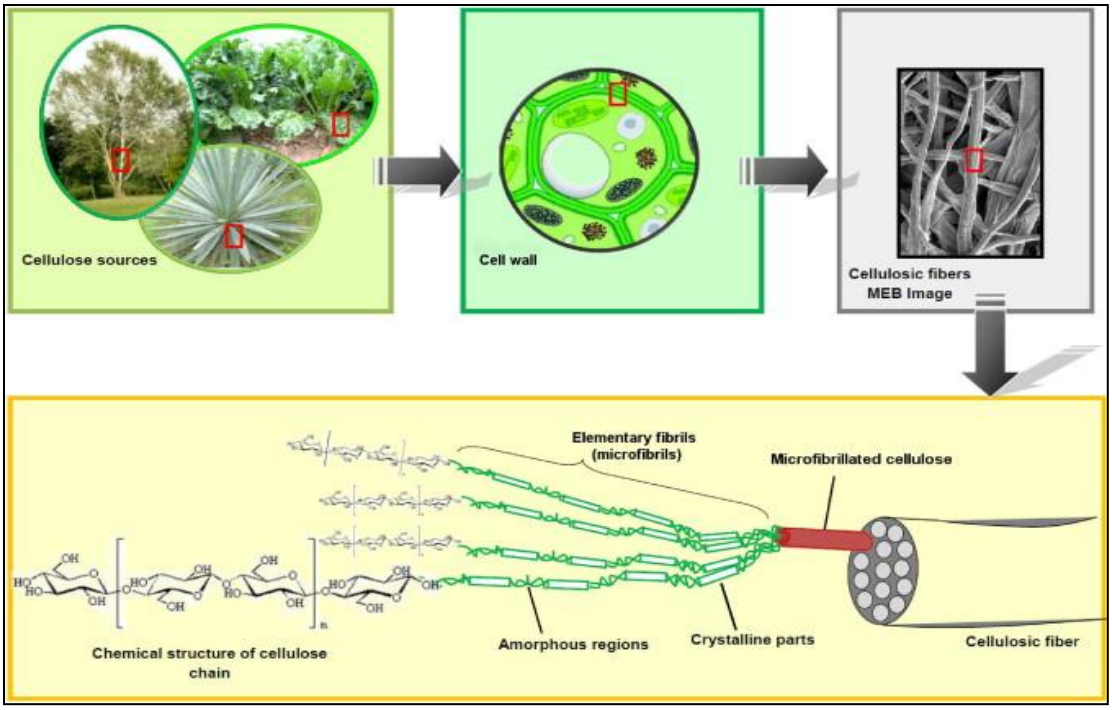

Figure 1.1: Natural sources of cellulose[21]

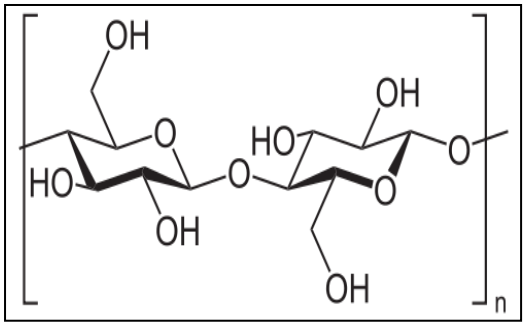

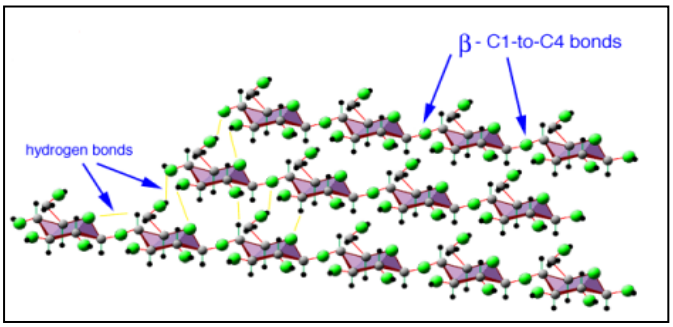

Scheme 1.1: Cellulose polymer chain, n is typically 400-1000(left) and triple strand of cellulose showing H-Bonds (right).

Cellulose is stabilized by intra- and inter-molecular hydrogen bonds so as to form very tough bundles. Multiple hydrogen bonding between cellulose molecules results in the formation of highly ordered crystalline regions. Furthermore, these are mixed or covered by lignin[22]. It is therefore almost impossible to solubilize cellulose with water and common organic solvents. This property causes difficulties in improving the processability and functionality of cellulose. The efficient dissolution of cellulose is a long-standing goal in cellulose research and development. To date, only a limited number of solvent systems for cellulose have been found. These include dimethylacetamide in lithium chloride (DMAc/LiCl)[23], DMF/N_2O_4[24], nitrogen-methylmorpholine nitrogen

oxide (NMNO)[25], DMSO/TBAF[26], and some molten salt hydrates such as $LiClO_4.3H_2O$[27]. Some mixed systems composed of organic solvents, water and salts have also been proposed.[22] In spite of the utility of these solvent systems, there remain some drawbacks such as volatility, generation of poisonous gas or waste, and difficulty to recover solvent(s) for reuse as well as instability in application and processing.[14]

1.3. Chitosan

Chitosan (CS), a natural biomaterial, is an N-deacetylated product of chitin. Chitin (which is the structural element in the exoskeleton of crustaceans, such as crabs and shrimp and cell walls of fungi) is the second most abundant natural polymer after cellulose. Both chitin and chitosan have a structure similar to cellulose.[28] Chitin has two hydroxyl groups and an acetamido group while chitosan has two hydroxyl groups and one amino group in their repeating hexosaminide residue. Chitosan is produced commercially by deacetylation of chitin, (Scheme 1.2). The degree of deacetylation (%DD) can be determined by FT-IR and NMR spectroscopy, and the %DD in commercial chitosans ranges from 60 to 100%. On average, the molecular weight of commercially produced chitosan is between 3800 and 20,000 Daltons. A common method for the synthesis of chitosan is the deacetylation of chitin using sodium hydroxide in excess as a reagent and water as a solvent. This reaction pathway, when allowed to go to completion (complete deacetylation) yields up to 98% product.[29]

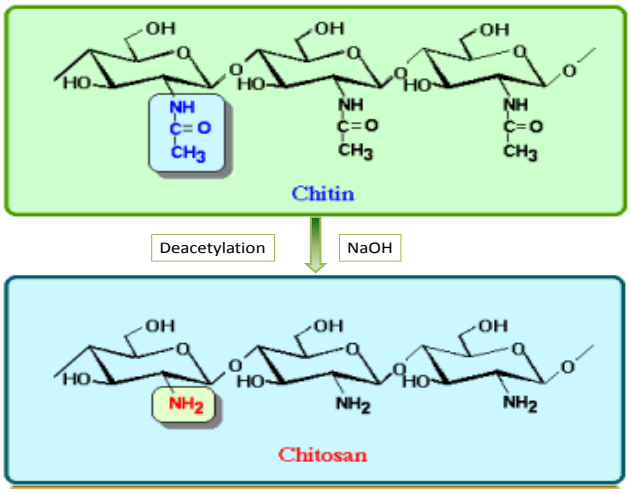

Scheme 1.2: Commercial production of chitosan by the deacetylation process.

The amino group in chitosan has a pKa value of ~6.5, which leads to protonation in acidic to neutral solution with a charge density dependent on pH and the %DA-value. Just like cellulose, chitosan is biocompatible and biodegradable. Chitosan and its derivatives, such as trimethylchitosan (where the amino group has been trimethylated), have been used in nonviral gene delivery.[30] Trimethylchitosan, or quaternized chitosan, has been shown to transfect breast cancer cells, with increased degree of trimethylation increasing the cytotoxicity; at approximately 50% trimethylation, the derivative is the most efficient at gene delivery. Oligomeric derivatives (3-6 kDa) are relatively nontoxic and have good gene delivery properties.[30]

1.4. Biomedical uses of chitosan

Chitosan's properties allow it to clot blood rapidly.[31,32] This occurs when the negatively charged outer membrane of the red blood cells attaches and fuses to the positively charged chitosan. Chitosan has recently gained approval in the United States and Europe for use in bandages and other hemostatic agents.[33] Chitosan hemostatic products have been shown in testing by the U.S. Marine Corps to quickly stop bleeding and to reduce blood loss, and result in 100% survival of otherwise lethal arterial wounds in swine.[33] Chitosan hemostatic products reduce blood loss in comparison to gauze dressings and increase patient survival.[7] Chitosan hemostatic products have been sold to the U.S. Army and are currently used by the UK military. Both the US and UK have already used the bandages on the battlefields of Iraq and Afghanistan.[33] Chitosan is hypoallergenic and has natural antibacterial properties, which further support its use in field bandages.[32]

Chitosan hemostatic agents are often chitosan salts made from mixing chitosan with an organic acid (such as succinic or lactic acid).[34] The hemostatic agent works by an interaction between the cell membrane of erythrocytes (negative charge) and the protonated chitosan (positive charge) leading to involvement of platelets and rapid thrombus formation.[35] The chitosan salts can be mixed with other materials to make them more absorbent (such as mixing with alginate),[36] or to vary the rate of solubility and bio absorbability of the chitosan salt.[34] The chitosan salts are biocompatible and biodegradable making them useful as absorbable hemostats. The protonated chitosan is

broken down by lysozyme in the body to glucosamine[35] and the conjugate base of the acid (such as lactate or succinate) are substances naturally found in the body.

Chitosan's properties also allow it to be used in transdermal drug delivery; it is mucoadhesive in nature, reactive (so it can be produced in many different forms), and most importantly, has a positive charge under acidic conditions. This positive charge comes from protonation of its free amino groups. Lack of a positive charge means chitosan is insoluble in neutral and basic environments. However, in acidic environments, protonation of the amino groups leads to an increase in solubility. The implications of this are very important to biomedical applications. The chitosan molecule will maintain its structure in a neutral environment, but will solubilize and degrade in an acidic environment. This means chitosan can be used to transport a drug to an acidic environment, where the chitosan packaging will then degrade, releasing the drug to the desired environment. One example of this drug delivery has been the transport of insulin.[37]

In recent years, there has been much scientific and industrial interest in utilizing chitin and Chitosan for a diverse range of applications such as pharmaceutical, waste water treatment, cosmetics, drug delivery, heavy metal chelation, heterogeneous catalysts and many other attractive utilizations.[38–40] For these applications, especially when chemical modification of these biopolymers is needed, it is essential to form stable homogenous solutions so as to improve efficiency of modification.[41] However, just like with cellulose, strong intra- and intermolecular hydrogen bonding decreases their solubility in many organic solvents. Traditionally, concentrated solutions of hydrochloric acid and sulfuric acid,[42] and an alkaline-ice mixture were used to dissolve chitin.

However, these solvents are highly corrosive and the resulting polymer solutions are not stable because chitin undergoes hydrolysis in strongly acidic conditions. Chitosan is an easily soluble polymer and is soluble in dilute aqueous solutions of organic and mineral acids, but an alkaline treatment process is necessary to remove the acid after the process. Furthermore, the polyelectrolyte solutions formed had limited application as transition metal sorbents[43] and drug carriers.[44] As a result, new processing strategies for developing potential applications of these bio renewable resources are required. In our composite materials, the poor mechanical and rheological properties of chitosan will look to be improved by cellulose.

1.5. Cyclodextrins

Unlike cellulose, cyclodextrins (sometimes called cycloamyloses) are a family of compounds made up of sugar molecules bound together in a ring (cyclic oligosaccharides) (Scheme 1.3a.). They are named according to the number of glucose units making up each molecule. α Cyclodextrin has 6 glucose units, β cyclodextrin consist of 7 glucose units and γ cyclodextrin is made up of 8 glucose units. Structurally cyclodextrins can be topologically represented as toroids (Scheme 1.3b.) with the larger and the smaller openings of the toroid exposing to the solvent secondary and primary hydroxyl groups respectively. Because of this arrangement, the interior of the toroids is not hydrophobic, but considerably less hydrophilic than the aqueous environment and thus able to host other hydrophobic molecules. In contrast, the exterior is sufficiently hydrophilic to impart cyclodextrins (or their complexes) water solubility.

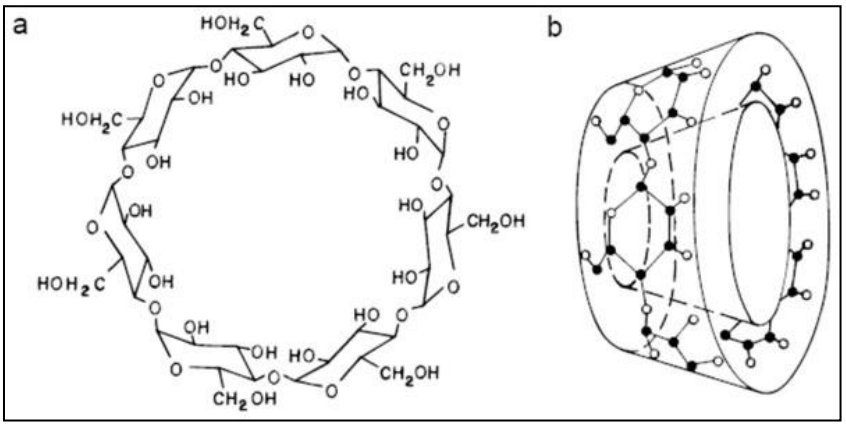

Scheme 1.3: Structure of cyclodextrins

1.6. Applications of cyclodextrins

Cyclodextrins are able to form host-guest complexes with hydrophobic molecules given the unique nature imparted by their structure. As a result, these molecules have found a number of applications in a wide range of fields including pharmaceutical industry.

In the food industry cyclodextrins are employed for the preparation of cholesterol-free products: the bulky and hydrophobic cholesterol molecule is easily lodged inside cyclodextrin rings that are then removed. Alpha-cyclodextrin (6 membered ring), beta-cyclodextrin (7 membered ring), and gamma-cyclodextrin (8 membered ring) are all generally recognized as safe by the FDA. Weight loss supplements are marketed from alpha-cyclodextrin which claim to bind to fat and be an alternative to other anti-obesity medications.[45,46] Other food applications include the ability to stabilize volatile or

unstable compounds and the reduction of unwanted tastes and odor. Alpha-cyclodextrin is used as emulsifier in food and cosmetic applications. Reportedly cyclodextrins are used in alcohol powder, a powder for mixing alcoholic drinks. Beta-cyclodextrin complexes with certain carotenoid food colorants have been shown to intensify color, increase water solubility and improve light stability.[47,48]

The strong ability of complexing fragrances can also be used for another purpose: first dry, solid cyclodextrin microparticles are exposed to a controlled contact with fumes of active compounds, and then they are added to fabric or paper products. Such devices are capable of releasing fragrances during ironing or when heated by human body.[49] Such a device commonly used is a typical 'dryer sheet'. The heat from a clothes dryer releases the fragrance into the clothing.[49]

The ability of cyclodextrins to form complexes with hydrophobic molecules has led to their usage in supramolecular chemistry[50]. In particular they have been used to synthesize certain mechanically-interlocked molecular architectures, such as rotaxanes and catenanes, by reacting the ends of the threaded guest. The photodimerization of substituted stilbazoles has been demonstrated using γ-cyclodextrin as a host. Based on the photodimer obtained, it is established that the halogen-halogen interactions, which are plays interesting role in solid state, can be observed in solution. Existence of such interactions in solution has been proved for the first time by V.Ramamurthy's group by selective photodimerization of dichloro substituted stiblazoles in cyclodextrin and cucurbiturils.[51]

The application of cyclodextrin as supramolecular carrier is also possible in organometallic reactions. The mechanism of action probably takes place in the interfacial region.[52] Wipff also demonstrated by computational study that the reaction occurs in the interfacial layer.[49] The application of cyclodextrins as supramolecular carrier is possible in various organometallic catalyses.

Another common application of cyclodextrins is in chiral chromatography. β-Cyclodextrins are used to produce HPLC columns allowing chiral enantiomers separation.[53]

Cyclodextrins however are highly soluble in water,[54] and also have poor mechanical and rheological properties which makes it impossible to process them into films. For our composite materials, cyclodextrins will be incorporated into cellulose and chitosan and take advantage of the film forming properties of these compounds to prepare cyclodextrin containing composite films.

1.7. Ionic Liquids

Ionic liquids (ILs) are organic salts designed to melt below 100 ^{0}C, or preferably near room temperature. Compared to molecular liquids, ILs have various advantages that include extremely low volatility, low flammability and high thermal stability. The most fascinating nature of ILs are their structural diversity. The physicochemical properties of ILs, including viscosity,[55] polarity,[56] and other properties[57] vary according to their ionic structures. As a result, their physicochemical properties can be tuned by exploiting the diversity of component organic

cations and organic or inorganic anions. ILs have consequently been described as designer solvents. Appropriate ILs might therefore act as eco-friendly polar solvents for cellulose and most other biopolymers. Because of these promising features, ILs should have diverse applications, and they have been extensively studied.[58] ILs have been studied as solvents in chemistry, especially for catalytic reactions. Examples of some ILs are shown in figure 1.1 below.

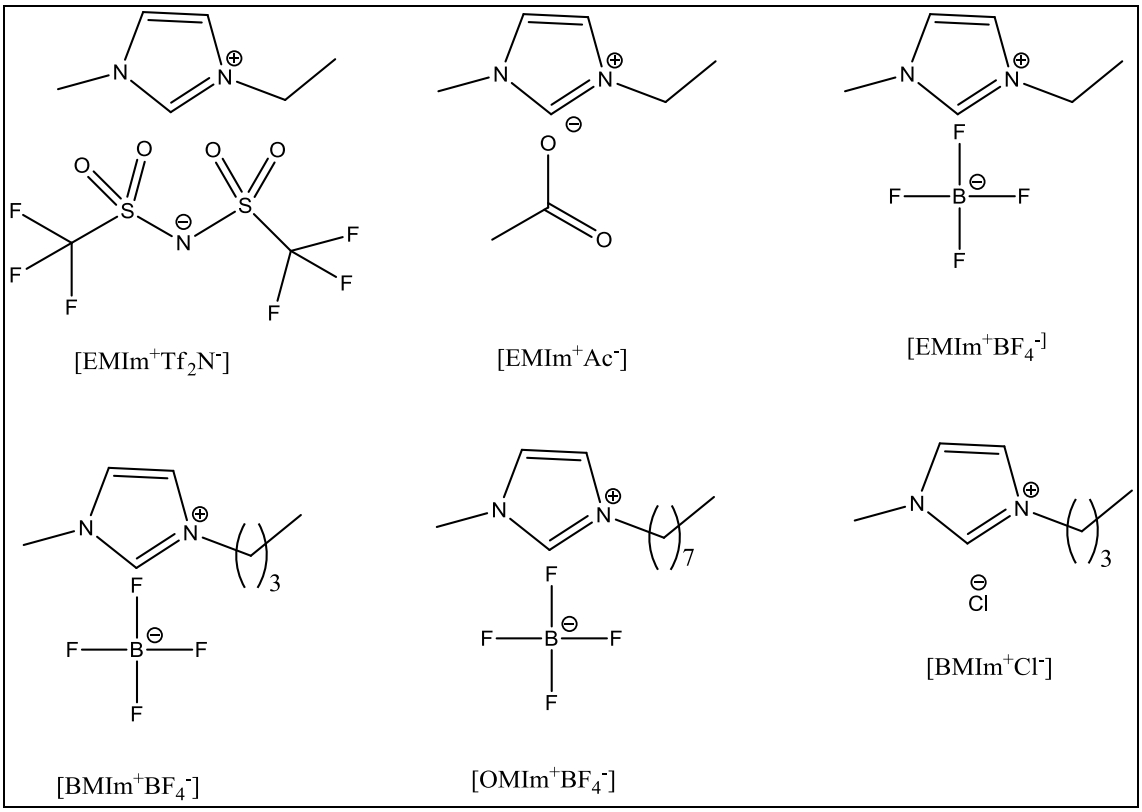

Figure 1.2: Structure of some common Ionic Liquids.

Ionic Liquids have received much attention as green and designable solvents with the development of green chemistry and the requirement of environmental protection. ILs have been applied as alternative solvents in many catalytic organic transformations.[59,60] Owing to their special structures, ionic liquids possesses many unique solubility characteristics. In particular, the 1-butyl-3-methylimidazolium chloride [$BMIm^+Cl^-$] and dicyanamide ionic liquids have a strong ability to disrupt hydrogen bonds, and hence can be used to dissolve biological macromolecules that are linked together by strong intra- and inter-molecular hydrogen bonds such as carbohydrates, cellulose, wool keratin and silk fibroin.[14,17,61–64] The development of a green and recyclable method to synthesize

novel polysaccharide composite materials using [$BMIm^+Cl^-$] as the sole solvent will be described in Chapter 2. The complete characterization of the regenerated composite materials using various spectroscopic techniques will also be described in Chapter 2. Techniques such as FT-IR, near IR, XRD, solid state NMR, AFM and SEM were used for the characterization of the composite materials. Tensile strength measurements were used study the effect of adding cellulose on the mechanical and rheological properties of the composite materials. In Chapter 3, the application of the regenerated composite materials to the adsorption of pollutants from aqueous solution would be described. Pollutants such as microcystin-LR, chlorophenols and bisphenol A were used for this study. Bulky 3, 4 dichlorophenol was used to investigate the effect of cyclodextrin on size selectivity of the regenerated composite materials. The possible application of our composite materials in controlled drug release systems and in the enantiomeric resolution of amino acids will be discussed in Chapter 4. Ciprofloxacin was used as a model drug compound for the drug release studies while tryptophan, tyrosine, histidine and phenylalanine were used in the investigation of the enantioselectivity of our composite materials.

Chapter 5 describes previous projects that were done for the applications of near IR spectroscopy and near IR multispectral imaging spectroscopy.

1.8. References

(1) Dai, T.; Tegos, G. P.; Burkatovskaya, M.; Castano, A. P.; Hamblin, M. R. *Antimicrobial agents and chemotherapy* **2009**, *53*, 393–400.

(2) Bordenave, N.; Grelier, S.; Coma, V. *Biomacromolecules* **2010**, *11*, 88–96.

(3) Rabea, E. I.; Badawy, M. E.-T.; Stevens, C. V; Smagghe, G.; Steurbaut, W. *Biomacromolecules* **2003**, *4*, 1457–1465.

(4) Altiok, D.; Altiok, E.; Tihminlioglu, F. *Journal of materials science Materials in medicine* **2010**, *21*, 2227–2236.

(5) Burkatovskaya, M.; Castano, A. P.; Demidova-Rice, T. N.; Tegos, G. P.; Hamblin, M. R. *Wound repair and regeneration official publication of the Wound Healing Society and the European Tissue Repair Society* **2008**, *16*, 425–431.

(6) Burkatovskaya, M.; Tegos, G. P.; Swietlik, E.; Demidova, T. N.; P Castano, A.; Hamblin, M. R. *Biomaterials* **2006**, *27*, 4157–4164.

(7) Pusateri, A. E.; McCarthy, S. J.; Gregory, K. W.; Harris, R. A.; Cardenas, L.; McManus, A. T.; Goodwin, C. W. *J Trauma* **2002**.

(8) Rossi, S.; Sandri, G.; Ferrari, F.; Bonferoni, M. C.; Caramella, C. *Pharmaceutical development and technology* **2003**, *8*, 199–208.

(9) Jain, D.; Banerjee, R. *Journal of biomedical materials research Part B Applied biomaterials* **2008**, *86*, 105–112.

(10) Varshosaz, J.; Tabbakhian, M.; Salmani, Z. *Open Drug De J* **2008**, *2*, 61 – 70.

(11) Nishiki, M.; Tojima, T.; Nishi, N.; Sakairi, N. Beta-cyclodextrin-linked chitosan beads: preparation and application to removal of bisphenol A from water. *Carbohydrate letters* **2000**, *4*, 61–7.

(12) Dang, Z.; Somg, L. X.; Guo, X. Q.; Du, F. Y.; Yang, J. *Current Organic Chemistry* **2011**, *15*, 848–861.

(13) Koontz, J. L.; Marcy, J. E.; O'Keefe, S. F.; Duncan, S. E. *J. Agric. Food Chem.* **2009**, *57*, 1162–1171.

(14) Zhang, H.; Wu, J.; Zhang, J.; He, J. S. *Macromolecules* **2005**, *38*, 8272.

(15) Xiao, W.; Chen, Q.; Wu, Y.; Wu, T.; Dai, L. *Carbohydrate Polymers* **2011**, *83*, 233–238.

(16) Stefanescu, C.; Daly, W. H.; Negulescu, I. I. *Carbohydrate Polymers* **2012**, *87*, 435–443.

(17) Swatloski, R. P.; Spear, S. K.; Holbrey, J. D.; Rogers, R. D. *Journal of the American Chemical Society* **2002**, *124*, 4974–4975.

(18) Pandey, A.; Soccol, C. R.; Nigam, P.; Soccol, V. T. *Bioresour. Technol.* **2000**, *74*, 69.

(19) Pandey, A.; Soccol, C. R.; Nigam, P.; Soccol, V. T.; Vandenberge, L. P. S.; Mohan, R. *Bioresour. Technol.* **2000**, *74*, 81.

(20) Richardson, S.; Gorton, L. *Anal. Chim. Acta.* **2003**, *497*, 27.

(21) No Title www.kdd.cl/cellulose-insulation-calculator.

(22) Ohno, H.; Fukaya, Y. *Chem. Lett.* **2009**, *38*.

(23) Araki, J.; Kataoka, T.; Katsuyama, N.; Teramoto, A.; Ito, K.; Abe, K. *Polymer* **2006**, *47*, 8241.

(24) Philipp, B.; Nehls, I.; Wagenknecht, W. *Carbohydrate research* **1987**, *164*.

(25) Rosenau, T.; Hofinger, A.; Potthast, A.; Kosma, P. *Polymer* **2003**, *44*, 6153.

(26) Ramos, L. .; Frollini, E.; Heinze, T. *Carbohydrate Polymers* **2005**, *60*, 259.

(27) Fischer, S.; Leipner, H.; Thummler, K.; Brendler, E.; Peters, J. *Cellulose* **2003**, *10*, 227.

(28) Kadokawa, J.; Murakami, M.; Kaneko, Y. *Composites Science and Technology* **2008**, *68*, 493–498.

(29) Zhuangdong, Y. *Chemical Industry Times* **2007**, *21*, 22–24.

(30) Kean, T.; Roth, S.; Thanou, M. *J Control Release* **2005**, *103*, 643–353.

(31) Ghosh, B.; Urban, M. W. *Science* **2009**, *323*, 1458–1460.

(32) McCue.k *Chemistry.org (American Chemical Society)* **2005**.

(33) Lurie, K. War bandages.

(34) Hardy, C.; Johnson, L.; Luksch, P. Hemostatic Material. US patent 8106030, 2012.

(35) Baldrick, P. *Regul Toxicol Pharmacol* **2009**, *56*, 290–299.

(36) Pandit, A. S. Hemostatic Wound Dressing. US patent 5836970, 1998.

(37) Agnihotri, S. A.; Mallikarjuna, N. .; Aminabhavi, T. M. *Journal of Controlled Release* **2004**, *100*, 5–28.

(38) Agboh, O. C.; Qin.y *Polym. Adv. Technol.* **1996**, *8*, 355.

(39) Hirano, S. *Polym. Int.* **1999**, *48*, 732.

(40) Macquarrie, D. J.; Hardy, J. J. E. *Ind. Eng. Chem. Res.* **2005**, *44*, 8499.

(41) Xie, H.; Zhang, S.; Li, S. *Green Chem.* **2006**, *8*, 630–633.

(42) Kunike, G. *J. Soc. Dyers Colour.* **1926**, *42*, 318.

(43) Weltrowski, M.; Martel, B.; Marcellet, M. *J. Appl. Plym. Sci.* **1996**, *59*, 647–654.

(44) Mah, J. W.; Jang, M. K. *J. Poly. Sci., Part A: Poly. Chem.* **2002**, *40*, 3796.

(45) Artiss, J. D.; Brogan, K.; Brucal, M.; Moghaddam, M.; Jen, K.-L. C. *metabolism* **2006**, *55*, 195–202.

(46) Grunberger, G.; Jen, K.-L. C.; Artiss, J. D. *Diabetes/Metabolism Research and Reviews* **2007**, *23*, 56.

(47) Marcolino, V. A.; Zanin, G. M.; Durrant, L. R.; Benassi, M. D. T.; Matioli, G. *Journal of Agricultural and Food Chemistry* **2011**, *59*, 3348–3357.

(48) De Oliveira, V. E.; Almeida, E. W. C.; Castro, H. V; Howell, G. M.; Dos Santos, H. F.; De Oliveira, L. F. C. *J. Phys. Chem. A* **2011**, *115*, 8511–8519.

(49) Chordiya, M. A.; Senthilkumaran, K. *Research and Reviews : Journal of Pharmacy and Pharmaceutical Sciences* **2012**, *1*, 19–29.

(50) Brocos, P.; Diaz-vergara, N.; Banquy, X.; PeRez-Casas, S.; Costas, M.; PinEiro, A. *J. Phys. Chem. B* **2010**, *114*, 12455–12467.

(51) Kalliappan, R.; Maddipatla, M. V. S. N.; Kaanumalle, L. S.; Ramamurthy, V. *Photochemical & Photobiological Sciences* **2007**, *6*, 737.

(52) Leclercq, L.; Bricout, H.; Tilloy, S.; Montflier, E. *J. of Colloid and Interface Science* **2007**, *307*, 481–487.

(53) Motoyama, A.; Suzuki, A.; Shirota, O.; Namba, R. *J. of Pharmaceutical and Biomedical Analysis* **2002**, *28*, 97–106.

(54) Challa, R. *AAPS PharmSciTech* **2005**, *6*, E329.

(55) Dzyuba, S. V; Bartsch, R. A. *ChemPhysChem* **2002**, *3*, 161.

(56) Poole, C. F. *J Chromatogr. A.* **2004**, *49*, 1034.

(57) Takuda, H.; Ishii, K.; Susan Md, A. B. H.; Tsuzuki, S.; Hayamizu, K.; Watanabe, M. *J. Phys. Chem.* **2006**, *110*, 2833.

(58) Ohno, H. *Electrochemical aspects of ionic liquids*; Wiley-intersciences: New York, 2005.

(59) Welton, T. *Chemical Reviews* **1999**, *99*, 2071–2083.

(60) Rogers, R. D.; Seddon, K. R. *Science* **2003**, *302*, 792.

(61) Forsyth, S. A.; MacFarlane, D. R.; Thompson, R. J.; M, V. I. *Chem. Commun.* **2002**, 714.

(62) Wu, J.; Zhang, J.; Zhang, H.; He, J.; Ren, Q.; Guo, M. *Biomacromolecules* **2004**, *5*, 266.

(63) Trulove, P. C.; Mantz, R. A. *J. Mater. Chem.* **2005**, *15*, 4206.

(64) Xie, H. B.; Li, S. H.; Zhang, S. B. *Green Chem.* **2005**, *7*, 606.

Chapter 2. SYNTHESIS, CHARACTERIZATION AND PROPERTIES OF BIOCOMPATIBLE AND BIODEGRADABLE POLYSACCHARIDE COMPOSITE MATERIALS

2.1. Background

2.1.1. Cellulose and Chitosan

As described in the Introduction, chitosan (CS) is a linear amino polysaccharide, obtained by N-deacetylation of chitin. Chitin is the second most abundant naturally occurring polysaccharide after cellulose (CEL)[1–4]. CS structure allows it to have some unique properties including antimicrobial, drug delivery, wound healing, hemostasis and pollutant adsorbant.[5–25] In addition, CS is also biocompatible and biodegradable. Despite all these attractive properties, there are some limitations to the application of CS. CS is relatively easier to dissolve, being soluble in dilute solutions of organic acids such as acetic acid. Subsequent alkaline treatment is required to neutralize the acidic solutions.[2–6] Such treatments (acid and alkaline) are undesirable as they may inadvertently lead to structural modifications which may alter some of the unique properties of the material. In addition, CS is structurally weak and is known to swell in wet environments. While the swelling is good for the diffusion of small molecules and compounds through the CS network, it also further weakens the CS structure in these wet environments. In fact, most commercial CS products are strengthened by grafting man-made polymers to the CS. While this improves the strengths of these products, grafting of man-made polymers may lessen the unique properties of CS and reduce its biocompatibility. This calls for a novel method to synthesize mechanically superior CS materials using natural materials that

preserves or enhance its unique properties. In CEL, the extensive hydrogen bonding network is responsible for giving it its superior mechanical strength, but it also inadvertently leads to challenges with the solubility of CEL. In fact, CEL is not soluble in most common organic solvents. Solubility of CEL is achievable in strong solvents such as methylmorpholine-N-oxide, dimethylthexylsilyl chloride or LiCl in dimethylacetamide (DMAc). The use of strong solvents for CEL is also undesirable as it may lead to some structural changes which can also affect its properties. Composite materials made from CS and CEL may be an alternative substitute to synthetic polymers. This is because [CEL+CS] composites are all natural, their preparation does not involve the use of volatile organic solvents with complicated grafting reactions, and since they are all natural, their individual unique properties are expected to remain intact including their biocompatibility. 1 Butyl-3-methylimidazolium chloride [$BMIm^+Cl^-$] is a simple ionic liquid that has been shown to be able to dissolve both CEL and CS.[26,27] This creates a unique opportunity to use a single solvent to process both CEL and CS.

2.1.2. Butyl methylimidazolium chloride ionic liquid

Butyl methylimidazolium chloride ([$BMIm^+Cl^-$]) belongs to a group of compounds known as ionic liquids (ILs). As described in Chapter 1, ILs are organic salts that are liquid at room temperature[28–34]. They have unique chemical and physical properties. These include their high solubilizing power, high stability, low reactivity and virtually zero vapor pressure. These properties, especially their extremely low vapor pressure eliminates a major pathway for environmental contamination. As a result, ILs can be used as green recyclable alternatives to the volatile organic compounds

traditionally used as solvents.[28–31,33–36] Due to their advantages, ILs have been used for applications which are not possible with other chemicals. For example, as described above, IL such as [$BMIm^+Cl^-$] can dissolve both CEL and CS.[31,33–36] This discovery is of particular significance as it makes it possible for the first time that CEL and CS can be dissolved, regenerated and chemically modified by use of a simple and green solvent which has high solubility power and low toxicity.

This shows that it may be possible to develop a novel and green method to prepare novel strong, biocompatible and biodegradable polysaccharide composite materials for effective adsorption and removal of pollutants, hemostasis, wound healing, bactericidal and drug delivery. This has prompted the initiation of this study which seeks to exploit the advantages of a simple IL such as [$BMIm^+Cl^-$] to develop a novel, environmentally friendly and recyclable method to prepare polysaccharide composite materials containing CEL and CS while retaining the unique properties of the materials.

2.1.3. Cyclodextrin-doped Composites

Supramolecular chemistry refers to chemical systems made up of a discrete number of assembled molecular subunits or components. The forces responsible for the spatial organization may vary from weak (intermolecular forces, electrostatic or hydrogen bonding) to strong (covalent bonding), provided that the degree of electronic coupling between the molecular component remains small with respect to relevant energy parameters of the component.[37,38] While traditional chemistry focuses on the covalent bond, supramolecular chemistry examines the weaker and reversible noncovalent interactions between molecules. These forces include hydrogen bonding, metal

coordination, hydrophobic forces, van der Waals forces, pi-pi interactions and electrostatic effects. Important concepts that have been demonstrated by supramolecular chemistry include molecular self-assembly, folding, molecular recognition, host-guest chemistry, mechanically-interlocked molecular architectures, and dynamic covalent chemistry.[39] Macrocycles are very useful in supramolecular chemistry, as they provide whole cavities that can completely surround guest molecules and may be chemically modified to fine-tune their properties. Cyclodextrins, calixarenes, cucurbiturils and crown ethers are readily synthesized in large quantities, and are therefore convenient for use in supramolecular systems.[40–45] Supramolecular composite materials containing cyclodextrins (CDs) are of particular interest because CD ((α-, β- and γ-CD) are known to form selective inclusion complexes with a variety of different compounds with different sizes and shapes[46,47]. CDs are highly soluble in water, and cannot be processed into films because of their poor mechanical and rheological strength. However, encapsulating CDs into polysaccharide composite materials can proved a way to make solid forms of CD based supramolecules in which the encapsulated CDs fully retain their unique properties. These types of CD based supramolecular composite materials will not only be superior to their man-made counterparts for their simplicity in preparation but they will also be based on all natural materials making them biocompatible as well. This chapter describes a novel method that has been developed to incorporate CDs into CEL and CS polysaccharide composite materials. The structures of the different CDs used in this method are shown in Scheme 2.1.

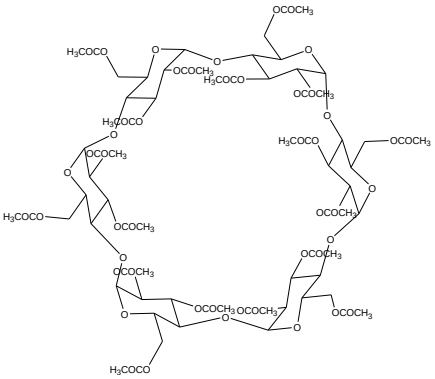

Hexakis (2,3,6-tri-O-acetyl)-α-cyclodextrin (α-TCD)

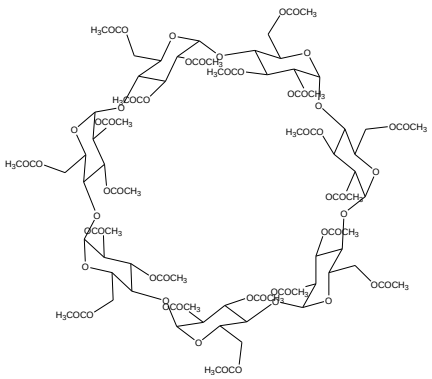

Heptakis (2,3,6-tri-O-acetyl)-β-cyclodextrin (β-TCD)

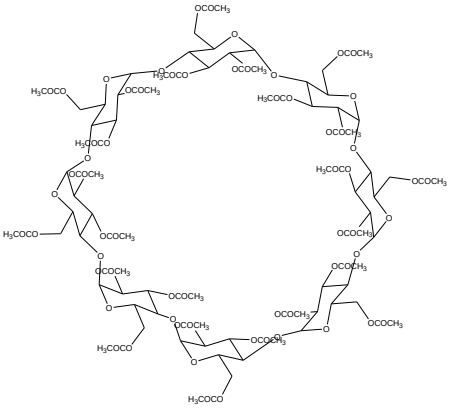

Octakis (2,3,6-tri-O-acetyl)-γ-cyclodextrin (γ-TCD)

Scheme 2.1: Structures of tri-O-acetyl-cyclodextrins (TCDs)

These CD derivatives were particularly chosen because they are insoluble in water, and as will be discussed in the preparation procedure, this is particularly important so that the CDs are retained in the composite material rather than leak out into water during the washing step.

2.2. Materials and Methods

2.2.1. Chemicals

Cellulose (microcrystalline powder or Avicel, DP≈ 300[48]) and chitosan (MW≈310-375kDa, 75% degree of deacetylation, Sigma-Aldrich), microcystin-LR (Enzo Life Sciences) were used as received. Heptakis(2,3,6-tri-O-acetyl)-β-cyclodextrin (β-TCD) (TCI America, Portland, OR), hexakis(2,3,6-tri-O-acetyl)-α-cyclodextrin (α-TCD) and octakis(2,3,6-tri-O-acetyl)-γ-cyclodextrin (γ-TCD) (Cyclodextrin-Shop, The Netherlands) were also used as received. 1-methylimidazole and 1-chlorobutane (Alfa Aesar) were further purified by vacuum and normal distillation respectively. [$BMIm^+$ Cl^-] was synthesized from freshly distilled 1-chlorobutane and freshly distilled 1-Methylimidazole using method previously reported[30,49]. Briefly, a 1:1 mole ratio mixture was refluxed in a three-neck flask under nitrogen at 70^{o}C for 3 days. Initially 2 layers were formed in the reaction flask but at the end of the reaction only one layer remained. After 3 days, the resulting viscous ionic liquid was cooled to room temperature and then washed 3 times with ethyl acetate. Residual ethyl acetate was removed at the rotor vapor before drying the ionic liquid at 70^{o}C under vacuum overnight. This IL is known to be hygroscopic and because any water presence is known to decrease its ability to dissolve polysaccharides[27], it was dried under vacuum at 70°C overnight before use.

2.2.2. Instruments

UV-visible spectra were measured on a Perkin Elmer Lambda 35 UV/Visible spectrometer. NIR spectra were taken on a home-built NIR spectrometer based on an acousto-optic tunable filter. Information on this NIR spectrometer was described in detail in previous papers[50,51]. Normally, each spectrum was an average of 1000 spectra taken at 2-nm intervals from 1300 to 2350 nm. FTIR spectra were measured on a PerkinElmer 100 spectrometer at 2 cm^{-1} resolution with either KBr or by a ZnSe single reflection ATR accessory (Pike Miracle ATR). Each spectrum was an average of 64 spectra.

X-ray diffraction (XRD) measurements were taken on a Rigaku MiniFlex II diffractometer utilizing the Ni filtered Cu Kα radiation (1.54059Å). The voltage and current of the X-ray tube were set at 30 kV and 15 mA respectively. The samples were measured within the 2θ angle range from 2.0^{o} to 60.0^{o}. The scan rate was 5^{0} per minute. The spectra were processed and analyzed with the Jade 8 program package[52]. Scanning electron microscopic images of surface and cross section of the polysaccharide composite materials were taken under vacuum with an accelerated voltage of 3 kV using Hitachi S4800 scanning electron microscope (SEM). Samples were coated with 3 nm Pd prior to measurement on SEM. AFM images were recorded with a Veeco Innova Atomic Force Microscope system. Measurements were done in the tapping mode. Tensile strength measurements were performed on an Instron 5500R Tensile Tester on the air-dried samples. TGA was measured using a TA instruments SDT Q600 using a heating rate of 10 ^{o}C/min. The samples were measured in alumina sample holders under N_2 atmosphere.

DSC measurements were performed using a NETZSCH DSC200 F3 instrument. Heating rate of 10 ^{o}C/min was also used.

2.2.3. Swelling behavior of the polysaccharide composite materials

Swelling behavior of [CEL+CS] composite materials was determined using a procedure previously reported[53,54]. Essentially, dried composite films measuring about 2 cm x 2 cm were accurately weighed before they were immersed in 100 mL of de-ionized water. At specific time intervals, the films were taken out from water, quickly blotted with a filter paper to remove water on the surface and then weighed immediately before being returned to the de-ionized water. The swelling ratio (S%) of the composite films in de-ionized water was calculated from the following equation[53,54]:

$$S\% = (\frac{W_s - W_d}{W_d})100 \qquad (2.1)$$

where W_s and W_d represent the weight of the swollen and dry films respectively.

The equilibrium water content (EWC) was calculated using the following equation[53,54]:

$$EWC(\%) = (\frac{W_e - W_d}{W_e})100 \qquad (2.2)$$

where W_e and W_d represent the weight of the swollen film at equilibrium and the dry film respectively.

2.3. Preparation of CEL, CS and [CEL+CS] composite films

The CS used in this study was specified by the manufacturer (Sigma-Aldrich) as having a degree of deacetylation (DA) value of 75%. Physicochemical properties of CS such as size, zeta potential, morphology and complex stability are known to be closely related to the degree of deacetylation.[55,56] Experiments were carried out to determine the exact degree of deacetylation of the CS that was used in our experiments. Two different methods, FT-IR and ^{1}H NMR, were employed for the determination[57–61]. For FT-IR method, the spectra were measured on a PerkinElmer 100 spectrometer at 2 cm^{-1} resolution. The CS sample was vacuum dried at 50^{o}C for 2 days. A small amount of the dried sample was then ground in KBr and pressed into a pellet for FT-IR measurements. Eight KBr pellets were prepared and their spectra were recorded. Degree of deacetylation (DA) was calculated from the eight spectra, and average value is reported together with standard deviation. The DA value was calculated based on the following equation:[57,58]

$$DA(\%) = 100 - [(A_{1655}/A_{3450}) * 100/1.33] \qquad (2.3)$$

where A_{1655} and A_{3450} are the absorbances at 1655 cm^{-1} of the amide C=O and 3450 cm^{-1} of the OH band respectively. The factor 1.33 denotes the value of the ratio of A_{1655}/A_{3450} for fully N-acetylated chitosan. Each spectrum was corrected for baseline according to a procedure previously reported.[62,63] A schematic representation of the baseline correction procedure is shown in Figure 2.1.

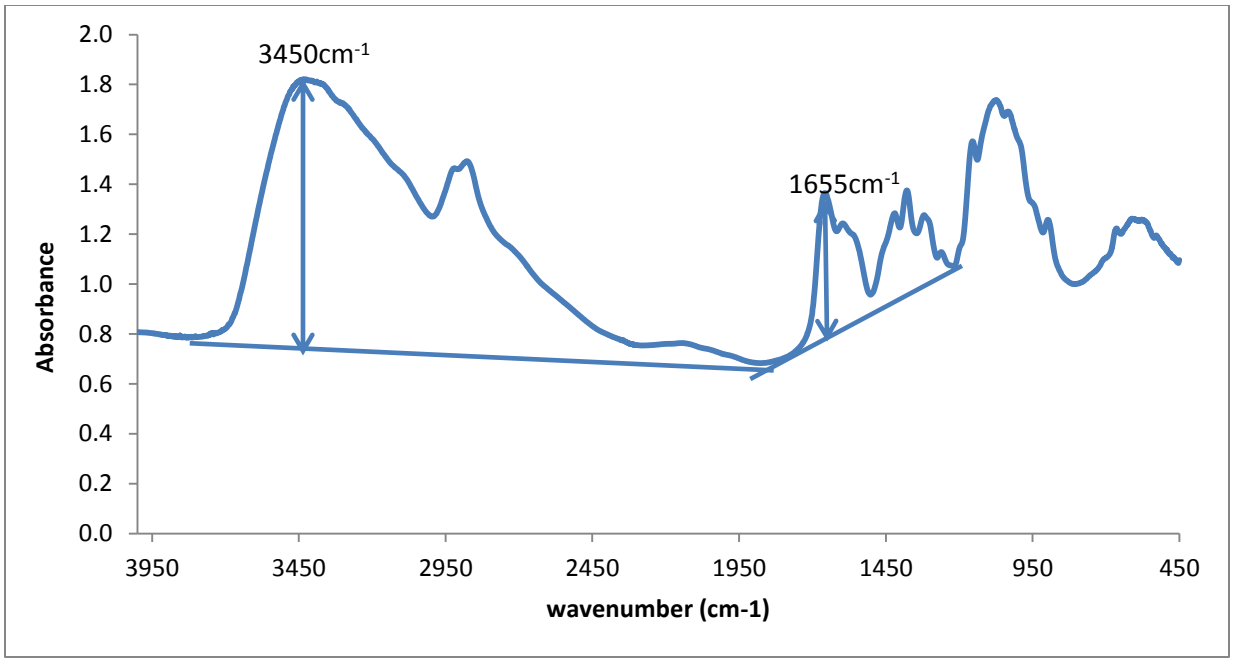

Figure 2.1: Baseline correction procedure used in the calculation of the DA from FT-IR spectra.

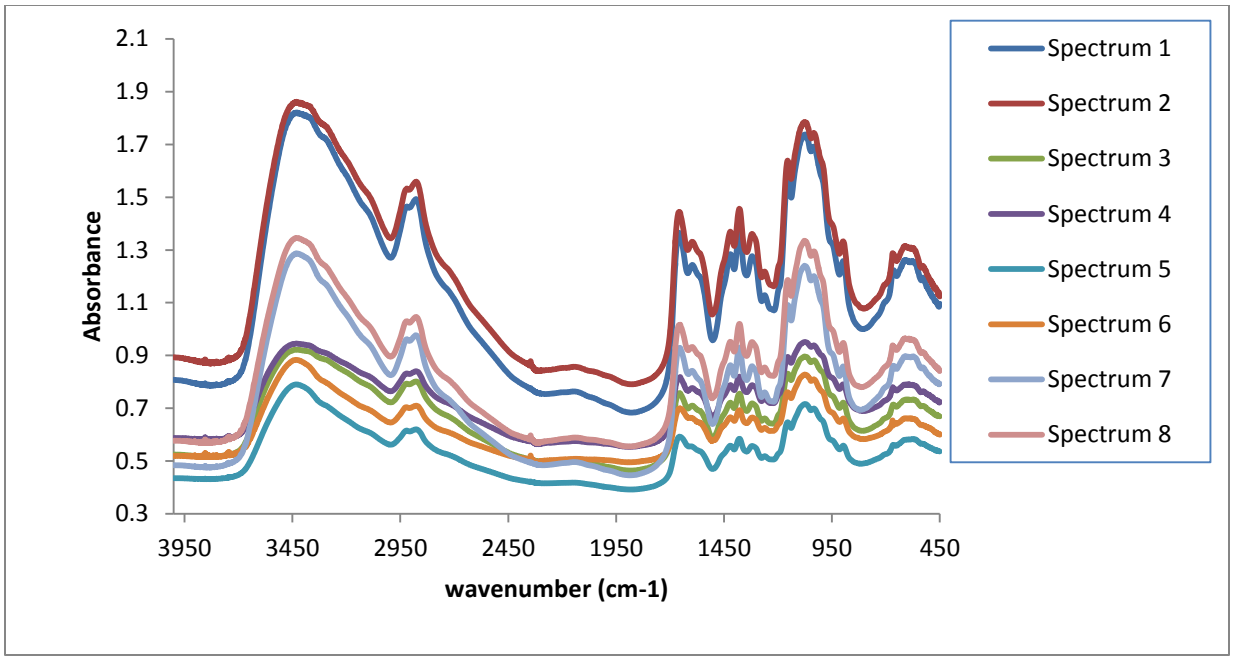

Figure 2.2: FT-IR spectra of CS used to calculate the Degree of Acetylation

Table 2.1: Degree of Acetylation calculated using FT-IR spectra shown in figure 2.2

Spectrum	**%DA**
Spectrum 1	77
Spectrum 2	78
Spectrum 3	81
Spectrum 4	83
Spectrum 5	85
Spectrum 6	86
Spectrum 7	77
Spectrum 8	79
Average	81
Standard Deviation	3

As illustrated in table 2.1, an average % DA of 81±3% was obtained by this method.

For ^{1}H NMR determination, the spectra were taken on a VNMRS 400 spectrometer at 70^{o}C. About 5 mg of chitosan sample which was previously vacuum dried at 50 ^{o}C for 2 days, was dissolved in 0.5 mL of 2 wt.% DCl/D2O solution at 70^{o}C. The degree of deacetylation (DA) was evaluated from the following equation using the integral intensity, I_{CH3}, of the CH_3 residue of N-acetyl, and the sum of the integral intensities, $I_{H2\text{-}H6}$, of protons 2-6 of the chitosan residue:[61]

$$DA(\%) = \left[1 - \left(\frac{1}{3} I_{CH_3} / \frac{1}{6} I_{H2-H6}\right)\right] 100 \qquad (2.4)$$

For the determination of DA by the 1H NMR method, a single solution was made and its NMR spectrum is shown in Figure 2.3 below. Using this method, the % DA of the CS was calculated to be about 78%. This value is very similar to the 75% DA specified by the manufacturer for this CS material.

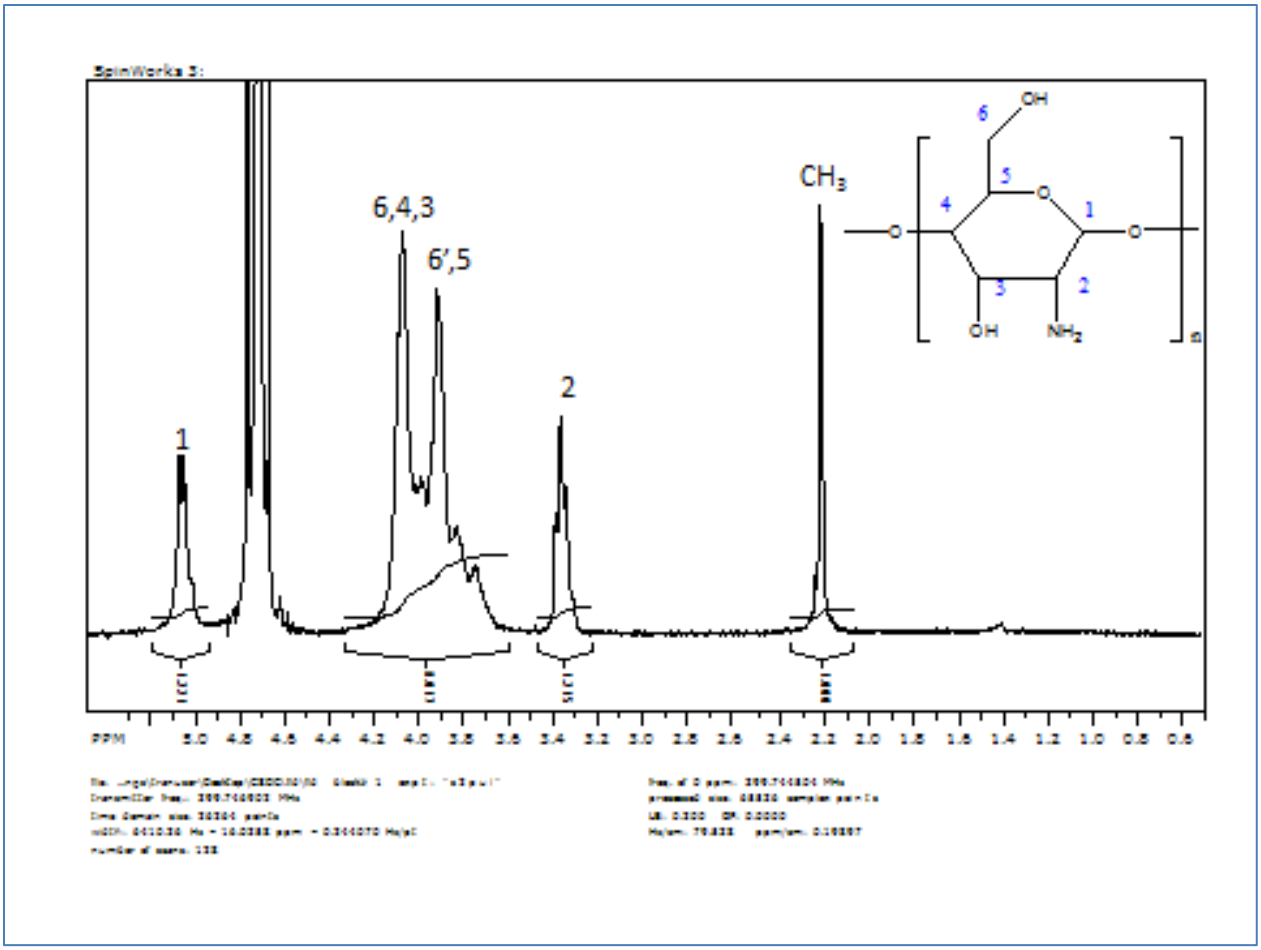

Figure 2.3: 1H NMR spectrum of CS dissolved in 2% w/w DCl/D2O at 70oC.

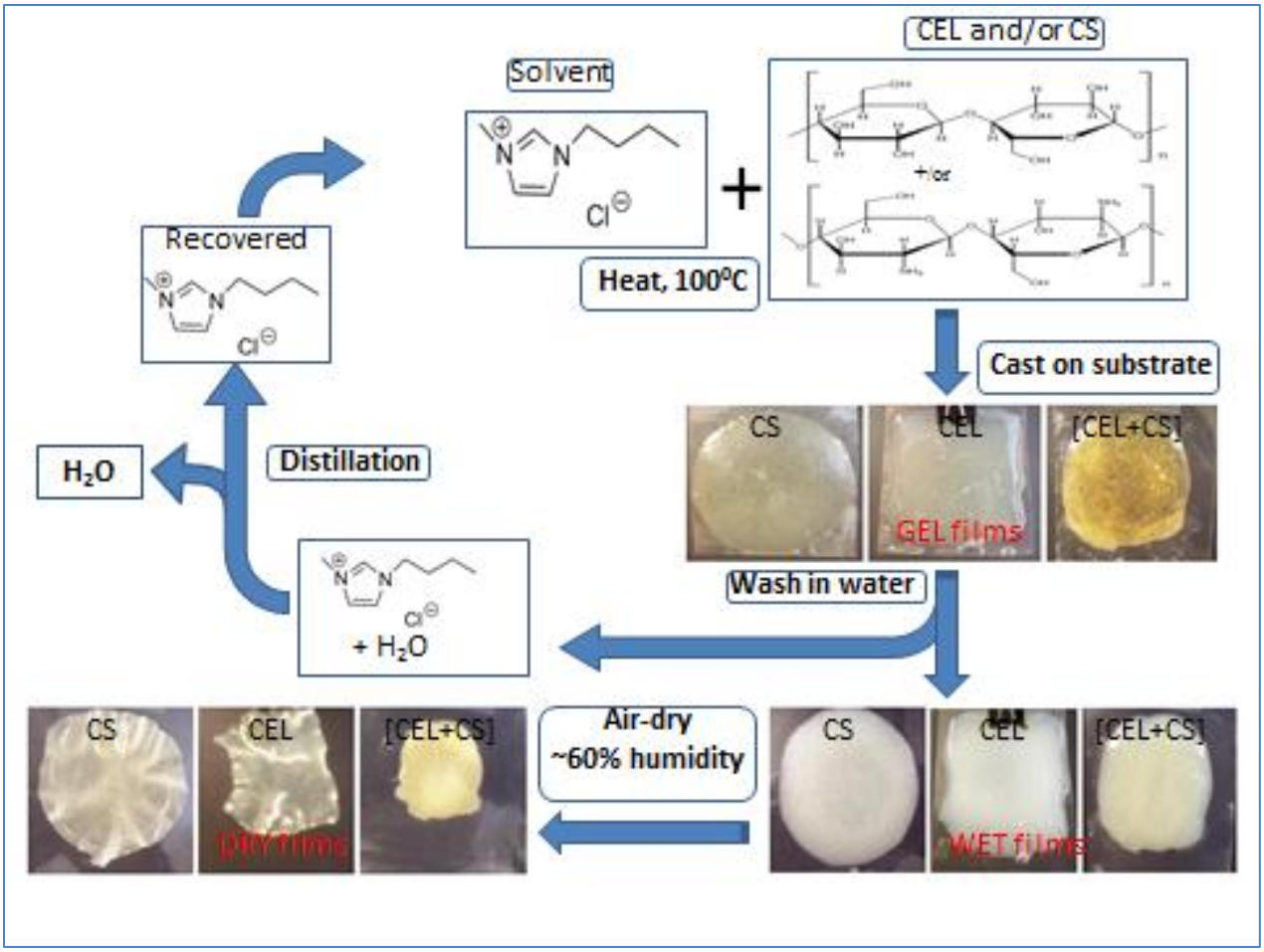

Scheme 2.2: Preparation procedure for the polysaccharide composite materials.

Scheme 2.2 summarizes the procedure used to dissolve and to regenerate films of CEL and/or CS with [$BMIm^+Cl^-$] as solvent. Homogeneous viscous solutions of CEL, CS or their composite mixtures were obtained by dissolving the polysaccharides in [$BMIm^+$ Cl^-] ionic liquid under magnetic stirring at 100 – 110 ^oC. Dissolution was performed in a 50 mL 3-neck round bottomed flask under Ar or N_2 atmosphere. For example, 15.0 g of [$BMIm^+$ Cl^-] ionic liquid was weighed into a 50 mL 3-neck round bottomed flask. 0.15 g (1%) of CS or CEL was added to the flask and the mixture stirred at about 200rpm at 100

^{o}C until the CS or CEL had completely dissolved. It was observed that CS would take longer to dissolve than CEL. Generally it would take just about one hour to completely dissolve a 1% w/w portion of CEL at 100^{0}C. However, it would take about 2.5 to 3 hr to dissolve the same amount of CS at the same temperature. A second portion of 0.15 g CS or CEL was then added to the flask and completely dissolved. Finally, a third portion of 0.15 g CS or CEL was added, bringing the total % wt. of the polysaccharides in the ionic liquid to 3%. The CS and CEL were dissolved in small portions. Each portion being approximately 1% w/w of the ionic liquid, as described in the example above. Each portion was completely dissolved before the next portion was added. 1% portions of either CEL or CS can be continued to be added to the flask until the desired concentration has been reached. For composite films, CEL was dissolved to the desired concentration first before dissolving CS. Using this procedure, solutions of CEL (containing up to 10% w/w (of IL)), CS (up to 4% w/w) and composite solutions containing CEL and CS in various proportions were prepared in about 6-8 hours. As described above, the actual time would depend on the final concentration of the composite that is being prepared.

Upon complete dissolution, the homogeneous solutions of the polysaccharides in [$BMIm^{+}$ Cl^{-}] were cast in to PTFE molds measuring about 105 mm x 79 mm x 3 mm on Mylar

sheets to produce thin films of the same dimensions with different compositions and concentrations of CEL and CS. If very thin films were desired, the homogeneous solutions of the polysaccharides in [$BMIm^{+}$ Cl^{-}] was cast on glass slides or Mylar sheets using a RDS stainless steel coating rod with appropriate size (RDS Specialties, Webster, NY) to produce the thin films.

The composites were then kept at room temperature for 24 hours to allow the solutions to undergo gelation . After 24 hours at room temperature, the polysaccharide composite solutions solidified to form GEL Films. The surface of the GEL films are sometimes covered by ionic liquid expelled from the gel matrix as they solidify. At this stage, the GEL films contain both the polysaccharides and the [$BMIm^+Cl^-$] ionic liquid. Taking advantage of the solubility of [$BMIm^+Cl^-$] in water, the ionic liquid was removed from the GEL films by a simple washing process in de-ionized water to yield "[$BMIm^+Cl^-$]-free" WET Films. The films were washed by soaking them in deionized water and stirring at about 250rpm. The ratio of water to gel film used during the washing process was about 50ml/g and the washing water was replenished with fresh deionized water once each day during the course of the 3-day washing period. As illustrated in Scheme 2.2, the [$BMIm^+ Cl^-$] used can be recovered by distilling the washed aqueous solution. Also taking advantage of the non-volatility property of the IL, the water can be easily distilled under vacuum at 100^oC. The recovered [$BMIm^+Cl^-$] was dried under vacuum at 70^oC overnight before reuse. If needed, recovered [$BMIm^+Cl^-$] can be decolorized by heating at 70°C with activated charcoal before removing the charcoal by filtration.

The amount of [$BMIm^+Cl^-$] that can be recovered from 1 synthesis cycle was calculated using two different composite films, a 100% CEL and 100% CS film. In this experiment, both CEL and CS were dissolved to 3% w/w using 38.7510g of [$BMIm^+Cl^-$] for each sample using the procedure described above. The samples were cast on Mylar substrates and left overnight. Each sample (now a gel film) was placed in a 2L beaker and about 1L of de-ionized water was added. The samples were then stirred on a magnetic

stirrer at room temperature and the washing water was replaced with fresh de-ionized water periodically. For this experiment, the washing water was replenished 3 times on the first day of washing and 2 times on day 2 and day 3. The UV spectrum of each washing solution was measured to determine the presence of [$BMIm^+Cl^-$] ionic liquid. Figure 2.4 shows the UV spectra obtained for a 100%CEL sample. The UV absorption spectrum of [$BMIm^+Cl^-$] is also included for reference. As expected, the amount of [BMIm+Cl-] in the washing solutions, indicated by the absorption bands around 214 nm and 290 nm progressively decreases with each washing solution. After 3 days of washing (6^{th} and 7^{th} washing) there was hardly any [$BMIm^+Cl^-$] detectable by the UV measurement.

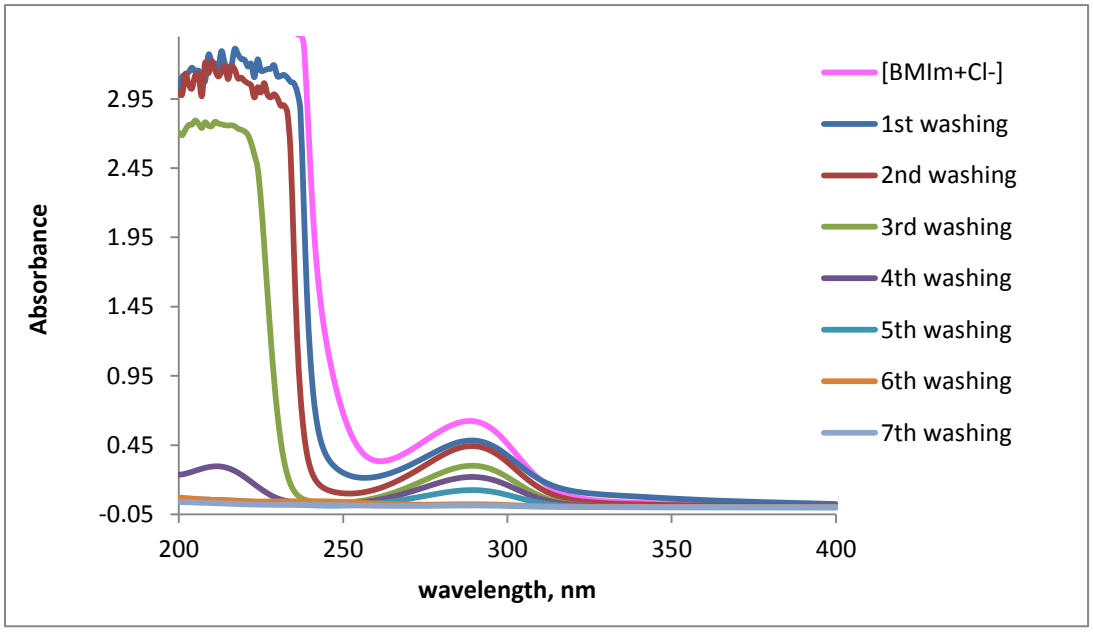

Figure 2.4: UV absorption spectra showing the progressive decrease in the amount of [BMIm+Cl-] present in the washing water at different stages of washing process for a 100%CEL sample.

Table 2.2: Amount of [BMIm+Cl-] recovered from the synthesis of 2 different composite films.

Sample	[$BMIm^+Cl^-$] used	Recovered [$BMIm^+Cl^-$]	% Recovery
100% CEL	38.7510g	34.4109g	88.80%
100% CS	38.7510g	33.8641g	87.40%
Average % Recovery			88.10%

The water in each washing solution was distilled to recover the ionic liquid and all the 7 portions were combined. Finally, the recovered ionic liquid was dried under vacuum at 70^0C overnight. After cooling to room temperature, the recovered ionic liquid weighed on a balance and the % recovery was calculated. Table 2.2 shows the amount of [$BMIm^+Cl^-$] used, the amount recovered and the calculated % recovery for each sample. As illustrated, the % recovered for the two films are very similar, giving an average % recovery of about 88.10%. The ability to recover a relatively high amount of the ionic liquid used is extremely important to the whole process because, in addition to the IL being non-volatile, it makes the whole process green and recyclable. The regenerated [CEL+CS] composite materials were then dried at room temperature in a chamber with humidity controlled at 60% to yield DRY Films. Drying time was found to be dependent on the thickness of the films but generally was in the range of 3 – 5 days. It was found that humidity control is important to ensure that the films do not become brittle and cracked during drying.

The amount of water remaining in the dried films was analyzed by Thermal Gravimetric Analysis (TGA). For this experiment, films were dried in the humidity

controlled chamber as described above for 5 days. After 5 days, the films were divided into 2. One piece was analyzed for the water content by TGA, and the other piece was placed in a desiccator and further dried under vacuum overnight, after which it was also analyzed for the water content by TGA. The two TGA curves are plotted together for 3 different composites in Figure 2.5. The film that was further dried in desiccator is shown in red and the other sample is shown in blue. The amount of water in the films appears as the first weight loss centered around 120^0C in the TGA curves. As illustrated in Figure 2.5, there seems to be little differences in the water content of the two films. The films that were further dried in the desiccator have lower water content than those that were only dried inside the humidity chamber. This is as expected considering the desiccant and low pressure inside the desiccator. More quantitative results can be obtained by further analysis of the TGA curves. An example of one such analysis, that was done using the TA Instruments weight loss analysis software, is show in Figure 2.6 below. Such analysis can give the amount of water lost during the heating ramp. The % water contend is obtained directly from this analysis. Results for the different samples are shown in Table 2.3.

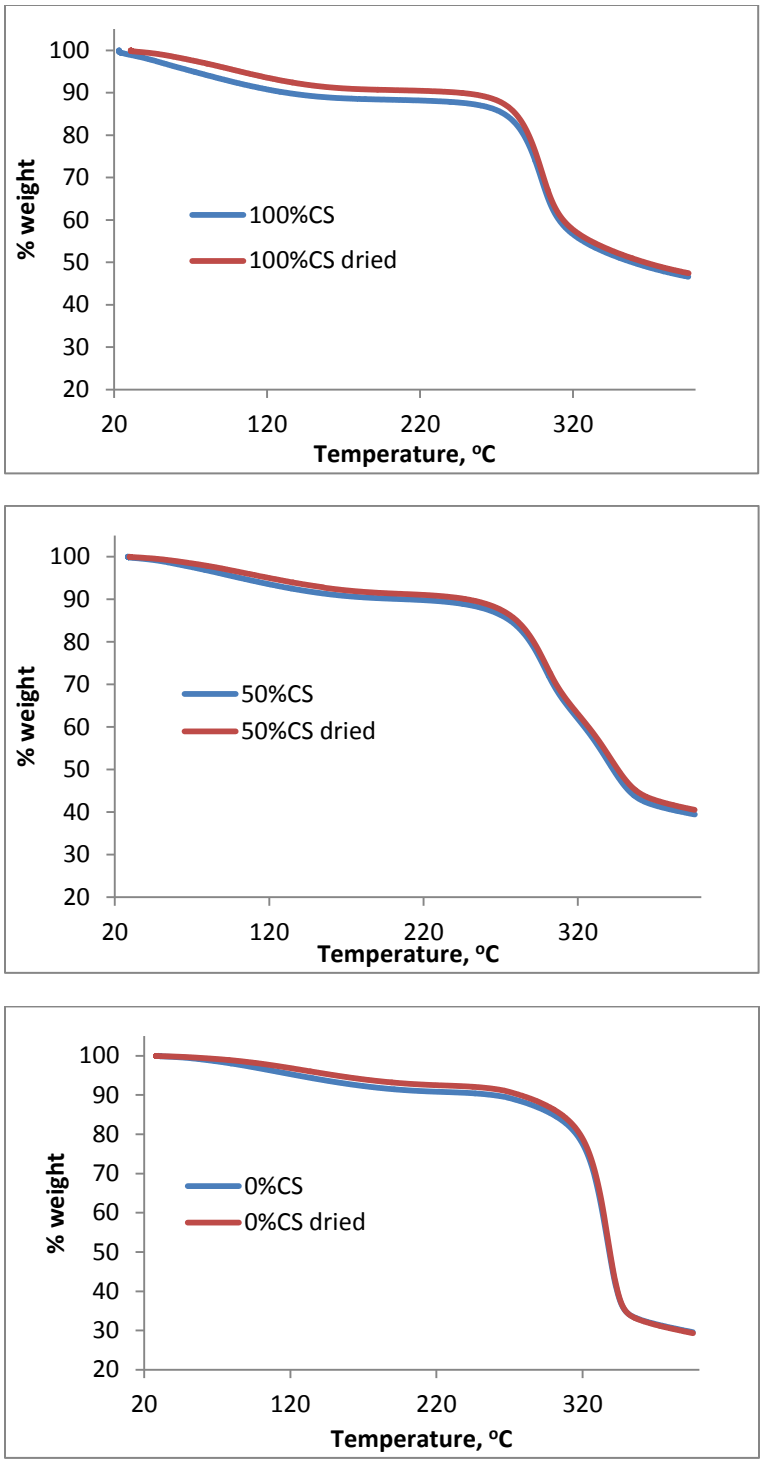

Figure 2.5: TGA curves showing water content in a film after drying in the humidity controlled chamber (blue curves) and after further drying in a desiccator (red curves).

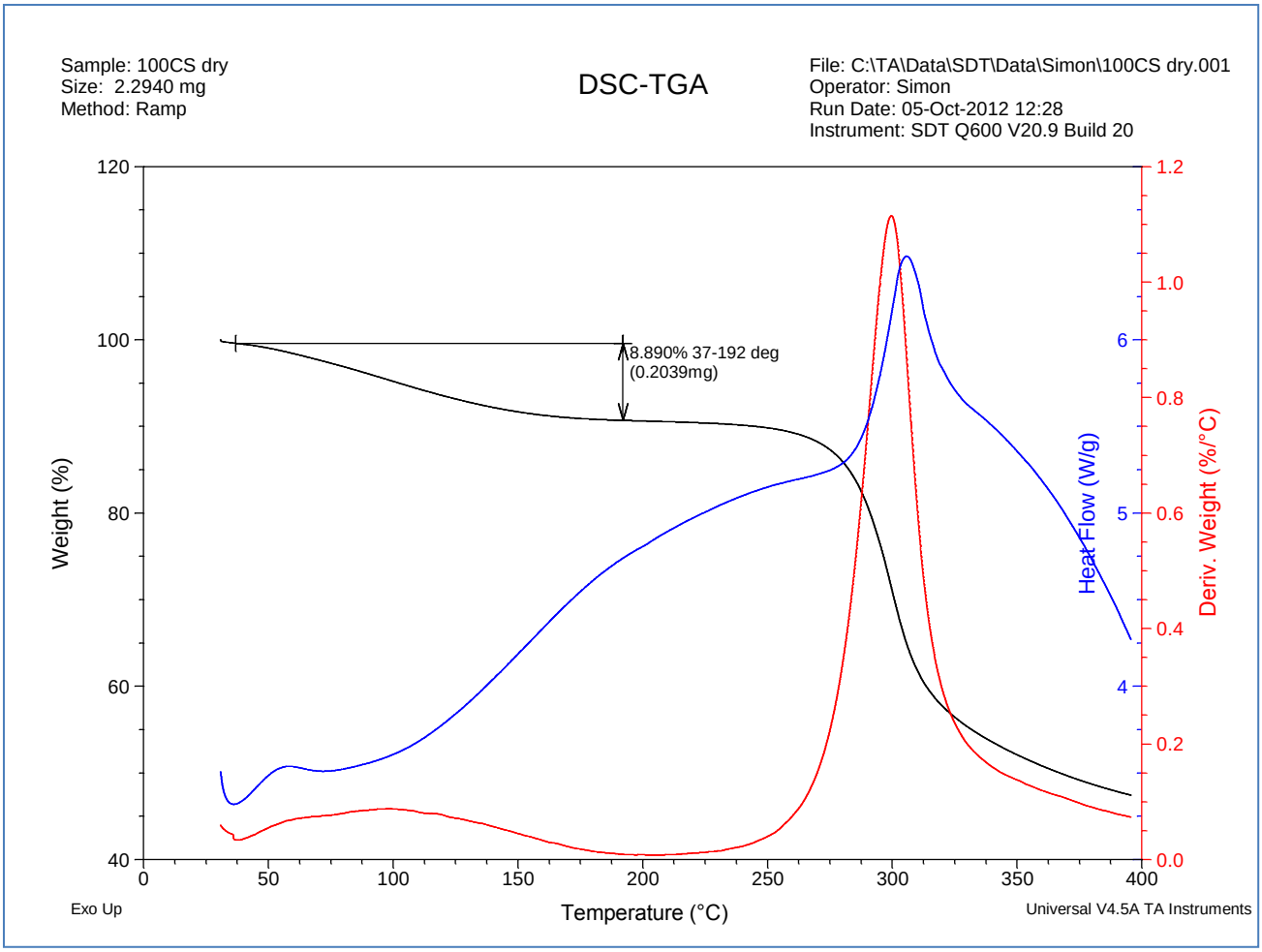

Figure 2.6: Illustration of the analysis of the water content in a given sample using TGA curve

Table 2.3: Comparison of the % water content in a normal dried film and after further drying in desiccator.

	Film composition		
Sample treatment	100% CS	50% CS	0% CS
Dry film	10.4%	9.5%	9.0%
Further Dried (Desiccator under vacuum overnight)	8.9%	8.5%	7.4%

The results in Table 2.3 indicate that further drying the samples in desiccator reduces the water content of the films by only about 1%. This is an indication of the effectiveness of the humidity chamber in drying the films. Another interesting trend observed from these results is the amount of water retained by films of different compositions. These results show that as the amount of CS in the composite is increased, the amount of water retained is also increased. It can be observed from Table 2.3 that 100%CS film has about 1.5% more water than its CEL counterpart.

Film composites with a porous, more open structure were obtained by lyophilizing the **wet films** instead of air-drying them. To lyophilize, the **wet films** in their PTFE molds were placed into a lyophilizing flask of appropriate size and cooled to liquid nitrogen temperature by immersing the lyophilizing flask containing the composites in liquid nitrogen for about 10 minutes. When the composites were equilibrated at the liquid nitrogen temperature, the flask was taken out and connected to the freeze-drying machine where the composites are freeze-dried under vacuum over 24 hrs.

2.4. Characterization of [CEL+CS] Composites

Scheme 2.2 contains photographs of CEL, CS and [CEL+CS] composite materials at various stages of preparation. Images of one-component (CEL or CS) film composites and two component [CEL+CS] film composites GEL films are shown in top center-right of the Scheme. After soaking in water for 3 days, [$BMIm^+Cl^-$] was removed from the gel film to yield corresponding wet films (shown on the bottom-right of the scheme). Finally, dried films (bottom-left) were obtained when the wet film was allowed to dry at room temperature in a humidity controlled chamber.

Various spectroscopic techniques including XRD, FTIR, NIR and ^{13}C Cross polarization-magic angle spinning NMR (CP-MAS-NMR) were used to follow and confirm the dissolution process, regeneration and to characterize the films. Details of the findings are described in the sections below.

2.4.1. XRD Spectroscopy

Powder XRD spectroscopy was used to confirm both the dissolution of the polysaccharides in [$BMIm^+Cl^-$] IL and their regeneration into solid dried films. Dried films were cut into small square pieces measuring about 2cm x 2cm and measured directly on the X-ray Diffractometer. A custom made holder was used to hold the samples in position during the measurement. [$BMIm^+Cl^-$] and GEL films were placed onto the normal XRD quartz sample holder and measured directly. Since [$BMIm^+Cl^-$] is viscous at room temperature, it was possible to measure this up to 2θ angles of about 60^o without losing any of the sample. Figure 2.7A shows the XRD spectra of CEL

composites at different stages of preparation. As illustrated, when microcrystalline CEL was dissolved in [$BMIm^+Cl^-$] (red spectrum), its crystalline diffraction peaks around, 14.7°, 16.3°, 22.5° and 34.6° completely disappears. In fact, the spectrum of the CEL gel is very similar to that of the [$BMIm^+Cl^-$] ionic liquid. This is confirmation of the dissolution of CEL in the ionic liquid. Similar results were also obtained for CS (Figure 2.7B), where the spectrum of the CS gel is similar to that of the [$BMIm^+Cl^-$] ionic liquid, meaning that this ionic liquid was able to completely dissolve the CS powder. The XRD spectra of the regenerated CEL film and 10:3 CEL:CS shows diffraction bands shifted from those of the microcrystalline CEL. The spectra seem to suggest that the morphological structure of the regenerated CEL films is less crystalline than that of the starting microcrystalline powder. The regenerated CS films however have XRD spectra much more similar to that of the starting CS powder.

As alluded to earlier, [$BMIm^+Cl^-$] is totally miscible with water, with an octanol-water partition coefficient (logP) of about -2.5. It is therefore easy to remove the [$BMIm^+Cl^-$] from the Gel Films by simply washing the films with water. Washing water (2L for a composite film of about 10cmX10cm) was repeatedly replaced with fresh water every 24 hrs until it was confirmed by monitoring UV absorption of the IL at 214 nm and 290 nm, that the IL was not detected in the washing water. It was found that after washing for 72 hours, no IL was detected in the washing water by UV measurements. Figure 2.8 shows the UV absorption spectra of the washing water taken over the 3 day washing period, one spectrum every 24 hrs. It can be observed from this figure that the UV spectrum of the washing water taken after 72 hrs does not have the characteristic UV absorption bands attributable to [$BMIm^+Cl^-$] which were clearly visible during the earlier stages of the

washing process. This is an indication that indeed, [$BMIm^{+}Cl^{-}$] can be removed to levels not detectable by UV by washing the films in water for about 3 days

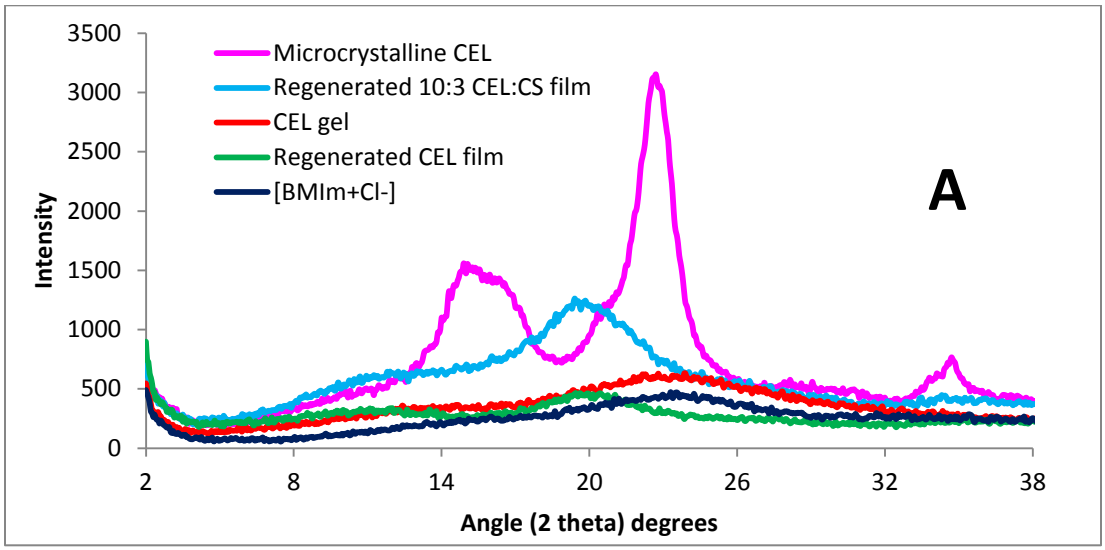

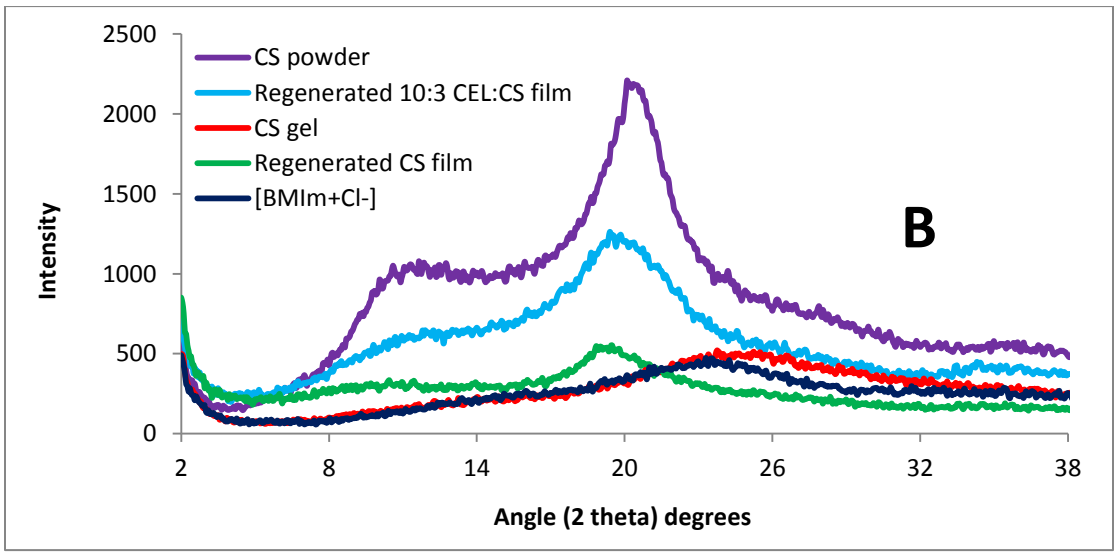

Figure 2.7: A) XRD spectra of microcrystalline CEL, regenerated [CEL+CS] film, CEL gel film, regenerated CEL film and [BMIm+Cl-] ionic liquid. B) XRD spectra of CS powder, regenerated [CEL+CS] film, CS gel film, regenerated CS film and [BMIm+Cl-] ionic liquid.

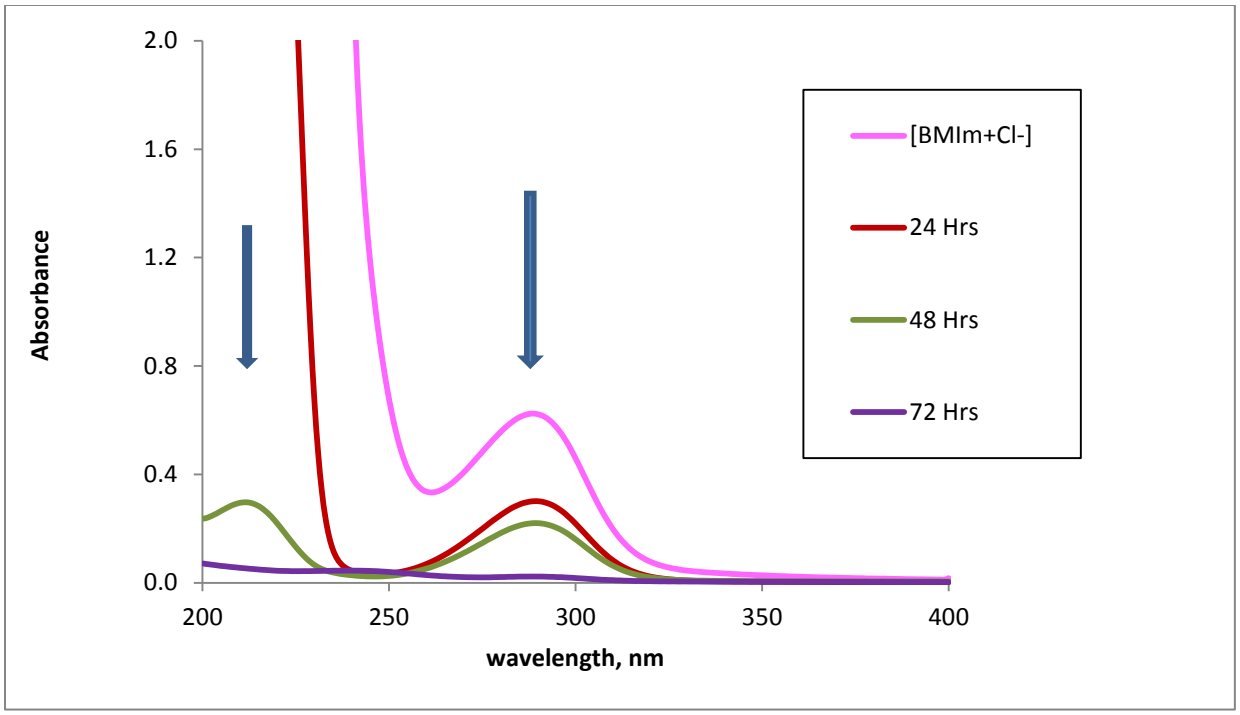

Figure 2.8: Disappearance of the [BMIm+Cl-] ionic liquid bands during washing.

2.4.2. Near-IR and FT-IR Spectroscopy

NIR and FT-IR techniques were also used to characterize the composite films. Figure 2.9A show the NIR spectra of three different types of gel films. At the gel stage of preparation, [$BMIm^+Cl^-$] ionic liquid is the major component in the films. Expectedly, the NIR of these gel films exhibit mostly the [$BMIm^+Cl^-$] indicator bands. These include the overtone and combination bands of the aliphatic C-H groups around 1388 nm and 1720 nm[64]

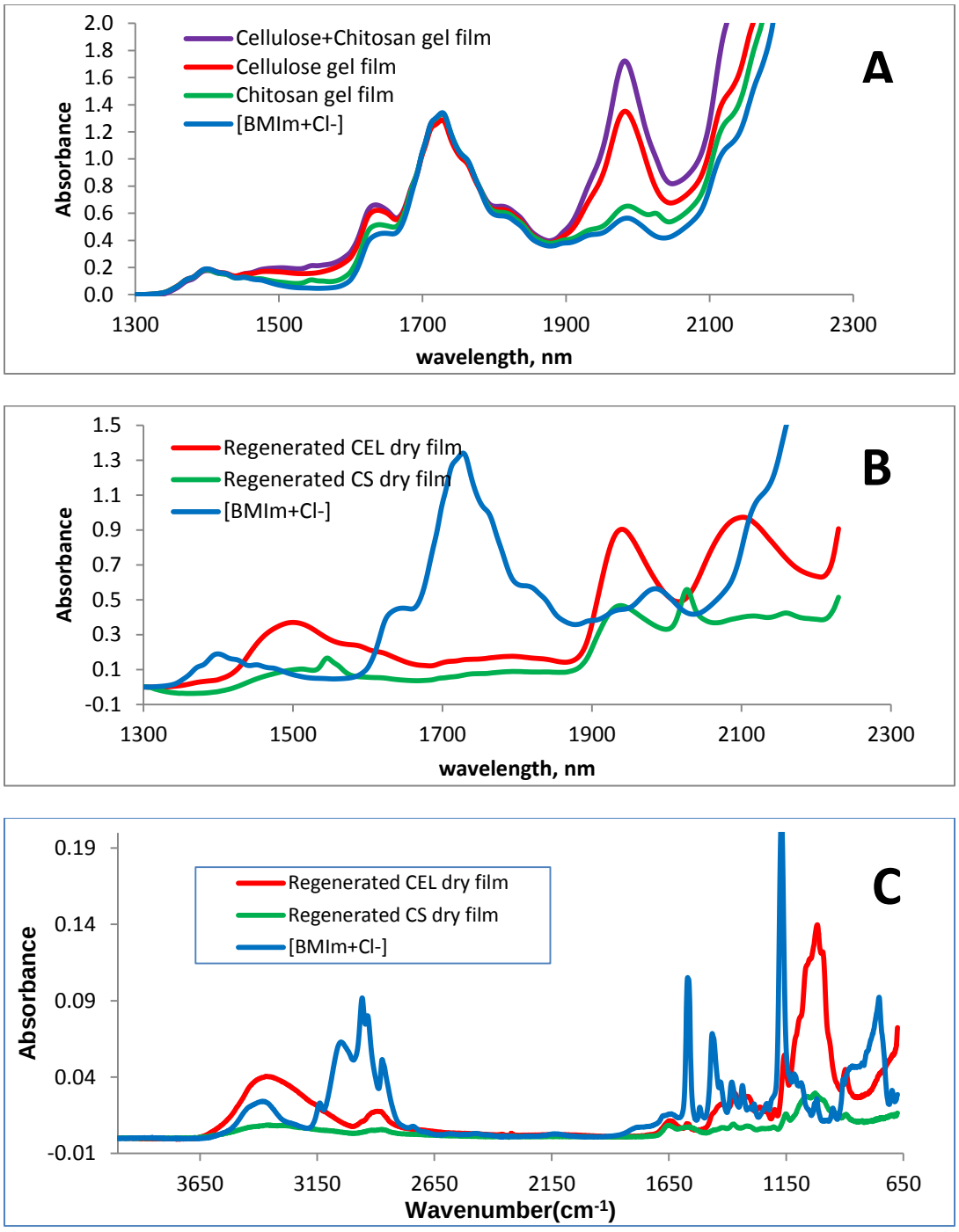

Figure 2.9: A) Near-IR spectra of [CEL+CS] Gel Film (purple), CEL Gel Film (red), CS Gel Film (green) and [BMIm+Cl-] ionic liquid (blue). B) Near-IR spectra of CEL Regenerated Dry Film (red), CS Regenerated Dry Film (green) and [$BMIm^{+}Cl^{-}$] ionic liquid (blue). C) FT-IR spectra of CEL Regenerated Dry Film (red), CS Regenerated Dry Film (green) and [BMIm+Cl-] ionic liquid (blue)

Figure 2.9B shows the NIR spectra of regenerated CS and regenerated CEL (dried) films. The NIR spectrum of the ionic liquid is also included for reference. It is clear from this figure that the NIR spectra of the regenerated films are much different from that of the ionic liquid. None of the [$BMIm^+Cl^-$] indicator bands are present in the NIR spectra of the CS and CEL regenerated films. This is also confirmation that the IL was successfully removed from the films to levels not detectable by the NIR technique. FT-IR of the same films further confirms this finding. Shown in Figure 2.9C are the FT-IR spectra of the same samples shown in Figure 2.9B with the spectra of [$BMIm^+Cl^-$] also included for reference. This IL has several FT-IR bands which can be attributed to aromatic C-H bending (756 cm^{-1}), -C=N- stretch (1173 cm^{-1}), aromatic C-H in plane bending (1468 cm^{-1}) and C=C stretch (1572 cm^{-1}). As illustrated in Figure 2.9C, these distinct IL bands are not present in the FT-IR spectra of the regenerated films. This further confirms the conclusion that by washing the films in water, the IL liquid is successfully removed from these films.

As previously described in the preparation section, the IL used was recovered by distilling the washed aqueous solution. As indicated in Figure 2.4, the UV spectra of the washing solutions does not show any more bands attributable to [$BMIm^+Cl^-$] ionic liquid after 72 hrs of washing (6^{th} and 7^{th} washing in Figure 2.4). The results in Table 2.2 showed that a similar amount of recovered from both 100%CS and 100%CEL films. The recovered [$BMIm^+Cl^-$] was dried under vacuum at 70^oC overnight before reuse. If needed, recovered [$BMIm^+Cl^-$] can be discolored by heating at 70°C with activated charcoal. As indicated in Table 2.2 at least 88% of [$BMIm^+Cl^-$] was recovered for reuse. As such, the method developed here is recyclable because [$BMIm^+Cl^-$] is the only

solvent used in the preparation and it is recovered for reuse. This is particularly important to the method developed here as it is not only green and recyclable, but is also economical in comparison to use of traditional solvents.

FT-IR and NIR spectroscopy were also used to analyze the chemical nature of the regenerated films. A comparison of the FT-IR spectra of the regenerated CEL film and the starting microcrystalline CEL is shown in Figure 2.10A. Similar comparison for CS powder and regenerated CS film is shown in Figure 2.10B. Microcrystalline CEL has bands characteristic bands for O-H vibrations (3400 cm^{-1}), C-H vibrations (2850 cm^{-1} – 2900 cm^{-1}) and the ether (-O-) group (890 cm^{-1} – 1150 cm^{-1}).[65–67] The regenerated CEL film exhibit similar bands, meaning that CEL was successfully regenerated without any chemical modifications. CS powder (Figure 2.10B) has characteristic FT-IR bands for O-H stretch (3400 cm^{-1}), N-H stretch (3250 cm^{-1} – 3350 cm^{-1}), C-H stretch (2850 cm^{-1} – 2900 cm^{-1}), C=O, amide 1 (1650 cm^{-1}), N-H deformation (1595 cm^{-1}), CH_3 deformation (1380 cm^{-1}), C-N stretch, amide III (1319 cm^{-1}) and –O-, ether bending (890 cm^{-1} – 1150 cm^{-1}).[65–67] It can be observed from Figure 2.10B that the FT-IR spectrum of the regenerated CS film is very similar to that of the starting CS powder, exhibiting all the characteristic bands described above.

A comparison of the NIR results of the same films further confirms the regeneration of the CS and CEL composite films without chemical modification. Shown in Figure 2.10C is a comparison of the NIR spectra of regenerated CEL film and microcrystalline CEL. CEL NIR band around 1492 nm, 1938 nm and 2104 nm can be attributed to overtone and combination bands for the O-H group. These bands are present in both the regenerated CEL film and the starting microcrystalline CEL. Figure 2.10D

also shows that the NIR spectra of CS powder and regenerated CS film are similar exhibiting bands around 1548 nm and 2028 nm in addition to the characteristic O-H bands described above for CEL. The additional bands in CS arise from the –NH modes.[50,51,67,68]

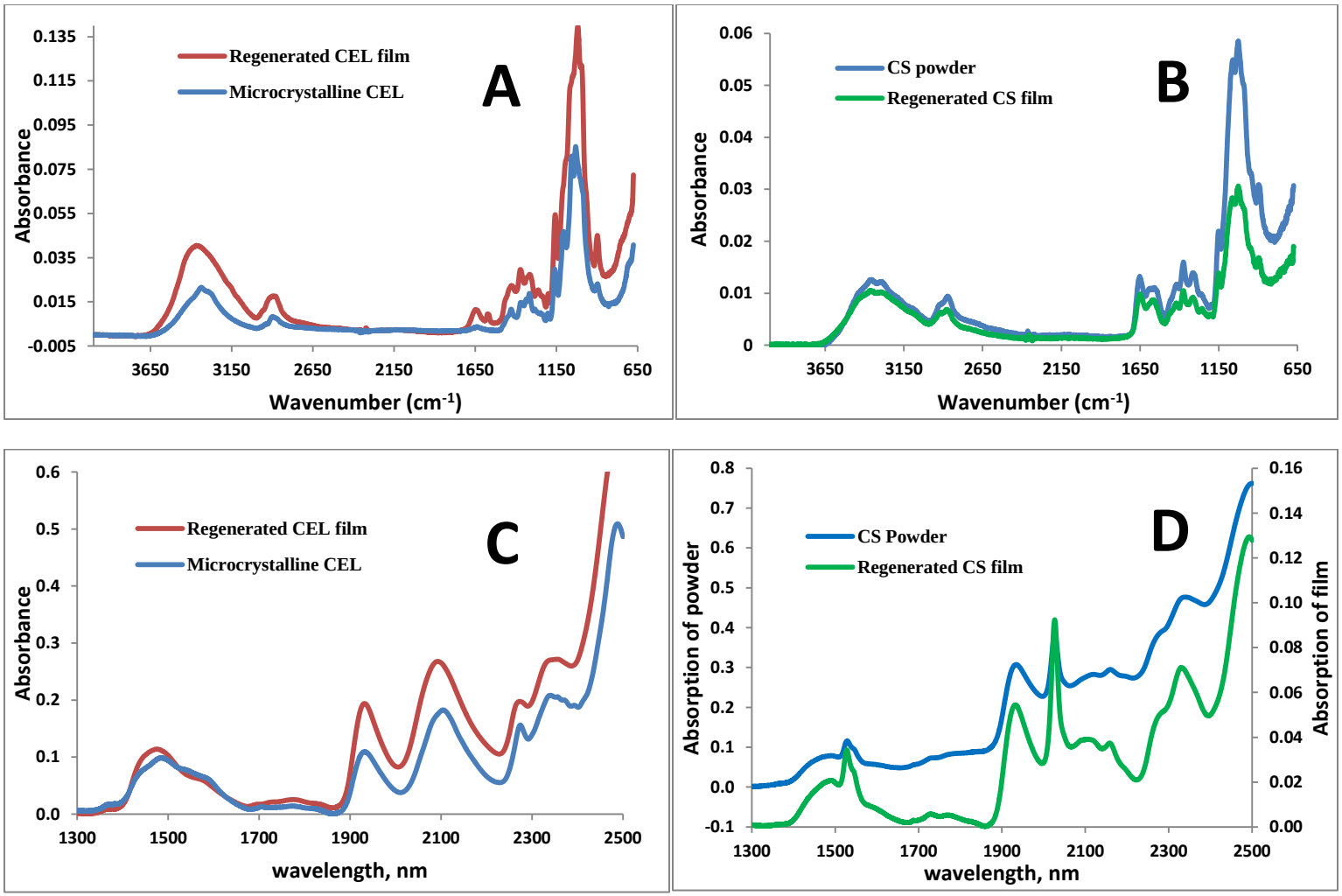

Figure 2.10: FTIR spectra (A and B) and NIR spectra (C and D) of microcrystalline CEL (blue), regenerated CEL film (red), CS powder (blue) and regenerated CS film (green) respectively

2.4.3. Characterization by solid state ^{13}C NMR spectroscopy

In the solid state, CEL exists in a variety of polymorphic forms, with two most common being cellulose I and cellulose II.[69] Cellulose I is the natural (native) polymorph and invariably occurs with a high degree of crystallinity; depending on the source,[69] the crystallinity can range from 60% to 90%. The cellulose II polymorph is obtained by mercerization or regeneration of cellulose from solution. If regeneration is carried out at high temperatures, cellulose IV can be produced. All regenerated celluloses have a much lower degree of crystallinity (e.g., ~40%) than the native form.[69] Several attempts at elucidating the three-dimensional structures of cellulose I and II have been made by using modern fiber diffraction methodology and sophisticated computer modeling.[70] The techniques of cross-polarization and magic-angle spinning have been developed in recent years to yield high-resolution NMR spectra of dilute nuclei (e.g., ^{I3}C) in the solid state.[69] In the particular case of cellulose, spectra have been reported by Earl and Vander Hart[69] and by Atalla and coworkers[71] that clearly indicate the utility of the technique. Both groups reported characteristic splittings for C- 1 in these spectra due to solid-state effects, giving rise to two peaks at 106.2 ppm and 107.9 ppm. In their study of cellulose II, Atalla and co-workers[71,72] interpreted the existence of two peaks for C-1 in terms of a nonequivalence of alternate glycosidic linkages along the molecular chain. This interpretation requires that dimeric anhydrocellobiose rather than anhydroglucose be considered the basic repeat unit of the cellulose II crystalline structure. It is clear from these studies that ^{13}C NMR technique can be used to study both structural and morphological nature of samples. We saw from the XRD results in Figure 2.7 that our

regenerated composite films do not exhibit the same crystalline morphology as that of the starting materials. ^{13}C CP-MAS-NMR technique was therefore employed to further confirm the chemical and morphological structure of our regenerated polysaccharide composite materials. Shown in Figure 2.11 are ^{13}C CP-MAS-NMR spectra obtained for regenerated dried films of CEL (purple spectrum D), CS (red spectrum B) and 5:3 CEL:CS composite (light blue spectrum A) together CS powder (green spectrum C) amorphous cellulose powder (black spectrum E) and microcrystalline cellulose powder (dark blue spectrum F). Chemical shifts of all six samples are listed in Table 2.4. As expected, the spectra of CS powder, amorphous CEL powder and microcrystalline CEL powder agree with the results previously reported[73–75]. As described above, Dudley et al.[69] and Atalla et al.[71,72] reported that in highly crystalline cellulose, the alternate glycosidic linkages along the chain are non-equivalent, giving rise to two peaks for C-1. Our results for both the microcrystalline cellulose and the regenerated cellulose films do not show any splitting for the C-1. This is an indication that our regenerated cellulose films and the starting microcrystalline cellulose powder are not as crystalline as those reported by Dudley et al.[69] and Atalla et al.[71,72] The 13C NMR spectrum of our regenerated cellulose film is very similar to that of the amorphous cellulose reported by Murata et al.[76] (black spectrum in Figure 2.11) which did not have splitting for the C-1 peak. The amorphous nature of the regenerated cellulose films observed here by 13C NMR also confirms the results obtained by XRD described in the previous section for the same films.

Table 2.4: ^{13}C NMR chemical shifts for different polysaccharides and regenerated films

	Carbon chemical shifts (ppm)						
	C_1	C_2	C_3	C_4	C_5	C_6	CH_3
Regenerated cellulose film	104.6	74.1	74.1	83.2	74.1	62.0	
Amorphous cellulose powder	105.7	74.8	74.8	84.4	74.8	63.0	
Microcrystalline cellulose powder	104.9	72.1	74.6	83.7, 88.7	74.6	64.7, 62.3	
Regenerated chitosan film	104.7	56.3	75.4	83.5	75.4	61.0	22.7
Chitosan powder	104.9	57.3	74.7	82.8	74.7	60.1	23.4
Regenerated cellulose+chitosan film	104.5	56.4	75.5	83.9	75.5	61.5	23.0

The observed similarity between spectra and chemical shifts of corresponding carbons of regenerated dried films of CS and CEL to those of powder CS and powder of amorphous CEL is a clear indication that CEL and CS were successfully regenerated. Of particular interest is the fact that the spectrum of regenerated CEL film is similar to that of the amorphous CEL powder, and is distinctly different from that of microcrystalline powder. This can be clearly seen at band corresponding to C_4 which is only a broad single band at 83.9 ppm, 84.4 ppm, respectively for regenerated CEL and amorphous CEL, but a

doublet at 88.7 ppm and 83.7 ppm for crystalline CEL powder. These results seem to indicate that when microcrystalline CEL was dissolved by and regenerated from the IL, the regenerated CEL has relatively lower crystallinity than the microcrystalline CEL because IL disrupted inter- and intramolecular hydrogen bond network during the dissolution process. As a consequence, the regenerated CEL adapts an amorphous structure.

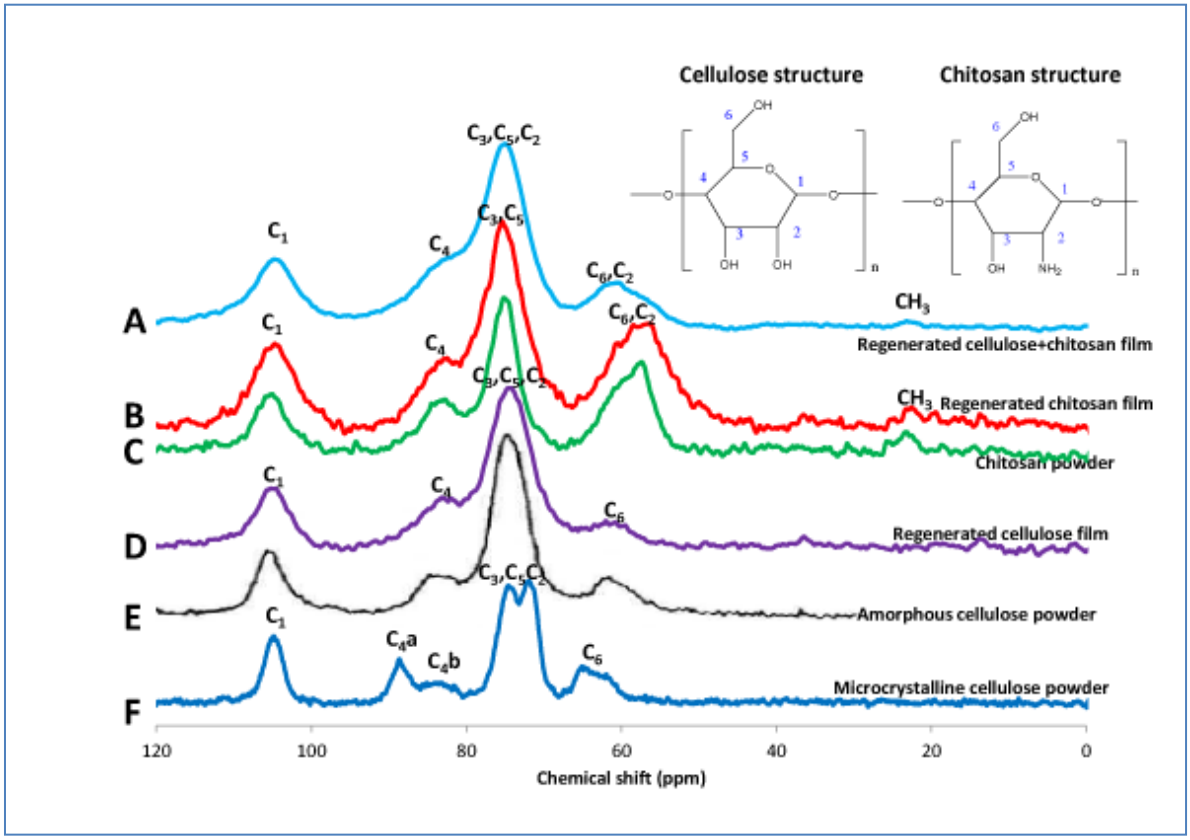

Figure 2.11: ^{13}C CP MAS NMR spectra of regenerated CEL, CS, [CEL+Cs] composite films, CS powder, Microcrystalline CEL, and amorphous CEL

These results not only confirm conclusion based on XRD results presented in previous section but also are in agreement with other previous studies[73–75]. CEL has relatively different chemical shifts compared to those of CS, particularly C2 and C6; i.e., in CEL, a single C6 band is at 62.0 ppm, C2 is together with C3 and C5 in a large band at 74.1 ppm whereas in CS, C2 and C6 are together in a band at around 61.0 ppm, and the large band at 75.4 ppm is due only to C3 and C5. Since these bands can be resolved into individual bands corresponding to C2, C3, C5 and C6 for each CEL and CS component of composite materials, it is possible to determine concentration of each polysaccharide component in composite materials using the CP-MAS-NMR technique. Of particular interest is the presence of the band corresponding to carbon of CH_3 group in CS and CEL:CS composite material (but not in CEL) at around 22.7 ppm. This band can be attributed to remaining acyl groups of chitin, namely, chitosan obtained from commercial sources is not 100% but, as specified by the manufacturer in our case, is only >75% converted from chitin. As reported earlier, the % DA of the chitosan used here was calculated to be 78% by ^{1}H NMR and 81% by FT-IR spectroscopy, meaning that indeed there are still some residual CH_3 groups which can give rise to the observed band at about 22.7ppm.

2.4.4. Morphological analysis of the [CEL+CS] composite materials

Scanning Electron Microscopy (SEM)

A scanning electron microscope (SEM) produces images of a sample by scanning it with a focused beam of electrons. The electrons interact with atoms in the sample, producing various signals that can be detected and that contain information about the sample's surface topography and composition. The types of signals produced by a SEM include secondary electrons, back-scattered electrons, characteristic X-rays, light (cathodoluminescence) (CL), specimen current and transmitted electrons. Secondary electron detection is standard in all SEMs, but it is rare that a single machine would have detectors for all possible signals. These various signals result from interactions of the electron beam with atoms at or near the surface of the sample. If a sample is made up of different compounds with different electrical properties, each compound can give rise to a different SEM signal. This can therefore yield information about the chemical composition of the sample. In the most common or standard detection mode, secondary electron imaging or SEI, the SEM can produce very high-resolution images of a sample surface, revealing details about the surface structure of a sample. SEM can be used to study both the surface and cross section of samples depending on the orientation of the sample during measurement. SEM was therefore used to study the morphological structure and chemical composition of the regenerated CEL, CS and [CEL+CS] composite materials. Shown in Figure 2.12 are surface images (left) and cross section images (right) of regenerated one component CEL film (top) and CS film (middle) as well as 50:50 CEL:CS composite film (bottom) images. One aspect that can be clearly

seen from the images is that in both the surface and cross section images, the 100%CEL and 100%CS composites are homogeneous. Even though the chemical difference between the CS and CEL are the few $-NH_2$ groups in CS, the SEM images of these two materials have some interesting morphological differences. CS seems to exhibit a much smoother structure, with CEL arranging itself into a fibrous structure with fibers having diameter of about ~0.5–1.0 micron.

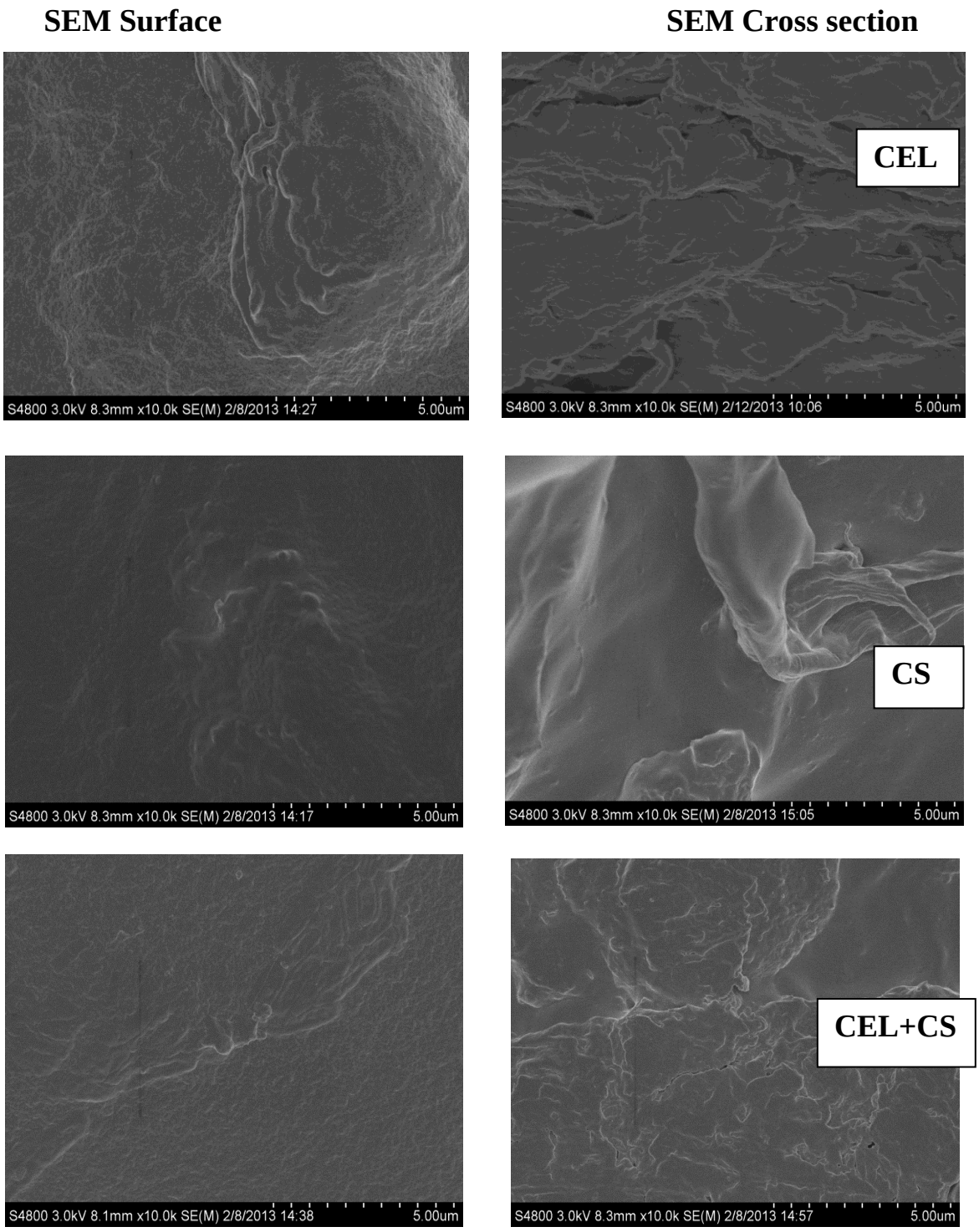

Figure 2.12: SEM images of surface (left) and cross section (left) of regenerated CEL film (top), regenerated CS film (middle) and 50:50 [CEL+CS] composite film (bottom)

The 50:50 CEL:CS composite material is interesting in that it is not only homogeneous but it is more similar to the structure of CS than that of CEL, namely, it has a rather smooth structure with much fewer fibrous forms than CEL. The results show that CEL and CS composite materials with a homogeneous morphological surface and cross section structure have been successfully prepared by dissolution in [$BMIm^{+}Cl^{-}$] ionic liquid and regeneration from water.

Analysis by Atomic Force Microscopy (AFM)

Surface-morphology characterization of polymeric films is essential because the surface properties influence the interactions that may occur between the film and the external environment. Advances in a number of scanning probe microscopy techniques have made obtaining nanoscale lateral information of surfaces possible for polymeric materials.[77–80]

Although scanning tunneling microscopy is effective for characterizing conducting materials, atomic force microscopy (AFM) is suited for examining nonconducting materials.

In AFM, a probe consisting of a sharp tip (nominal tip radius on the order of 10 nm) located near the end of a cantilever beam is scanned across the sample surface using piezoelectric scanners. Changes in the tip-sample interaction are often monitored using an optical lever detection system, in which a laser is reflected off of the cantilever and onto a position sensitive photodiode. During scanning, a particular operating parameter is maintained at a constant level, and images are generated through a feedback loop

between the optical detection system and the piezoelectric scanners. Three imaging modes can be used to produce topographic
images of sample surfaces. These are contact mode, noncontact mode, and tapping mode AFM (TMAFM). TMAFM tends to be more applicable to general imaging of soft samples, such as biological and polymeric materials, under ambient conditions[77,79,81–87] and was used exclusively in this work.

In tapping mode, the cantilever oscillates close to its first bending mode resonance frequency (normally on the order of 100 kHz) so that the tip makes contact with the sample only for a short duration in each oscillation cycle. As the tip approaches the sample, the tip-sample interactions alter the amplitude, resonance frequency, and phase angle of the oscillating cantilever. During scanning, the amplitude at the operating frequency is maintained at a constant level, called the set-point amplitude, by adjusting the relative position of the tip with respect to the sample. This method of operation results in lower surface forces, particularly lateral forces, compared to those of contact mode so less surface damage is inflicted while maintaining higher lateral resolution than can often be achieved with noncontact mode.[77]

One recent development in TMAFM is the use of the changes in phase angle of the cantilever probe to produce a second image, called a phase image or phase contrast image. This image often provides significantly more contrast than the topographic image and has been shown to be sensitive to material surface properties, such as stiffness, viscoelasticity, and chemical composition.[78,81,88,89] In general, changes in phase angle during scanning are related to energy dissipation during tip-sample interaction[90] and can be due to changes in topography, tip-sample molecular interactions, deformation at the

tip-sample contact, and even experimental conditions.[91] However, while the relationship between changes in energy dissipation and changes in material properties is not well understood, the enhanced contrast that can be obtained often allows for distinguishing different material phases and constituents.[78,81] The tapping phase and topography images of cellulose, chitosan and [CEL+CS] composite films are shown in Figure 2.13. The dimensions of the images are 2 μm x 2 μm.

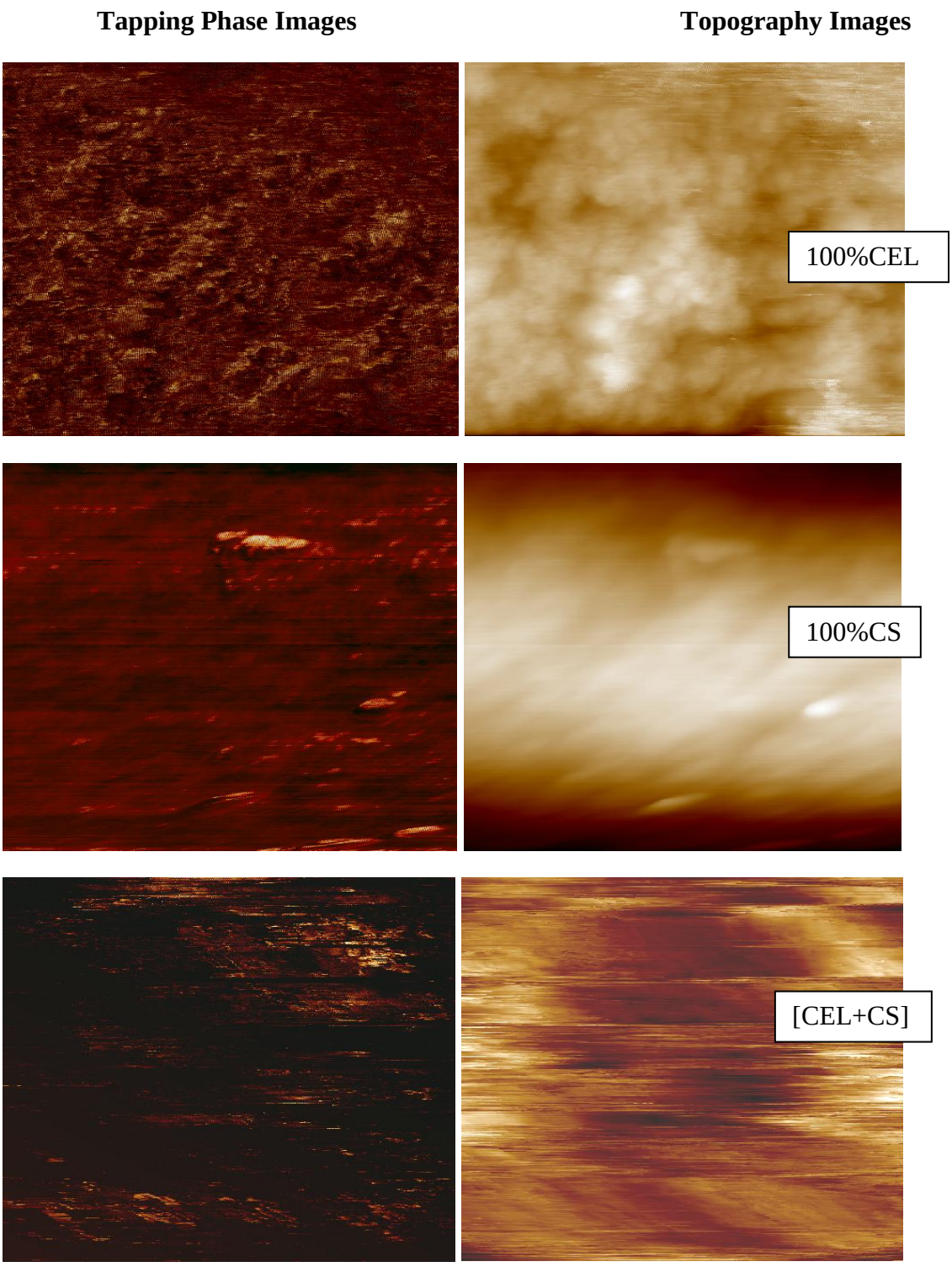

Figure 2.13: AFM tapping phase(left) and topography images (right) for 100%CEL (top) 100%CS (middle) and [CEL+CS] composite materials. All images are 2 µm x 2 µm.

As illustrated above, the tapping phase image of the 100%CEL shows that the surface of this film is not smooth but is relatively ‘rough’ across its whole surface. Besides the roughness of the surface, the sample seems to appear the same throughout. This could be an indication that while the surface may be rough and not smooth, the sample itself may be homogeneous. In contrast, the AFM tapping phase image of the 100%CS sample appears to be much smoother than that of the 100%CEL sample. However, this sample also appears to be homogenous. These results are also confirmed by the topography images of the samples shown on the right in Figure 2.13. The 100%CEL topography images clearly shows some ‘valley’ areas (appear dark in the image) and some ‘high’ areas (which appear bright in the image). The 100%CS topography image however is smooth and bright across its center and is darker on the edges. This could be caused by a curved sample, where the center of the sample is curving upwards (hence appear bright) and the edges curving downwards (hence appear dark). The AFM images of the [CEL+CS] composite film appear somewhat intermediate between those of the 100%CEL and 100%CS. The [CEL+CS] images are not as smooth as the 100%CS images, but they also are not as rough as the 100%CEL. The AFM results obtained here are in complete agreement with the SEM results, which also showed a smoother surface for the 100%CS sample, whereas the 100%CEL appeared much less smooth with some fibrous structures.

2.5. Properties of CEL, CS and [CEL+CS] Composites

2.5.1. Mechanical properties

As described above, the mechanical strength of CS is so poor that practically it cannot be used by itself for applications based on its unique properties. Measurements were made to determine tensile strength of pure CS film and (CS+CEL) composite films with different CEL concentrations in order to determine if by adding CEL into CS, the [CEL+CS] composite material would have adequate mechanical strength for practical applications. Results obtained, shown in Table 2.5 and graphically in Figure 2.14, clearly indicate that adding CEL into CS substantially increase its tensile strength. For example, up to 5X increase in tensile strength can be achieved by adding 80% of CEL into CS, and that the tensile strength of the composite material can be adjusted by adding judicious amount of CEL. The tensile strengths of [CS+CEL] composite materials made by our method are comparable with those of existing CS materials including those prepared by either grafting or copolymerization with other chemicals[92–97].

Table 2.5: Mechanical strength of [CEL+CS] composite materials

%CS	%CEL	Tensile strength(MPa)
100	0	12±4
67	33	17±4
50	50	23±5
40	60	41±9
29	71	52±9
20	80	72±5
0	100	83±5

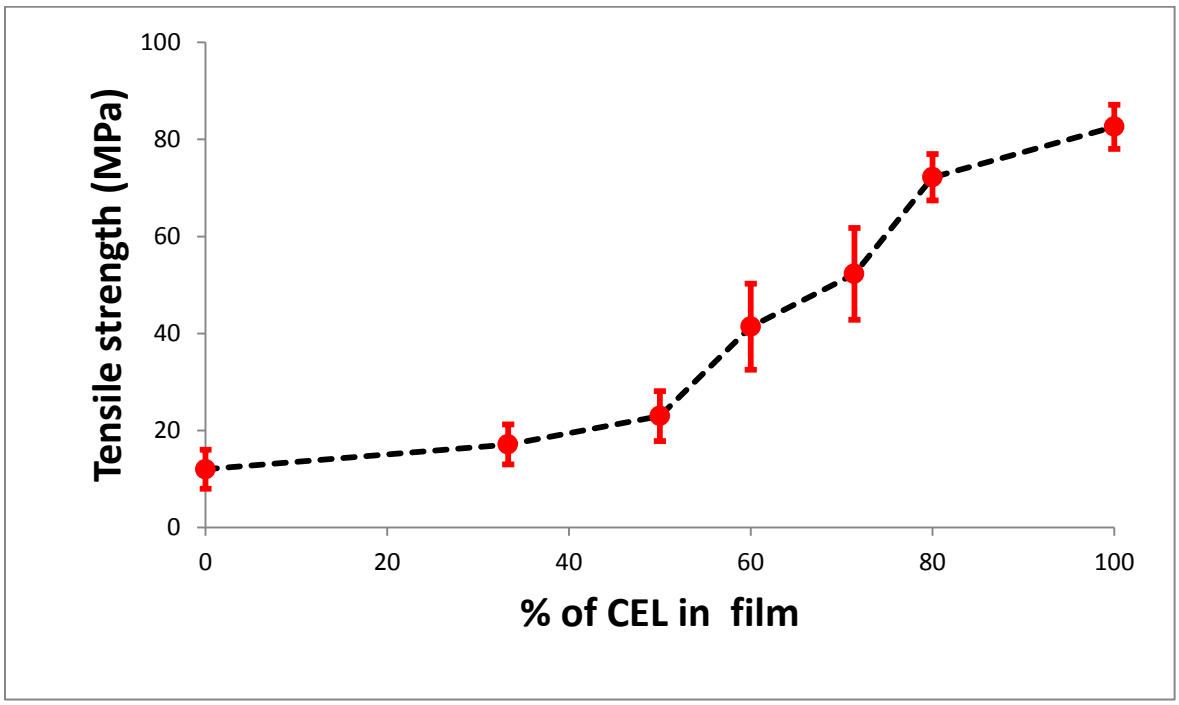

Figure 2.14: Plot of tensile strength as a function of CEL concentration in [CS+CEL] composite films

2.5.2. Rheological properties

The swelling of CS in water is good for the diffusion of small molecules through its structure for some applications such as pollutant adsorption and drug delivery systems. However, this seemingly attractive feature of CS inadvertently leads to a further weakening of the CS structure. The tensile strength measurements showed that addition of CEL to CS improves the mechanical properties of the resultant composites. Since CEL still undergoes swelling in water, it was important to investigate the rheological properties of the [CEL+CS] composite in order to determine the best possible composition which has good mechanical and rheological properties but still retaining the attractive CS properties. Kinetics of swelling of different [CEL+CS] composites were measured. The results are shown in Figure 2.15A. The results show that swelling in water occurred rapidly for all composites, reaching equilibrium in about 120 minutes. However, the swelling ratio was found to be proportional to the concentration of CEL in the composite. The results of the kinetics of swelling are shown in Table 2.6. 100%CEL had the highest swelling ratio of about 270% while 100%CS had the least value of about 80%. The equilibrium water content (EWC%) gives a more quantitative of the amount of water absorbed by the composites during swelling. EWC values are plotted together with tensile strength results in Figure 2.15B. While tensile strength increases with CEL concentration, EWC decreases with CEL concentration. Interestingly, the increase in tensile strength with CEL content is much larger than the decrease in EWC. This is particularly important as it allows the synthesis of composite materials with substantial tensile strength by adding only a small amount of CEL. Also, both the tensile strength

and the swelling properties of the [CEL+CS] composite materials can be ‘tuned’ to a desired level by carefully adjusting the concentration of CEL in the composites.

Table 2.6: Parameters of swelling kinetics of [CEL+CS] composite materials

	Pseudo 2nd order					Swelling Power		
	Equilibrium Swelling, Seq(%)	**Equilibrium water content, EWC(%)**	**Initial swelling rate $(dS/dt)_{0,}$ $g_{water}(g_{gel})^{-1}min^{-1}$**	**Swelling rate constant, k, $g_{gel}(g_{water})^{-1}min^{-1}$**	**r^2**	**Swelling exponent, n**	**Swelling constant, K**	**r^2**
100% CS	282.1	73.6	110.0	0.00138	0.9993	0.52	1.49	0.9939
67% CS	229.9	69.9	141.5	0.00268	0.9999	0.61	1.33	0.9891
50% CS	163.3	62.2	80.4	0.00302	0.9999	0.51	0.64	0.9636
29% CS	141.3	58.5	82.9	0.00415	0.9999	0.71	0.77	0.9934
0% CS	86.6	46.4	166.4	0.02219	0.9997	0.69	0.57	0.9943

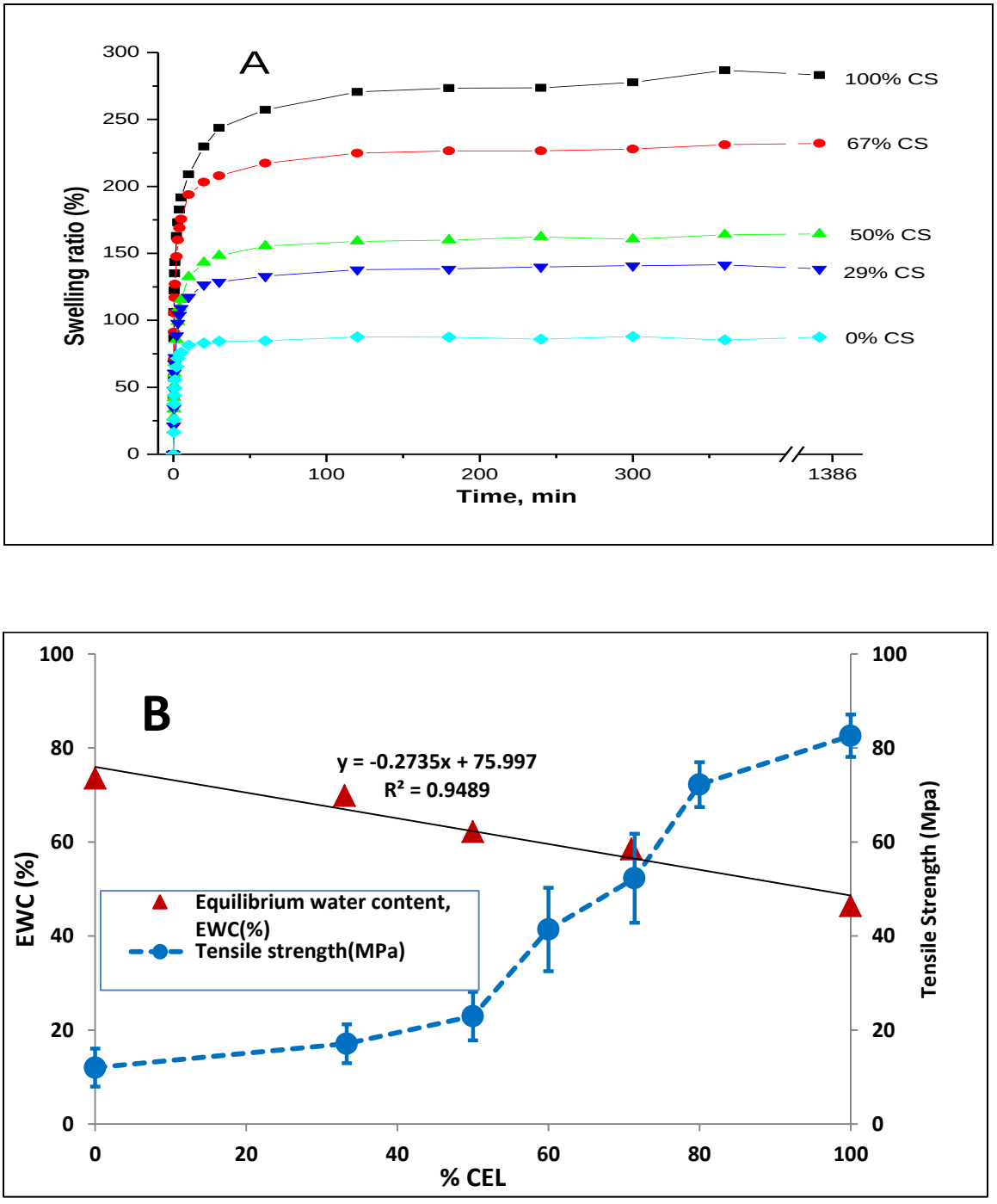

Figure 2.15: A) Swelling kinetics of different [CEL+CS] composite films. B) Plot of tensile strength and equilibrium water content (EWC%) as a function of CEL concentration

However, the relative increase in the tensile strength is much larger than the decrease in the swelling. For example, tensile strength of 100% CEL is 82.6 MPa which is 588% higher than that of 0% CEL (12.0 MPa) whereas its EWC% value of 46.4% is only 58% lower than the value for 73.6% for 0%CEL. This finding is particularly important because it clearly indicates that mechanical strength of the composite can be substantially strengthened by adding CEL. The composite still can retain its unique properties which are due solely to CS.

2.5.3. Thermal properties

Thermal gravimetric analysis (TGA) was also performed to determine thermal properties of the composite materials. The results are shown in Figure 2.16. Also shown as an insert in Figure 2.16 is % weight loss for composite films plotted as a function of CEL content in the films. Two main weight loss steps are seen in the Figure 2.16. The first weight loss occurs around 100^{o}C and is predominant in low CEL containing films and is attributed to loss of moisture. The second major weight loss occurs from about 250^{o}C to 350^{o}C. This weight loss is associated with chemical transformation leading to thermal degradation of the films. As illustrated by the insert in the figure, the onset of this degradation occurs at higher temperatures for high CEL containing films (greater than 70% CEL) than for low CEL containing films. In fact the decomposition temperature is generally the same from 0% CEL to about 70% CEL, thereafter it increased with increasing CEL content. Figure 2.17 shows the derivative of the TGA weight loss curves, which shows in more detail the various steps in the degradation process. As illustrated in this figure, the 0% CEL (i.e., film with only CS) has only one major degradation step at

about 287^{o}C. Hundred percent CEL also shows one major degradation step at about 323^{o}C. However, composite films have two major degradation steps. As illustrated for a 50:50 CEL:CS composite film in the insert in Figure 2.17, the two steps in the degradation of this composite film seem to correspond to that of CS and CEL, respectively.

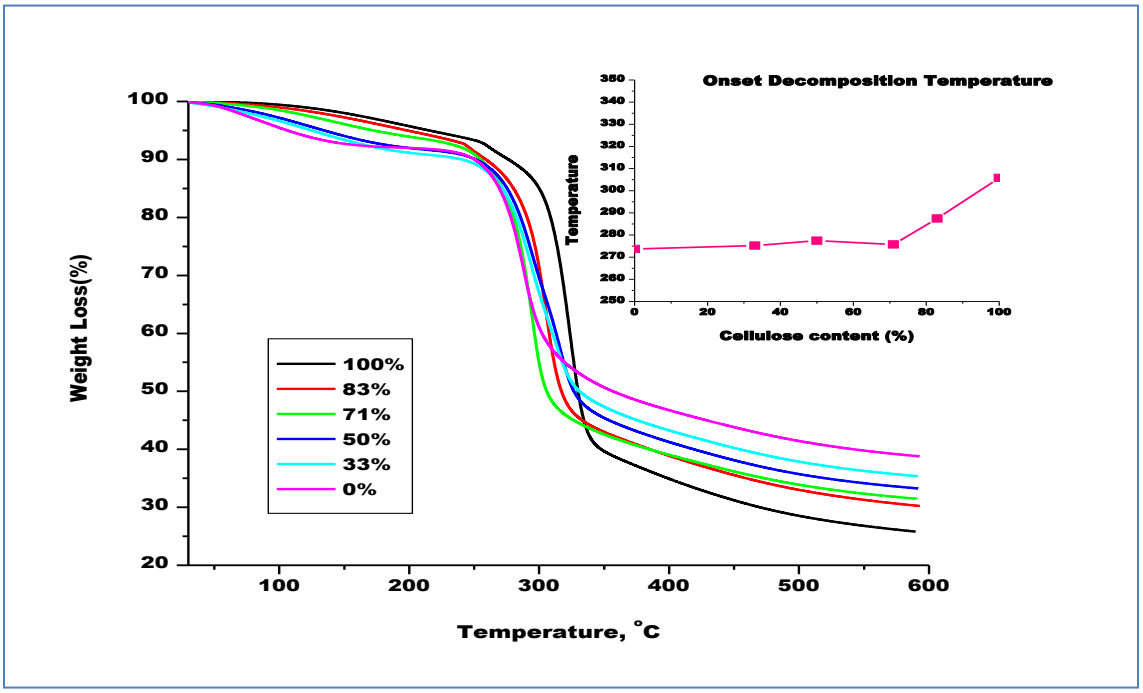

Figure 2.16: Thermal gravimetric analysis (TGA) weight loss curves of different compositions of [CEL+CS] composite materials. Insert: Plot of decomposition temperature as a function of CEL content in [CEL+CS] composite films

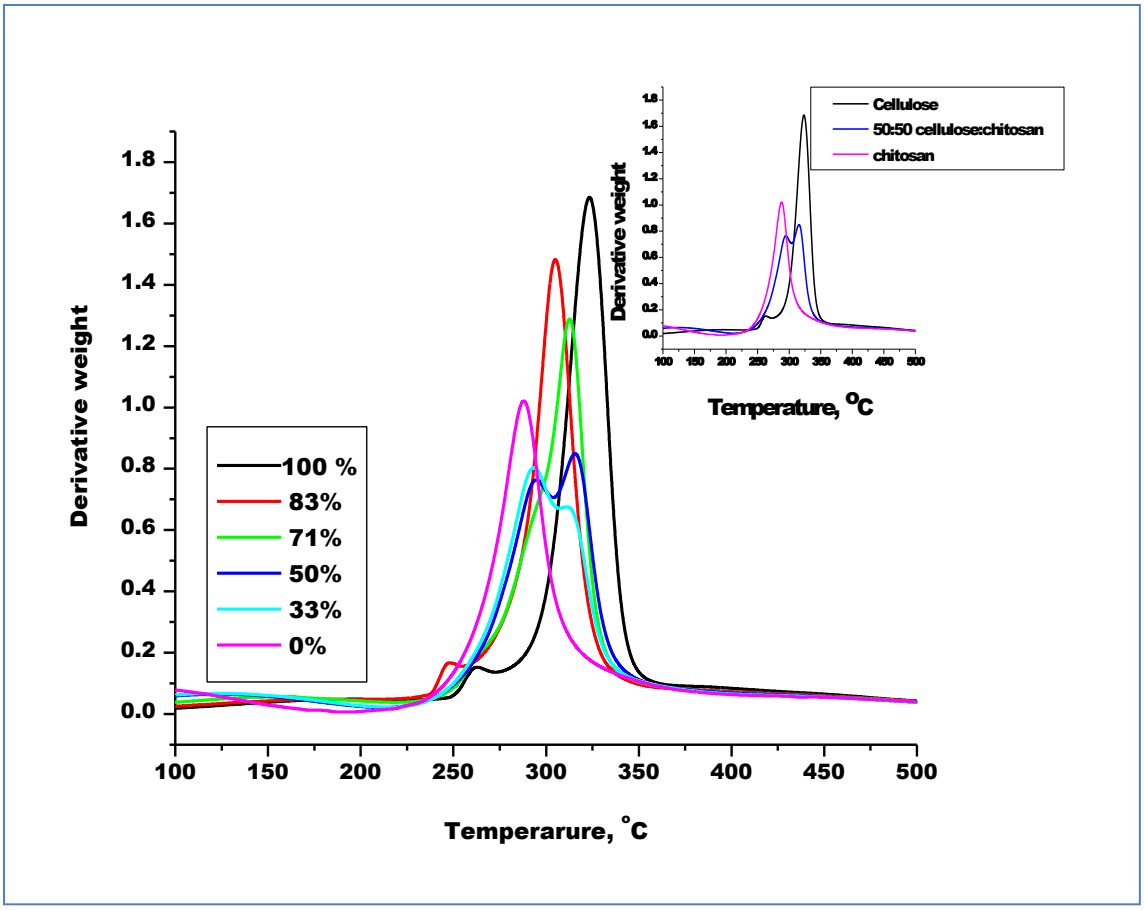

Figure 2.17: Thermal gravimetric analysis (TGA) derivative weight loss curves of different compositions of [CEL+CS] composite materials.

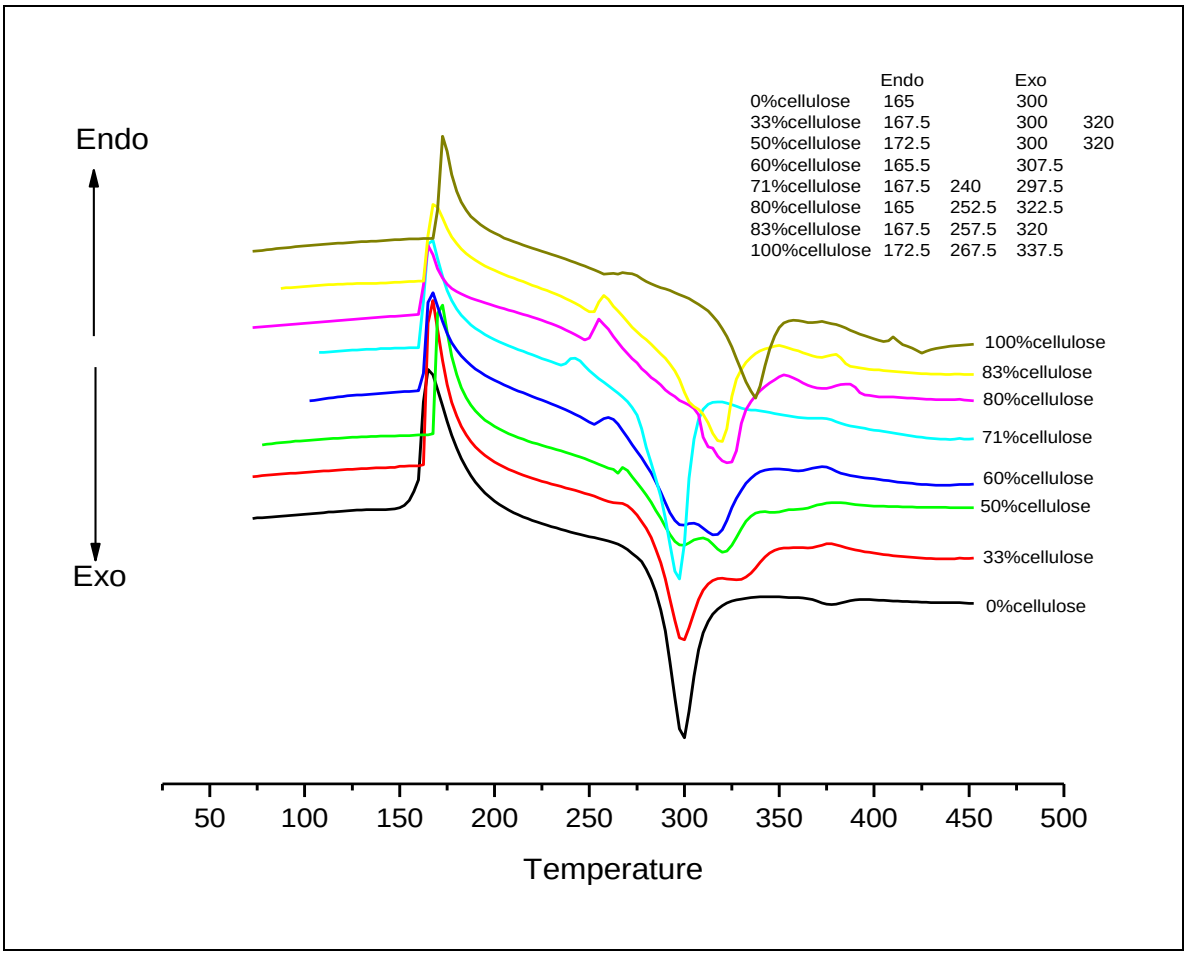

Figure 2.18: Differential Scanning Calorimetric (DSC) curves for different [CEL+CS] composite materials. Insert: Table showing the position of the exothermic and endothermic peaks.

The Differential Scanning Calorimetric (DSC) for the various [CEL+CS] composite materials was measured and the results are shown in Figure 2.18. The table inserted in the top right corner of this figure shows the positions of the peaks on the temperature scale. There are two major peaks in the [CEL+CS] composite films. An endothermic peak that is around 165^0C and an exothermic peak around 300^0C. Except for the 50% CEL and the 100% CEL film which have endothermic peaks at about 172^0C, the rest of the composites

have their exothermic peak around 165^0C. Another trend observed from the DSC measurement is the emergency of a small second endothermic peak for compositions containing 71% CEL and above. The position of this small peak increases with CEL composition from about 240^0C in 71% CEL to about 267^0C in 100 % CEL films. The position of the exothermic peak seems to be depended upon the amount of CEL in the composite films. The peak seems to shift from about 300^0C for a 0 % CEL (100%CS) to about 337^0C for the 100% CEL composite film. This exothermic peak seems to be associated with the thermal degradation of the composite materials. The fact that this degradation is occurring at progressively higher temperatures is another indication of the improved stability that CEL brings to the composite materials.

The results presented above clearly indicate that a novel, green and recyclable and economically viable method has been developed that can be used to prepare all natural biocompatible polysaccharide composite materials. Addition of CEL into CS was found to substantially improve the mechanical strengths, swelling properties and thermal stability of the resultant [CEL+CS] composite materials. This is a major step in overcoming one of the major drawbacks of current CS materials, i.e., its structural weakness. Of particular importance is the fact that this has been achieved not by using man-made polymers but by adding CEL, another natural polymer of unlimited abundance. This is expected to preserve most the unique properties of CS, especially its biocompatibility.

2.6. Preparation of cyclodextrin-doped polysaccharide composite films

As was described earlier, cyclodextrins (CDs) can confer some extra unique properties such as size and shape selectivity, which CEL and CS do not have by themselves. To investigate this concept further, CEL and CS composite materials doped with hexakis(2,3,6-tri-O-acetyl)-α-cyclodextrin (α-TCD), heptakis(2,3,6-tri-O-acetyl)-β-cyclodextrin (β-TCD) and octakis(2,3,6-tri-O-acetyl)-γ-cyclodextrin (γ-TCD) were prepared and their performance in several applications were investigated and compared to non-doped composites. The 2,3,6-tri-O-acetyl- derivatives were used instead of the native CDs because these are insoluble in water and will not be lost (or washed off) during the washing step. Initially, native (underivatized) β-CD was used to dope CEL and CS films. However, attempts to positively confirm the presence of the β-CD in the regenerated films did not yield any positive results. Figures 2.19 and 2.20 below show the results of an attempt to positively confirm the presence of β-CD in CS and CEL composites by FT-IR spectroscopy. To increase the sensitivity, the films in this figure were measured in the transmission mode and the β-CD powder (included for reference) was mixed with KBr and pressed into a pellet. Chemically, CEL and β-CD are the same, but are structurally very different, with CEL being linear and CD being cyclic. Structurally, CS is similar to CEL but it contains some NH_2 (and some residual –NH-CO(CH_3)) groups. The similarity of the chemical composition of CDs to both CEL and CS makes it extremely hard to positively confirm the presence of CD in either CEL or CS. However, as illustrated in Figure 2.19 and 2.20, the cyclic nature of CDs seem to be enough to cause some subtle shifts and differences in the FT-IR spectra of these compounds. Figure 2.19A is a

comparison of the FT-IR spectra of a 100%CS film, [CS+β-CD] film and β-CD powder. A closer view of the region 650 cm^{-1} to 1900 cm^{-1} is shown in Figure 2.19B. The vertical lines in this figure shows the indicator FT-IR bands and the very subtle shifts in some bands, whose presence in a β-CD doped film would have confirmed the successful regeneration of composite films doped with native β-CD. Unfortunately, as illustrated in Figure 2.19B, the FT-IR spectrum of the [CS+β-CD] film is identical to that of the 100%CS film with none of the bands that could be attributed to the β-CD. Similar results (shown in Figure 2.20) were obtained for CEL where none of the β-CD indicator bands are present in the FT-IR spectrum of [CEL+β-CD] composite film. These results led us to believe that β-CD was not successfully incorporated into the composite materials, but was somehow being lost at one of the stages during the preparation procedure. The solubility of native β-CD is reported to be about 1.85g/100mL.[98] While this is a relatively small solubility, the large amounts of water used during the washing step and the constant replenishment of this washing water with fresh de-ionized water could be enough to cause the β-CD to leak out of the composite materials during this washing step. Also some interactions may occur between the [$BMIm^{+}Cl^{-}$] and β-CD which can aid the solubility of this CD in water. As a result, a decision was made to use the 2,3,6-tri-O-acetyl- derivatives, which are completely insoluble in water , instead of the native CDs.

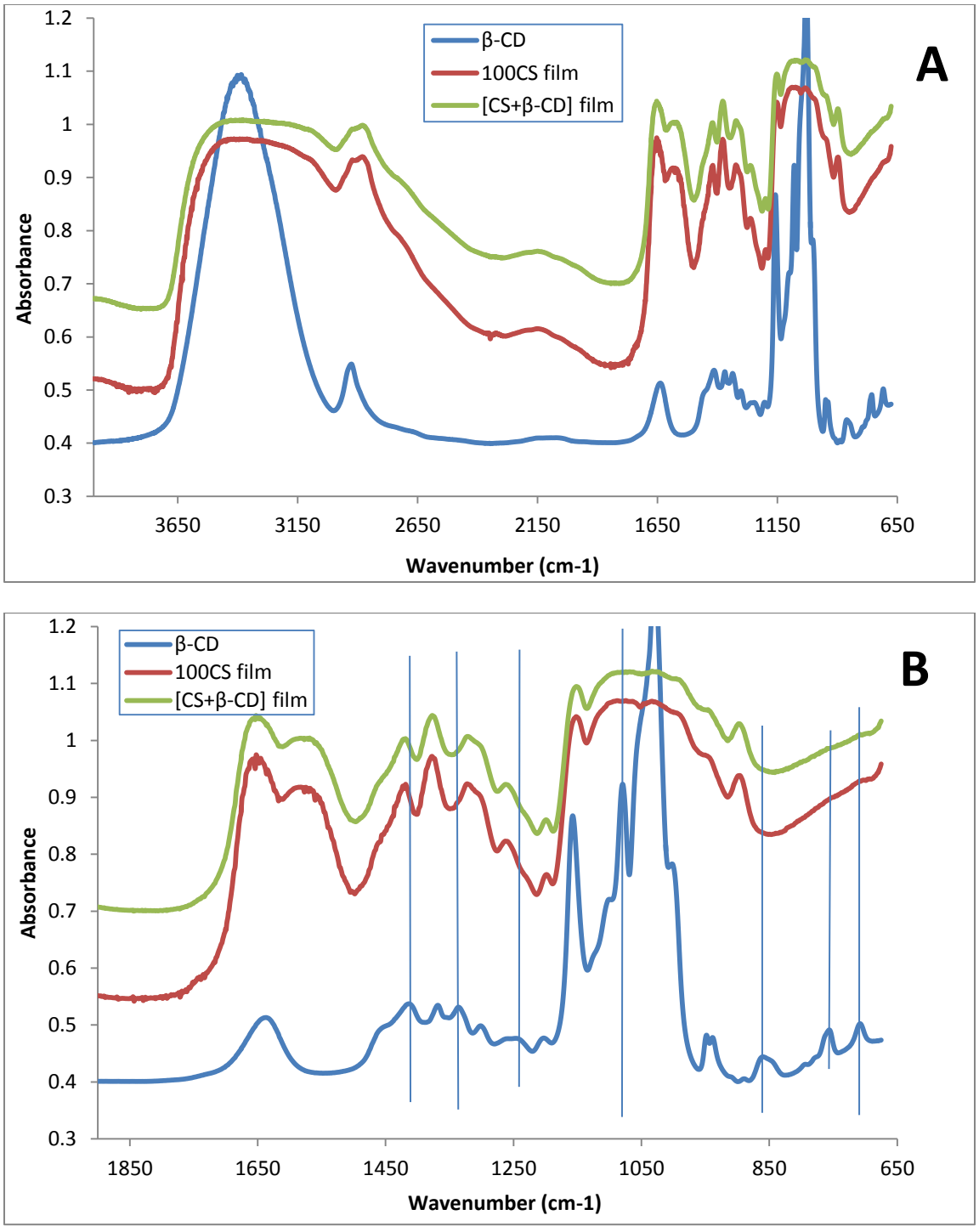

Figure 2.19: FT-IR spectra of 100CS film compared to that of a CS film doped with native β-CD.

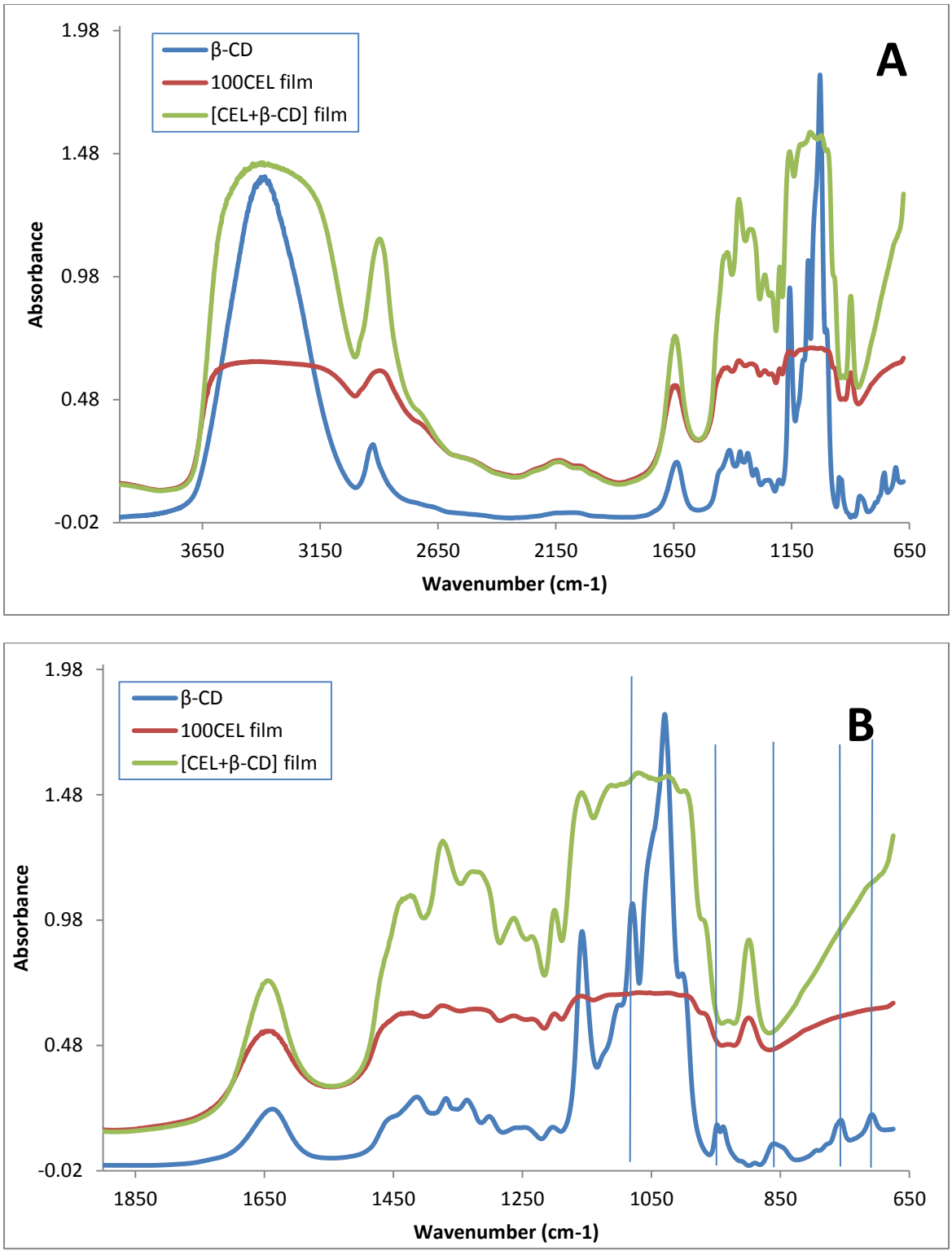

Figure 2.20: FT-IR spectra of 100CEL film compared to that of a CEL film doped with native β-CD.

[CEL+α-TCD, β-TCD and γ-TCD] and [CS+α-TCD, β-TCD and γ-TCD] composite materials were synthesized using a procedure similar to the one described above for the synthesis of CEL, CS and [CEL+CS][99–101]. Essentially, as shown in Scheme 2.3, [$BMIm^+$ Cl^-], was again used again as the solvent to dissolve CEL, CS, α-TCD, β-TCD and γ-TCD. Dissolution was performed at 100°C and under Ar or N_2 atmosphere. Similarly, all polysaccharides were added in portions of approximately 1% w/w of the ionic liquid. Succeeding portions were only added after the previous addition had completely dissolved until the desired concentration has been reached. For these composite films, the components were dissolved one after the other, with CEL (or CS) being dissolved first and TCDs last.

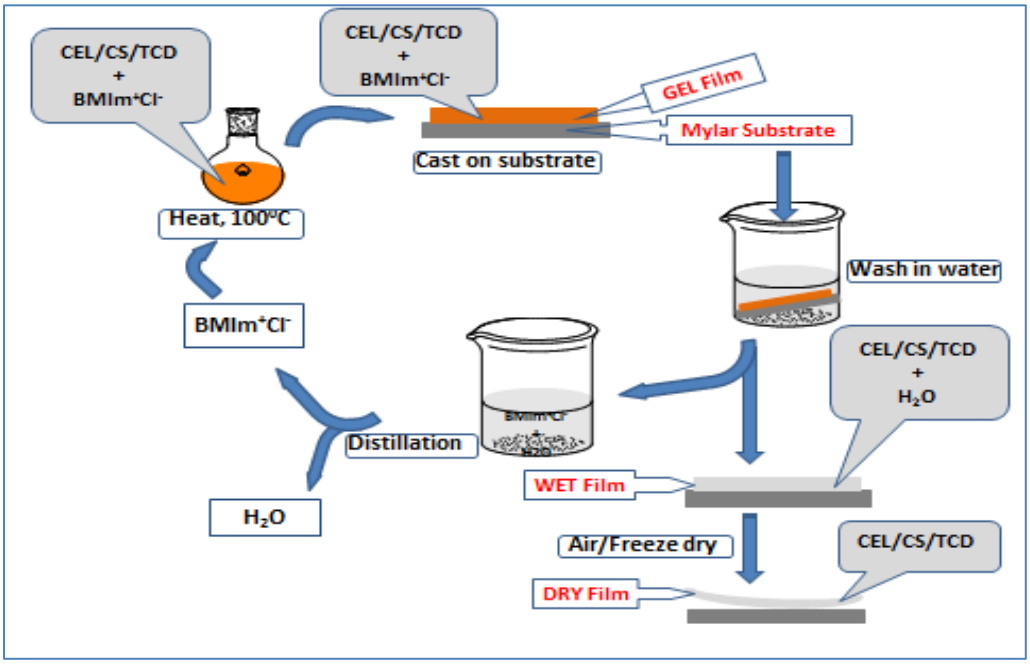

Scheme 2.3: Procedure used to prepare cyclodextrin-doped polysaccharide composites

2.7. Characterization of CEL/CS +α-TCD, β-TCD and γ-TCD composites

As described above in the preparation procedure, [$BMIm^+$ Cl^-] was used as the sole solvent to dissolve CEL, CS and the different TCDs to prepare the [CEL+-TCD] and [CS+-TCD] composite materials. Similar to the procedure described above for [CEL+CS] composites, [$BMIm^+$ Cl^-] was also removed from the Gel Films of the TCD composites by washing the films with water. Again, the washing water was repeatedly replaced with fresh water until it was confirmed by UV measurement that there no ionic liquid remaining in the washing solution. The IL used can also be recovered by distillation of the washings, and dried under vacuum at 70^{o}C overnight before it can be reused.

2.7.1. XRD spectroscopy of the TCD-doped composites

The dissolution of CS and TCD in [$BMIm^+Cl^-$] ionic liquid and their regeneration in the composite materials was followed and studied by X-ray diffraction. Figure 2.21 shows the XRD spectra of the different [CS+TCD] composites at various stages of preparation. The XRD spectra of the α-, β- and γ-TCD (powders) suggest that these starting materials have different structural morphologies. While the XRD spectrum of the β-TCD powder is consistent with a highly crystalline structure, the XRD spectra of α-TCD and γ-TCD suggest that these two CDs have more of an amorphous structure.[102] The XRD pattern of the gel films was measured to determine the dissolution of the CS and TCDs in the [$BMIm^+Cl^-$] ionic liquid. As illustrated in Figure 2.21, the XRD spectra of the gel films do not exhibit any of the CS or TCD diffraction peaks. Similar to what was observed for

the CEL and CS composites, the XRD spectra of the gel films is just identical to the XRD pattern of [$BMIm^+Cl^-$] ionic liquid. The non-appearance of the X ray diffraction peaks of CS and TCDs and the similarity between the spectrum of the gel films to that of the [$BMIm^+Cl^-$] ionic liquid clearly indicates that [$BMIm^+Cl^-$] was able to disrupt the inter- and intramolecular hydrogen bonds of CS and was able to completely dissolve both CS and the TCDs. The XRD spectra of the regenerated composite films (DRY films) are also shown in Figure 2.21 (light blue spectra). Interestingly, the XRD spectra of the 50:50 CS: α-TCD and 50:50 CS:β-TCD regenerated composite films exhibit some X ray diffraction peaks which can be attributed to the α-TCD and β-TCD respectively. However, the XRD spectrum of the 50:50 CS: γ-TCD regenerated composite film does not show a similar pattern, with the spectrum being very similar to the 100%CS film. Taken together, these results suggest that while the γ-TCD is regenerated in an amorphous form, the α-TCD and the β-TCD seem to be regenerated in a more crystalline form. The amorphous or crystalline nature of these TCDs in the composite materials could affect the way they interact with other compounds and can be a critical factor in their technological applications. Figure 2.22 shows the XRD spectra of the composites at different stages of preparation for CS:β-TCD (Figure 2.22A) and CS:γ-TCD (Figure 2.22B) composites. What is interesting about this figure is the ability of the XRD technique in revealing the morphological changes that the samples undergo during the various stages of preparation. Since the XRD spectra of the GEL film, WET film and DRY film are all different, it can be taken to mean that the samples have different morphological structure at these various stages of preparation.

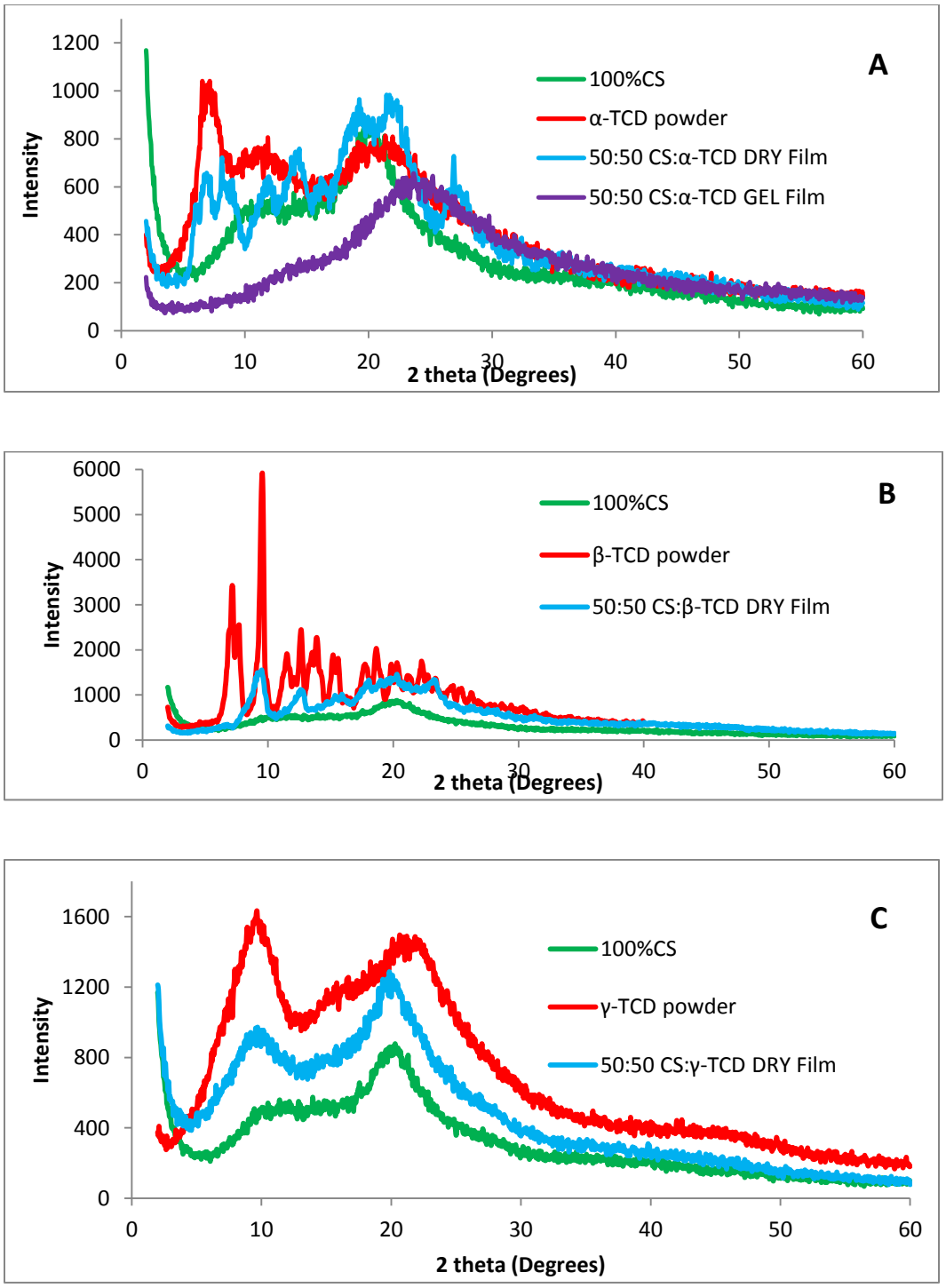

Figure 2.21: X-ray powder diffraction spectra of [BMIm+Cl-], CS powder, α-TCD, β-TCD and γ-TCD powder, and regenerated [CS+α-TCD] (A), [CS+β-TCD] (B) and [CS+γ-TCD] (C) composite materials at different stages of synthesis

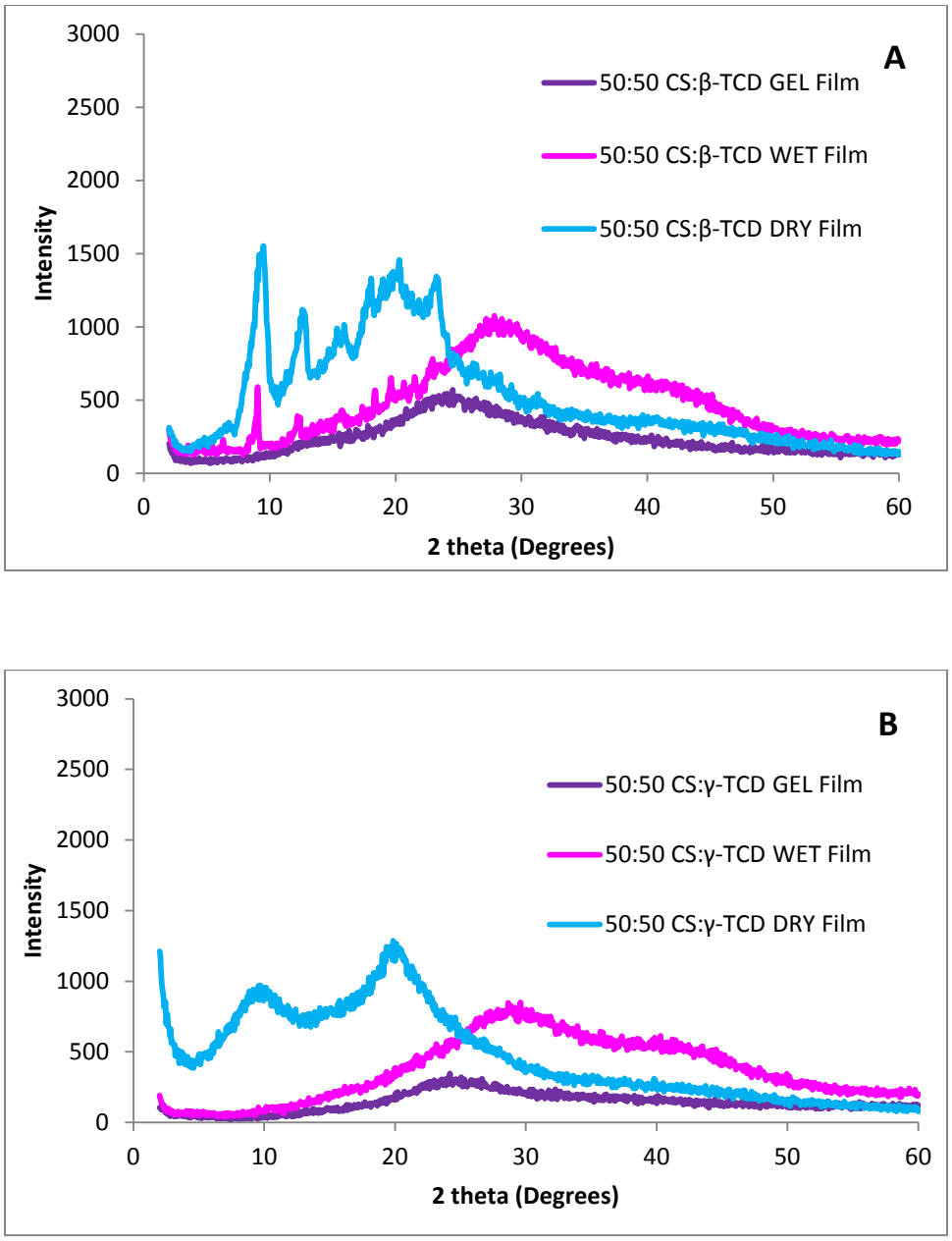

Figure 2.22: X-ray powder diffraction spectra of [CS+β-TCD] (A) and [CS+γ-TCD] (B) composite materials at different stages of synthesis

2.7.2. Near-IR and FT-IR spectroscopy of the TCD-doped composites

FT-IR and NIR spectroscopy was used to characterize the chemical composition of the regenerated TCD composite films. The FT-IR spectra of the [CS+TCD] composite materials are shown in Figure 2.23. As illustrated, the FT-IR spectrum of a 100%CS dried film display characteristic CS bands for O-H stretching vibrations as already described in the previous section for [CEL+CS] composites. These include characteristic bands for O-H stretch (3400 cm^{-1}), N-H stretch (3250 cm^{-1} – 3350 cm^{-1}), C-H stretch (2850 cm^{-1} – 2900 cm^{-1}), C=O, amide 1 (1650 cm^{-1}), N-H deformation (1595 cm^{-1}), CH_3 deformation (1380 cm^{-1}), C-N stretch, amide III (1319 cm^{-1}) and –O-, ether bending (890 cm^{-1} – 1150 cm^{-1}).[65–67] The FT-IR spectra of α-, β- and γ-TCD are also shown in the same figure. As expected, the three spectra are very similar to each other since the three compounds only differ in the number of glucose moieties making up the ring. The dominant absorption bands are those due to C=O stretching vibration at ~ 1746 cm^{-1}, the medium and weak bands at ~ 1372 cm^{-1} and 1434 cm^{-1} can be attributed to the symmetric and asymmetric deformation of CH_3 group of acetates, C – O asymmetric stretching vibration of acetates at ~ 1216 cm^{-1} and the asymmetric stretching vibration of the O – CH_2 – C groups for acetates.[103,104] It is clear from the FT-IR spectra of the [CS+TCD] composites that these spectra have FT-IR bands that can be attributed to both CS and TCDs as described above.

Results from NIR measurements further confirm the successful incorporation of the TCDs into CS (Figure 2.24). The 100% CS film exhibits NIR absorption bands

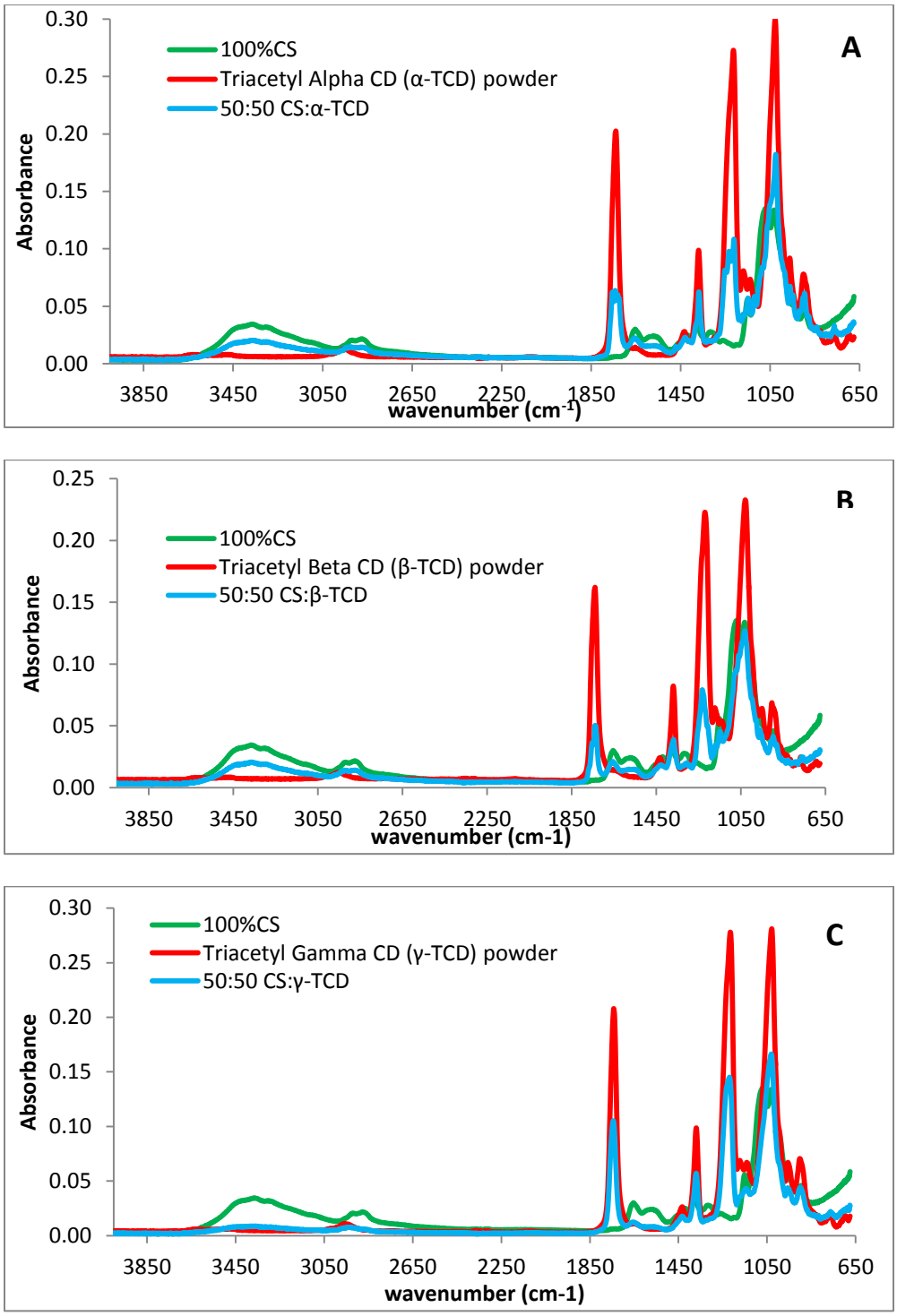

Figure 2.23: FT-IR spectra of [CS+TCD] composite materials. A) α-TCD, B) β-TCD and C) γ-TCD

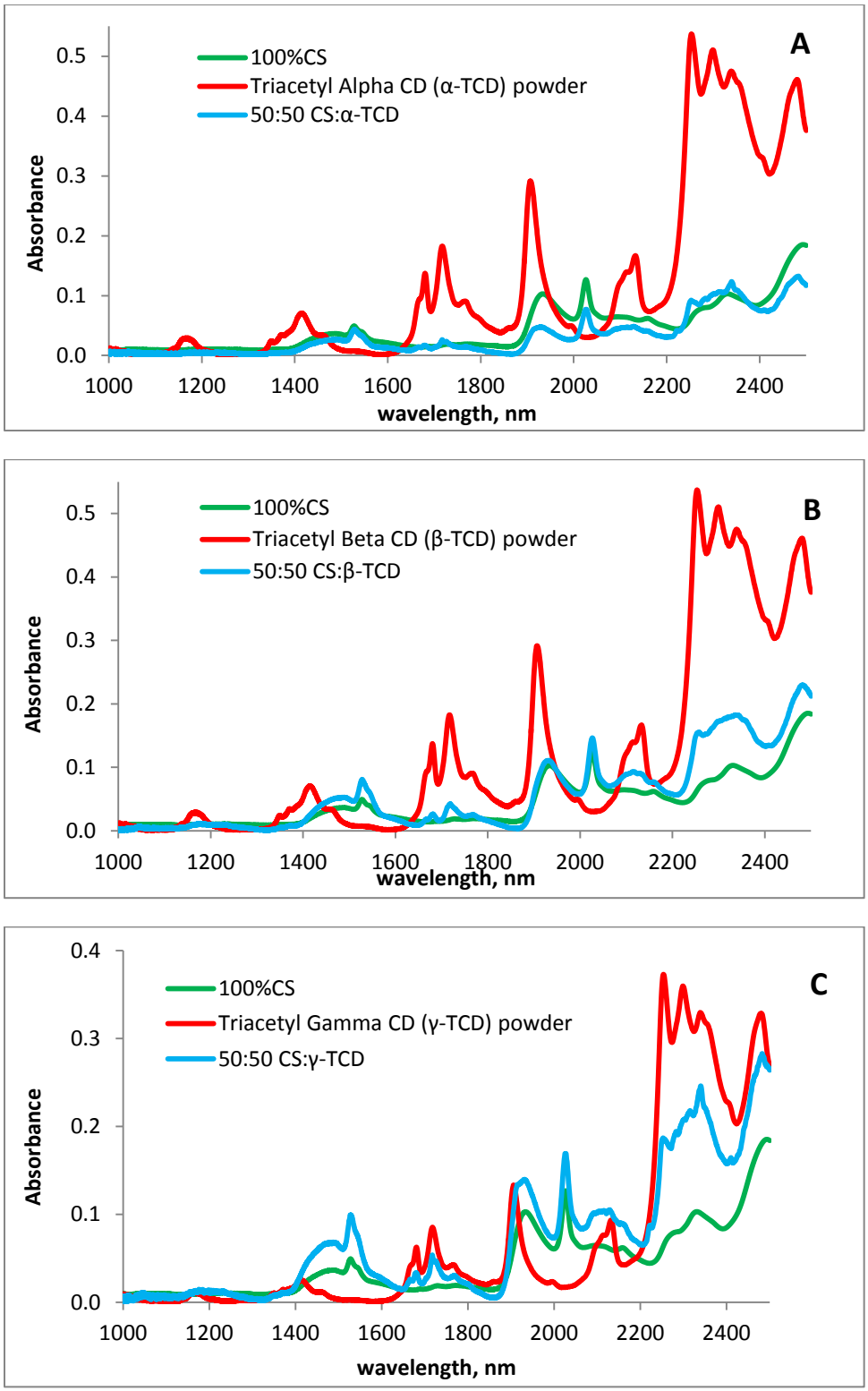

Figure 2.24: NIR spectra of [CS+TCD] composite materials. A) α-TCD, B) β-TCD and C) γ-TCD

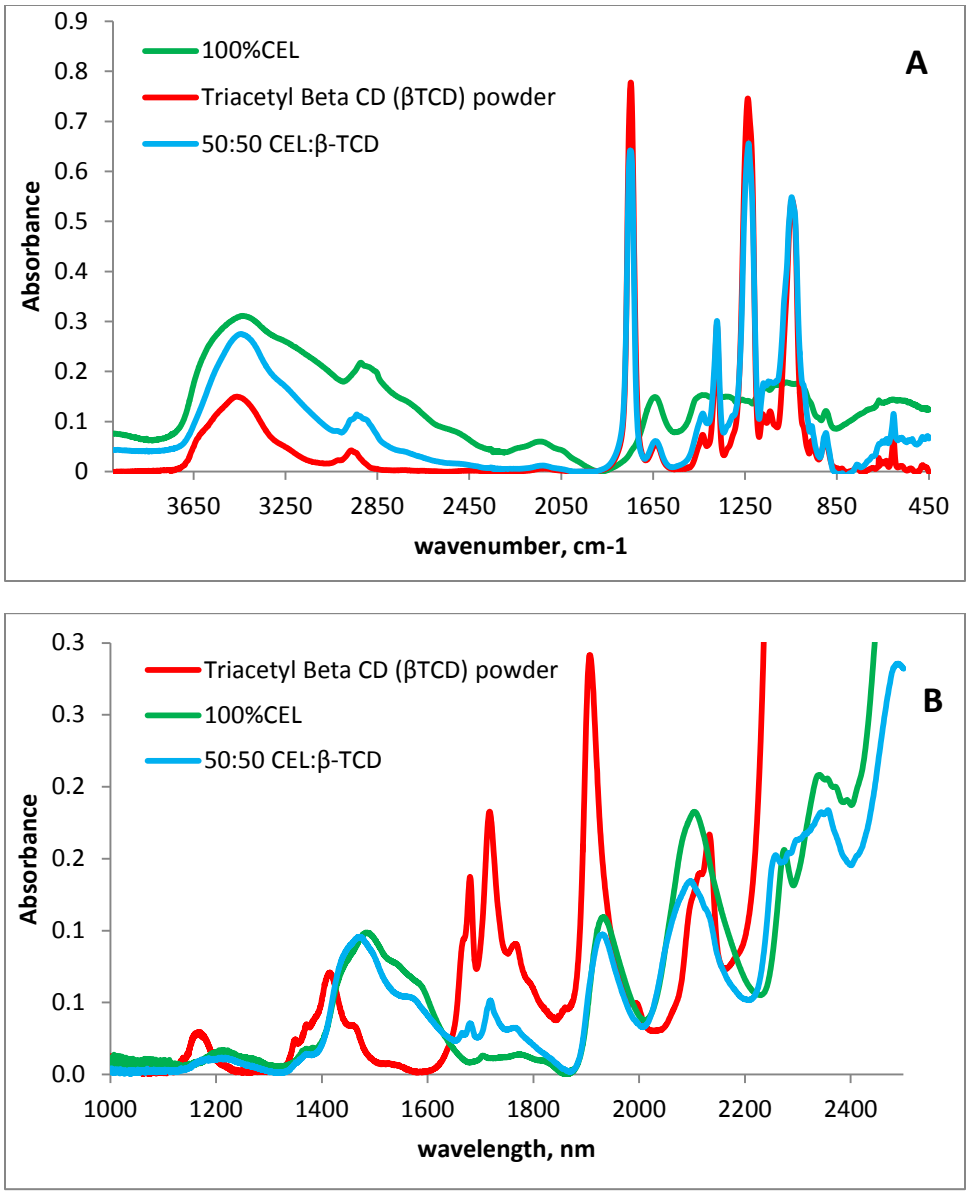

Figure 2.25: A) FT-IR and B) FT-NIR spectra of [CEL+β-TCD] composite materials

around 1492 nm, 1938 nm and 2104 nm which can be assigned to the overtone and combination transitions of the –OH group[52,67,101,104]. In addition, CS also exhibits bands ~1548 nm and 2028 nm, which is due to the –NH groups.[68].

Similar to FT-IR, the NIR spectra of α-, β- and γ-TCD are also very similar. The major bands for these are around 1415 nm (first overtone of methyl -CH group), 1680 nm and 1720 nm (first overtone of -CH group), 1908 nm and 2135 nm (-C=O, acetyl group)[105]. As shown in Figure 2.24, the NIR spectra of [CS+α-TCD], [CS+β-TCD] and [CS+γ-TCD] composite materials contain bands due to both CS and TCDs.

Similarly, FT-IR and NIR results also confirm that α-TCD, β-TCD and γ-TCD were successfully incorporated into CEL. For clarity, FT-IR and NIR spectra of only β-TCD powder, 50:50 CEL:β-TCD together with 100% CEL film are shown in Figure 2.25A and 2.25B, respectively. 100% CEL film (green curves in Figure 2.14A) exhibits three pronounced bands at around 3400 cm^{-1}, 2850 – 2900 cm^{-1} and 890 – 1150 cm^{-1}. These bands can be tentatively assigned to stretching vibrations of O-H, C-H and -O- group, respectively[65]. Similar to CS composite materials, FT-IR and NIR spectra of [CEL+β-TCD] composite material also exhibit bands due to both TCD and CEL.

2.7.3. Analysis of [CEL+γ-TCD] and [CS+γ-TCD] composites by ^{13}C NMR

The successful incorporation of the TCDs into the CEL and CS and the chemical composition of the regenerated films was also verified by ^{13}C CP MAS NMR spectroscopy. The results are shown in Figure 2.26 below. As explained earlier, the TCDs used in the composite materials are the –O-acetyl derivatives. This means the resultant

composite materials should have distinct ^{13}C signals arising from the methyl carbon and the carbonyl carbon. As expected, the ^{13}C NMR spectrum of the γ-TCD starting material (deep blue spectrum) in Figure 2.18 has two intense bands around 20.7ppm and about 170.7ppm corresponding to the methyl and carbonyl carbons respectively.[106] As illustrated in Figure 2.26, these same band are clearly visible in the ^{13}C NMR spectra of the [CEL+γ-TCD] and [CS+γ-TCD] composite materials confirming the successful incorporation and regeneration of TCD-doped CEL and CS composite materials.

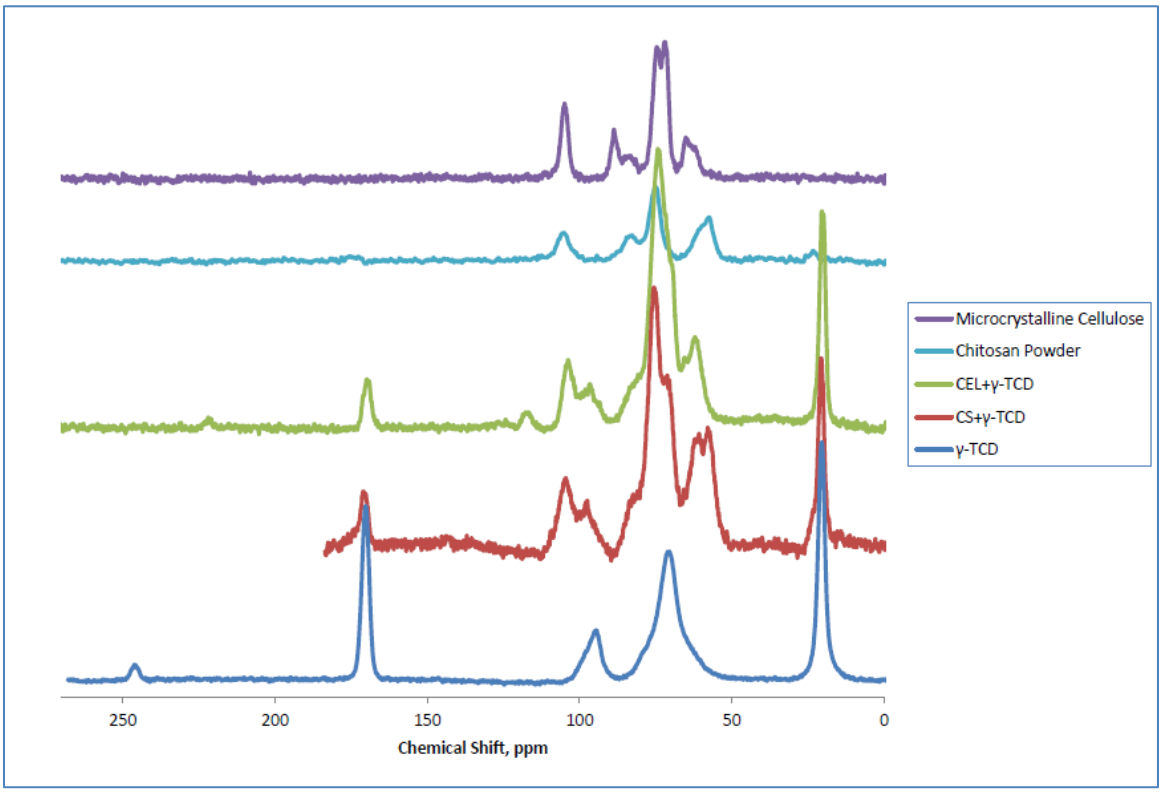

Figure 2.26: ^{13}C CP MAS NMR spectra of regenerated [CEL+γ-TCD], [CS+γ-TCD] composite films, γ-TCD powder, CS powder and Microcrystalline CEL.

2.7.4. Morphological analysis of cyclodextrin-doped composites

Chemical and morphological structure of the resultant TCD-doped composites was measured using SEM. The SEM images of the various compositions prepared are shown in Figure 2.15A and Figure 2.15B. The SEM images for 100%CEL and 100%CS are the same as the ones already described previously for [CEL+CS] composites. They are however included in this figure for easy of comparison. Figure 2.15B shows that the SEM images of the CS:β-TCD has a much smoother structure, both surface and cross section, that its CS:γ-TCD counterpart. The SEM images of CEL:β-TCD and CEL:γ-TCD are also showing some clear differences. β-TCD is relatively small and rigid while γ-TCD because of its larger size is more flexible. Such differences in the structures of the starting materials could have to the observed morphological differences in the corresponding TCD composites. It should however be noted that the SEM images of all the composites look homogenous. This may suggest that despite the differences in microstructure for the β-TCD and γ-TCD, both these TCDs are homogeneously distributed in the CEL and CS polymer network.

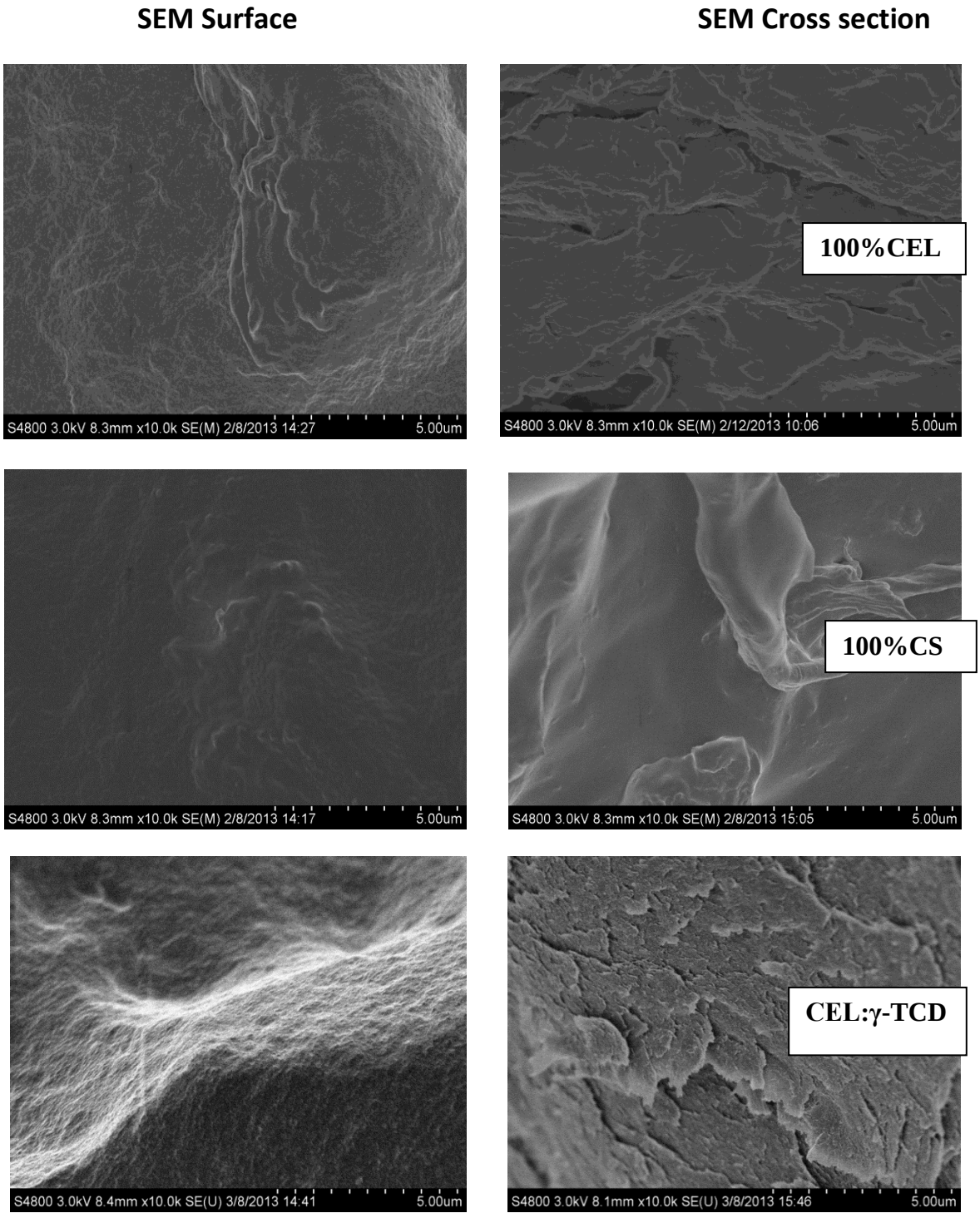

Figure 2.27A: SEM images of surface (left) and cross section (left) of regenerated CEL film (top), regenerated CS film (middle) and 50:50 [CEL:γ-TCD] composite film (bottom)

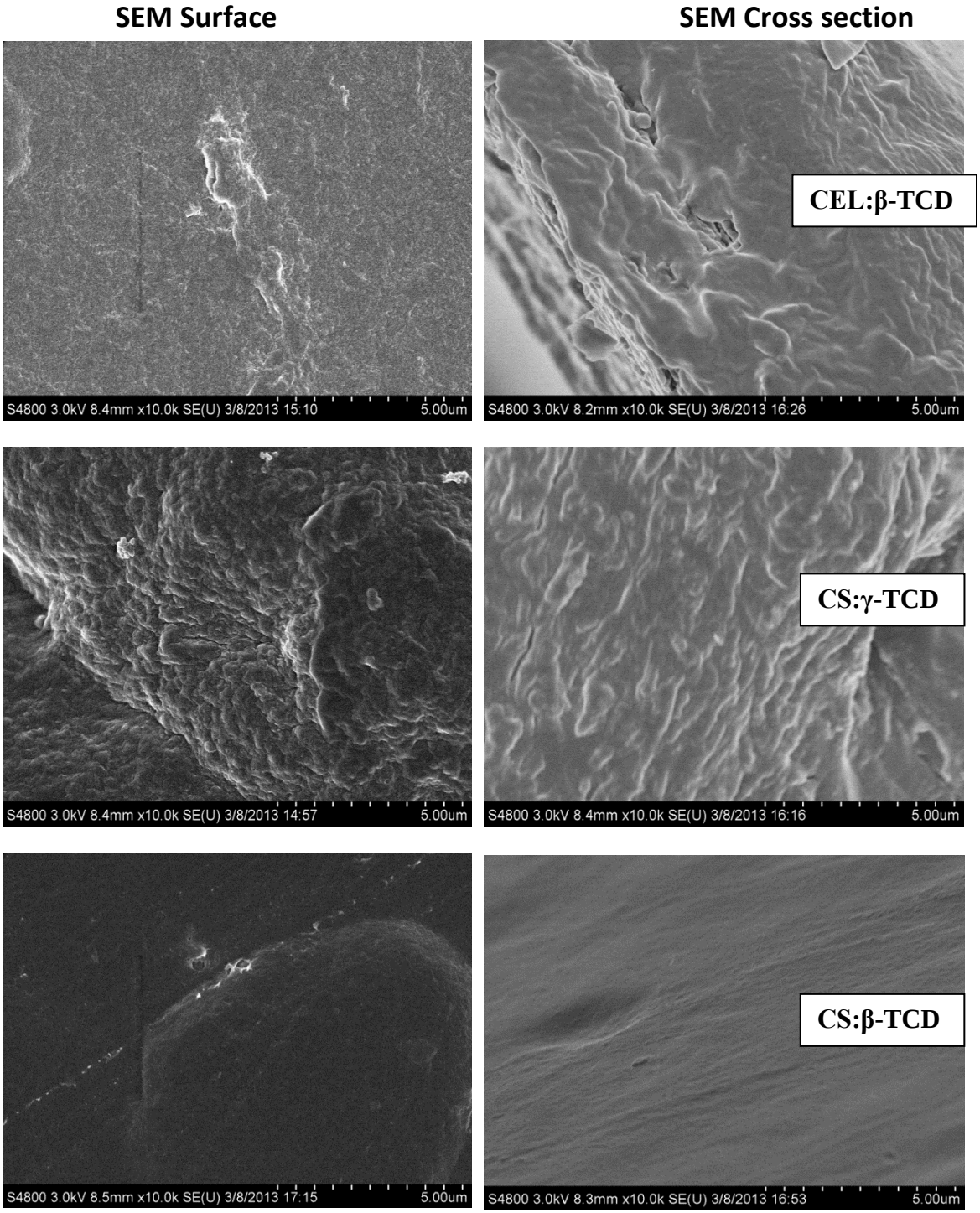

Figure 2.27B. SEM images of surface (left) and cross section (left) of regenerated 50:50 [CEL:β-TCD] film (top), regenerated 50:50 [CS:γ-TCD] film (middle) and 50:50 [CS:β-TCD] composite film (bottom)

2.7.5. Mechanical properties of cyclodextrin-doped composites

As alluded to earlier, CDs have poor mechanical properties such that there is often a need to graft them to some man-made polymers for them to be used in many practical apllications.[2,4,22,107] It is hoped that the CEL and CS used in our composite materials will help to improve the mechanical and rheological properties of the TCDs and therefore eliminate the need for complicated grafting reactions. The use of natural polymers (CEL and CS) will also enable us to maintain the biocompatibility and biodegradability of our composite materials. [CEL+TCDs] and [CS+TCDs] composite films with different CEL and CS concentrations were prepared and tensile strengths measurements were made in order to determine if the addition of CEL or CS would provide the composite material adequate mechanical strength for practical applications. Results obtained, shown in Table 2.7 and Figure 2.28, clearly indicate that adding either CEL or CS into the composite materials substantially increase their tensile strength. For example,

Table 2.7: Mechanical strength of [CS+γ-TCD] and [CEL+γ-TCD] composite materials

% TCD	Tensile strength, MPa	
	[CS + γ-TCD]	[CEL + γ-TCD]
0	14±3	52±3
10	11±4	35±13
25	6±2	26±12
40	2±0	18±9
50	1±0	13±5

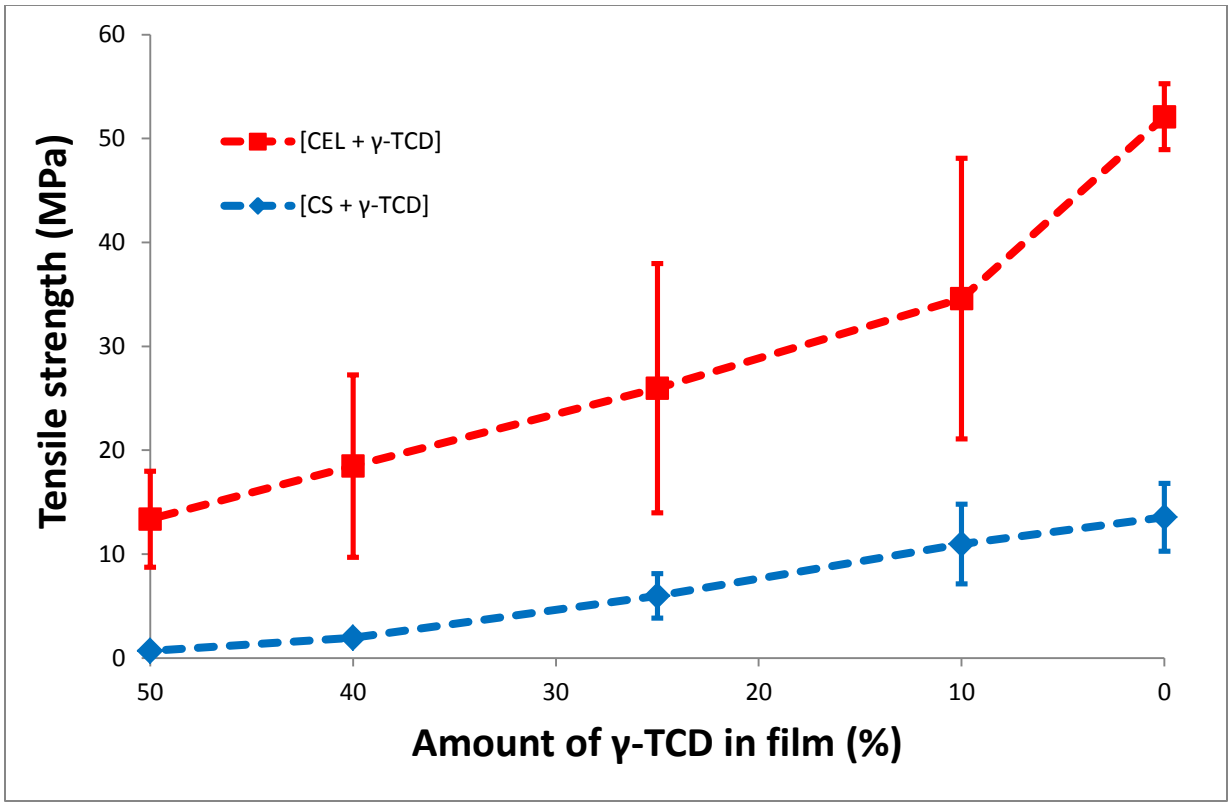

Figure 2.28: Plot of tensile strength as a function of γ-TCD concentration in [CEL+γTCD] composites (red curve) and [CS+γTCD] composites (blue curve)

up to 2X (or 6X) increase in tensile strength can be achieved by increasing concentration of CEL in [CEL+γ-TCD] composite (or CS in [CS+γTCD]) from 50% to 75%. Also, the tensile strength of the [CEL+γ-TCDs] composite is relatively higher than the corresponding [CS+γ-TCDs] composite. This is hardly surprising considering the fact that the mechanical and rheological strength of CEL is relatively higher than that of CS. It is thus, evidently clear that the [CEL+TCD] and [CS+TCD] composite materials have overcome the major hurdle currently imposed on utilization of the materials, namely they have the required mechanical strength for practical applications.

The results presented above clearly indicate that novel all polysaccharide composite materials containing CEL, CS and α-TCD, β-TCD and γ-TCD were successfully synthesized by use of [$BMIm^+Cl^-$], an ionic liquid, as the sole solvent. Since at least 88% of the [$BMIm^+Cl^-$] used was recovered for reuse, the method is green and recyclable. The successful dissolution of the polysaccharides in [$BMIm^+Cl^-$] and their regeneration from water and subsequent drying into usable films was followed by XRD spectroscopy. The chemical nature and composition of these composite materials were characterized by FT-IR, NIR and 13C CP MAS NMR spectroscopy. Tensile strength and rheological measurements confirmed that adding CEL to CS can indeed lead to improvement in these properties for CS. Also, CD-doped composites with improved mechanical properties were successfully prepared without the need for complicated grafting reactions or the use of man-made polymers, which would have otherwise lessened the biocompatibility of our materials. It is expected that these composites may also retain properties of CS and TCDs, namely, they would be good adsorbents for pollutants, still show some antimicrobial activity, and have controlled drug releasing properties (from CS) and selectively form inclusion complexes with substrates of different sizes and shapes (from TCDs). The investigation of these properties for the various applications and our findings are discussed in the next 2 chapters.

2.7.6. References

(1) Finkenstadt, V. L.; Millane, R. P. *Macromolecules* **1998**, *31*, 7776–7783.

(2) Augustine, A. V; Hudson, S. M.; Cuculo, J. A.; Hudson, S. M. A.; J, C. *Cellulose Sources and Exploitation*; Kennedy, J. F. P. G. O. W. P. A., Ed.; Horwood: New York, 1990; p. 59.

(3) Kadokawa, J.; Murakami, M.; Kaneko, Y. *Composites Science and Technology* **2008**, *68*, 493–498.

(4) Dawsey, T. R. *Cellulosic Polymers, Blends and Composites*; Gilbert, R. D., Ed.; Carl Hanser Verlag: New York, 1994; p. 157.

(5) Cai, J. I. E.; Liu, Y.; Zhang, L. *J. Pol. Sci. B. Pol. Phys.* **2006**, 3093–3101.

(6) Fink, H. P.; Weigel, P.; Purz, H. J.; Ganster, J. *Progress in Polymer Science* **2001**, *26*, 1473–1524.

(7) Dai, T.; Tegos, G. P.; Burkatovskaya, M.; Castano, A. P.; Hamblin, M. R. *Antimicrobial agents and chemotherapy* **2009**, *53*, 393–400.

(8) Bordenave, N.; Grelier, S.; Coma, V. *Biomacromolecules* **2010**, *11*, 88–96.

(9) Rabea, E. I.; Badawy, M. E.-T.; Stevens, C. V; Smagghe, G.; Steurbaut, W. *Biomacromolecules* **2003**, *4*, 1457–1465.

(10) Altiok, D.; Altiok, E.; Tihminlioglu, F. *Journal of materials science Materials in medicine* **2010**, *21*, 2227–2236.

(11) Burkatovskaya, M.; Tegos, G. P.; Swietlik, E.; Demidova, T. N.; P Castano, A.; Hamblin, M. R. *Biomaterials* **2006**, *27*, 4157–4164.

(12) Gustafson, S. B.; Fulkerson, P.; Bildfell, R.; Aguilera, L.; Hazzard, T. M. *Prehospital emergency care official journal of the National Association of EMS Physicians and the National Association of State EMS Directors* **2006**, *11*, 172–178.

(13) Pusateri, A. E.; McCarthy, S. J.; Gregory, K. W.; Harris, R. A.; Cardenas, L.; McManus, A. T.; Goodwin, C. W. *J Trauma* **2002**.

(14) Keong, L. C.; Halim, A. S. *International journal of molecular sciences* **2009**, *10*, 1300–1313.

(15) Kiyozumi, T.; Kanatani, Y.; Ishihara, M.; Saitoh, D.; Shimizu, J.; Yura, H.; Suzuki, S.; Okada, Y.; Kikuchi, M. *Journal of biomedical materials research Part B Applied biomaterials* **2006**, *79*, 129–136.

(16) Rossi, S.; Sandri, G.; Ferrari, F.; Bonferoni, M. C.; Caramella, C. *Pharmaceutical development and technology* **2003**, *8*, 199–208.

(17) Jain, D.; Banerjee, R. *Journal of biomedical materials research Part B Applied biomaterials* **2008**, *86*, 105–112.

(18) Varshosaz, J.; Tabbakhian, M.; Salmani, Z. *Open Drug De J* **2008**, *2*, 61 – 70.

(19) Elmotasem, H. *Journal of Pharmaceutical Sciences* **2008**, *3*, 12–29.

(20) Naficy, S.; Razal, J. M.; Spinks, G. M.; Wallace, G. G. *Sensors and Actuators A Physical* **2009**, *155*, 120–124.

(21) Tirgar, A.; Golbabaei, F.; Hamedi, J.; Nourijelyani, K.; Shahtaheri, S. .; Moosavi, S. . *Int. J. Environ. Sci. Tech.* **2006**, *3*, 305–313.

(22) Nishiki, M.; Tojima, T.; Nishi, N.; Sakairi, N. Beta-cyclodextrin-linked chitosan beads: preparation and application to removal of bisphenol A from water. *Carbohydrate letters* **2000**, *4*, 61–7.

(23) Hassam, M. A. .; Hui, L. .; Noor, Z. . *J. Chem. Nat. Res. Eng.* **2009**, *4*, 1–11.

(24) Dhakal, R. .; Oshima, T.; Baba, Y. *World. Acad. Sci. Eng. Tech.* **2009**, *56*, 204–208.

(25) Ngah, W. S. W. A. N.; Isa, I. M. **1997**, 1067–1070.

(26) Xie, H.; Zhang, S.; Li, S. *Green Chem.* **2006**, *8*, 630–633.

(27) Swatloski, R. P.; Spear, S. K.; Holbrey, J. D.; Rogers, R. D. *Journal of the American Chemical Society* **2002**, *124*, 4974–4975.

(28) El Seoud, O. A.; Koschella, A.; Fidale, L. C.; Dorn, S.; Heinze, T. *Biomacromolecules* **2007**, *8*, 2629–2647.

(29) Pinkert, A.; Marsh, K. N.; Pang, S.; Staiger, M. P. *Chemical reviews* **2009**, *109*, 6712–6728.

(30) Tran, C. D.; De Paoli Lacerda, S. H. *Analytical chemistry* **2002**, *74*, 5337–5341.

(31) Han, X.; Armstrong, D. W. *Accounts of chemical research* **2007**, *40*, 1079–1086.

(32) Tran, C. D. *ACS Symbosium Series* **2010**, *1038*, 35–54.

(33) Welton, T. *Chemical Reviews* **1999**, *99*, 2071–2083.

(34) Tran, C. D. *Analytical Letters* **2007**, *40*, 2447–2464.

(35) Tran, C. D. In *ACS Symbosium Series*; 2010; pp. 35–54.

(36) Wasserscheid, P.; Welton, T. *Ionic Liquids in synthesis*; Wiley-VCH: Weinheim, 2003.

(37) Lehn, J. M. *Supramolecular Chemistry*; Wiley-VCH, 1995.

(38) Lehn, J. M. *Science* **1993**, *260*, 1762–1763.

(39) Oshovsky, G. V; Reinhoudt, D. N.; Verboom, W. *Angewandte Chemie International Edition* **2007**, *46*, 2366–2393.

(40) Kim, K.; Selvapalam, N.; Oh, D. H. *Journal Of Inclusion Phenomena And Macrocyclic Chemistry* **2004**, *50*, 31–36.

(41) Chen, Y.; Zhang, Y.-M.; Liu, Y. *Israel Journal of Chemistry* **2011**, *51*, 515–524 ST – Molecular Selective Binding and Nano.

(42) Laza-Knoerr, A. L.; Gref, R.; Couvreur, P. *Journal of Drug Targeting* **2010**, *18*, 645–656.

(43) Del Valle, E. M. M. *Process Biochemistry* **2004**, *39*, 1033–1046.

(44) Buschmann, H. P.; Mutihac, L.; Schollmeyer, E. *Supramolecular Chemistry* **2005**, *17*, 447–451.

(45) Gerasko, O. A.; Samsonenko, D. G.; Fedin, V. P. *Russian Chemical Reviews* **2002**, *71*, 741–760.

(46) Hinze, W. L.; Armstrong, D. W. *ACS Symbosium Series* **1987**, *342*, 2 – 82.

(47) Fakayode, S. O.; Lowry, M.; Fletcher, K. A.; Huang, X. D.; Powe, A. M.; Warner, I. M. *Current Analytical Chemistry* **2007**, *3*, 171–181.

(48) Battista, O. A.; Smith, P. A. *Ind. Eng. Chem.* **1962**, *54*, 20 – 29.

(49) Frez, C.; Diebold, G.; Tran, C. D.; Yu, S. *J Chem Eng Data* **2006**, *54*, 1250 – 1255.

(50) Baptista, M. S.; Tran, C. D.; Gao, G. H. *Analytical chemistry* **1996**, *68*, 971–976.

(51) Tran, C. D.; Kong, X. *Anal. Biochem.* **2000**, *286*, 67–74.

(52) Duri, S.; Majoni, S.; Hossenlopp, J. M.; Tran, C. D. *Analytical Letters* **2010**, *43*, 1780–1789.

(53) Kim, S. J.; Shin, S. R.; Kim, N. G.; Kim, S. I. *J. Macromol. Sci. Part A: Pure and Applied Chemistry* **2005**, *42*, 1073–1083.

(54) Karadag, E.; Saraydin, D. *Polymer Bulletin* **2002**, *48*, 299–307.

(55) Kofuji, K.; Qian, C.-J.; Nishimura, M.; Sugiyama, I.; Murata, Y.; Kawashima, S. *European Polymer Journal* **2005**, *41*, 2784–2791.

(56) Liu, X.; Howard, K. A.; Don, M.; Anderson, M. Q.; Rahbek, U. L.; Johnsen, M. G.; Hansen, O. C.; Bessenbacher, F.; Kjems, J. *Biomaterials* **2007**, *28*, 1280–1288.

(57) Baxter, A.; Dillion, M.; Taylor, K.; Roberts, G. *Int. J. Biol. Macromol.* **1992**, *14*, 166–169.

(58) Domzy, J.; Roberts, G. *Makromol. Chem.* **1985**, *186*, 1671–1677.

(59) Berth, G.; Dautzenberg, H. *Carbohydrate Polymers* **2002**, *47*, 39–51.

(60) Fereira, M.; Marvao, m. r; Duarte, M. L.; Nunes, T. *Chitin World, [Proceedings from the International Conference on Chitin and Chitosan], 6th, Gdynia, Pol.* **1994**, 480–488.

(61) Hirai, A.; Odami, H.; Nakajima, A. *Polymer Bulletin* **1991**, *26*, 87–94.

(62) Jeon, Y.; Sung, J.; Seo.c; Lim, H.; Cheong, H.; Kang, M.; Moon, B.; Ouchi, Y.; Kim, D. *J. Phys. Chem. B* **2008**, *112*, 4735–4740.

(63) Seethalakshmi, K.; Jasmine Vasantha Rani, E.; Padmavathy, R.; Radha, N. *Int. J. Cur. Res. Rev.* **2012**, *4*, 31–36.

(64) Tran, C. D.; De Paoli Lacerda, S. H.; Oliveira, D.; Lacerda, S. H. D. E. P. *Applied spectroscopy* **2003**, *57*, 2–7.

(65) Da Róz, A. L.; Leite, F. L.; Pereiro, L. V; Nascente, P. A. P.; Zucolotto, V.; Oliveira, O. N.; Carvalho, A. J. F. *Carbohydrate Polymers* **2010**, *80*, 65–70.

(66) Dreve, S.; Kacso, I.; Bratu, I.; Indrea, E. *J Phy: Conference Series* **2009**, *182*, 1 – 4.

(67) Burns, D. A.; Ciurczak, E. W. *Handbook of Near-Infrared Analysis*; Marcell Dekker: New York, 1992.

(68) Ellis, J. W. *Journal of the American Chemical Society* **1928**, *50*, 685 – 695.

(69) Dudley, R. L.; Fyfe, C. A.; Stephenson, P. J.; Deslandes, Y.; Hamer, G. K. **1983**, 2469–2472.

(70) Gardner, K. H.; Blackwell, J. *Biopolymers* **1974**, *13*, 1975–2000.

(71) Atalla, R. H. **1980**, 3249–3251.

(72) Atalla, R. H.; Vanderhart, D. L. *Solid state nuclear magnetic resonance* **1999**, *15*, 1–19.

(73) Zhang, L.; Ruan, D.; Gao, S. *Journal of Polymer Science Part B: Polymer Physics* **2002**, *40*, 1521–1529.

(74) Mori, T.; Chikayama, E.; Tsuboi, Y.; Ishida, N.; Shisa, N.; Noritake, Y.; Moriya, S.; Kikuchi, J. *Carbohydrate polymers* **2012**, *90*, 1197–203.

(75) Sebe, G.; Ham-Pichavant, F.; Ibarboure, E.; Koffi, A. L. .; Tingaut, P. *Biomacromolecules* **2012**, *13*, 570–578.

(76) Murata, S.; Suzuki, M.; Noyori, R. *J. Am. Chem. Soc.* **1980**, *102*, 3249–3251.

(77) Sauer, B. B.; McLean, R. S.; Thomas, R. R. *Langmuir* **1998**, *14*, 3045.

(78) Magonov, S. N.; Ellings, V.; Whangbo, M. H. *SurfSci* **1997**, *375*, L385.

(79) Bierwagen, G. P.; Twite, R.; Chen, G.; Tallman, D. E. *Prog. Org. Coat.* **1997**, *32*, 25.

(80) Raghavan, D.; Egwim, K. *J. Appl. Polym. Sci.* **2000**, *78*, 2000.

(81) Bar, G.; Thomann, Y.; Brandsch, R.; Cantow, H. J.; Whangho, M. H. *Langmuir* **1997**, *13*, 3807.

(82) Bar, G.; Thomann, Y.; Brandsch, R.; Whangho, M. H. *Langmuir* **1998**, *14*, 1219.

(83) Zhang, D.; Gracias, D. H.; Ward, R.; Gauckler, M.; Tian, Y.; Shen, Y. R.; Somarjai, G. A. J. *J Phy Chem B* **1998**, *102*, 6225.

(84) McLean, R. S.; Sauer, B. B. *Macromolecules* **1997**, *30*, 8314.

(85) Akhremitchev, B. B.; Mohney, B. K.; Marra, K. G.; Chapman, T. M.; Walker, G. C. *Langmuir* **1998**, *14*, 3976.

(86) Shao, Z.; Yang, J. Q. *Rev Biophys* **1995**, *28*, 195.

(87) Umemura, K.; Arakawa, H.; Ikai, A. *Japan J Appl Phys Part 1* **1993**, *2*, L1711.

(88) Vishwanathan, R.; Tian, J.; Marr, D. W. M. *Langmuir* **1997**, *13*, 1840.

(89) Tamayo, J.; Garcia, R. *Langmuir* **1996**, *12*, 4430.

(90) Cleveland, J. P.; Anczykowski, B.; Schmid, A. E.; Elings, V. B. *App Phys Lett* **1998**, *72*, 2613.

(91) Magonov, S. N.; Elings, V.; Papkov, V. S. *Polymer* **1997**, *38*, 297.

(92) Kiuchi, H.; Kai, W.; Inoue, Y. *Journal of Applied Polymer Science* **2008**, *107*, 3823–3830.

(93) Khamhan, S.; Baimark, Y.; Chaichanadee, S.; Phinyocheep, P.; Kittipoom, S. . *Internt'l. J. Polym. Anal. Charact* **2008**, *13*, 224–231.

(94) Alam, R.; Khan, M. A.; Khan, R. A.; Ghosha, l S.; Mondal, M. I. H. *J Pol Env* **2008**, *16*, 213 – 219.

(95) Liang, S.; Liu, L.; Huang, Q.; Yam, K. L. *Carbohydrate Polymers* **2009**, *77*, 718–724.

(96) Khan, M. A.; Alam, R.; Noor, F. G.; Khan, R. A.; Rahman, M. A. *J Macrom Sci Part A: Pure and Applied Chemistry* **2009**, *46*, 751 – 758.

(97) Radhakumary, C.; Nair, P. D.; Nair, C. P.; Mathew, S. *J Appl Pol Sci* **2009**, *114*, 2873 – 2886.

(98) Challa, R. *AAPS PharmSciTech* **2005**, *6*, E329.

(99) Tran, C. D.; Duri, S.; Delneri, A.; Franko, M. *Journal of hazardous materials* **2013**, *252-253*, 355–66.

(100) Duri, S.; Tran, C. D. *Langmuir* **2013**, *29*, 5037–49.

(101) Tran, C. D.; Duri, S.; Harkins, A. L. *Journal of biomedical materials research. Part A* **2013**, 1–10.

(102) Rebek, J. J. *Proc. Nat. Acad. Sci* **2009**, *106*, 10423 – 10424.

(103) Socrates, G. *Infrared characteristic group frequencies*; 2nd ed.; John-Wiley: New York, 1994.

(104) Bettinetti, G.; Sorrenti, M.; Catenacci, L.; Ferrari, F.; Rossi, S. *Journal of Pharmaceutical and Biomedical Analysis* **2006**, *41*, 1205–1211.

(105) Miller, C. . In *Near-Infrared technology in the agricultural and food industries*; Williams, P; Norris, K., Ed.; American Association of Cereal Chemists: Minnesota, 2001; pp. 19–37.

(106) Saito, H.; Tabeta, R.; Ogawa, K. *Macromolecules* **1987**, *20*, 2424 – 2430.

(107) Kitaoka, M.; Hayashi, K. *J. Incl. Phe. Macro. Chem.* **2002**, *44*, 429–431.

Chapter 3. ADSORPTION OF MICROCYSTIN, CHLOROPHENOLS AND BISPHENOL A FROM AQUEOUS SOLUTION USING POLYSACCHARIDE COMPOSITE MATERIALS

3.1. Background

3.1.1. Microcystin

Microcystins (MCs) are hepatotoxic cyclic peptides. They are an important group of cyanobacterial toxins in water.[1–7]They are produced by strains of *Microcystis*, *Oscillatoria*, *Anabaena* and *Nostoc* species.[8] They are involved in poisoning of animals, and also involved in human health problems.[8] Microcystins are extremely stable and resistant to chemical hydrolysis and oxidation at near neutral pH. In natural waters and in the dark, microcystins may persist for months or years.[8] Cyclic heptapeptide microcystins consist of 5 invariant amino acids and 2 variable amino acids. The invariant amino acids are in the D-configuration and the variable amino acids are in the L-configuration.[9–12] The MCs are very soluble in water and consist of over 80 reported variants; however, four MCs, MC-LR, MC-RR, MC-LA, and MC-YR are of special concern to the Environmental Protection Agency (EPA) and are on EPA Contaminant Candidate List III.[13] The letters in the name represent the amino acid residues for each particular MC, i.e. L – Lysine, R – Arginine, A – Alanine and Y – Tyrosine. The structures of some of the common MCs are shown in Scheme 3.1. The World Health Organization (WHO) has set a provisional drinking water guideline of 1 µg/L for MC-LR.[14] The toxicity of MCs is due to their strong binding and inhibition of protein phosphatases. MCs are also known to

Microcystin LR

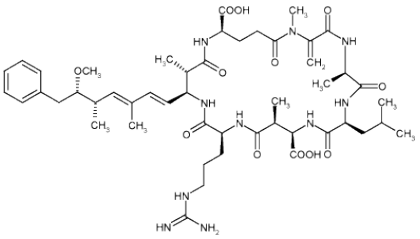

Microcystin RR

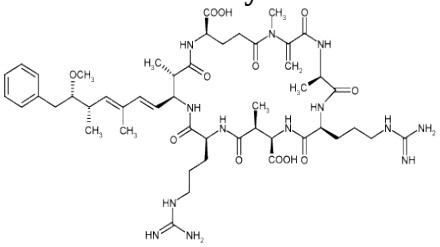

Microcystin YR

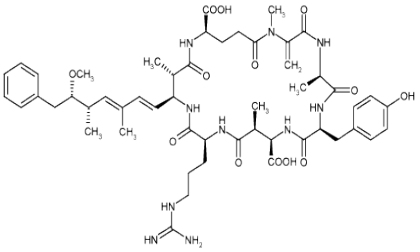

Microcystin LA

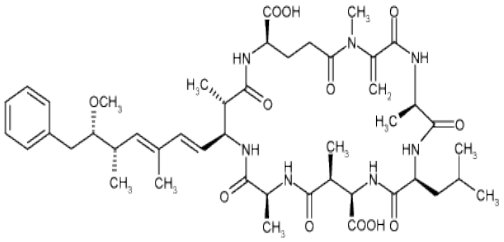

Microcystin LW

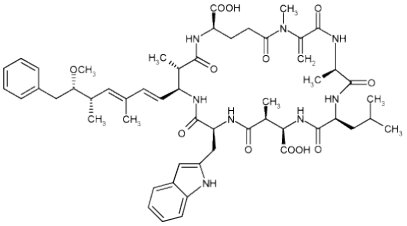

Microcystin LF

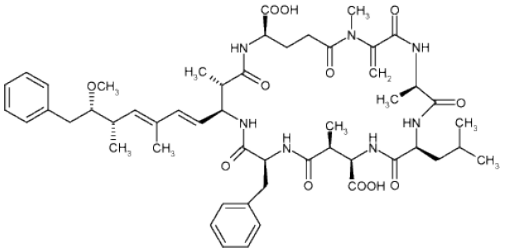

Microcystin LY

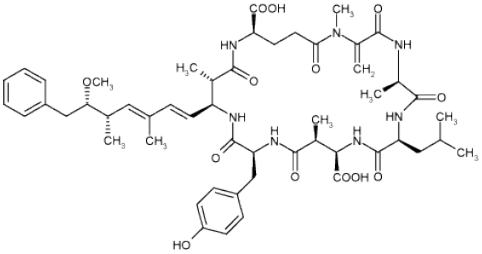

Microcystin WR

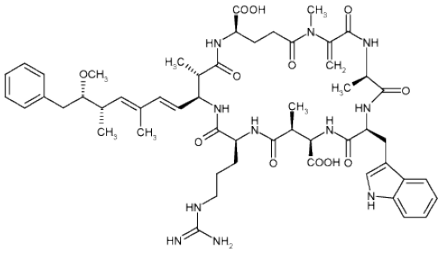

Scheme 3.1: Structures of some common microcystins

promote the growth of tumors and have a genotoxic effect as well as strong mutagenicity[1–7].

Conventional water treatment practices such as pre-chlorination, agulation/sedimentation, filtration and post-chlorination have been shown to be ineffective in removing microcystins.[15,16] Even though activated carbon has been shown to be effective in removing MCs, powdered activated carbon was shown to remove MCs at doses higher than those normally used at water treatment plants.[16,17]

There is still therefore a particular need to develop low cost adsorbents that can effectively remove MCs from our water sources. It has been reported that CS, when modified with fly ash or immobilized on clay, can adsorb and remove algae such as *Chlorella pyrenoidosa* or *Microcystis aeruginosa* in water[18–22]. Such reports have prompted us to initiate this study, which seeks to investigate the possible application of our polysaccharide composite materials to the removal of MCs. The polysaccharide composite materials, whose preparation and characterization was described in detail in Chapter 2, will be used in this study using MC-LR as a model compound.

3.1.2. Chlorophenols

Endocrine disrupting chemicals are naturally occurring or man-made chemicals in the environment, which interfere with the normal function of the hormonal systems of humans and animals. Polychlorinated phenols and bisphenol A are an example of such chemicals. Chlorophenols and their salts are broad spectrum biocides that have been used

in agriculture, industry and public health since the 1920s.[23] These include in the wood industry, in the production of pesticides and as additives to inhibit microbial growth in a wide array of products, such as adhesives, oils, textiles, and pharmaceutical products. Chlorophenols have been designated as priority pollutants in the list of hazardous wastes.[23] They are toxic, resistant to microbial attack, and they accumulate in the food chain.[24] Misuse, accidental spillage, and improper disposal have resulted in extensive groundwater pollution.[25] Even though the groundwater chlorophenol levels have gone down in recent years due to strict controls, chlorophenols have been shown to be lethal to a wide variety of organisms at the level of $1 mgL^{-1}$.[26]

The sorption of pollutants from aqueous solution using adsorbents plays an important role in water pollution control. In recent years, there has been considerable interest in the use of low cost sorbents. A number of reports have described microbial degradation of chlorophenols into non-toxic products, in both natural water bodies and in simulated systems.[27,28] However, such kind of bioremediation of low level chlorophenol polluted water bodies requires a long enrichment period and is susceptible to inhibition by relatively low concentrations of pentachlorophenol.[29] In addition, the ground water characteristics such as low temperature, coexistence of different chlorophenols,[30] and varied pH values and salinity,[31] may further decrease the microbial viability and effectiveness in treatment units. Development of methods and materials for the efficient removal of chlorophenols from aqueous sources is therefore particularly important. The ability of our polysaccharide composite materials to effectively remove chlorophenols will be studied. The performance of the materials will be evaluated in terms of both the kinetic and thermodynamic isotherm sorption parameters.

3.1.3. Bisphenol A

Bisphenol A (BPA), structure shown in Scheme 3.2, is a well-known endocrine disrupting chemical with estrogenic activity.[32] BPA has been widely used as the monomeric substance for the production of polycarbonate and epoxy-phenolic resins, and as the stabilizer or antioxidant for many types of plastics.[33] As a result, BPA is inevitably released in to the aquatic environment through various routes. The potential adverse effects of BPA on human health and reproductive biology include breast and prostate cancer, sperm count reduction, abnormal urethra development in males, early sexual maturity in females, neurobehavioral problems, prevalence of obesity, type 2 diabetes and immunodeficiency.[32] A 2010 report from the United States Food and Drug Administration (FDA) raised further concerns regarding exposure of fetuses, infants and young children.[34] As a result, the removal of BPA from aqueous solutions is important in controlling some of the health hazards posed by this compound. The structures of the chlorophenols and BPA used in this study are illustrated in Scheme 3.2.

As described earlier in Chapter 2, cellulose (CEL) and chitosan (CS) are two of the most abundant biorenewable biopolymers on the earth. We saw that in these polysaccharides, an extensive network of intra- and inter-hydrogen bonds enables them to adopt an ordered structure. While such structure is responsible for CEL to have superior mechanical strength and CS to exhibit

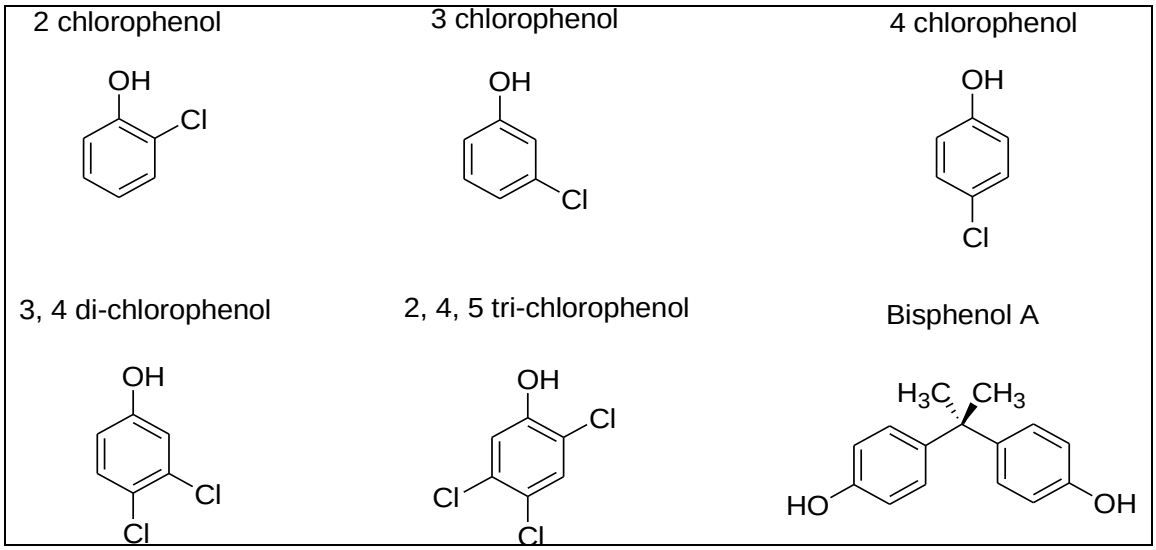

Scheme 3.2: Structures of the chlorophenols and BPA analytes

remarkable properties it also makes them insoluble in most solvents[35–42]. This is rather unfortunate because with their superior mechanical strength and unique properties, CEL and CS would be excellent supporting polymer for cyclodextrin (CD). It is expected that the [CEL and/or CS+TCD] composite materials prepared in Chapter 2 would have properties that are a combination of those of all of its components. That is, they may have superior mechanical strength (from CEL), can stop bleeding, heal wound, kill bacteria, deliver drugs (from CS) and selectively form inclusion complexes with a wide variety of compounds of different types, sizes and shapes (from CDs). The method described in Chapter 2 exploited the advantages of a simple ionic liquid, butyl methylimidazolium chloride ($BMIm^+Cl^-$), a green solvent[43–49], to develop an innovative, simple, pollution-free method to dissolve not only CS but also other polysaccharides including CEL without using any acid or base, thereby avoiding any possible chemical or physical changes, and used only naturally occurring biopolymers such as CEL as

support materials to strengthen structure and expand utilities while keeping the biodegradable, biocompatible and anti-infective and drug carrier properties of CS-based materials intact. The incorporation of TCDs into the composite materials is expected to impart some selectivity to the resultant composites. Our efforts to investigate the application of these polysaccharide composite materials for the removal of microcystin, chlorophenols and bisphenol A from aqueous solution are described below.

3.2. Adsorption kinetics and thermodynamic isotherms

Experiments were designed to determine if our polysaccharide composite materials can adsorb MC, chlorophenols and BPA. The mechanism of the adsorption processes in terms of rate constants and adsorbed amounts at equilibrium were also evaluated. Efforts were also made to evaluate the optimum composite material which gives the highest adsorption capacity. These tasks were accomplished by fitting kinetic data to both pseudo-first order and pseudo-second order models in order to determine appropriate reaction order for the adsorption processes based on R^2 and MSC (Model Selection Criteria, eqn [3.11]) values[50–52]. The effect of adding CDs to the polysaccharide composite materials on their adsorption selectivity was also investigated.

3.2.1. Adsorption kinetics

The pseudo-first-order, pseudo-second-order and intra-particle diffusion kinetic models were used to evaluate the adsorption kinetics of different chlorophenols, BPA and MC and to quantify the extent of uptake in the adsorption process

Pseudo-first-order kinetic model

The linear form of Lagergren's pseudo-first-order equation is given as[53,54]:

$$\ln(q_e - q_t) = \ln q_e - k_1 t \qquad [3.1]$$

where q_t and q_e (mg g^{-1}) are the amount of pollutant adsorbed at time t and at equilibrium respectively and k_1 (min^{-1}) is the pseudo first order rate constant calculated from the slope of the linear plot of ln ($q_e - q_t$) versus t.

Pseudo-second-order kinetic model

According to the Ho model[50], the rate of pseudo second order reaction may be dependent on the amount of species on the surface of the sorbent and the amount of species sorbed at equilibrium. The equilibrium sorption capacity, q_e, is dependent on factors such as temperature, initial concentration and the nature of solute-sorbent interactions. The linear expression for the Ho model can be represented as follows[50]:

$$\frac{t}{q_t} = \frac{1}{k_2 q_e^2} + \frac{1}{q_e} t \qquad [3.2]$$

where k_2 (g/mg.min) is the pseudo-second order rate constant of sorption, q_e (mg/g) is the amount of analyte adsorbed at equilibrium, q_t (mg/g) is the amount of analyte adsorbed at any time t.

If the initial adsorption rate h is

$$h = k_2 q_e^{\ 2} \qquad [3.3]$$

Then Eq 3.2 can be rearranged as

$$\frac{t}{q_t} = \frac{1}{h} + \frac{1}{q_e} t \qquad [3.4]$$

A linear plot can be obtained by plotting t/q_t against t. q_e and h, can obtained from the slope and intercept; k2 can be calculated from h and q_e according to Eq 3.3.

Intra-particle diffusion model

The intra-particle diffusion equation is given as follows[55,56]:

$$q_t = k_i t^{0.5} + I \qquad [3.5]$$

where k_i (mg g^{-1} $min^{-0.5}$) is the intra-particle diffusion rate constant and *I* (mg g^{-1}) is a constant that gives the information regarding the thickness of the boundary layer[55,56]. According to this model, if the plot of qt versus $t^{0.5}$ gives a straight line, then the adsorption process is controlled by intra-particle diffusion, while, if the data exhibit multi-linear plots, then two or more steps influence the adsorption process.

3.2.2. Thermodynamic sorption isotherms

Different isotherm models have been developed for describing thermodynamic sorption equilibrium. The Langmuir, Freundlich and Dubinin–Radushkevich (D–R) isotherms were used in the present study.

Langmuir isotherm.

The Langmuir sorption isotherm describes that the uptake occurs on a homogeneous surface by monolayer sorption without interaction between adsorbed molecules and is commonly expressed as[57]:

$$\frac{C_e}{q_e} = \frac{C_e}{q_m} + \frac{1}{K_L q_m} \qquad [3.6]$$

where q_e (mg g^{-1}) and C_e (mg L^{-1}) are the solid phase concentration and the liquid phase concentration of adsorbate at equilibrium respectively, q_m (mg g^{-1}) is the maximum adsorption capacity, and K_L (L mg^{-1}) is the adsorption equilibrium constant. The constants K_L and q_m can be determined from the slope and intercept of the plot between C_e/q_e and C_e.

Freundlich isotherm.

The Freundlich isotherm is applicable to non-ideal adsorption on heterogeneous surfaces and the linear form of the isotherm can be represented as[58]:

$$\log q_e = \log K_F + \left(\frac{1}{n}\right) \log C_e \qquad [3.7]$$

where q_e (mg g^{-1}) is the equilibrium concentration on adsorbent, C_e (mg L^{-1}) is the equilibrium concentration in solution, K_F (mg g^{-1}) (L g^{-1})$^{1/n}$ is the Freundlich constant related to sorption capacity and n is the heterogeneity factor. K_F and 1/n are calculated from the intercept and slope of the straight line of the plot log q_e versus log C_e.

Dubinin–Radushkevich (D–R) isotherm.

The Dubinin–Radushkevich (D–R) isotherm model can be represented by the following equation[59,60]:

$$\ln q_e = \ln q_m - \beta \varepsilon^2 \qquad [3.8]$$

$$\varepsilon = RT \ln\left(1 + \frac{1}{C_e}\right) \qquad [3.9]$$

where q_m (mg g^{-1}) is the maximum adsorption capacity, β ($mmol^2 J^{-2}$) is a coefficient related to the mean free energy of adsorption, ε (J $mmol^{-1}$) is the Polanyi potential (the energy that is required to remove the molecule from that location to a point outside the attractive force field of the solid surface), R is the gas constant (8.314 J mol^{-1} K^{-1}), T is the temperature (K) and C_e (mg L^{-1}) is the equilibrium concentration. The D–R constants q_m and β can be determined from the intercept and slope of the plot between ln q_e and ε^2.

3.3. Materials and Methods

The polysaccharide composite materials used in this study are those that were synthesized and characterized according to the procedures described in Chapter 2.

3.3.1. Chemicals

Microcystin-LR (MC-LR) (Enzo Life Sciences), 2-chlorophenol (2 Cl-Ph), 3 chlorophenol (3 Cl-Ph), 4-chlorophenol (4 Cl-Ph), 3,4 dichlorophenol (3,4 di Cl-Ph), 2,4,5 trichlorophenol (2,4,5 tri Cl-Ph) and bisphenol A (BPA) (Sigma Aldrich, Milwaukee, WI) were all used as received.

3.3.2. Procedure used to measure kinetics of adsorption

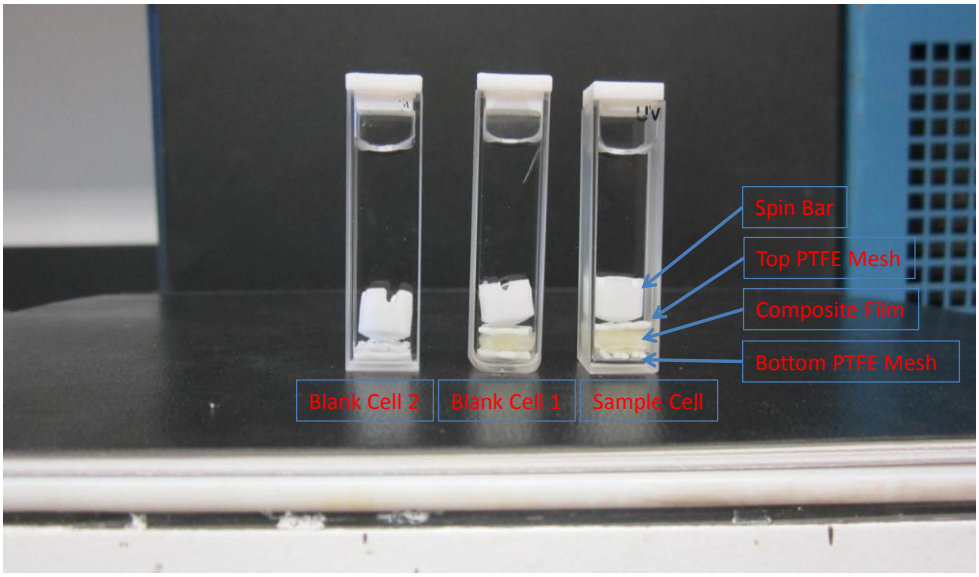

Figure 3.1. Photograph of experimental setup for kinetic measurements

Figure 3.1: Photograph of experimental setup

The adsorption of MC, chlorophenols and BPA was followed by measuring the change in the UV absorption of solutions of these pollutants in the presents of our composite materials. Three matching cuvettes were used for all adsorption measurements, one for adsorption of the pollutant by the composite and the other two as the blanks. Photograph of the experimental setup with the three cells is shown in Figure 3.1. The samples (about 0.02g of dry film of the composite material) was washed thoroughly in water prior to the adsorption experiments to further insure that [$BMIm^{+}Cl^{-}$] was completely removed because absorption of any residual IL may interfere with that of MC,

chlorophenols or BPA. To wash the samples, the weighed composite materials were placed in a thin cell fabricated from PTFE whose windows were covered by two PTFE meshes. The meshes ensured free circulation of water through the material during the washing process. The PTFE mold containing the samples was placed in a 2L beaker which was filled with de-ionized water and was stirred at room temperature for 24 hours. During this time, absorbance of washing water was monitored at 214 and 290 nm to determine the presence of any residual [$BMIm^+$ Cl^-]. The water in the beaker was replaced with fresh de-ionized water every 4 hours. Figure 3.2 below shows typical UV absorption spectra obtained during the course of the 24 hr washing period The UV spectrum of [$BMIm^+Cl^-$] (pink spectrum)is also included for reference. The results show that the absorption bands at 214nm and 290nm progressively decreases and after 24 hrs of continuous washing, the two bands were no longer present in the spectrum of the washing solutions. This means that any residual [$BMIm^+Cl^-$] has now been reduced to level which will not interfere with the UV absorption measurements of the pollutants to be studied.

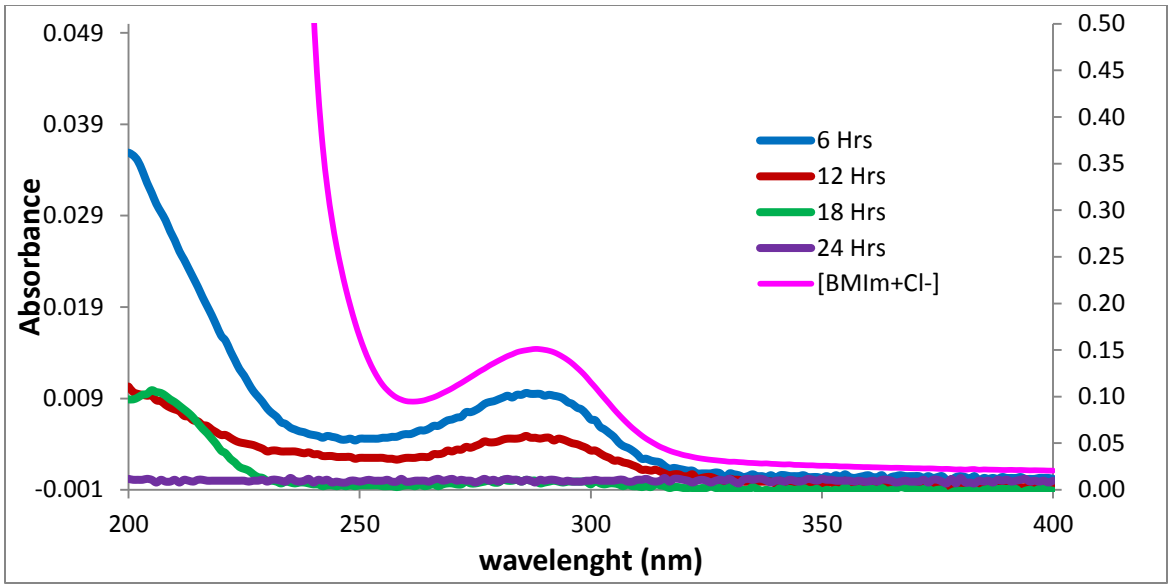

Figure 3.2: UV absorption spectra of the washing solutions showing the removal of residual ionic liquid from the composite materials over a 24 hr washing period.

After 24 hours, the composite material was taken out of the water and placed into the sample cuvette (cell on the right in the experimental setup photograph shown in Figure 3.1). Both sample and the two blank cells were stirred using a small magnetic spin bar during the measurement. In order to prevent damage to the sample by the magnetic spin bar and to maximize the circulation of the solution during measurement, the samples inside the cuvette were sandwiched between two PTFE meshes. Specifically, a piece of PTFE mesh was placed at the bottom of the spectrophotometric cell. The washed film sample was laid flat on top of the PTFE mesh. Another piece of PTFE mesh was placed on top of the sample and finally the small magnetic spin bar was placed on top of the second mesh. The blank cell 1, shown in the center of the photograph in Figure 3.1, had the same contents as the sample cell (i.e., PTFE mesh, composite film, PTFT mesh and magnetic spin bar) but without the pollutant. This blank cell 1 had de-ionized water

instead of the solution of the pollutant. Exactly 2.70 mL of 1.55 x 10^{-4}M aqueous solution of the MC-LR, chlorophenols or BPA was added to both sample and blank cell 2. This blank cell 2 (shown on the left of Figure 3.1) had the same contents as the sample cell but without the composite material. This blank 2 was used to correct for any possible adsorption of the pollutants onto the cell contents (PTFE meshes, and magnetic spin bar) other than the composite material. Any residual ionic liquid that may leak from the composites into the cell is corrected for using blank absorbance data from blank cell 1. Measurements were carried out on a Perkin Elmer Lambda 35 UV/VIS spectrometer set to the appropriate wavelength for each pollutant, i.e., 274 nm for 2- and 3-chlorophenol, 280nm for 4-chlorophenol, 282 nm and 289 nm for 3,4-dichloro- and 2,4,5-trichlorophenol, respectively, and 276 nm for bisphenol A. Microcystin was measured at 238 nm.

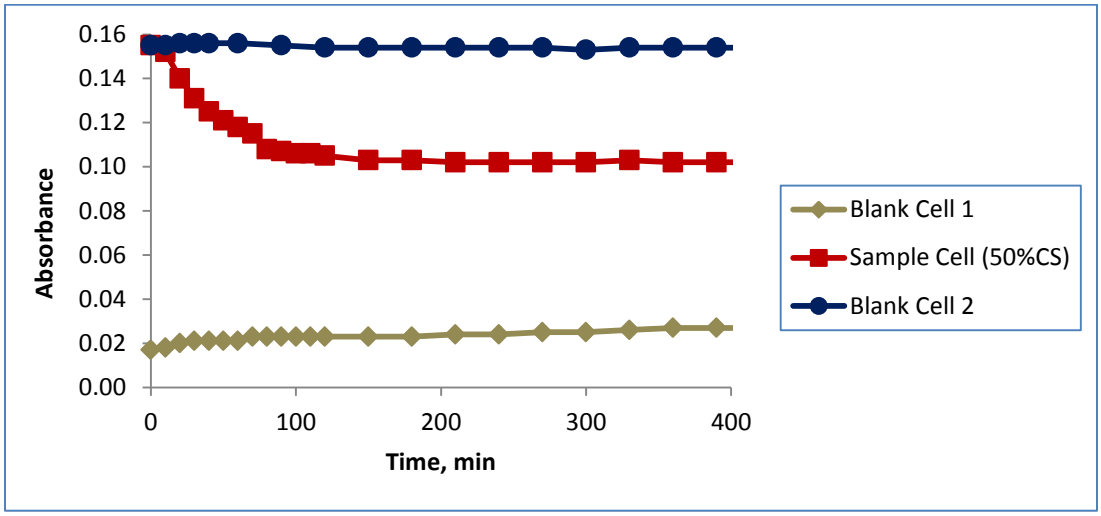

Figure 3.3: Absorbance data for the two blank cells and one sample (50%CS) for the adsorption of MC (Blank cell 1 has all sample contents with de-ionized water instead of pollutant solution and Blank cell2 contains all sample cell contents but no film).

Measurements were taken at specific time intervals and the cell was returned to a magnetic stirrer for continuous stirring. An example of the absorbance changes that are observed for the two blank cells and one of the sample composites is shown in Figure 3.3. Blank cell 1 contains de-ionized water instead of the pollutant solution, and as expected, the absorbance of this cell starts off very low and only increases marginally during the course of the experiment. Blank cell 2 contains pollutant solution with all the other components of the sample cell except for the composite material. As shown in Figure 3.3, the absorbance of this cell remains relatively the same over the course of the experiment. This indicates other components of the sample cell (meshes and stir bar) have negligible contribution to the absorbance changes that are observed in the sample. The absorbance of a typical sample cell (50%CS in Figure 3.3) decreases rapidly before leveling off. Taking into consideration the results of the blank cell 1 and blank cell 2, the observed absorbance change for the sample cell shown in Figure 3.3 suggest that the composite material in the sample cell is adsorbing some pollutant from the solution reducing its concentration, resulting in the observed decrease in absorbance.

3.3.3. Procedure used to measure equilibrium sorption isotherms

Batch sorption experiments were carried out in 50mL stoppered vials containing 10 mL of the pollutant solution of known initial concentration. A weighed amount (0.1g) of the composite material was added to the solution. The samples were agitated at 250 rpm in a shaking water bath at 25^0C for 72 hours. The residual amount of pollutant in each flask was analyzed by UV/Vis spectrophotometry. The amount of pollutant

adsorbed onto the composite material was calculated using the following mass balance equation:

$$q_e = \frac{(C_i - C_e)V}{m} \qquad [3.10]$$

where q_e (mg/g) is the equilibrium sorption capacity, C_i and C_e (mg/L) are the initial and final pollutant concentrations respectively. V (L) is the volume of the solution and m (g) is the weight of the composite film material.

3.4. Kinetics of adsorption of Microcystin

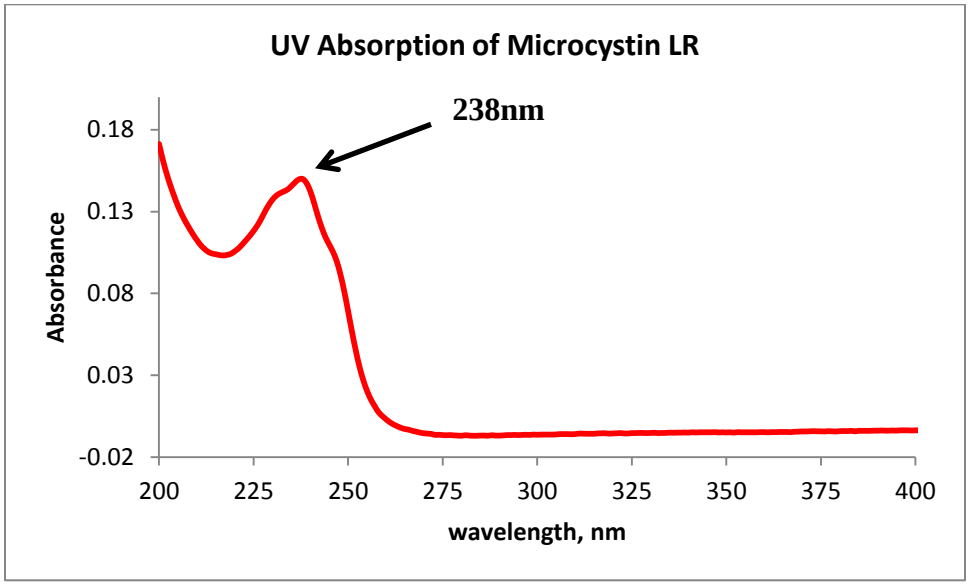

Figure 3.4: UV absorption spectrum of 1.55x10-4M MC-LR solution

As described in the experimental section, kinetics of adsorption of MC by composite materials was determined by measuring the decrease in absorbance as a function of time in a solution containing a composite film. Figure 3.5 show the UV absorption spectrum of MC-LR. The spectrum has an absorption band with a maximum at 238 nm. Consequently, 238 nm was used as the analytical wavelength for MC. Figure 3.5 show some typical absorbance changes observed for MC with different [CEL+CS] composite materials. As expected, the absorbance of the MC solution decreases rapidly in the first 100 minutes and begins to slow down before eventually leveling off after about 400 minutes. This shows that there is an initial rapid sorption of the MC by the composite materials before an equilibrium is established between the sorbed MC and the MC still in solution. An illustration of the adsorption process and the possible equilibrium that can be established is shown in Figure 3.6. The results in Figure 3.5 show that there is a correlation between the magnitude of the absorbance change and the amount of CS in the composite material during the adsorption of MC by [CEL+CS] composite materials. As illustrated, the absorbance of a 0%CS (100% CEL) sample remains virtually the same throughout the entire experiment. This is a clear indication that 100%CEL composite material is not capable of adsorbing MC. Consequently, the magnitude of the absorbance change for the [CEL+CS] composite increase with a decrease in the amount of CEL in the respective composite. As described earlier in Chapter 2, it is CS that has good pollutant adsorption capability and CEL was added to the composites to improve their rheological and mechanical properties.

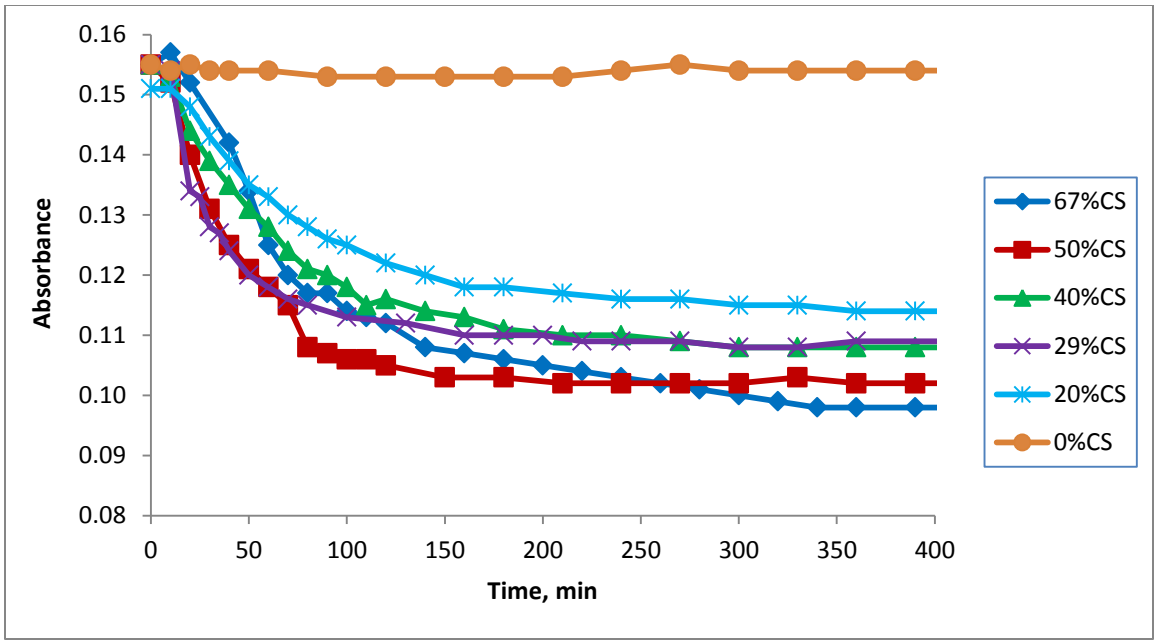

Figure 3.5: Typical absorbance changes obtained for different [CEL+CS] composite materials for the adsorption of MC.

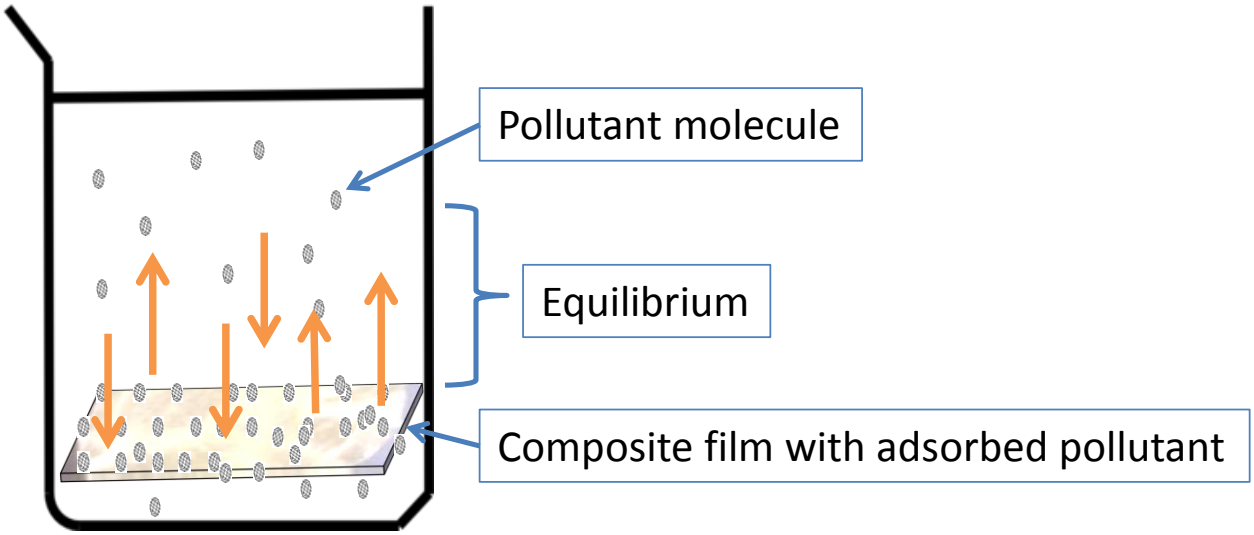

Figure 3.6: A cartoon representing the adsorption and equilibrium processes.

From the measured absorbances, the amount of MC that has been adsorbed on to the composite material at time t (i.e., q_t) can then be calculated. Shown in Figure 3.7 are the plots of q_t as a function of time for six different [CEL+CS] materials with different compositions ranging from 0% to 67% CS. These are the same samples whose absorbance changes are plotted in Figure 3.5. As already explained earlier, increasing CS concentration in the composite material led to increase in amount of microcystin adsorbed at equilibrium. The plot for the 0%CS (100%CEL) shows that this particular film does not adsorb MC. Detailed information on adsorption kinetics can be obtained by fitting the data to both pseudo-first order (eqn 3.1) and pseudo-second order (eqn 3.2) model. Typical linearized plots for pseudo-1st order (equation 3.1) and pseudo-2nd order (equation 3.2) for the [CEL+CS] composite materials are shown in Figure 3.8.

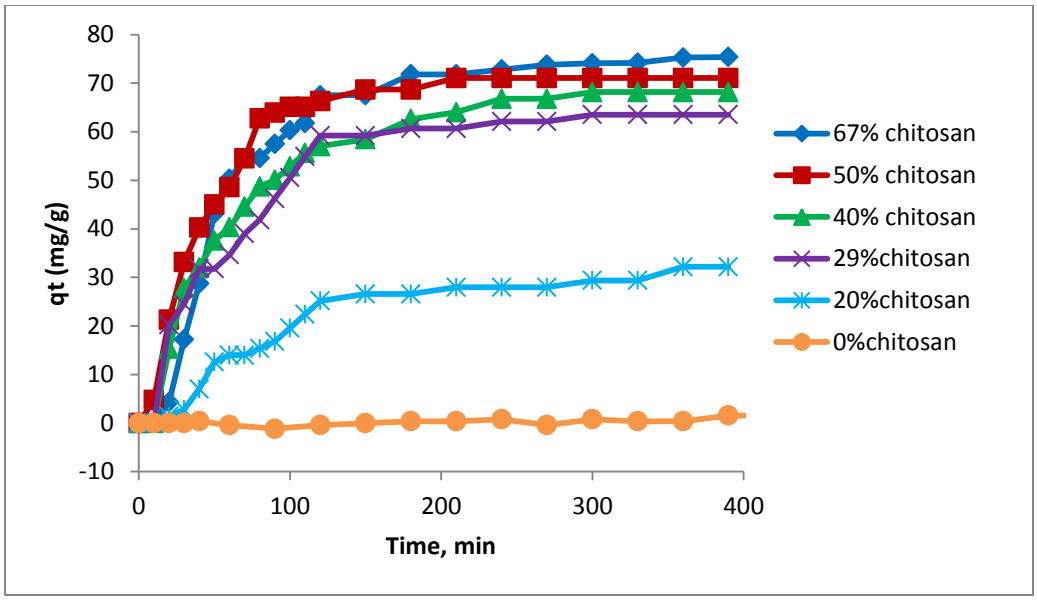

Figure 3.7: Plot of qt as a function of time for the adsorption of MC-LR by [CEL+CS] composite materials with different composition ranging from 0%CS to 67% CS

Table 3.1: Kinetic adsorption parameters for the sorption of MC-LR by [CEL+CS] composite materials

Composite Material			Pseudo-First Order				Pseudo-Second Order			
% CS	% CEL	qe (Exptal) (mg/g)	q_e (mg/g)	k_1 (min^{-1})	R^2	MSC	Q_e (mg/g)	$k_2 . 10^4$ (g/mg. min)	R^2	MSC
67	33	75	94±8	0.020±0.001	0.9714	2.84	96±3	1.6±0.1	0.9894	4.18
50	50	71	72±1	0.02±0.01	0.9794	3.86	79±2	5±3	0.9953	5.46
40	60	68	52±1	0.010±0.007	0.937	2.72	73±9	3±1	0.9965	5.66
29	71	64	44±1	0.01±0.02	0.9419	2.73	71±2	5±2	0.9987	6.52
20	80	32	31±5	0.007±0.001	0.7254	1.98	42±4	1.9±0.3	0.9932	5.00

The results of these linear plots indicate a general goodness of fit to both models but the pseudo 2nd order model seem to have better linear plots for most composites with the exception of the 20%CS sample. Listed in Table 3.1 are the pseudo 1st order and pseudo 2nd order fitting parameter results obtained for [CEL+CS] composite materials with different composition ranging from 20% to 67% of CS. The correlation coefficient (R^2) for the pseudo 1st order ranges from about 0.7254 to about 0.9794 while that for the pseudo 2nd order was found to vary from 0.9894 to about 0.9987. Another figure of merit which is used to evaluate how well a given process can be described by a given model is the Model Selection Criteria (MSC). MSC is calculated by the following equation:

$$MSC = ln\left\{\frac{\sum_{i=1}^{n} wi(Y_{observed}-\bar{Y}_{observed})^2}{\sum_{i=1}^{n} wi(Y_{observed}-Y_{calculated})^2}\right\} - \frac{2p}{n} \qquad [3.11]$$

Where w represents the weighting, n is the number of points and p is the number of parameters. Similar to the R^2 value, the higher the MSC, the better is the fit. The MSC results in Table 3.1 follows a similar trend to the R^2 values where the values for the pseudo 2nd order model are higher than their corresponding 1st order counterparts. It is evident from the linear plots as well as from the fact that R^2 and MSC values in all cases are higher for pseudo-2nd order than for pseudo-1st order indicating that the adsorption of MC by [CEL+CS] composite materials is better described by the pseudo 2nd order model. Results obtained clearly show that CS composite materials can adsorb MC very well. Material without CS (i.e., 0%CS or 100% CEL) does not adsorb MC at all (yellow curve in Figure 3.7), and that up to 96 mg of MC can be adsorbed per g of the composite by the 67% CS composite. The adsorptivity was found to be dependent on the concentration of CS in the composite, namely, increasing concentration of CS leads to an increase in

amount of adsorbed MC. For example, increase of CS concentration from 20% to 67% led to 128% increase in the amount of adsorbed MC. This is expected because only CS is responsible for the adsorption of MC. The role of CEL in the composite is, as was explained in Chapter 2, to strengthen mechanical and rheological properties of the material. Again there is a concern that CS had two opposite effects on the properties of the composites: namely, it is responsible for the adsorption of MC but it also undergoes swelling in water which leads to weakening structure of the composites. The swelling properties of the [CEL+CS] composite materials were measured and the results were discussed in Section 2.5.2. As was observed from the swelling results, increase in CS concentration from 20% to 67% led to about 29.2% increase in % EWC. However, as shown in Table 3.1, a similar increase in CS concentration led to about 128% in the amount of MC adsorbed. This suggests that [CEL+CS] composites with relatively good adsorption capacities can be prepared while maintaining low swelling ratio.

As described in the introduction, currently there are several absorbents available for removal of MC. The results in Table 3.2 shows some of the materials which are commonly used for the removal of MC. Our [CEL+CS] composite materials reported here are shown to be better adsorbents for MC. The best performing material, Fe_3O_4@SiO2 magnetic microspheres,[61] was reported to adsorb 20mg of MC per gram of adsorbent. This amount is 4.8 times less than the 96 mg of MC removed by our 67% CS composite material.

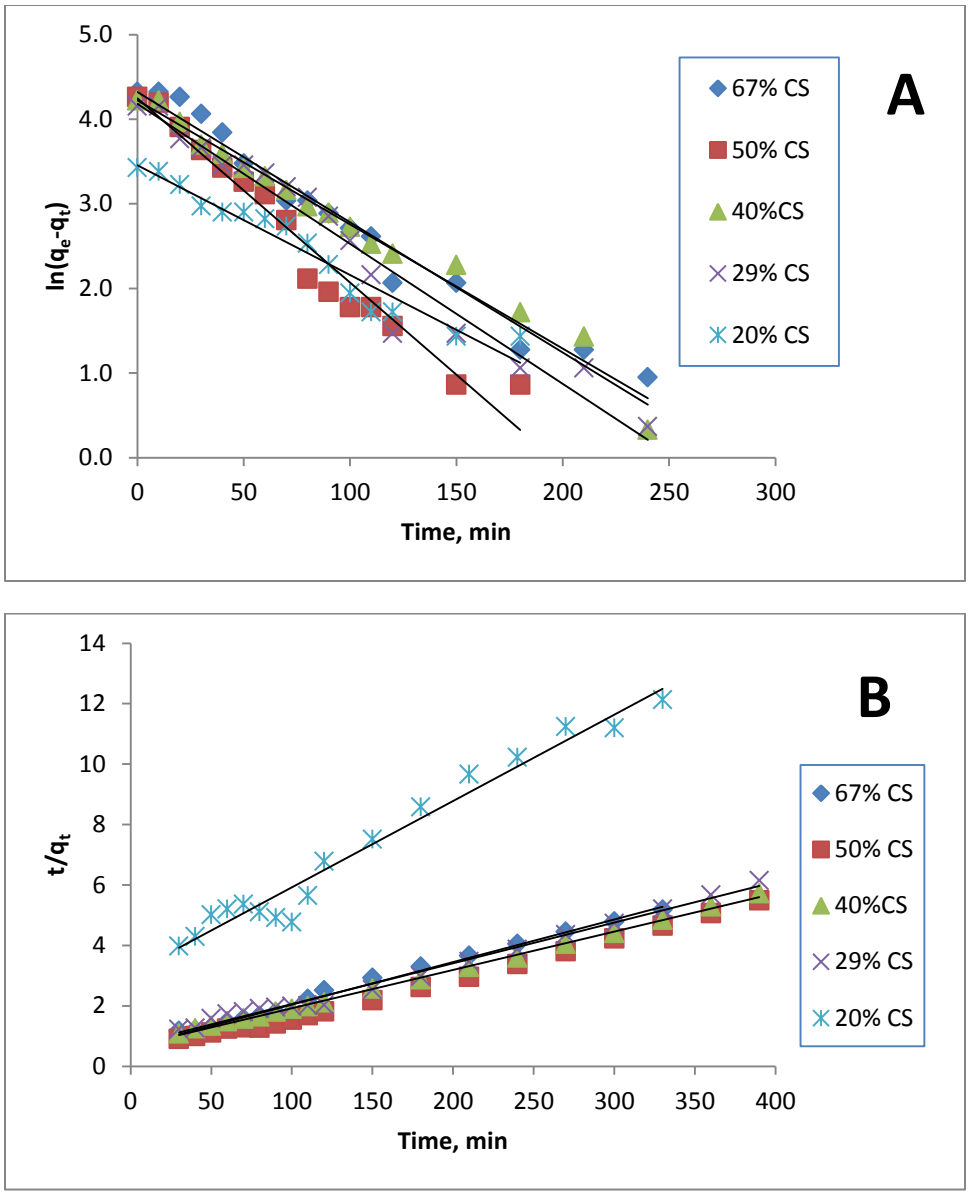

Figure 3.8: Typical linearized plots for (A) pseudo-first order and (B) pseudo-second order models for [CEL+CS] composite films containing 67%CS and 50%CS

Table 3.2: Comparison of the adsorption efficiency of MC-LR by commonly used materials

Adsorber	mg of adsorbed MC-LR /g adsorber	Reference
Iron Oxide Nanoparticles	0.15	[62]
Fe_3O_4@copper silicate nanotube microspheres	0.5	[63]
Powdered activated carbon (PAC)	0.75	[6]
Natural clay particles	4.6	[64]
Carbon nanotubes	5.9	[65]
PAC/UF (membrane ultrafiltration)	9.9	[66]
Activated carbon fibers (ACF)	17	[67]
Fe_3O_4@SiO_2 magnetic microspheres	20	[61]
[CEL+CS] composite	96	This work

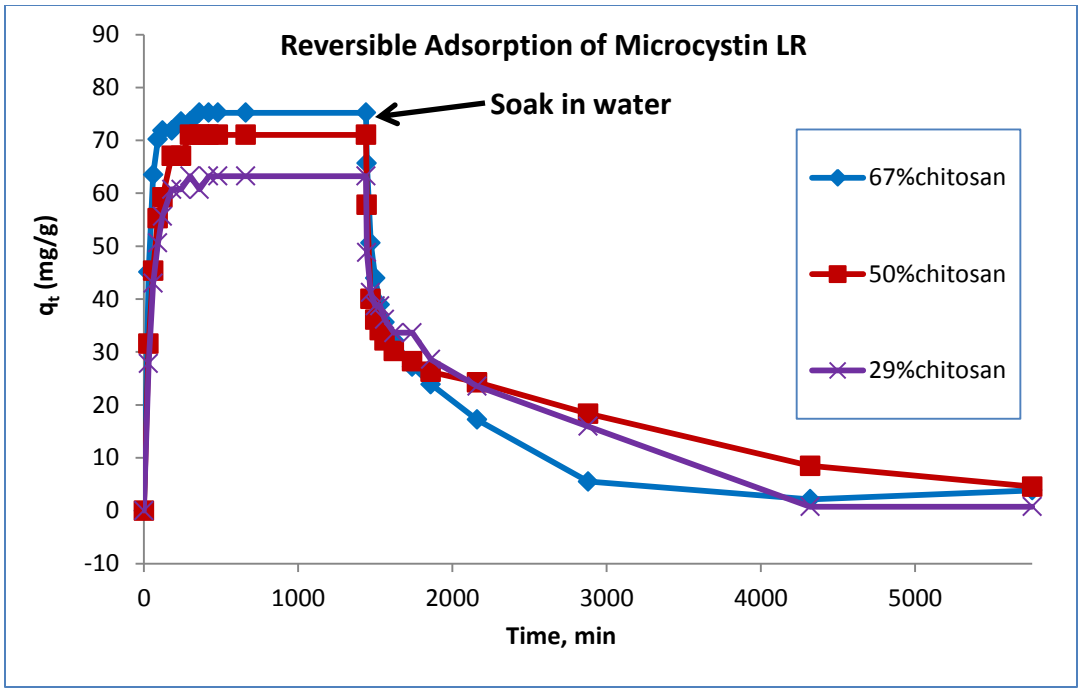

Figure 3.9: Plot of qt of adsorption of MC-LR as a function of time by [CS+CEL] composite materials illustrating the reversibility of the adsorption process

It was shown in Chapter 2 that the method used to synthesize these [CEL+CS] composite materials is recyclable with ionic liquid recovery efficiency of at least 88%. Experiments were also carried out to determine whether these [CEL+CS] composites, synthesized by a recyclable method, can also be recycled. That is, will it possible to desorb the adsorbed MC and reuse them for a similar (or same) application and whether their adsorption efficiency changes on the second adsorption. Three composite materials were used in this experiment, i.e. 29%CS, 50%CS and 67%CS. Shown in Figure 3.9 is plot of q_t as a function of time during the adsorption and desorption process for these composite materials. The first portion of this plot is very similar to the adsorption process described above for these materials. Adsorption equilibrium was reached after about 400

minutes, but the measurement was continued up to 24 hrs just to make sure that adsorption equilibrium was properly established for all samples. After 24 hrs, the composite materials were removed from the MC solutions, quickly blotted with a dry filter paper to remove an excess MC solution from the films. The spectrophotometric cells, the meshes and the magnetic spin bar were thoroughly washed and rinsed with de-ionized water. The [CEL+CS] composite materials, which now have MC adsorbed on them were placed back into the clean spectrophotometric cells in an arrangement similar to the one used for the adsorption process. Exactly 2.7mL of de-ionized water were pipetted into the cells and the absorbance of the solution was monitored just like in the adsorption process. This time, the MC previously adsorbed in the composite underwent desorption from the composites into the water (in both adsorption and desorption process, q_t values, which is the amount of MC in the composites at time t, were plotted. These values were calculated from measured concentrations of MC in solution). As illustrated in Figure 3.9, the MC that was previously adsorbed on to 29% CS, 50% CS and 67% CS was quantitatively removed from the composite materials. It was interesting to note that almost 50% of the adsorbed MC was desorbed in about 120 minutes only. Even though the complete quantitative removal of the MC eventually took longer, this could be speed up by adding fresh de-ionized water in to the cells, which was not done in this experiment. These results clearly indicate that [CEL+CS] composites are not only very efficient adsorbents for MC but also that the adsorbed MC can be quantitatively desorbed to enable the composites to be reused.

Another concern that needed investigation was the efficiency of the materials if they are to be reused. Measurements were therefore performed to determine if there are

any changes in adsorption efficiency of the composite materials when they are reused for the second time, i.e., composite materials in which previously adsorbed MC are desorbed. For this experiment, two composite films were used, a 50% CS composite material and a 67% composite material. MC was adsorbed onto these two composite materials using the same procedure described above for the adsorption of MC by the [CEL+CS] composite materials and the absorbance change of the MC solution was also monitored as described above. After this first adsorption process, the composite materials were taken out of the spectrophotometric cells and placed in small vials. About 50 mL of de-ionized water was added to each vial and they were agitated on a mechanical shaker at room temperature for 72 hrs to wash off the adsorbed MC. In this particular experiment, the absorbance of the solutions were not monitored during this desorption process. 72 hrs was chosen because that was the time required to quantitatively desorb MC from the composites when the desorption process was monitored as described in the previous section. In this current experiment, a larger volume of de-ionized water was used (50mL compared to 2.7mL) and the washing water replaced with fresh de-ionized water every 24 hrs. This was done to ensure complete desorption of previously adsorbed MC. After 72 hrs, the composite materials were taken out of water and then used for a second adsorption process. The second adsorption process was performed in exactly the same way as the first one and as all the other adsorption experiments described above. The results obtained for the 1^{st} and 2^{nd} adsorption process are plotted together in Figure 3.10 for the two composite materials. Shown in Figure 3.10 are plots of q_t of adsorption of microcystin as a function of time by 67%CS (A) and 50% CS (B). The blue curves are for the 1^{st} adsorption process (i.e., by freshly prepared composites) and red curves are for 2^{nd} adsorption process (i.e.,

adsorption by composites that were regenerated by desorbing MC previously adsorbed). As illustrated, for both composites, adsorption efficiency of the composite materials remains just about the same after they were regenerated by desorbing MC previously adsorbed. This indicates that the polysaccharide composite materials developed here can indeed be reused and they retain their adsorption efficiency for MC.

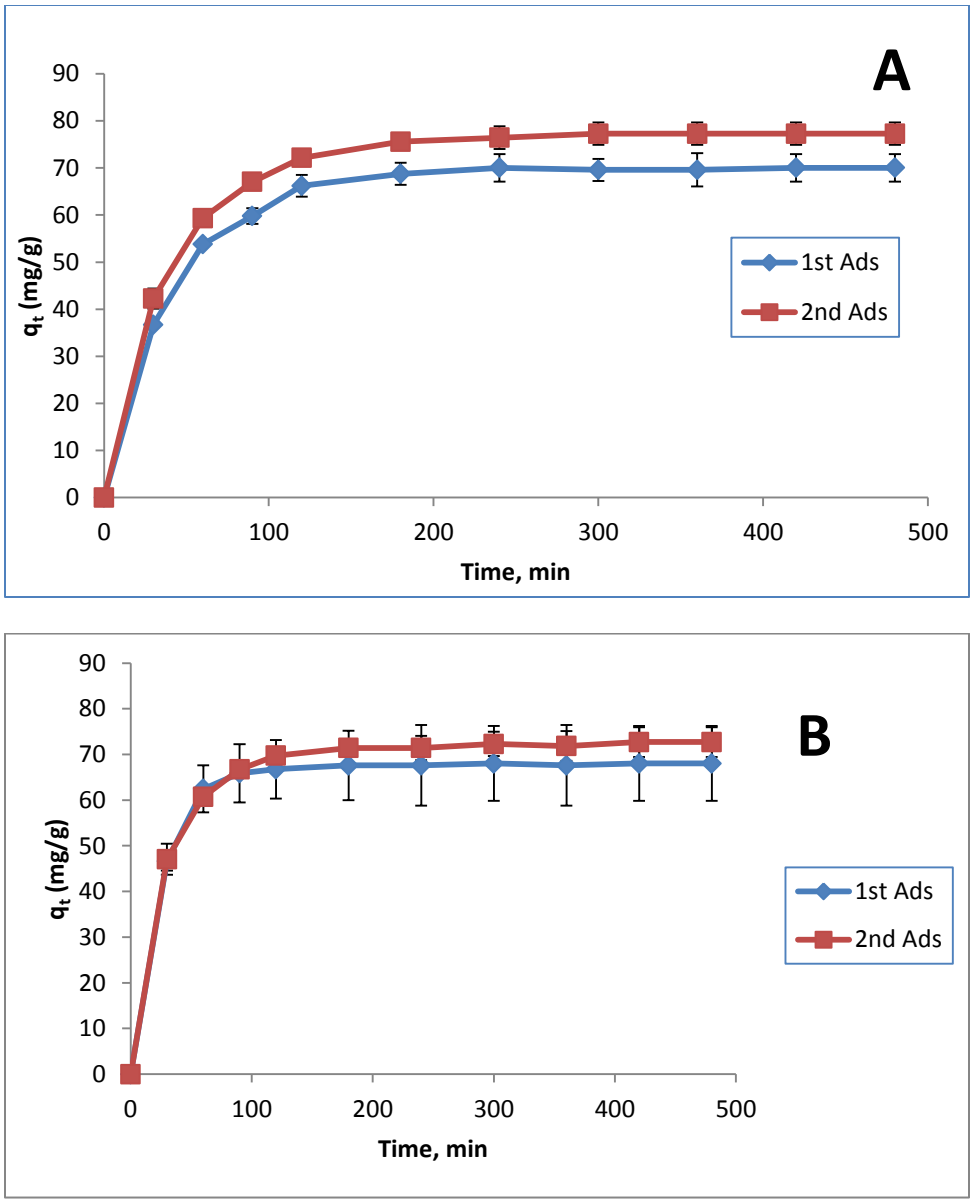

Figure 3.10: Plot of qt of adsorption of microcystin as a function of time by [CS+CEL] composite films containing 67%CS (A) and 50% CS (B): Blue curves are for 1st adsorption (i.e., by freshly prepared films) and red curves are for 2nd adsorption

In summary, and the polysaccharide composite materials developed here were found to have excellent adsorption capacity for MC-LR, a deadly toxin produced by

cyanobacteria. This excellent adsorption capability is principally due to the CS in the composites. Additionally, the [CS+CEL] composite material reported here were also found to be much better adsorbents for MC than all other adsorbents currently available. For example, one gram of the best reported adsorbent, $Fe_3O_4@SiO_2$ magnetic microspheres, can only adsorb 20 mg of MC whereas 1 g of the [67%CS+23%CEL] material can remove up to 96 mg of MC (i.e., 4.8X more than the magnetic microspheres). More importantly, not only that the MC adsorbed on the composite materials can be quantitatively desorbed to enable the [CS+CEL] composite material to be reused, but that adsorption efficiency of the reused composites remain the same as those used for the first time.

3.4.1. Adsorption of endocrine disruptors (2-, 3-, and 4-chlorophenol, 3,4-dichlorophenol, 2,4,5-trichlorophenol and bisphenol A)

3.4.2. Adsorption kinetics

It was observed above that the [CEL+CS] polysaccharide composite materials can effectively adsorb MC-LR, a deadly toxin. The application of these composite materials was therefore widened to include other pollutants such as chlorophenols and bisphenol A. Experiments were designed to determine if the CEL, CS, [CEL+TCD] and [CS+TCD] polysaccharide composite materials can also be used to effectively adsorb chlorophenols and bisphenol A. The rate constants, equilibrium sorption capacities and mechanisms of the adsorption process were evaluated by fitting kinetic and thermodynamic isotherm data to a variety of models. The presence of the TCDs in the composite materials was evaluated for their ability to impart size and shape selectivity to the polysaccharide composites. Appropriate reaction order for the adsorption processes was determined based on the correlation coefficients (R^2) and the Model Selection Criteria (MSC) values. Rate constants and q_e values were then obtained from the kinetic results[53–55]. Subsequent fitting of data to intra-particle diffusion model together with results of adsorption isotherm measurements yielded additional insight into the adsorption process.

Table 3.3: Analytical wavelengths used for the endocrine disruptors

Analyte	Analytical λ
2 ClPh	274
3 ClPh	274
4 ClPh	280
3,4 di-ClPh	282
2,4,5 tri-ClPh	289
BPA	276

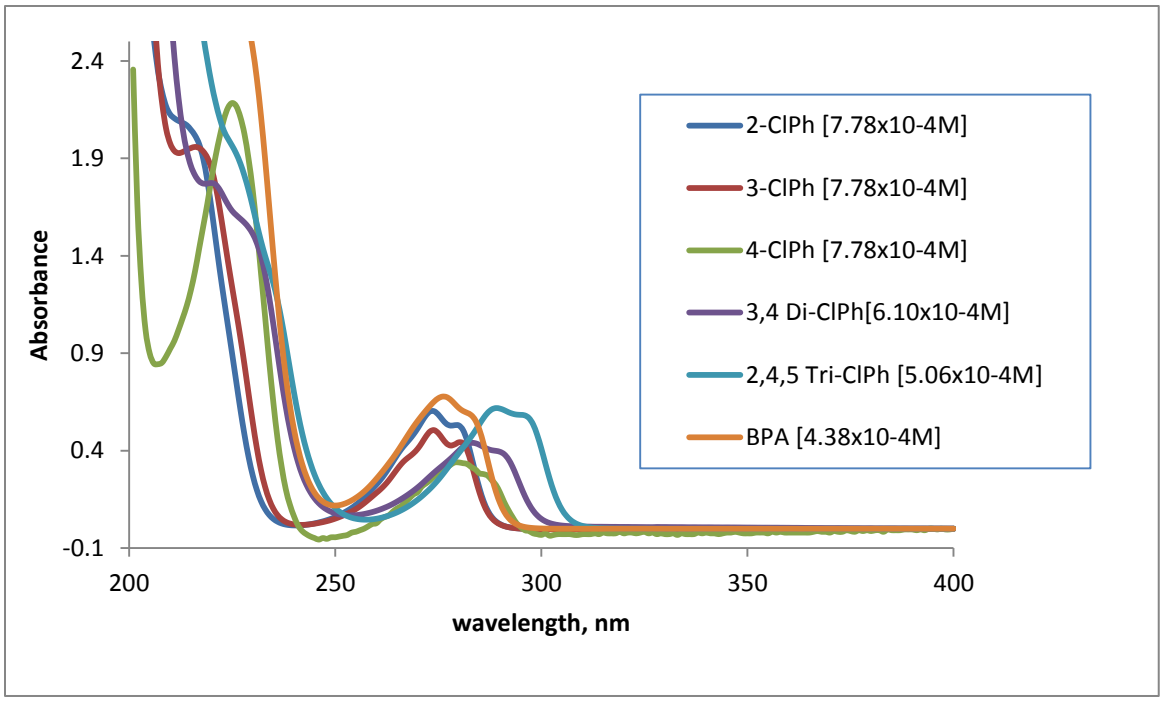

Figure 3.11: UV absorption spectra on the endocrine disruptors

The UV absorption spectra of the various endocrine disruptors are shown in Figure 3.11. The respective concentrations of the solutions are given in square brackets. The analytical wavelengths used for each analyte are shown in Table 3.3 Kinetic

adsorption experiments for 2-chlorophenol (2-ClPh), 3-chlorophenol (3-ClPh), 4-chlorophenol (4-ClPh), 3,4-dichlorophenol (3,4-di-ClPh), 2,4,5-trichlorophenol (2,4,5-tri-ClPh) and bisphenol A (BPA) by the various composites studied were measured using the same procedures and experimental setup described above for the adsorption of microcystin. Plots of q_t vs. t for the various analytes onto 4 different composites are shown in Figure 3.12A and 3.12B. The general trend observed is that with the exception of 2,4,5-tri-ClPh, there is an initial rapid adsorption of these analytes within the first 40 minutes followed adsorption equilibrium which is achieved after about 100 minutes for most composites. For 2,4,5-tri-ClPh, the CEL containing composites (100%CEL and 50%CEL:50%β-TCD) seem to follow a similar adsorption profile to all the other analytes. However, the adsorption of this analyte on to CS containing composites (100%CS and 50%CS:50%β-TCD) seem to exhibit a very different adsorption profile. The adsorption of this analyte on to these CS containing composites show a gradual increase in the amount adsorbed throughout, reaching equilibrium only after about 300 minutes. In addition, the equilibrium adsorption capacity of 2,4,5-tri-ClPh for most composites is almost an order of a magnitude higher than the equilibrium adsorption capacity for all the other analytes onto the corresponding CS containing composites. The pseudo first order and pseudo second order kinetic models were used to obtain the rate constants and equilibrium adsorption capacity of 100%CEL, 100%CS, 50:50 CS:β-TCD and 50:50 CEL:β-TCD composite materials for the different chlorophenols and bisphenol A analytes. The linear plots for the two models for the adsorption of the different analytes by the 4 different composite materials are shown in Figure 3.13A (for pseudo 1st

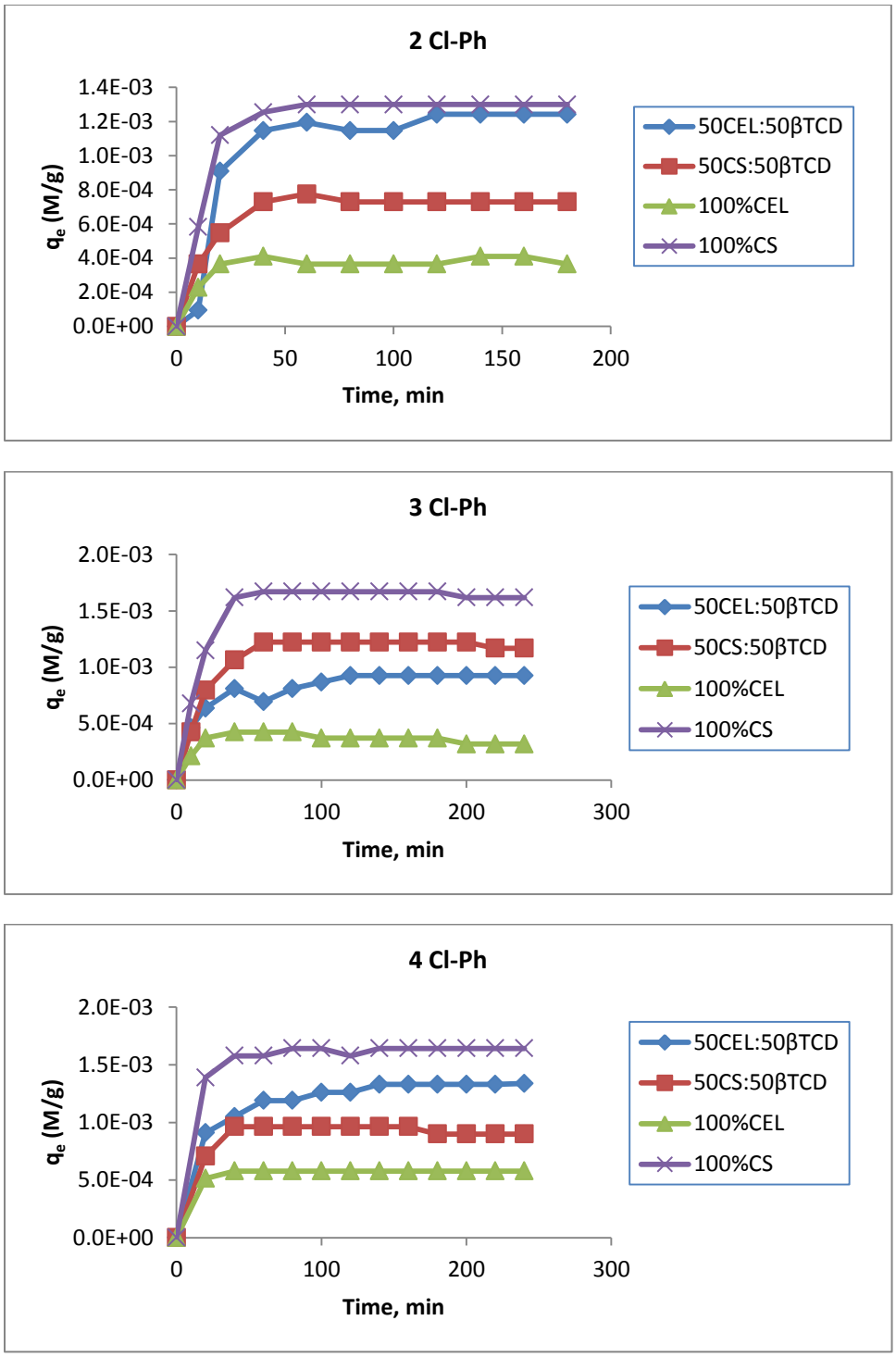

Figure 3.12A: Plots of qt as a function of time for the adsorption of 2-chlorophenol, 3-chlorophenol and 4-chlorophenol by CEL, CS, [CEL+β-TCD] and [CS+β-TCD] regenerated composite materials

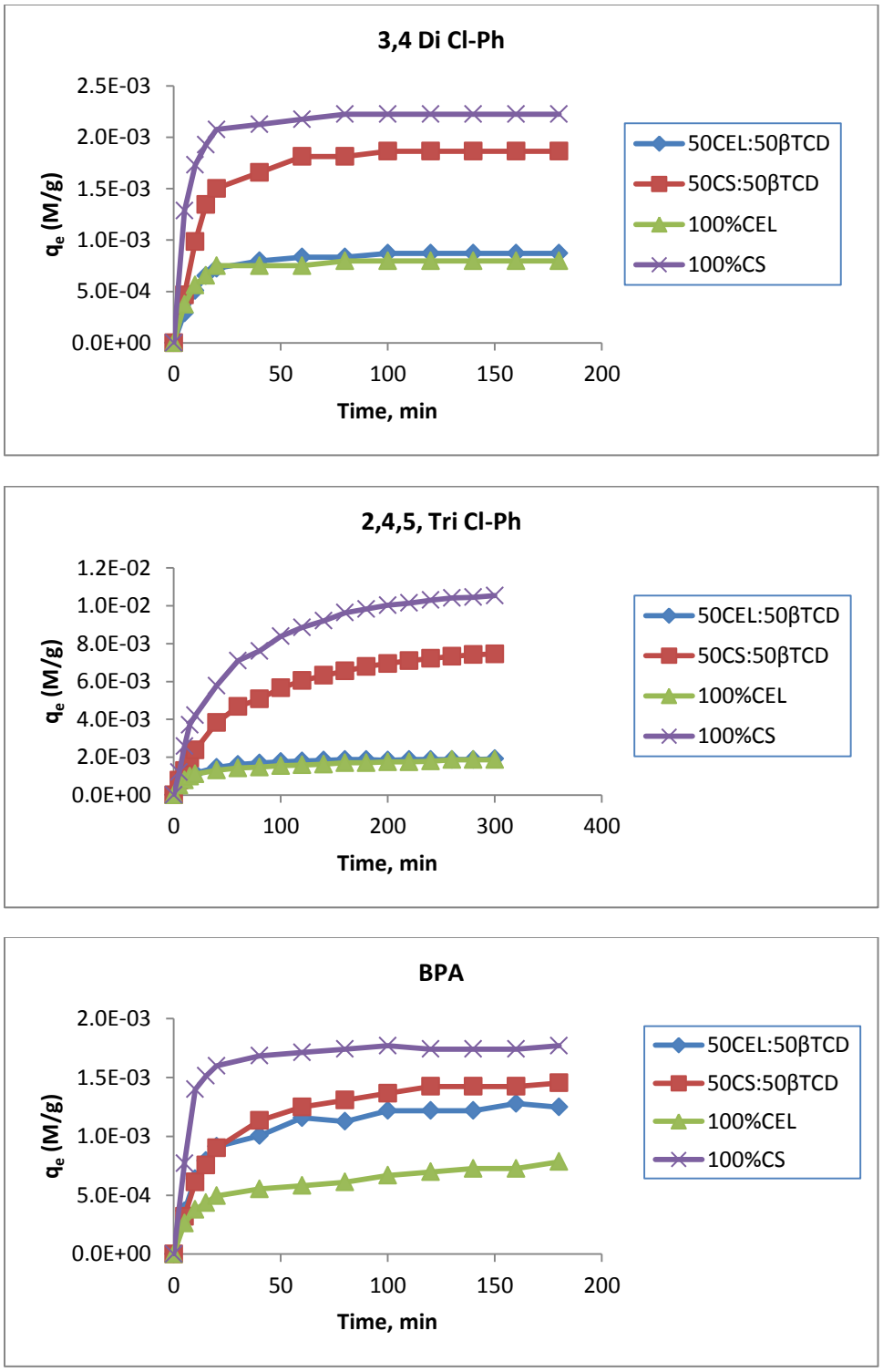

Figure 3.12B: Plots of q_t as a function of time for the adsorption of 3,4-dichlorophenol, 2,4,5-trichlorophenol and BPA by CEL, CS, [CEL+β-TCD] and [CS+β-TCD] regenerated composite materials

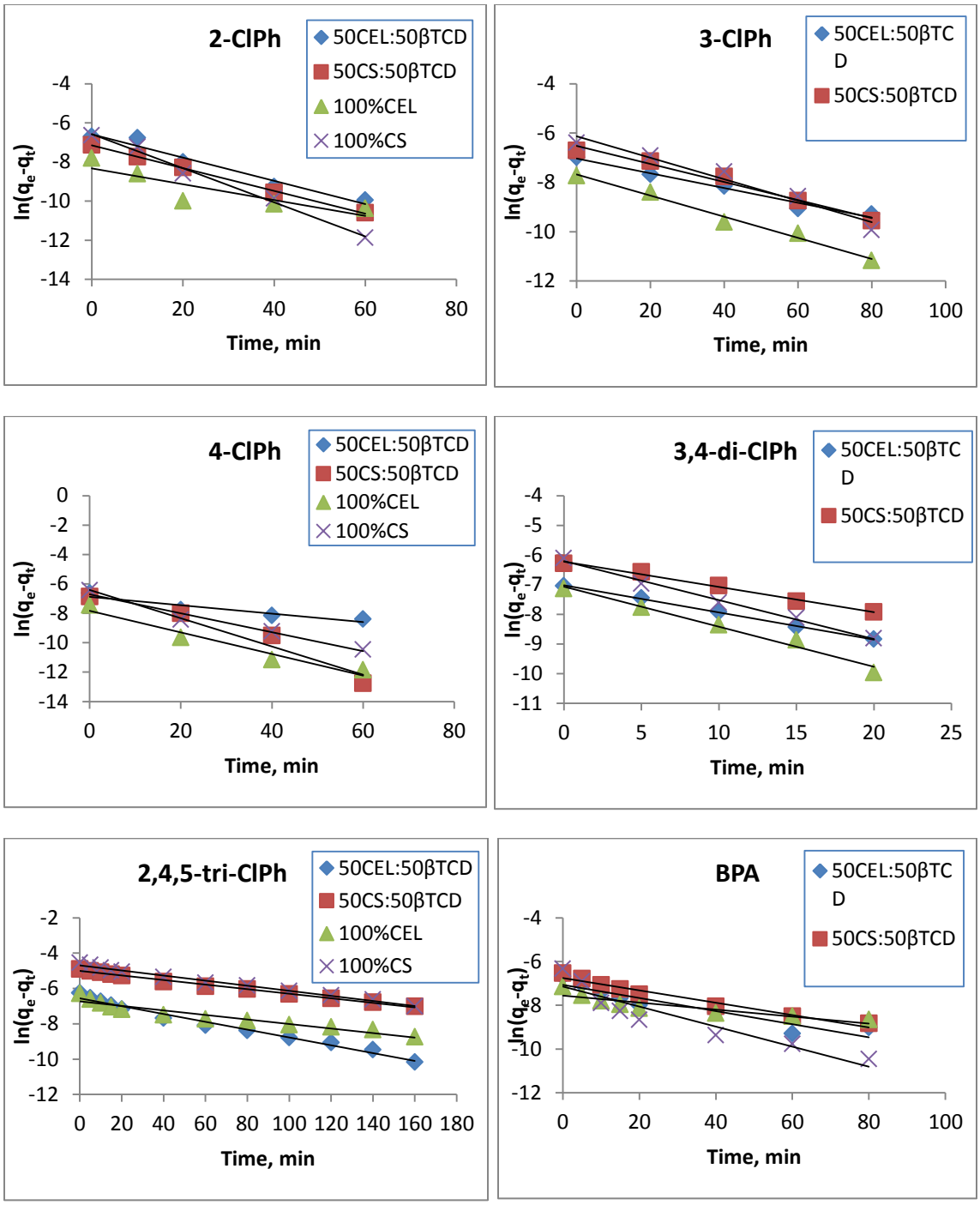

Figure 3.13A: Linearized pseudo 1st order model plots for different analytes

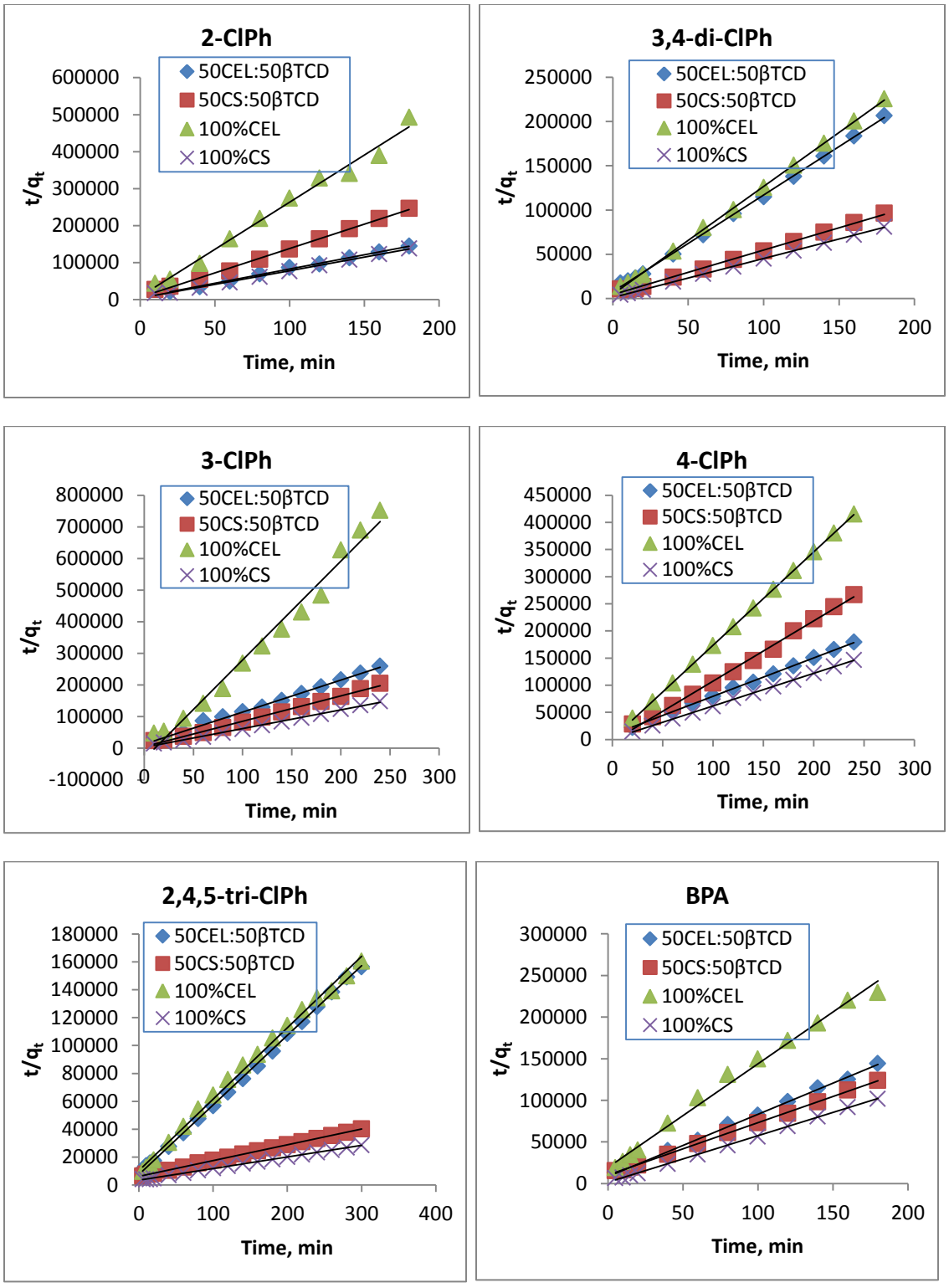

Figure 3.13B: Linearized pseudo 2nd order model plots for different analytes

Table 3.4: Kinetic parameters for adsorption of Chlorophenols and BPA onto CEL film

		Pseudo first-order kinetic model				Pseudo second-order kinetic model			
Analyte	**qe, expt (M/g)**	**qe(M/g)**	**k (min^{-1})**	**R^2**	**MSC**	**qe(M/g)**	**k (M^{-1} min^{-1})**	**R^2**	**MSC**
2-ClPh	4.11E-04	1.45E-04	0.029	0.6469	0.041	3.93E-04	702.3	0.9871	3.95
3-ClPh	3.19E-04	4.95E-04	0.044	0.9747	2.678	3.20E-04	293.8	0.9822	3.72
4-ClPh	5.79E-04	1.69E-04	0.055	0.9559	1.788	5.81E-04	2054.2	0.9999	9.13
3,4 Di-ClPh	7.98E-04	9.44E-04	0.142	0.9665	2.397	8.19E-04	315.6	0.9996	7.47
2,4,5 Tri-ClPh	1.87E-03	1.01E-03	0.011	0.9714	3.287	1.95E-03	25.4	0.9967	5.32
BPA	7.27E-04	4.62E-04	0.014	0.9715	3.156	8.05E-04	78.9	0.9911	4.39

Table 3.5: Kinetic parameters for adsorption of Chlorophenols and BPA onto CS film

		Pseudo first-order kinetic model				Pseudo second-order kinetic model			
Analyte	**qe, expt (M/g)**	**qe(M/g)**	**k (min^{-1})**	**R^2**	**MSC**	**qe(M/g)**	**k (M^{-1} min^{-1})**	**R^2**	**MSC**
2-ClPh	1.30E-03	1.48E-03	0.089	0.9865	3.305	1.32E-03	385.9	0.9998	8.02
3-ClPh	1.62E-03	3.25E-03	0.050	0.9745	2.669	1.68E-03	133.5	0.9960	5.21
4-ClPh	1.64E-03	6.49E-04	0.051	0.9849	2.861	1.66E-03	214.6	0.9996	7.52
3,4 Di-ClPh	2.23E-03	7.23E-04	0.048	0.8769	0.761	2.27E-03	169.8	0.9999	8.72
2,4,5 Tri-ClPh	1.05E-02	9.90E-03	0.016	0.9843	3.917	1.20E-02	2.1	0.9991	6.60
BPA	1.74E-03	5.88E-04	0.040	0.8947	1.680	1.80E-03	168.3	0.9995	7.24

Table 3.6: Kinetic parameters for adsorption of Chlorophenols and BPA onto 50:50 CEL:β-TCD film

		Pseudo first-order kinetic model				Pseudo second-order kinetic model			
Analyte	**qe, expt (M/g)**	**qe(M/g)**	**k (min^{-1})**	**R^2**	**MSC**	**qe(M/g)**	**k (M^{-1} min^{-1})**	**R^2**	**MSC**
2-ClPh	1.24E-03	8.70E-04	0.041	0.8960	1.597	1.30E-03	100.2	0.9975	5.57
3-ClPh	9.26E-04	5.55E-04	0.020	0.9410	2.259	9.87E-04	77.9	0.9964	5.33
4-ClPh	1.33E-03	1.04E-03	0.028	0.8161	1.122	1.41E-03	58.0	0.9993	6.93
3,4 Di-ClPh	8.71E-04	5.28E-04	0.047	0.9422	2.185	9.12E-04	160.6	0.9992	6.84
2,4,5 Tri-ClPh	1.92E-03	1.31E-03	0.021	0.9867	3.957	2.00E-03	33.2	0.9995	7.26
BPA	1.28E-03	7.93E-04	0.030	0.9291	2.147	1.34E-03	65.5	0.9987	6.28

Table 3.7: Kinetic parameters for adsorption of Chlorophenols and BPA onto 50:50 CS:β-TCD film

		Pseudo first-order kinetic model				Pseudo second-order kinetic model			
Analyte	**qe, expt (M/g)**	**qe(M/g)**	**k (min^{-1})**	**R^2**	**MSC**	**qe(M/g)**	**k (M^{-1} min^{-1})**	**R^2**	**MSC**
2-ClPh	7.30E-04	7.76E-04	0.058	0.9981	5.249	7.58E-04	268.4	0.9967	5.32
3-ClPh	1.22E-03	1.96E-03	0.041	0.9936	4.046	1.25E-03	118.6	0.9934	4.71
4-ClPh	9.64E-04	4.79E-03	0.119	0.9567	1.806	8.99E-04	313.1	0.9957	5.11
3,4 Di-ClPh	1.87E-03	1.45E-03	0.055	0.9636	2.647	1.99E-03	57.1	0.9978	5.77
2,4,5 Tri-ClPh	7.45E-03	7.92E-03	0.015	0.9548	2.861	8.84E-03	2.1	0.9996	7.41
BPA	1.42E-03	1.12E-03	0.028	0.9782	3.381	1.59E-03	37.6	0.9994	7.11

order) and Figure 3.13B (for pseudo 2nd order). The adsorption kinetic parameters obtained for both the pseudo 1st order and pseudo 2nd order for the adsorption of all analytes by 100%CEL, 100%CS, 50:50 CS:β-TCD and 50:50 CEL:β-TCD are listed in Tables 3.4 – 3.7. Similar to what was observed for the adsorption of microcystin by the [CEL+CS] composite materials, the R^2 and the MSC values are higher for the pseudo 2nd order kinetic model than for the pseudo 1st order kinetic model in all cases. In addition, the theoretical and experimental equilibrium adsorption capacities, q_e, obtained for the pseudo 1st order kinetic model varied widely for the different analytes while the qe for the pseudo 2nd order kinetic model is much closer to the experimental qe value. These results seem to suggest that the adsorption of various chlorophenols and BPA onto 100%CEL, 100%CS, 50:50 CS:β-TCD and 50:50 CEL:β-TCD composite materials are best described by the pseudo-2nd order kinetic model. The pseudo 2nd order kinetic model assumes that the chemical reaction mechanisms, and the adsorption rate is controlled by chemical adsorption through sharing or exchange of electrons between the sorbent and adsorbate.[68] Hence the good correlation of the adsorption process provided by the pseudo 2nd order kinetic model suggest that chemical sorption involving valence forces through sharing or exchange of electrons between the polysaccharide composite materials and analyte might be significant[53,54].

Additional information on mechanism of adsorption can be gained by analyzing data using the intra-particle diffusion model. This model describes the behavior of intraparticle diffusion as the rate limiting step of the adsorption process. According to this model, if the plot of equation 3.5 (qt versus $t^{1/2}$) gives a straight line, then the

adsorption process is controlled by intra-particle diffusion, while, if the data exhibit multi-linear regions, then two or more steps influence the adsorption process.

Shown in Figure 3.14 are representative intra-particle pore diffusion plots (q_t versus $t^{1/2}$) for three of the analytes studied, 3,4-Di-Cl-Ph, 2,4,5-Tri-Cl-Ph and BPA adsorbed on 100%CEL and 100%CS, 50:50 CEL: β-TCD and 50:50 CS: β-TCD composites. As illustrated, plots of q_t versus $t^{1/2}$ are not linear throughout but rather non-linear and can be fitted to two linear segments for all analytes and composites with the exception that the data for 2,4,5-Tri-Cl-Ph on 50:50 CS: β-TCD may possibly be fitted to a single linear region with R^2=0.9819. According to this model, the 1st sharper linear region can be assigned to the instantaneous adsorption or external surface adsorption, while the second region may be due to gradual adsorption stage where intra-particle diffusion is the rate limiting step.[42,44] The intraparticle diffusion rate constant (k_i) and correlation coefficient (R^2) for each region are listed in Table 3.8. The rate constants k_i1 and k_i2 are for the 1st and 2nd linear regions respectively. It is clear from this table that there are two regions where the rate of adsorption is faster in the first region ($k_i1>k_i2$). These results seem to imply that the intra-particle diffusion is not the sole rate controlling step but other mechanisms may also contribute to the adsorption process.

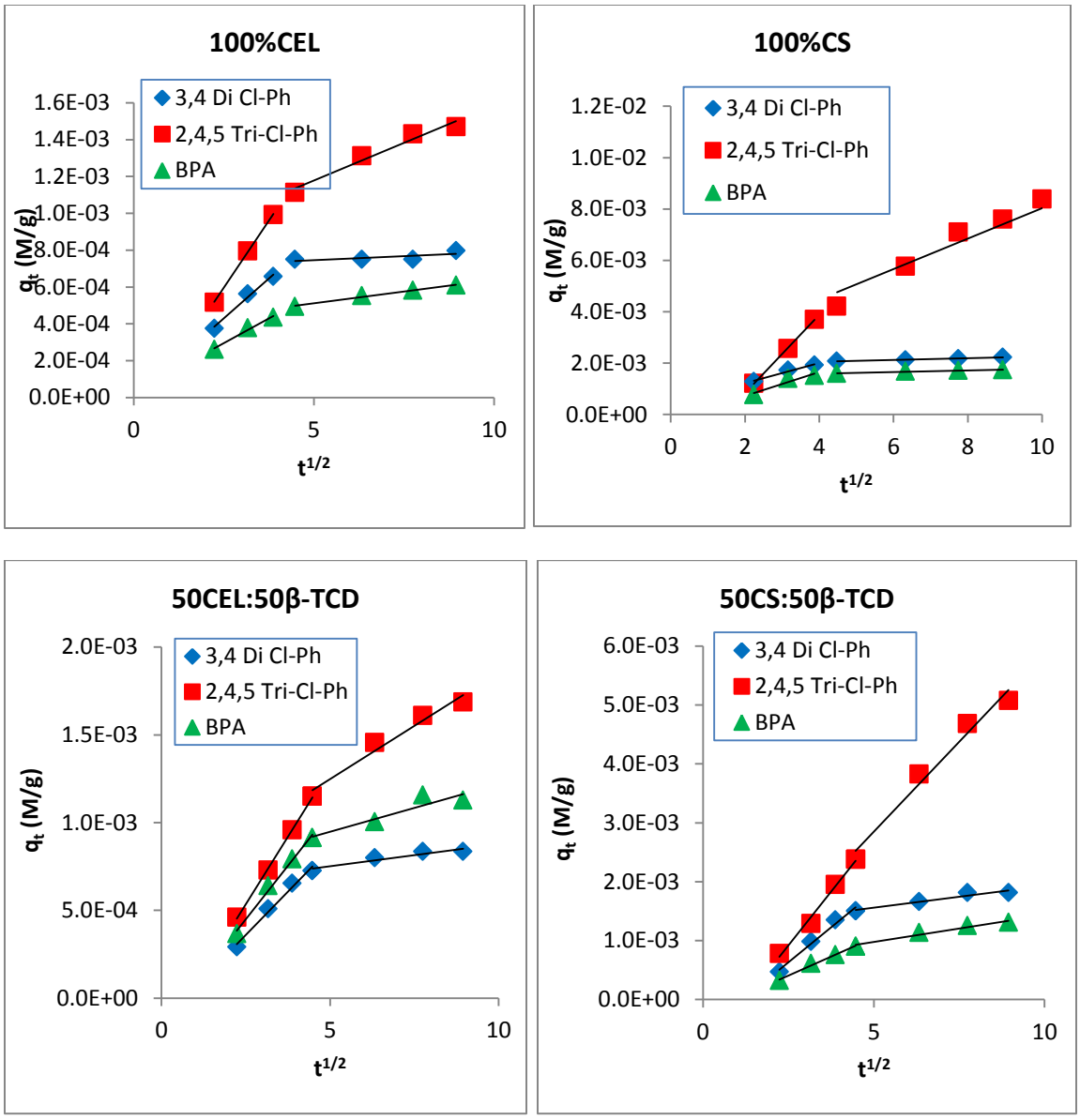

Figure 3.14: Intraparticle diffusion plots for CEL, CS, [CEL+β-TCD] and [CS+β-TCD] composite materials for 3 of the analytes

Table 3.8: Intraparticle diffusion parameters for the sorption of various analytes by the different composites.

	100%CEL				100%CS				50:50 CEL:β-TCD				50:50 CS:β-TCD			
Analyte	**k_i1**	**R^2**	**k_i2**	**R^2**	**k_i1**	**R^2**	**k_i2**	**R^2**	**k_i1**	**R^2**	**k_i2**	**R^2**	**k_i1**	**R^2**	**k_i2**	**R^2**
2-ClPh	0.000080	0.9917			0.000238	0.9559	0.000041	0.8613	0.000171	0.6218	0.000055	0.6775	0.000121	0.9980	0.000043	0.6688
3-ClPh	0.000080	0.9769	0.000011	0.6906	0.000249	0.9832	0.000115	0.7658	0.000143	0.9995	0.000028	0.3959	0.000170	0.9620	0.000100	0.9137
4-ClPh	0.000115	1.0000	0.000014	0.6906	0.000311	1.0000	0.000053	0.8591	0.000204	1.0000	0.000067	0.9350	0.000158	0.9137	0.000056	0.6906
3,4 Di-ClPh	0.000170	0.9979	0.000009	0.5152	0.000475	0.9774	0.000033	0.9902	0.000167	0.9856	0.000025	0.8995	0.000350	0.9570	0.000075	0.9350
2,4,5 Tri-ClPh	0.000254	0.9971	0.000082	0.9636	0.000971	0.9465	0.000783	0.9853	0.000256	0.9870	0.000121	0.9652	0.000526	0.9526	0.000612	0.9748
BPA	0.000112	0.9964	0.000026	0.9910	0.000380	0.9690	0.000031	0.9591	0.000208	0.9882	0.000054	0.8653	0.000204	0.9774	0.000092	0.9652

Results obtained from the pseudo 2nd order kinetic model in terms of equilibrium sorption capacity (q_e) and rate constant (k_2) were then used to evaluate sorption performance of the composite materials. Table 3.9 lists q_e and k_2 values for the 5 different chlorophenols and BPA on 100%CEL, 50:50 CEL:β-TCD, 100%CS and 50:50 CS:β-TCD. The data from Table 3.8 was then used to construct column graphs shown in Figure 3.15 for the different composite materials. Figure 3.16 is a combined plot for all the results obtained for all analytes by all composite materials. It is evident from Fig 3.15A that, for all analytes, equilibrium sorption capacities for 100% CS material are much higher than those corresponding for 100%CEL material; e.g., for 2,4,5-Tri-Cl-Ph, the 100%CS material exhibits up to 6X more equilibrium sorption capacity than the 100%CEL material. Even for BPA, where the difference between CEL and CS materials are smallest, the CS material still has a q_e value twice as much as that of the CEL material. This is as expected, because CEL is known to be inert whereas CS is reported to be an effective adsorbent for various pollutants.

Table 3.9: Pseudo-second order kinetic adsorption parameters for 4 different composite materials

	100%CEL				100%CS				50:50 CEL:β-TCD				50:50 CS:β-TCD			
Analyte	**qe(M/g)**	**K (M^{-1} min^{-1})**	**R^2**	**MSC**	**qe(M/g)**	**k (M^{-1} min^{-1})**	**R^2**	**MSC**	**qe(M/g)**	**k (M^{-1} min^{-1})**	**R^2**	**MSC**	**qe(M/g)**	**K (M^{-1} min^{-1})**	**R^2**	**MSC**
2-ClPh	3.93E-04	702.3	0.9871	3.95	1.32E-03	385.9	0.9998	8.02	1.30E-03	100.2	0.9975	5.57	7.58E-04	268.4	0.9967	5.32
3-ClPh	3.20E-04	293.8	0.9822	3.72	1.68E-03	133.5	0.9960	5.21	9.87E-04	77.9	0.9964	5.33	1.25E-03	118.6	0.9934	4.71
4-ClPh	5.81E-04	2054.2	0.9999	9.13	1.66E-03	214.6	0.9996	7.52	1.41E-03	58.0	0.9993	6.93	8.99E-04	313.1	0.9957	5.11
3,4 Di-ClPh	8.19E-04	315.6	0.9996	7.47	2.27E-03	169.8	0.9999	8.72	9.12E-04	160.6	0.9992	6.84	1.99E-03	57.1	0.9978	5.77
2,4,5 Tri-ClPh	1.95E-03	25.4	0.9967	5.32	1.20E-02	2.1	0.9991	6.60	2.00E-03	33.2	0.9995	7.26	8.84E-03	2.1	0.9996	7.41
BPA	8.05E-04	78.9	0.9911	4.39	1.80E-03	168.3	0.9995	7.24	1.34E-03	65.5	0.9987	6.28	1.59E-03	37.6	0.9994	7.11

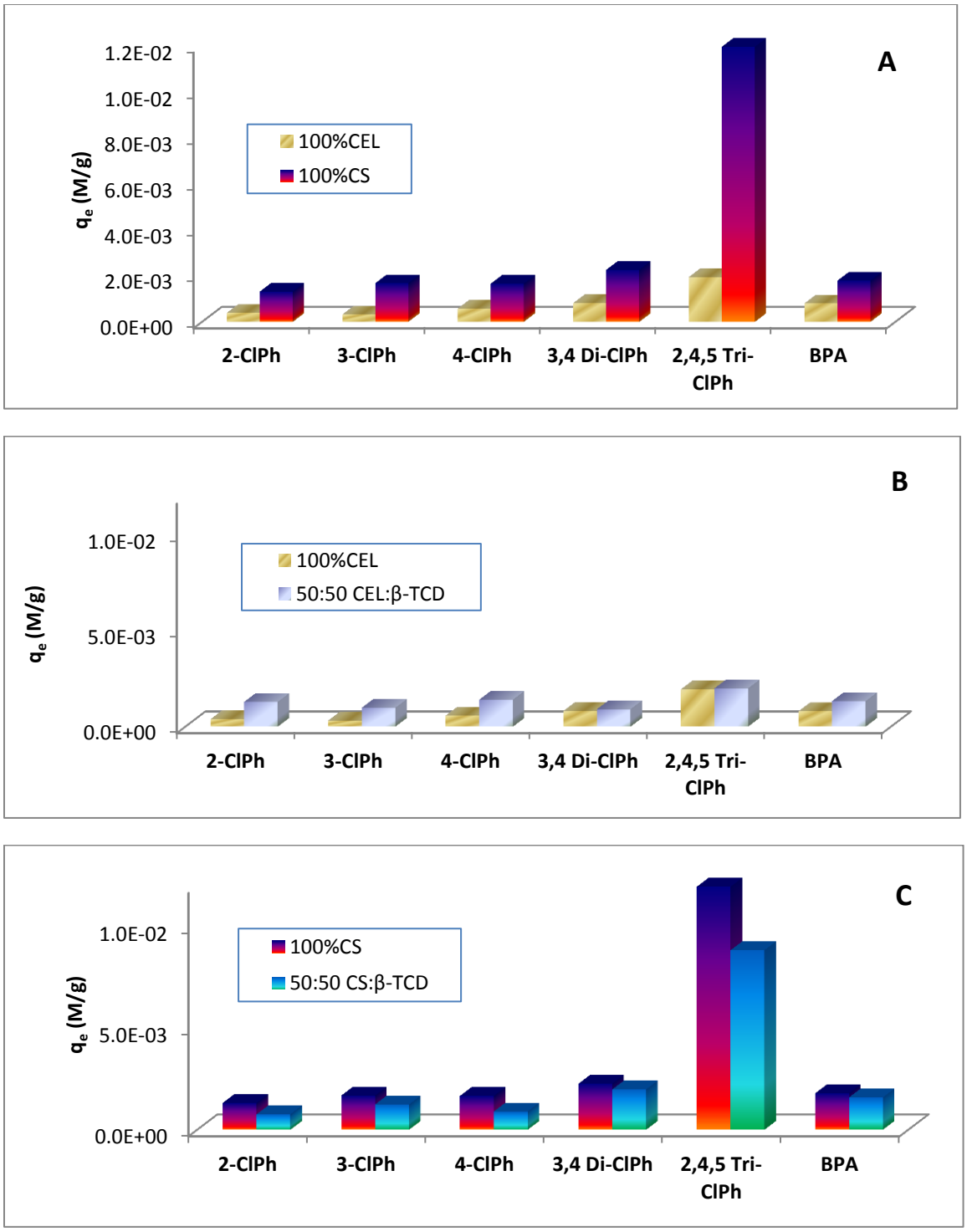

Figure 3.15: Plot of equilibrium sorption capacity (qe) of all analytes by (A) 100%CEL and 100%CS; (B) 100%CEL and 50:50 CEL:β-TCD; (C) 100%CS and 50:50 CEL:β-TCD

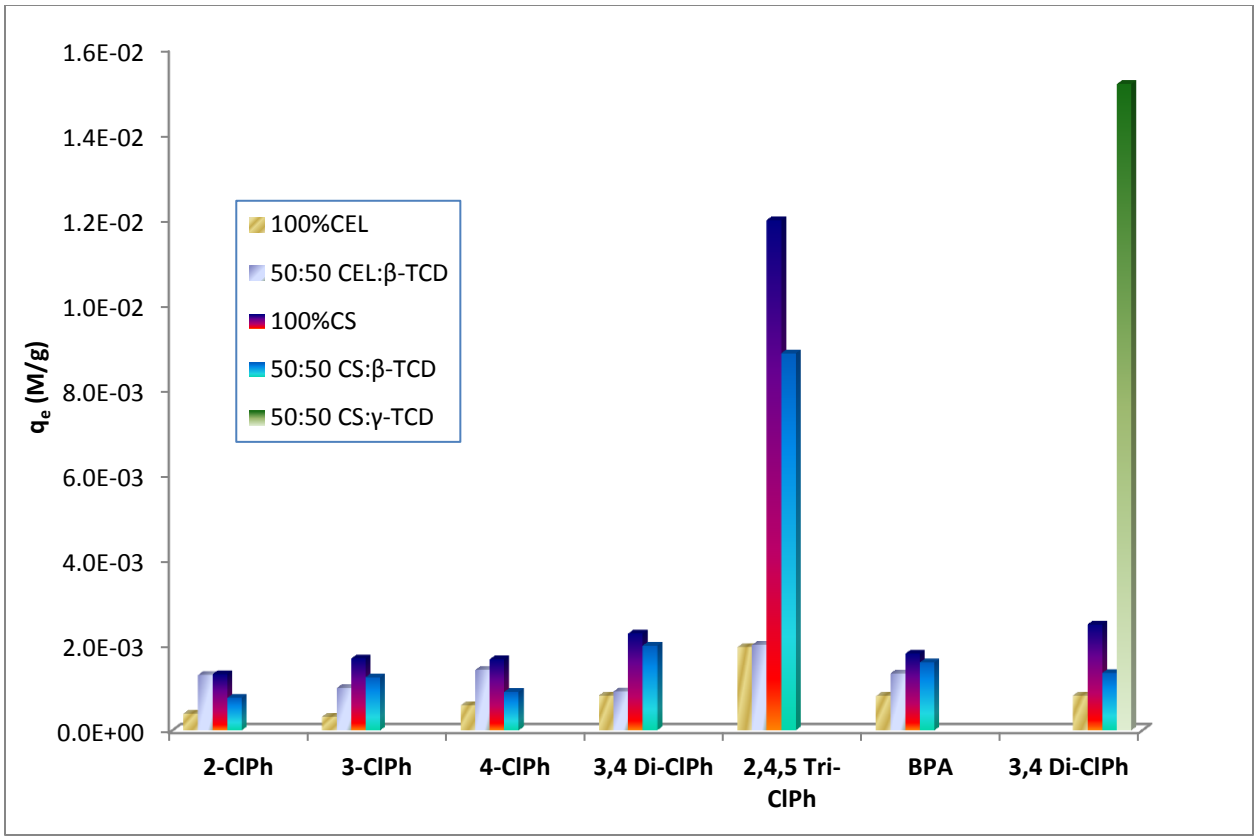

Figure 3.16: Comparison of equilibrium sorption capacity (qe) of all analytes by 100%CEL, 100%CS; 50:50 CEL:β-TCD; 50:50 CEL:β-TCD; and 50:50 CS:γ-TCD composite materials

Results in Figure 3.15A show that for analytes studied, adsorption from CS films is higher than that of CEL films. Such kind of results are expected as the $–NH_2$ groups in CS are responsible for its good adsorption capability. To confirm these findings, [CEL+CS] composites with increasing CS concentration were prepared and their adsorption of 2,4,5 tri-ClPh was measured. The results are plotted in Figure 3.17. As illustrated in this figure, the equilibrium adsorption capacity (q_e) expectedly increased with increase in CS concentration in the films. The addition of 50% CS into CEL improved the adsorption capacity by about 5 times. The rate constant, k, was found to

decrease with increasing CS concentration. This follows from the fact that as CS concentration is increased, it takes longer and longer to reach equilibrium as more pollutant is adsorbed. This clearly confirms that CS is principally responsible for the adsorption of the endocrine disruptors. As explained earlier on, CEL is added to improve on the poor rheological and mechanical properties of CS.

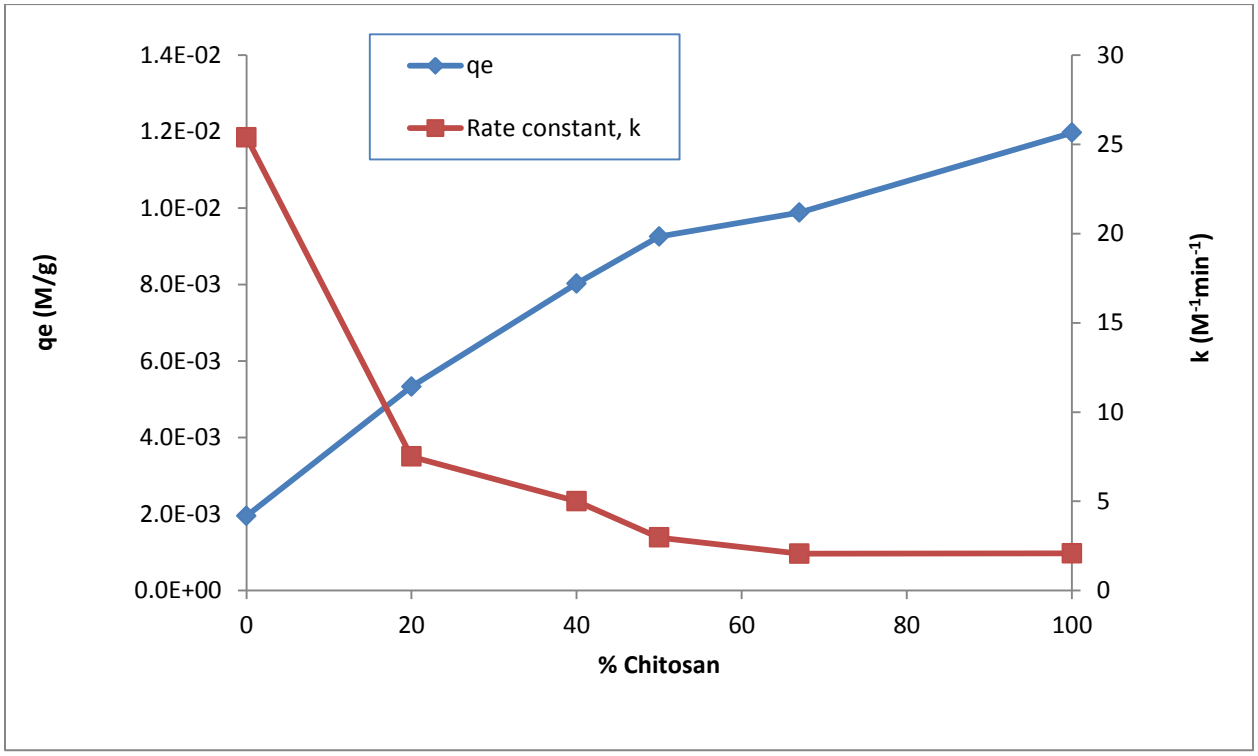

Figure 3.17: Variation of qe and k for different [CEL+CS] composite materials for 2,4,5 tri-chlorophenol

Addition of β-TCD to CEL and CS seem to have a different effect in the two polysaccharides. While there was no enhancement of qe values when β-TCD was added to CS (Figure 3.15C), results in Figure 3.15B shows some enhancement for 2-ClPH, 3-ClPh, 4-ClPh and BPA when it was added to CEL. However, no enhancement in qe was observed for 3,4 di-ClPh and 2,4,5 tri-ClPh. One of the most likely reasons for this observation is probably due to the bulky nature of the dichloro- and trichlorophenol compounds which sterically hinders their ability to form inclusion complexes with β-TCD. The results in Figure 3.15 seem to suggest that when added to CEL, β-TCD enhances the adsorption capacity of the smaller mono chlorophenols possibly by forming inclusion complexes. However, because of steric hindrance, no such enhancement was observed with the bulky di- and tri-chlorophenols. As explained earlier, CS is a good adsorbent on its own hence no enhancement was observed when β-TCD was added to CEL.

To further investigate this theory, a larger γ-TCD was added to CS. The adsorption of the bulky 3,4 di-ClPh with this new 50:50 CS:γ-TCD composite was measured and the results are plotted together those of 100CEL, 100CS, 50:50 CEL:β-TCD and 50:50 CS:β-TCD for the same analyte as the last group in Figure 3.16. The results show that because its small size, there was suppression of qe when β-TCD was added to CS. However, when the larger γ-TCD was added to CS, even the bulky 3,4 di-ClPh was still able to be accommodated in the cavity of the γ-TCD resulting in enhanced qe.

Figure 3.18A shows the sorption profiles for 3,4-dichlorophenol by 50:50 CS:α-TCD, 50:50 CS:β-TCD and 50:50 CS:γ-TCD. As expected, because the cavities of α-

TCD and β-TCD are too small to accommodate 3,4-dichlorophenol, this analyte can only be adsorbed onto 50:50 CS:α-TCD and 50:50 CS:β-TCD by surface adsorption which led to low and similar adsorption curve for both composite materials. However, 50:50 CS:γ-TCD with its larger γ-TCD, was able to form inclusion complexes with 3,4-dichlorophenol, and hence its qe value is much larger.

CS composites with different concentration of α-, β- and γ-TCD were prepared and their qe values are plotted in Figure 3.18B as a function of TCD concentration. The pseudo 2^{nd} order qe values for these composites are shown in table 3.10. Again, since 50:50 CS:α-TCD and 50:50 CS:β-TCD cannot form inclusion complexes with 3,4-dichlorophenol, their q_e values are independent of TCD concentration. However, the q_e values for 50:50 CS:γ-TCD are much higher than those of α- and β-TCD for the corresponding concentration and were found to be proportional to concentration of γ-TCD.

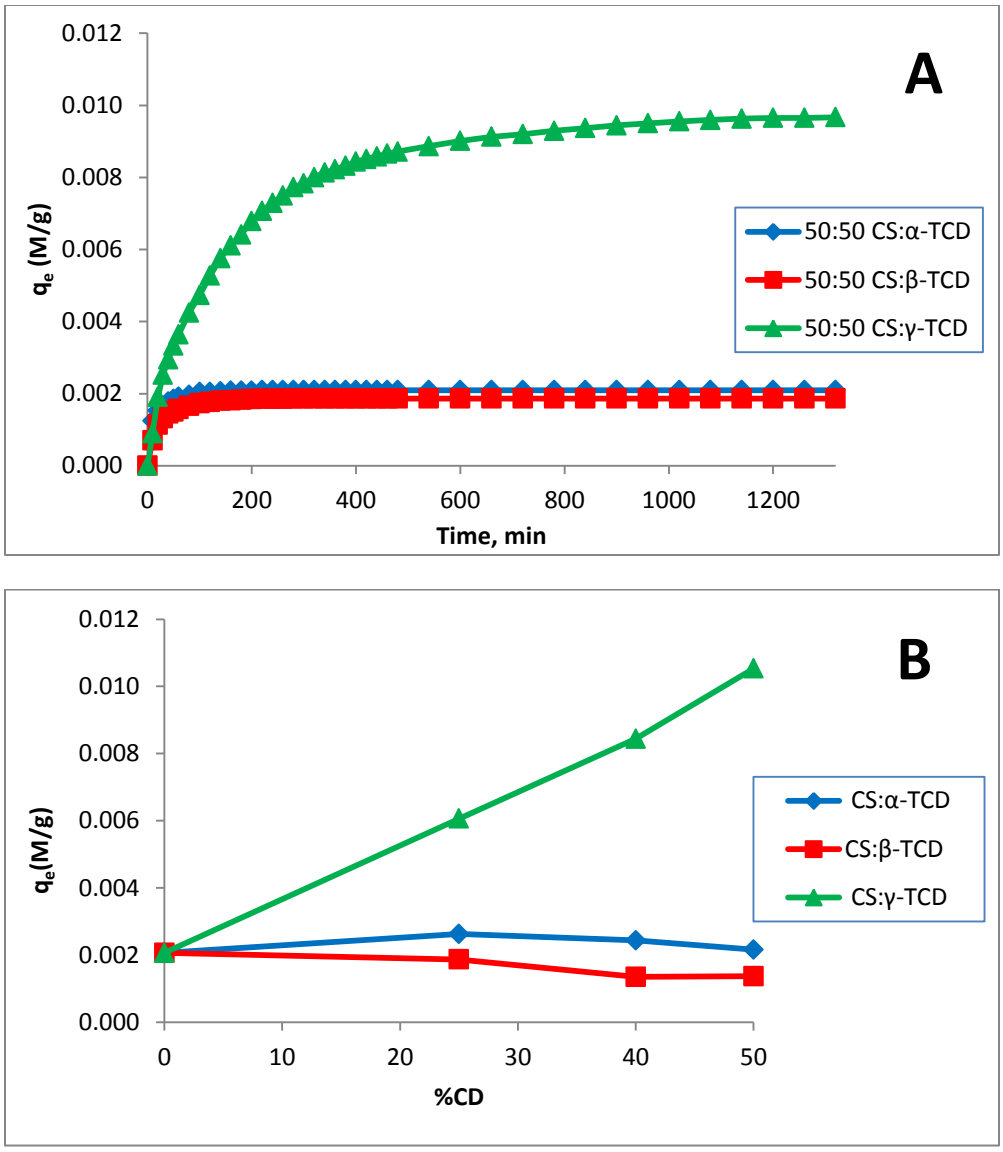

Figure 3.18: Sorption profiles of 50:50 CS:α-TCD, 50:50 CS:β-TCD and 50:50 CS:γ-TCD composite materials for 3,4-dichlorophenol (A); and Equilibrium sorption capacity for 3,4-dichlorophenol by CS+TCD composite materials as a function of α-TCD, β-TCD and γ-TCD concentration.

Table 3.10: Pseudo 2nd order equilibrium sorption capacities for different CS+TCD composites

% TCD	Pseudo 2^{nd} order q_e value (M/g)		
	CS+α-TCD	CS+β-TCD	CS+γ-TCD
0	0.0021	0.0021	0.0021
25	0.0026	0.0019	0.0061
40	0.0024	0.0014	0.0084
50	0.0022	0.0014	0.0105

As shown in Table 3.11, a similar trend to the size and shape selectivity that we observed in our composite materials brought about by the presence of the cyclodextrins has previously been observed in the binding constants in solution of some selected cyclodextrin complexes. It can be observed from this table that in most cases, when the larger water soluble β-CD was used in solution, the binding constant increased in comparison to that of the smaller α-CD, with the exception of 2,6-di-ClPh. There is a significant increase in the binding constant in solution for the larger β-CD with some bulky tri-substituted analytes such as 3,4-di-ClPh, 2,4-di-ClPh, (3,4-dimethoxyphenethyl)-ammonium and 5-methylresorcinol compared to α-CD. Flurbiprofen is a drug whose structure includes a tri-substituted benzene ring and it can be observed from table 3.11 that the solution binding constant for this bulky analyte increase with the size of the cyclodextrin ring, with γ-CD having the largest binding constant. These binding constants clearly indicate that in solution, the stability of the cyclodextrin complex depends on the size of the analyte and also on the size of the cavity of the cyclodextrin being used. This brings about the size and shape selectivity in the

cyclodextrin-containing composites. It can also be noted from table 3.11 that for derivative cyclodextrins in solution, the stability of the complex may be different from that of the native cyclodextrin even for the same ring size. The solution binding constants of 2-ClPh, 3-ClPh and 4-ClPh were lower for the β-tri-O-methyl CD derivative compared to that of the native β-CD. The presence of some bulky groups, such as the –O-methyl groups, on the cyclodextrin molecule may bring about increased steric hindrance effects on the complex formation or can result in some conformational changes that may result in lower binding constants. This may explain why in our composites, selectivity was observed with the much larger γ-CD ring cavity and not with the β-CD. The presence of the bulky –O-acetyl groups on our cyclodextrin derivatives may have resulted in increased steric hindrance and conformational changes which may have made it difficult to get stable complex formation with the smaller ring cavity of the β-CD derivative. Dramatic conformational and structural changes that may occur on the cyclodextrin structure upon derivatization have recently been reported by Caira.[69] It was reported that chemical substitution of each hydroxylic H atom on the β-CD molecule by a methyl group results in the elimination of intramolecular O-H…..O hydrogen bonding and consequent loss of macrocyclic 'roundness'.[69] Such structural changes were found to have dramatic consequences on the conformation of the CD which include (a) a significantly wider range of tilt angles adopted by the individual glucose rings as a result of repulsive interactions between sterically bulky $–OCH_3$ substituents, (b) flipping of one of the seven glucose rings resulting in a partial 'self-inclusion' of one of its $–OCH_3$ substituents, (c) closing of the top of the cyclodextrin ring by a 'lid' created by the bulky methoxyl groups, and (d) elliptical distortion of the cavity.[69] Such kind of distortions

would obviously affect the complex forming ability of the cyclodextrin and this may be the reason why the solution binding constant of the β-tri-O-methyl-CD in table 3.11 are less than those of the native β-CD for same analyte. It may be possible that similar distortions can occur with our –O-acetyl derivatives, resulting in lower adsorption capacity for the smaller β-tri-O-acetyl-CD than the larger γ-tri-O-acetyl-CD. In addition, I our study, the cyclodextrins were not in solution but in the polysaccharide matrix, in solid form. In the solid form, the CD structure may be more rigid than it is in solution and this rigidity may result in a smaller ring cavity for the γ-CD enabling it to form stable complexes with the guest molecules. Caira et al. were able to get structural information on the solid form of the γ-tri-O-acetyl-CD.[70] They observed that there was a pronounced self-inclusion of the acetyl groups which effectively divided the ring cavity into two 'voids'. These sub-cavities were found to be able to accommodate small molecules such as isopropanol.[70] It may be possible that these sub-cavities in the γ-tri-O-acetyl-CD were responsible for the improved adsorption capacity that we observed with this CD in our composites.

The free energy changes (ΔG) of formation in solution, (table 3.12), are shown to be negative, which also indicates the favorability in the formation of cyclodextrin complexes with some of the analytes we used in our study. The bulky tri-substituted analytes ((2,5-dimethoxyphenethyl)-ammonium and (3,4-dimethoxyphenethyl)-ammonium) also show a favorable free energy change of formation and as was observed with their binding constants, the ΔG values are shown to be more favorable for the larger β-CD than the α-CD. These results indicate that the analytes studied here can indeed form complexes with cyclodextrins and their stability is dependent on the size and shape of the

analyte relative to the size of the cyclodextrin ring, which ultimately brings about the size and shape selectivity in our composite materials.

Table 3.11: Binding constants for the formation of several cyclodextrin complexes in solution

	Binding constant, K, M^{-1}				
	α-CD	**β-CD**	**β-tri-O-methyl-CD**	**γ-CD**	**Reference**
2-ClPh		200	85		Hamai et al.[71]
2-ClPh	35	110			Leyva et al.[72]
2-nitrophenol	5012				Rekharsky et al.[73]
3-ClPh		200	120		Hamai et al.[71]
3-ClPh	200	200			Leyva et al.[72]
3-nitrophenol	123	275			Rekharsky et al.[73]
4-ClPh	274	427			Leyva et al.[72]
4-ClPh	251	251	100		Hamai et al.[71]
4-ClPh	324	371			Politi et al.[74]
4-ClPh	292	410			Bertrand et al.[75]
4-nitrophenol	219	1000			Rekharsky et al.[73]
3,4-di-ClPh	320	1000			Leyva et al.[72]
2,4-di-ClPh	210	350			Leyva et al.[72]
2,6-di-ClPh	100	50			Leyva et al.[72]
(2,5-dimethoxyphenethyl)-ammonium	35	39			Rekharsky et al.[73]
(3,4-dimethoxyphenethyl)-ammonium	8	32			Rekharsky et al.[73]
Flurbiprofen	69	1950		3020	Rekharsky et al.[73]
5-methylresorcinol	15	48		5	Rekharsky et al.[73]
2,4,6-tri-ClPh				1800	Narita et al.[76]
BPA		80000			Chelli et al.[77]
BPA		35000			Kitano et al.[78]

Table 3.12: Free energy of formation of some cyclodextrin complexes in solution

	ΔG (kJ/mol)				
	α-CD	β-CD		β-tri-O-methyl-CD	
	Experimental	Experimental	Calculated	Experimental	Reference
2-ClPh		-13.1		-11.0	Rekharsky et al.[73]
3-ClPh		-13.1		-11.9	Rekharsky et al[73].
3-ClPh		-13.0	-13.1		Katritsky et al.[79]
4-ClPh	-13.8	-13.7		-11.4	Rekharsky et al[73].
4-ClPh		-14.9	-13.1		Katritsky et al.[79]
BPA			-13.3		Chelli et al.[77]
BPA		-25.9			Kitano et al.[78]
(2,5-dimethoxyphenethyl)-ammonium	-8.81	-9.08			Rekharsky et al.[73]
(3,4-dimethoxyphenethyl)-ammonium	-5.1	-8.58			Rekharsky et al.[73]

3.4.3. Adsorption isotherms

To gain more insight into adsorption process, investigation was then carried out to determine adsorption isotherm for adsorption of 4-ClPh and 3,4-dichlorophenol by 100%CS and 50:50 CS: γ-TCD composite materials. These two composites were selected because kinetic results presented above indicate that they adsorb 3,4-dichlorophenol by two distinct different mechanisms: surface adsorption and inclusion complex formation. Experimental results were fitted to three different models, Langmuir isotherm[57], Freundlich isotherm[58] and the Dubinin-Radushkevich (D-R) isotherm[59,60]. Fitting of experimental values to these three models for the two composites are shown in Figure 3.17A and 3.17B for 3,4-di-ClPh and 4-ClPh respectively. The parameters obtained from fits to these models are listed in Table 3.10. As shown in Figure 3.17, experimental

values fit relatively well to theoretical models. For example, for 3,4-di-ClPh, R^2 values for fit of 100%CS and 50:50 CS:γ-TCD composites to the Langmuir, the Freundlich and the D-R model were found to be 0.977 and 0.984, 0.970 and 0.949, and 0.972 and 0.912, respectively. Relatively good agreement was also found for the saturation adsorption capacity q_{max} values obtained with the Langmuir model and the D-R model: 137.6 mg/g and 102.6 mg/g by 50:50 CS:γ-TCD, and 63.2 mg/g and 26.7 mg/g by 100% CS. The saturation adsorption capacity values for 4-ClPh were lower than those for 3,4-di-ClPh for the same composite materials. However, for both analytes, the q_{max} for 50:50 CS:γ-TCD is larger than that of the 100%CS composite material. The good fit between the Langmuir isotherm model and the experimental data suggests that the sorption is monolayer, sorption of each molecule has equal activation energy and that the analyte-analyte interaction is negligible[53].

Additional information on the adsorption process can be obtained from the Freundlich isotherm model, particularly from the constant n in Eq 3.7 because it is known to be a measure of the favorability of the sorption process[53]. Because n was found to be 1.0 and 1.4 for 100%CS and 50:50 CS:γ-TCD, respectively, the adsorption of 3,4 dichlorophenol by the latter seems to be more favorable than that of the former. Similarly, n was found to be 1.6 and 3.1 for the sorption of 4-ClPh by 100%CS and 50:50 CS:γ-TCD, respectively, also indicating the favorability of sorption by the γ-TCD doped CS material for this analyte. The constant β in the D-R isotherm model (Eqn 3.8) is known to relate to the mean free energy E (KJ mol^{-1}) of the sorption process per mole of the analyte which in

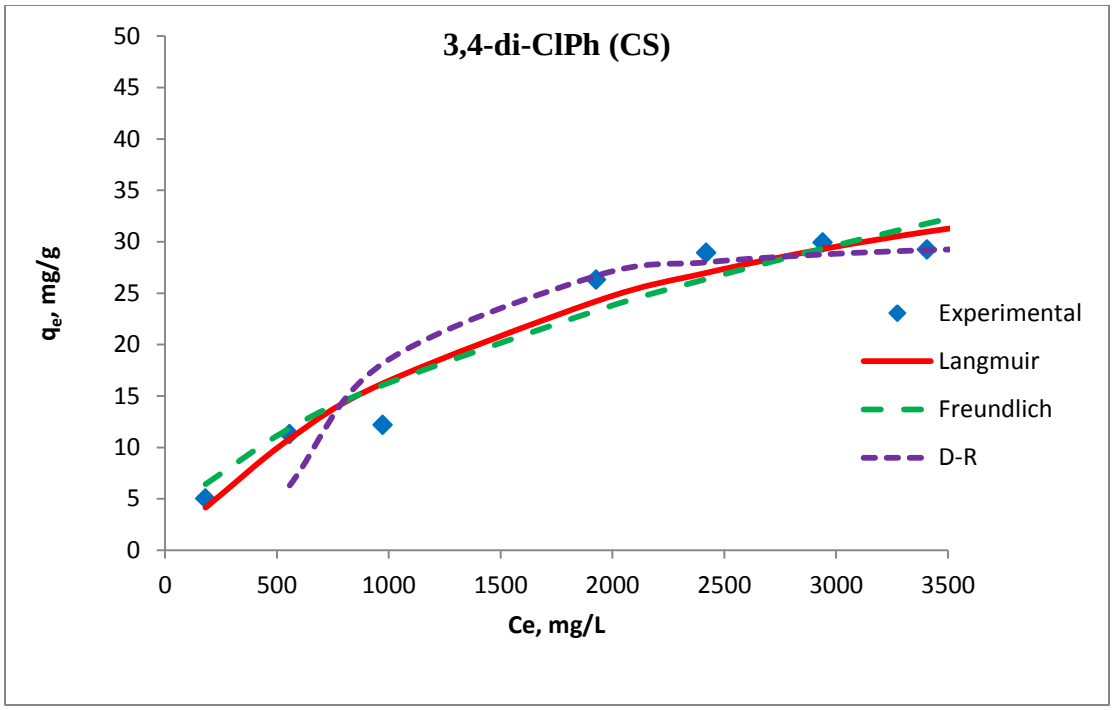

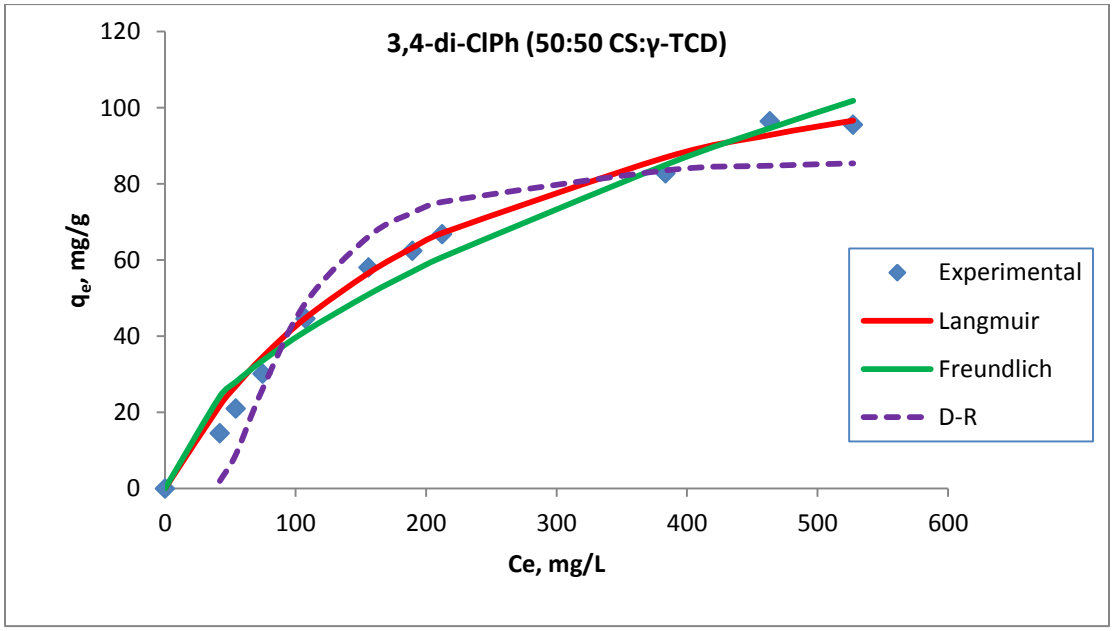

Figure 3.19A: Comparison between experimental and theoretical isotherm fits for the adsorption of 3,4 di Cl-Ph onto 100CS and 50:50 CS:γ-TCD composite materials

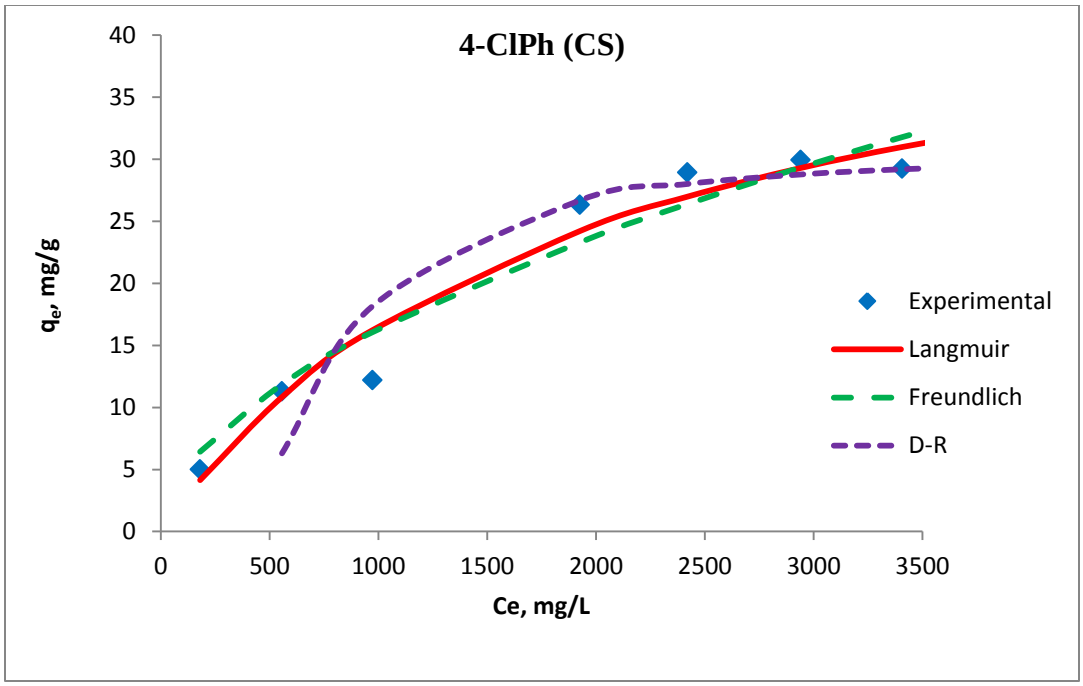

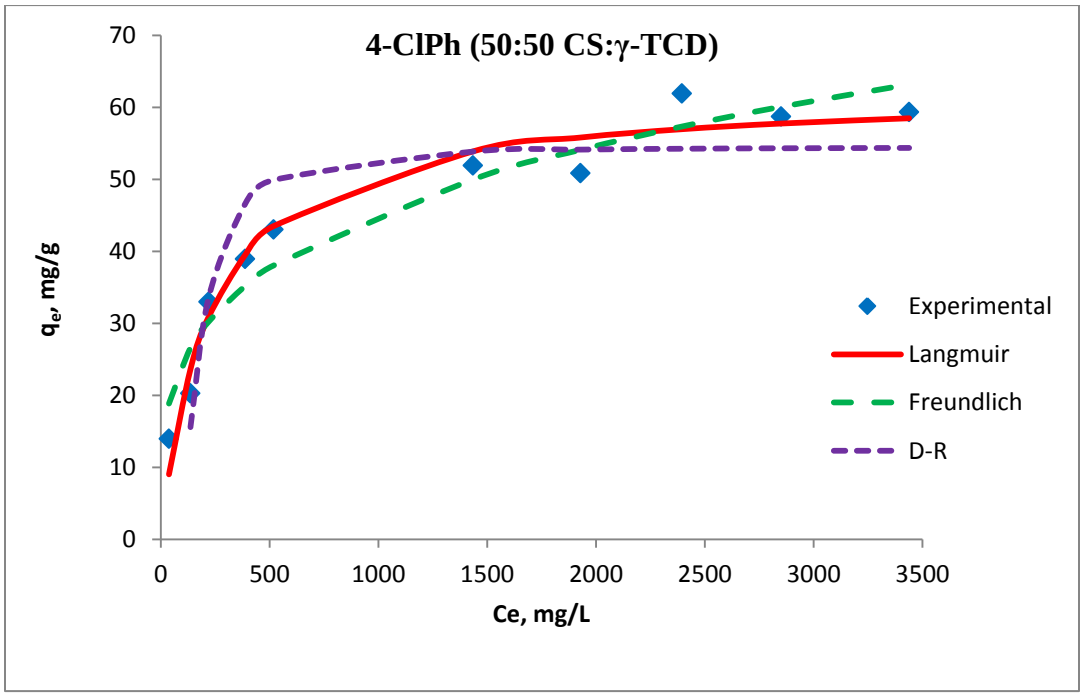

Figure 3.19B: Comparison between experimental and theoretical isotherm fits for the adsorption of 4-ClPh onto 100CS and 50:50 CS:γ-TCD composite materials

Table 3.13: Adsorption isotherm parameters for the adsorption of 3, 4 di Cl-Ph onto 50:50 CS:γ-TCD film

4-ClPh										
	Langmuir Isotherm parameters			**Freundlich isotherm parameters**			**D-R isotherm parameters**			
	q_{max}(mg/g)	**K_L(L/mg)**	**R^2**	**n**	**K_F(mg/g)(L/mg)1/n**	**R^2**	**q_{max}(mg/g)**	**β($mmol^2J^{-2}$)**	**E (kJ/mol)**	**R^2**
100% CS	45.6	0.0005	0.7635	1.6	0.20032	0.8967	23.1	0.0088	7.6	0.6609
50:50 CS:γ-TCD	63.8	0.0038	0.9852	3.1	5.009425	0.9211	48.0	0.0027	13.6	0.9551
3, 4-di-ClPh										
	Langmuir Isotherm parameters			**Freundlich isotherm parameters**			**D-R isotherm parameters**			
	q_{max}(mg/g)	**K_L(L/mg)**	**R^2**	**n**	**K_F(mg/g)(L/mg)1/n**	**R^2**	**q_{max}(mg/g)**	**β($mmol^2J^{-2}$)**	**E (kJ/mol)**	**R^2**
100% CS	63.2	0.0004	0.9765	1.0	0.015185	0.9697	26.7	0.0805	2.5	0.9720
50:50 CS:γ-TCD	137.6	0.0045	0.9840	1.4	1.34975	0.9487	102.6	0.0026	13.9	0.9120

turn can give information about the sorption mechanism. E can be calculated using the equation:[80]

$$E = \frac{1}{\sqrt{2\beta}} \qquad [3.12]$$

According to this model, the adsorption process is supposed to proceed via chemisorb if E is between 8 and 16 kJmol^{-1}whereas for values less than 8 kJmol^{-1}, the sorption process is often governed by physical nature.[80] From the fitting to Dubinin–Radushkevich isotherm model, the mean free energy E values of the sorption process per mole of 3,4 di Cl-Ph were found to be 2.5 kJ/mol and 13.9 kJ/mol for 100%CS and 50:50 CS:γ-TCD, respectively. The mean free energy of adsorption of 4-ClPh were found to be 7.5kJ/mol and 13.6kJ/mol for 100%CS and 50:50 CS:γ-TCD, respectively. Therefore, the sorption of 4-ClPh and 3,4 di Cl-Ph onto 50:50 CS:γ-TCD composite film is chemisorption and is much stronger than onto 100%CS which is more by physisorption. This finding is as expected because as described above, 50:50 CS:γ-TCD composite material can readily form inclusion complexes and adsorption by inclusion complex formation is relatively stronger and is chemisorb by nature compared to 100%CS which can adsorb the analyte only by surface adsorption.

Taken together, adsorption isotherm results fully support kinetic results. Specifically, both results clearly indicate that 50:50 CS:γ-TCD with its ability to form inclusion complexes with 3,4-dichlorophenol, can strongly and effectively adsorb much more analyte compared to 100% CS which can only adsorb by surface adsorption which is relatively weaker and less effective.

Any structural and chemical changes that could have occurred upon adsorption of the analytes could help understand further the nature and mechanism of adsorption. Efforts were made to make various spectroscopic measurements on the films before and after exposure to the analytes. For this experiment, the films were cut into small pieces measuring about 2cm x 2cm. Different pieces of the different composite materials were placed in analyte solutions of about 1000mg/L and agitated on a mechanical shaker at room temperature for 24 hrs. The analyte concentrations for this experiment were deliberately made higher than the concentrations used for the kinetic experiments to try and maximize the amount of analyte that will be adsorbed. Another set of blank films were treated the same way but placed in de-ionized water instead of the pollutant solution. After 24 hrs, the films were taken out of the analyte solutions, blotted by a filter paper to remove excess analyte solution on the surface, and dried in the humidity controlled chamber. The UV, Near IR, FT-IR and XRD of the dry films were measured. UV and Near IR spectra of these films were measured in the transmission mode while FT-IR spectra were recorded by ATR and for XRD, the 2 cm x 2 cm films were held on a custom made sample holder and measured without any further treatment. The UV spectra of the [CS+β-TCD] and [CEL+β-TCD] composites could not be measured as no light was transmitting through the sample. The results obtained are shown in Figure 3.18. For reference, the UV and near IR spectra of the pollutants are also included. In this figure, the unused films (blue spectra) are the blank films placed in de-ionized water instead of the pollutant solution. The UV spectra of the composites after exposure to the analytes clearly shows the presence of the analytes on the films (Figure 3.18A and 3.18B). However, comparison of the near IR, FT-IR and XRD of the films before (unused films)

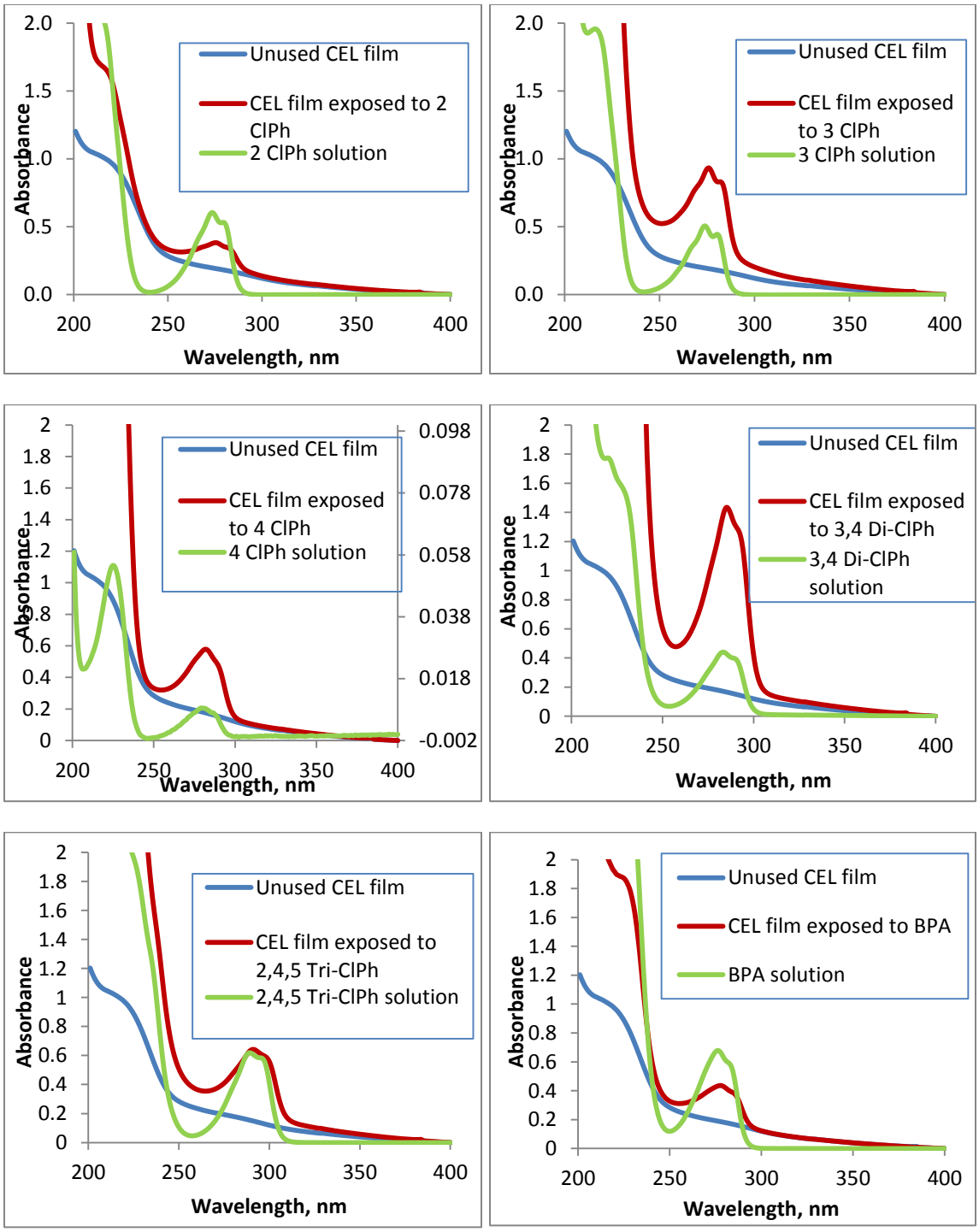

Figure 3.20A: UV absorption spectra comparing CEL films before and after exposure to different analytes.

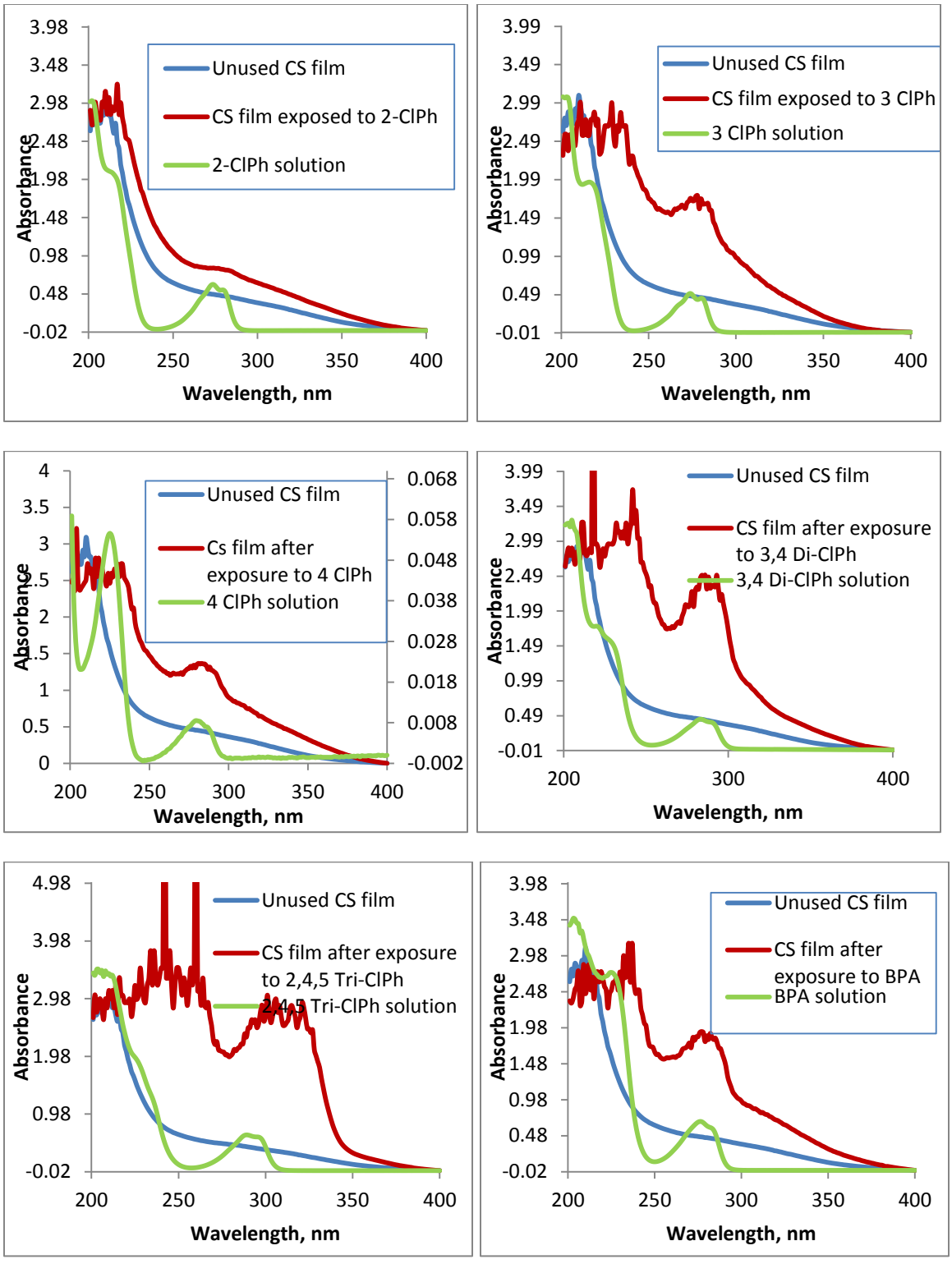

Figure 3.20B: UV absorption spectra comparing CS films before and after exposure to different analytes.

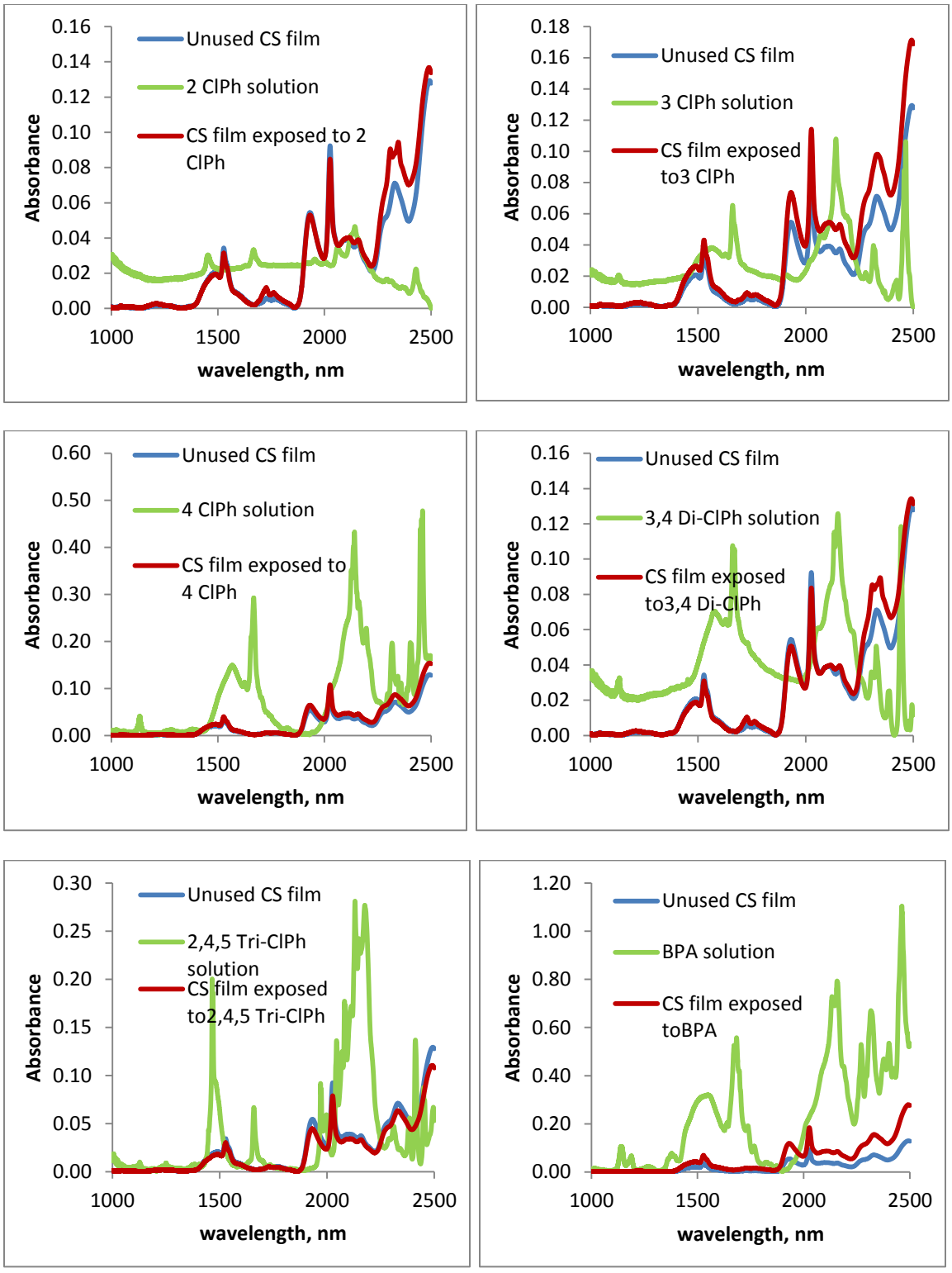

Figure 3.20C: Near IR spectra comparing CS films before and after exposure to different analytes.

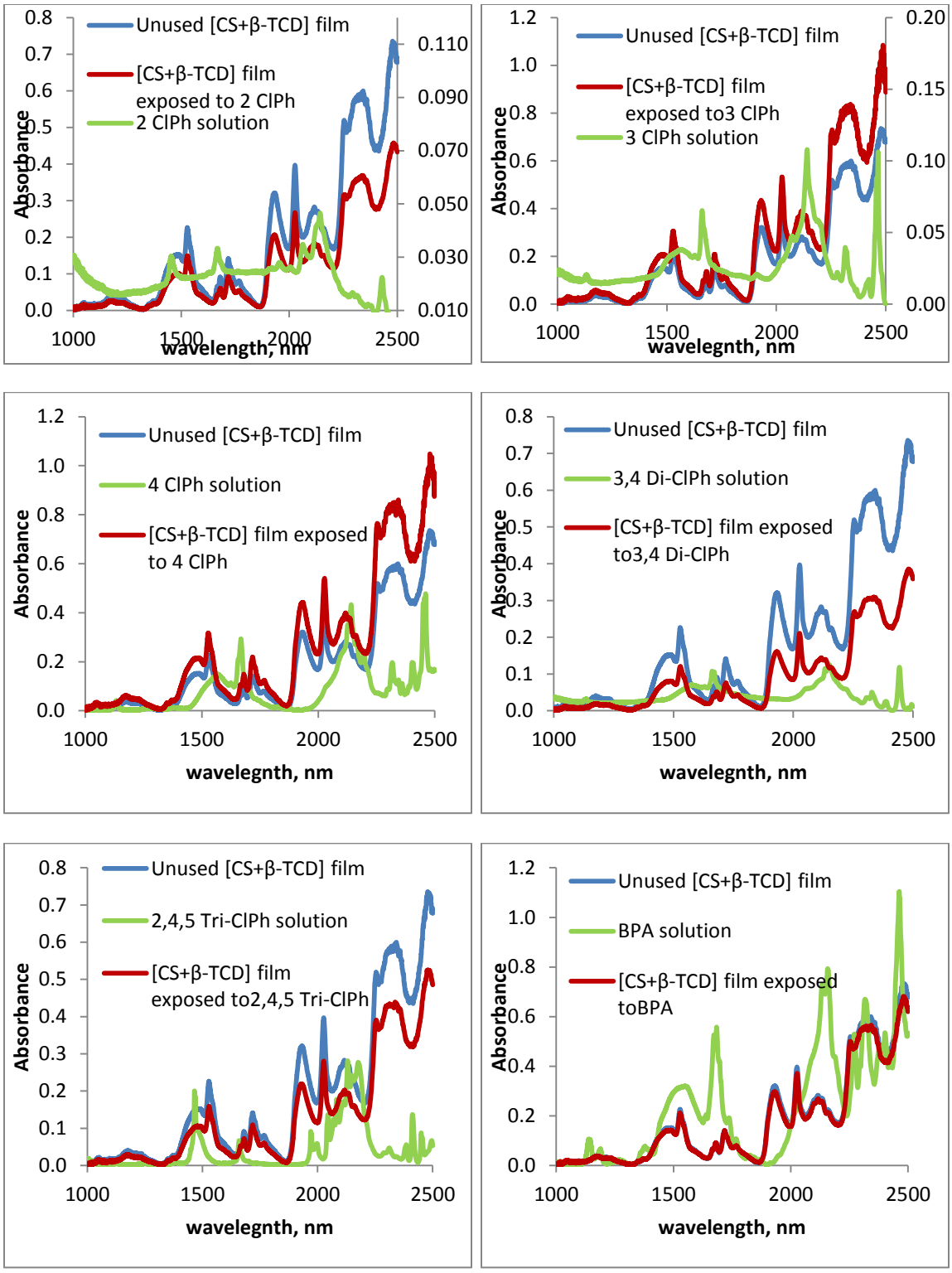

Figure 3.20D: Near IR spectra comparing [CS+β-TCD] films before and after exposure to different analytes.

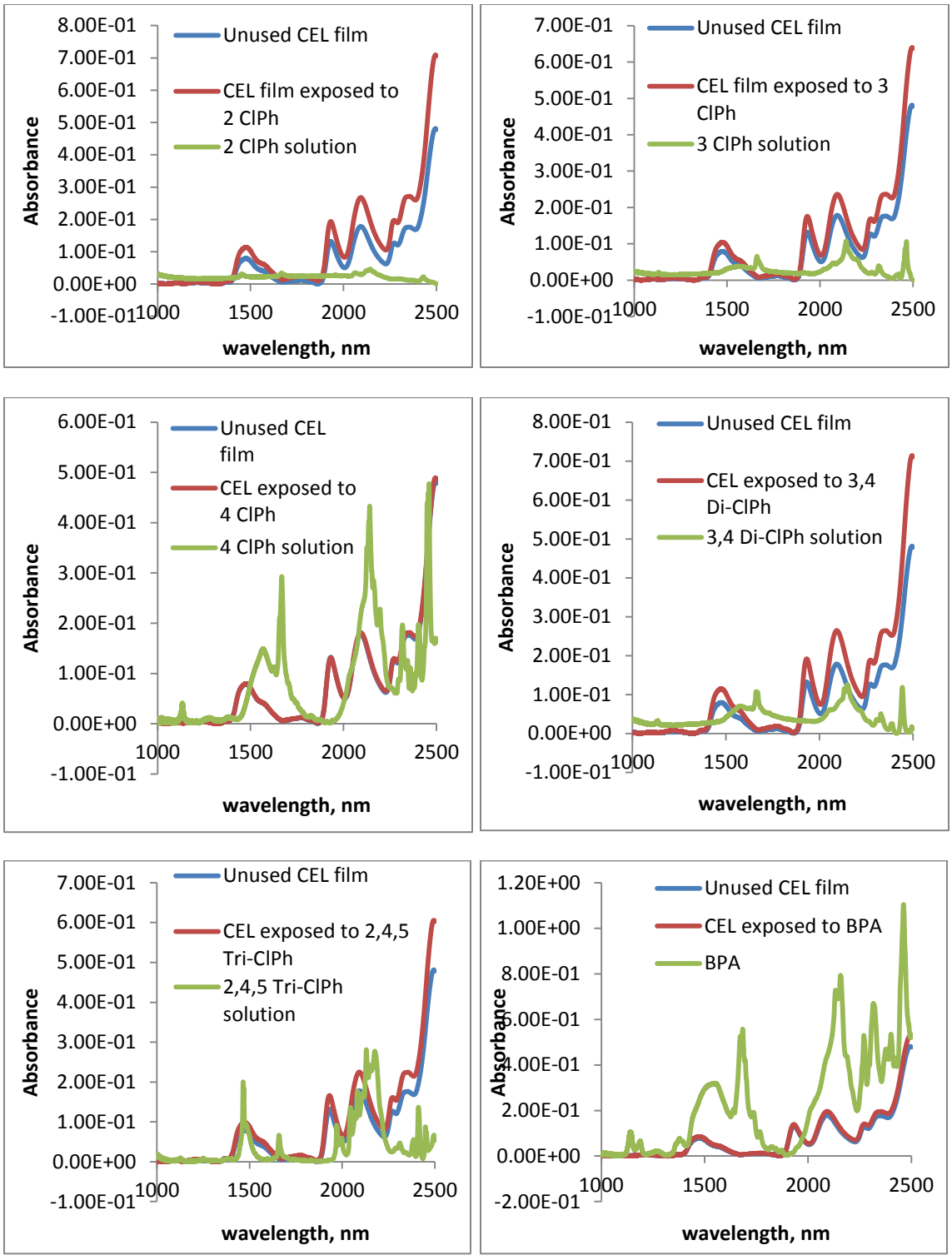

Figure 3.20E: Near IR spectra comparing CEL films before and after exposure to different analytes.

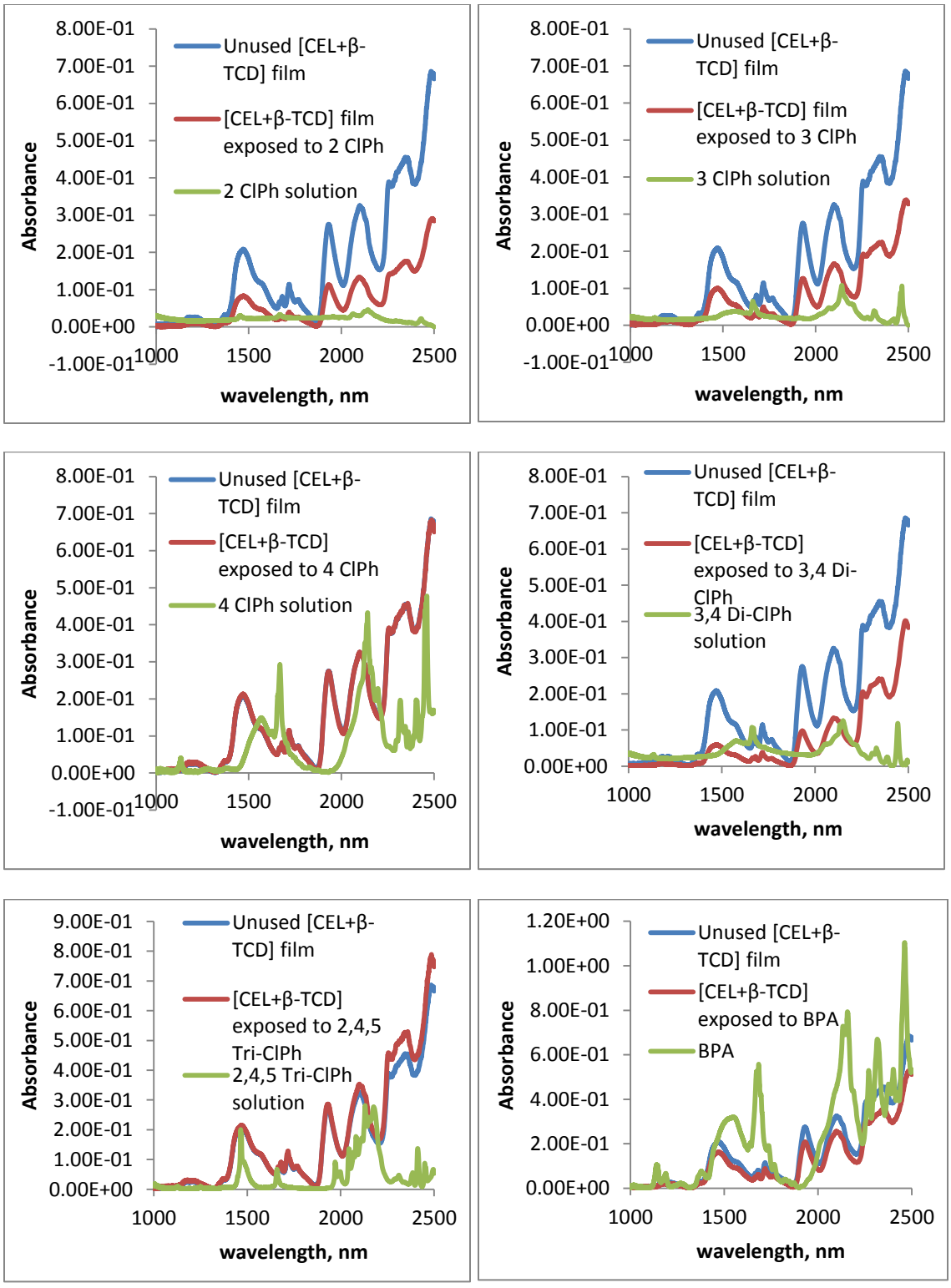

Figure 3.20F: Near IR spectra comparing [CEL+β-TCD] films before and after exposure to different analytes.

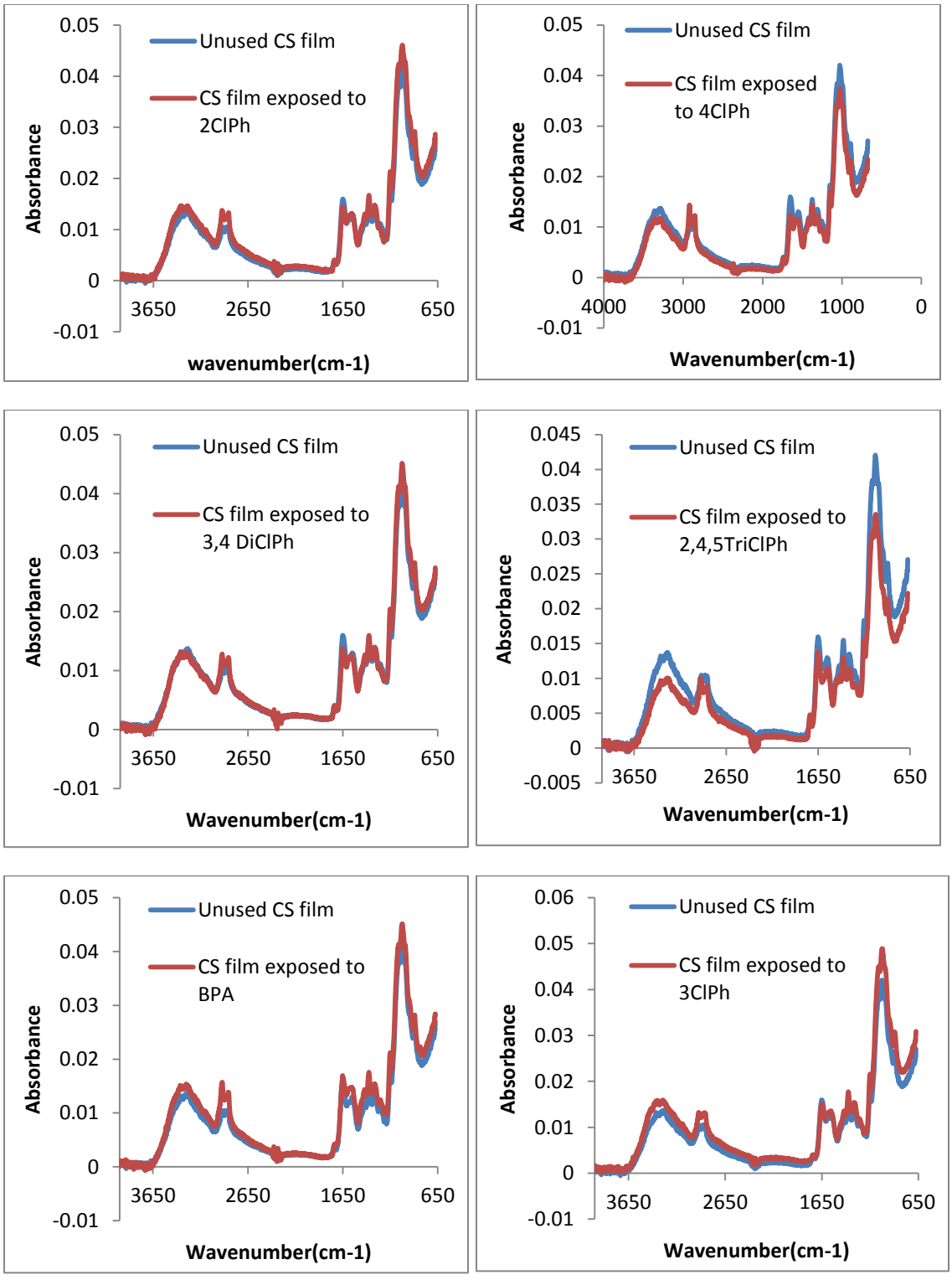

Figure 3.20G: FT-IR spectra comparing CS films before and after exposure to different analytes.

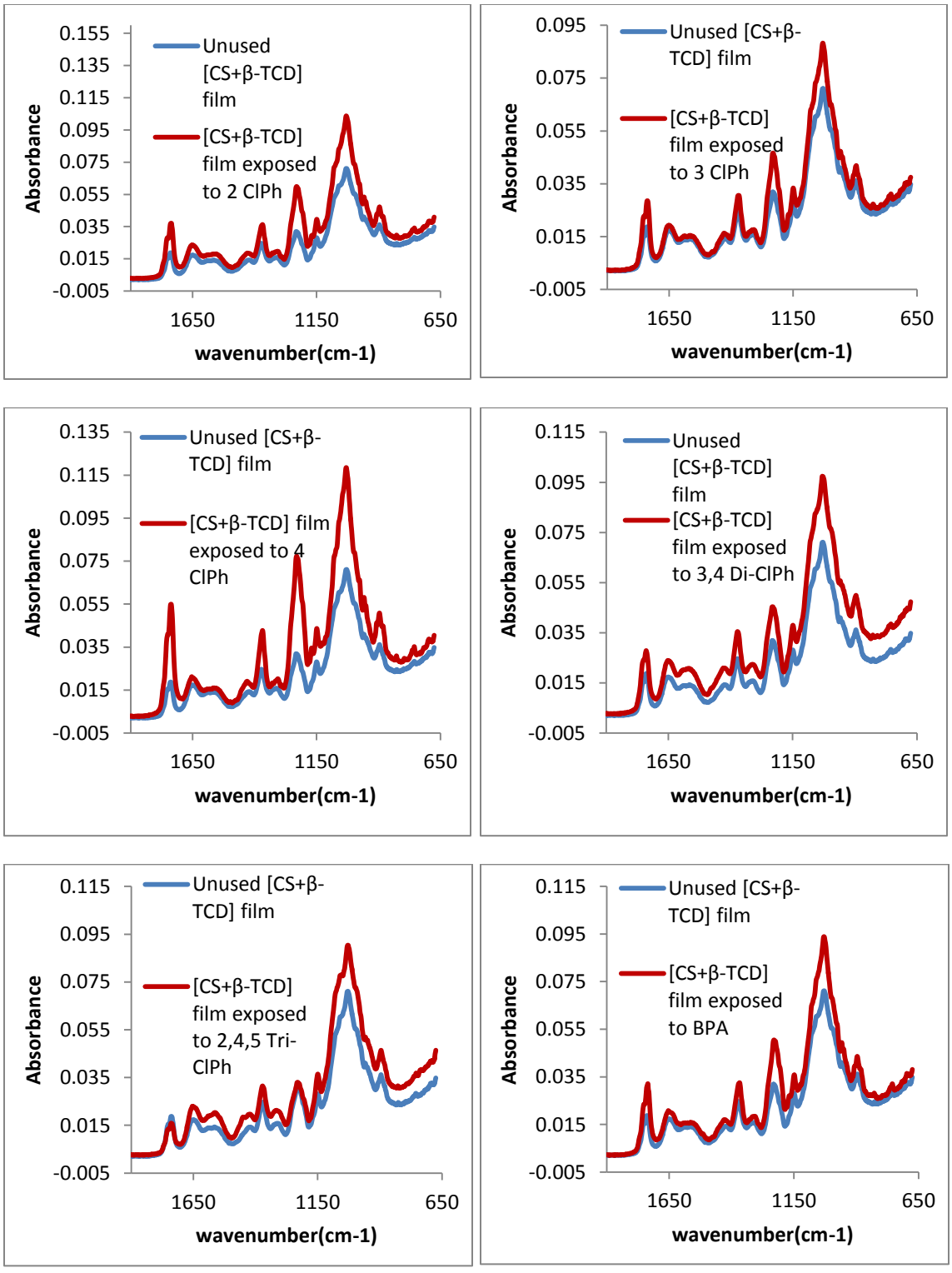

Figure 3.20H: FT-IR spectra comparing [CS+β-TCD] films before and after exposure to different analytes.

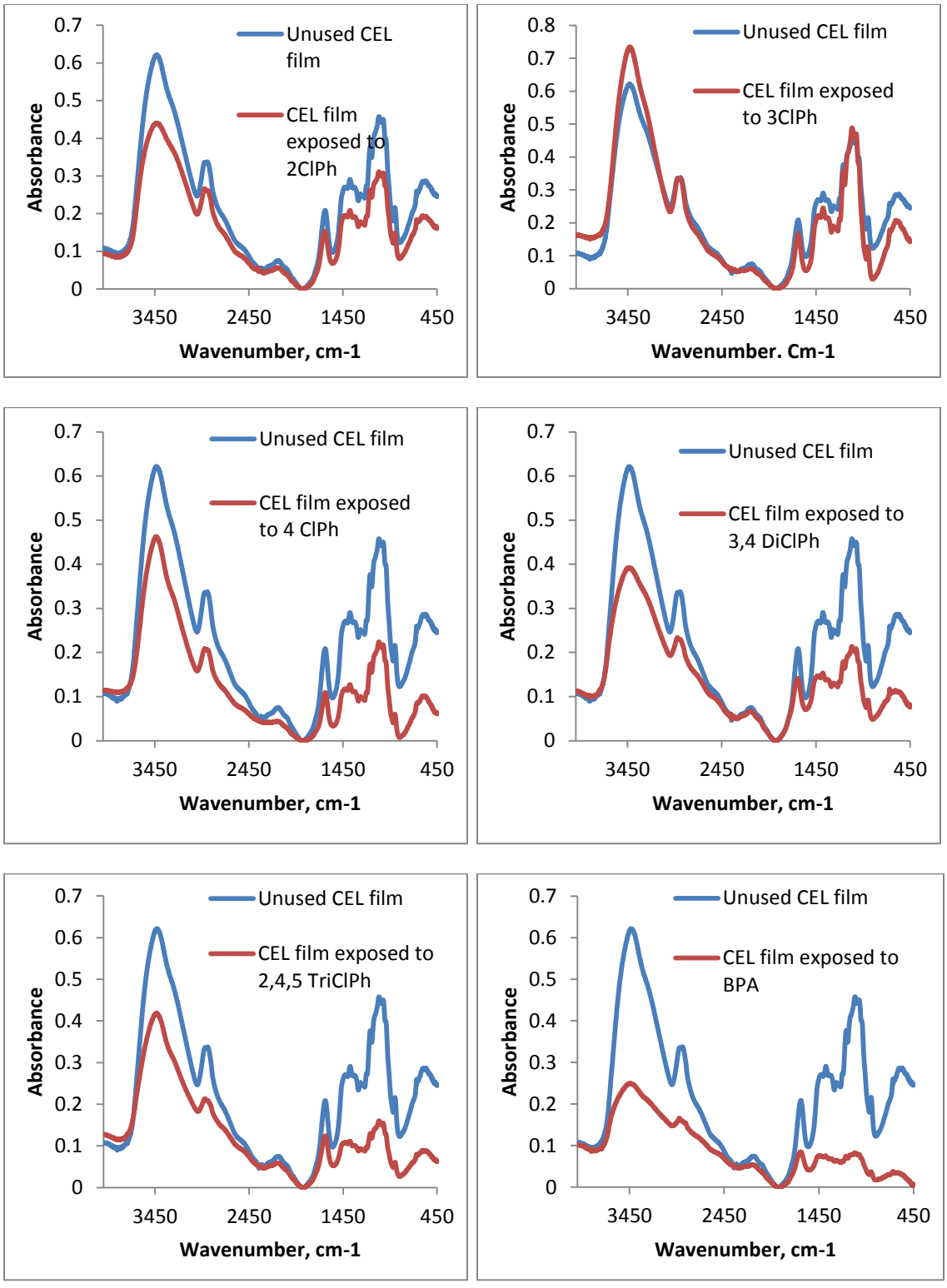

Figure 3.20I: FT-IR spectra comparing CEL films before and after exposure to different analytes.

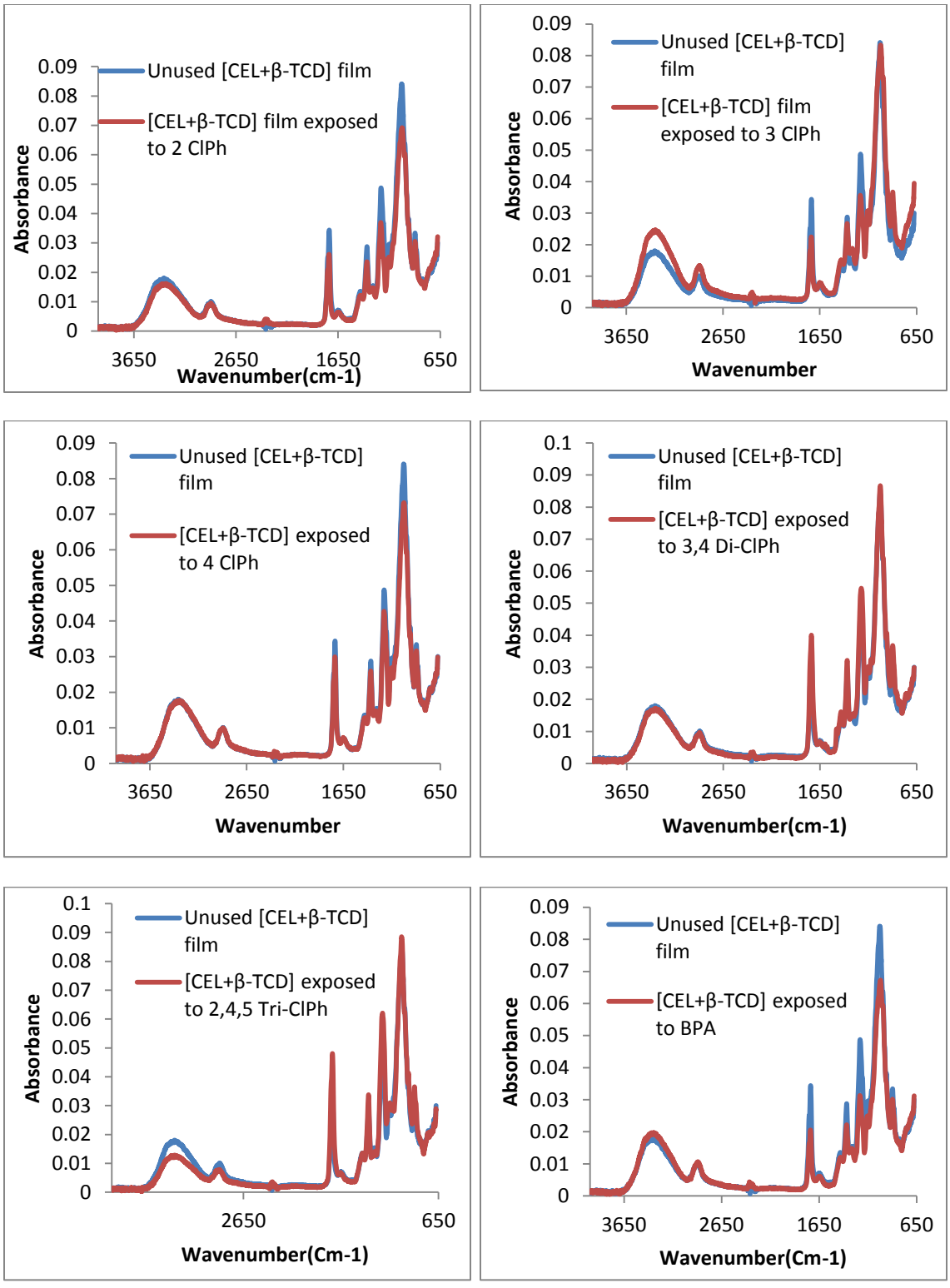

Figure 3.20J: FT-IR spectra comparing [CEL+β-TCD] films before and after exposure to different analytes.

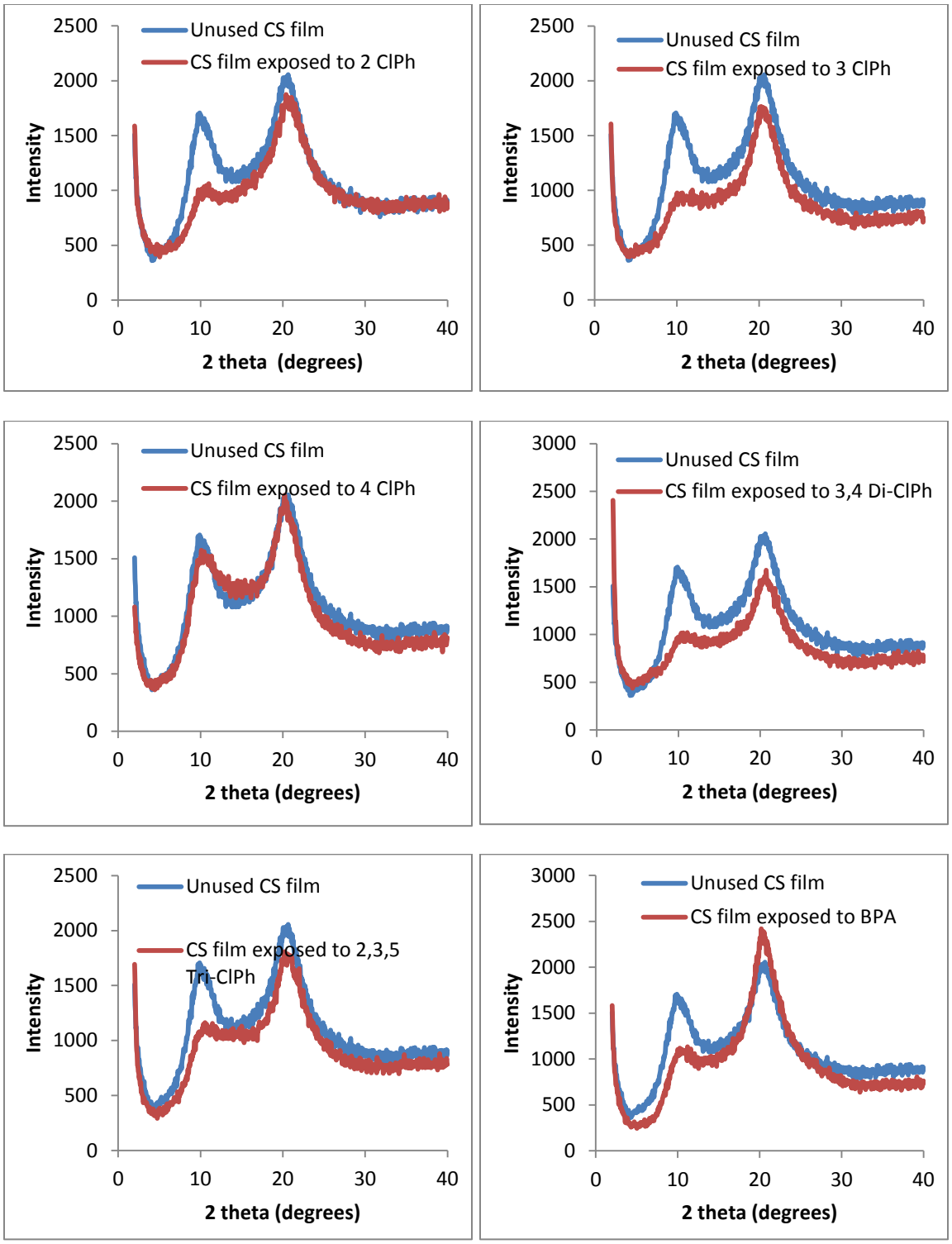

Figure 3.20K: XRD spectra comparing CS films before and after exposure to different analytes.

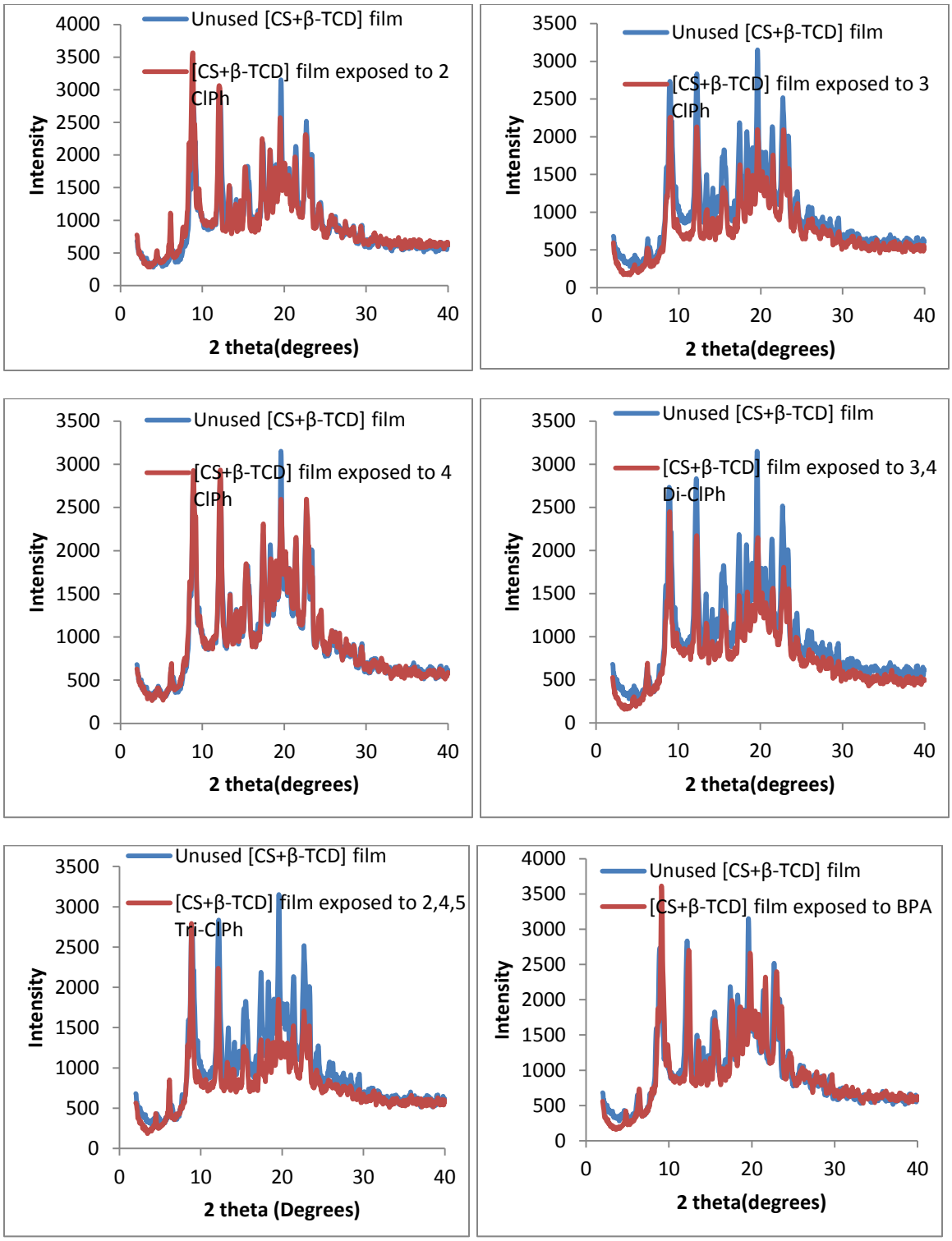

Figure 3.20L: XRD spectra comparing [CS+β-TCD] films before and after exposure to different analytes.

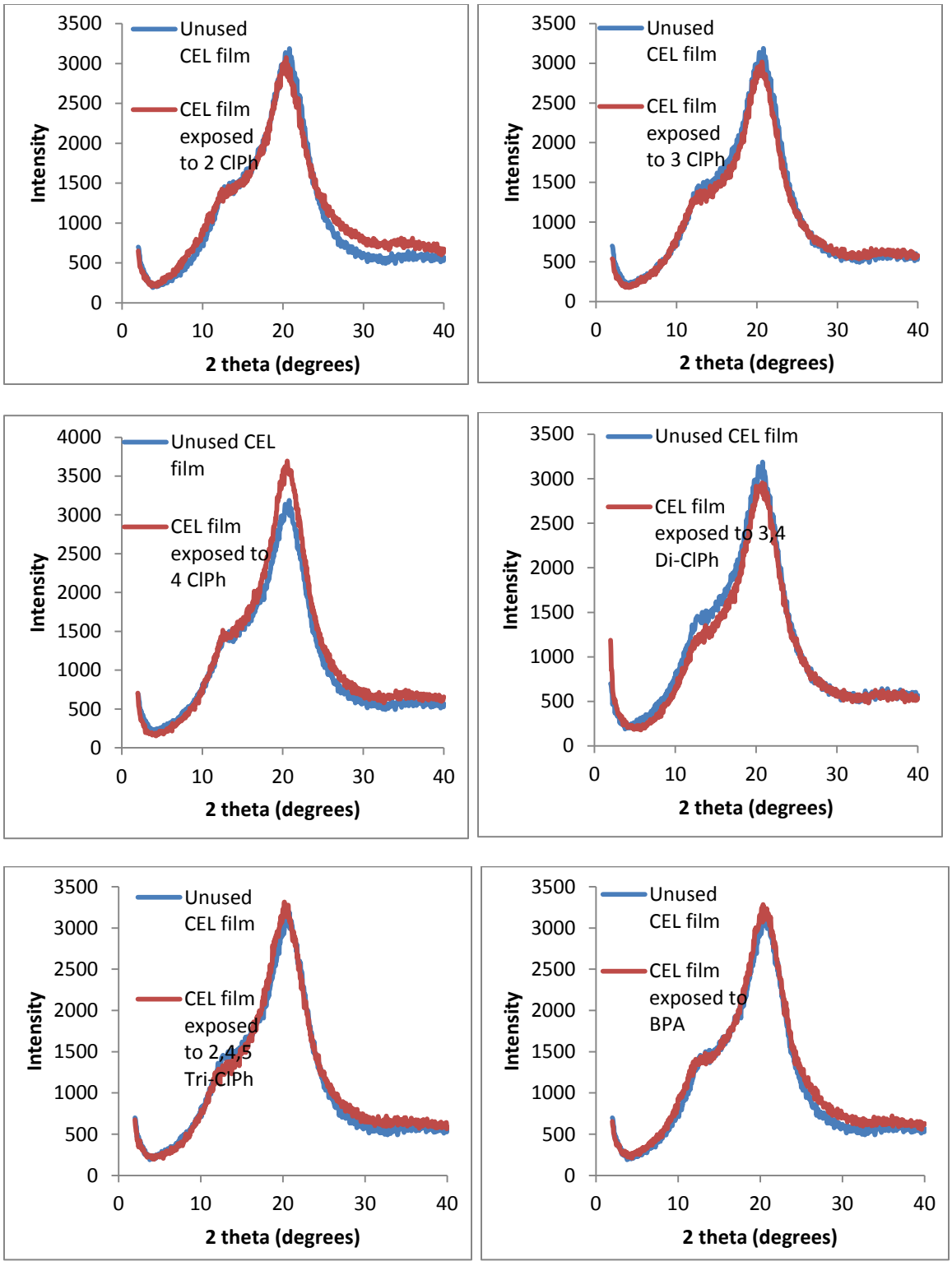

Figure 3.20M: XRD spectra comparing CEL films before and after exposure to different analytes.

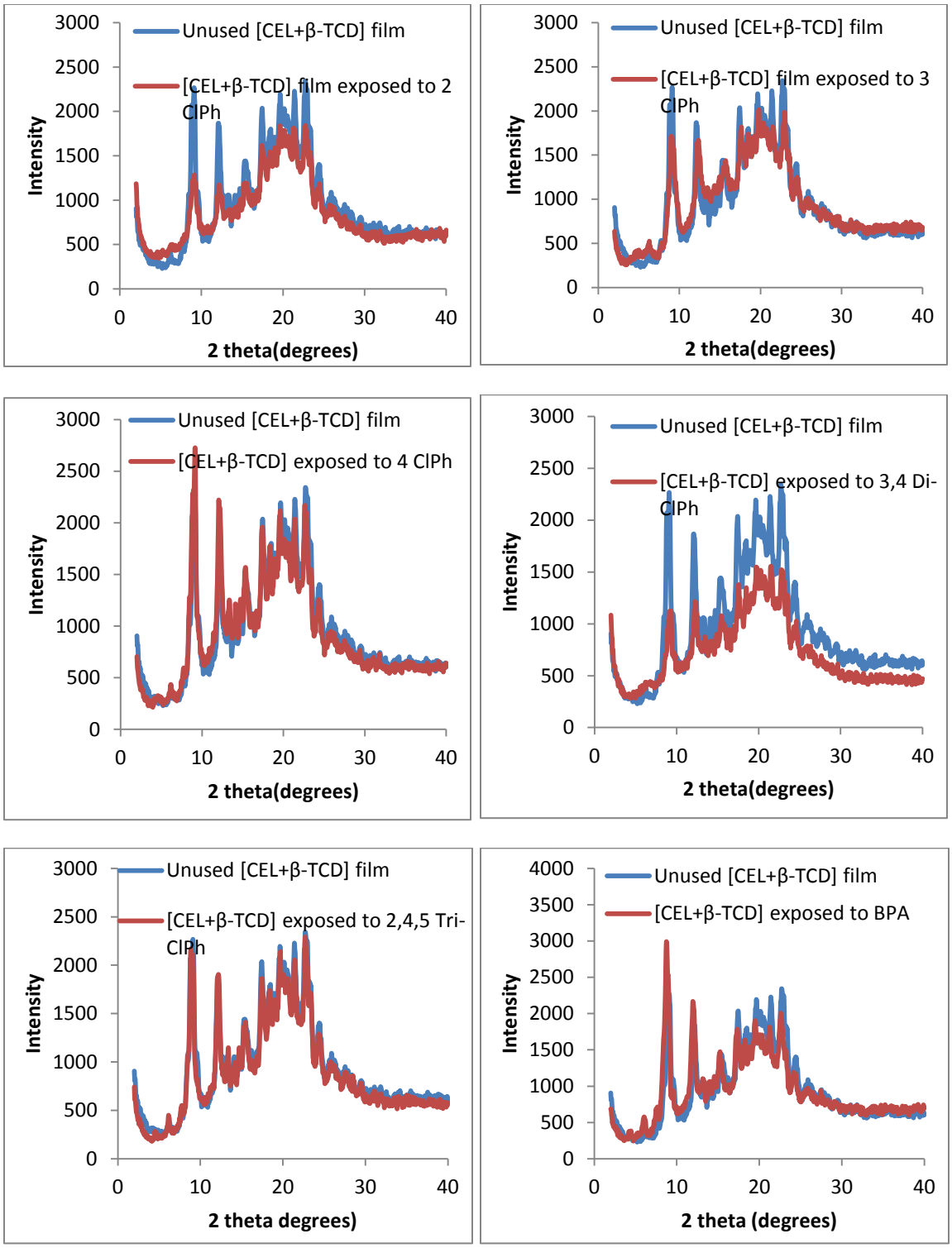

Figure 3.20N: XRD spectra comparing [CEL+β-TCD] films before and after exposure to different analytes.

and after exposure to the pollutants does not show any differences. This could possibly be due to the relatively lower sensitivity of these techniques compared to UV absorption as well as to the fact that the adsorption of the various analytes does not cause any structural or chemical changes in the composites detectable by these spectroscopic techniques.

Taken together, the results presented above showed that the polysaccharide developed here have potential applications in the adsorption of pollutants and endocrine disruptors. The adsorption of microcystin L-R by our [CEL+CS] composites showed higher adsorption capacities than other materials currently in use. The gain in tensile strength by adding CEL was found to be greater than the loss in adsorption capacity for these composites. While CS adsorbs analytes by surface adsorption, the ability of CDs to form inclusion complexes with analytes of different shapes and sizes allows the synthesis of composites with size and shape selectivity. It was observed that γ-TCD with its larger cavity was able to form inclusion complexes with bulky analytes such as 3,4 di-ClPh and enhance its adsorption by our composites. The results from the adsorption isotherms fully support kinetic results. Specifically, both results clearly indicate that 50:50 CS:γ-TCD with its ability to form inclusion complexes with 3,4-dichlorophenol, can strongly and effectively adsorb much more analyte compared to 100% CS which can only adsorb by surface adsorption which is relatively weaker and less effective. The application of our polysaccharide composites in drug delivery systems and in enantioselectivity will be discussed in Chapter 4.

3.5. References

(1) Svircev, Z.; Krstic, S.; Miladinov-Mikov, M.; Baltic, V.; Vidovic, M. *Journal of environmental science and health Part C Environmental carcinogenesis ecotoxicology reviews* **2009**, *27*, 36–55.

(2) Giannuzzi, L.; Sedan, D.; Echenique, R.; Andrinolo, D. *Marine Drugs* **2011**, *9*, 2164–75.

(3) Zegura, B.; Straser, A.; Filipič, M. *Mutation Research* **2011**, *727*, 16–41.

(4) Pearson, L.; Mihali, T.; Moffitt, M.; Kellmann, R.; Neilan, B. *Marine Drugs* **2010**, *8*, 1650–1680.

(5) Newcombe, G.; Nicholson, B. *J. Water Suppl. Res. Tech.* **2004**, *534*, 227–239.

(6) Westrick, J. A.; Szlag, D. C.; Southwell, B. J.; Sinclair, J. *Analytical and Bioanalytical Chemistry* **2010**, *397*, 1705–1714.

(7) Chen, L.; Dionysiou, D. D.; O'Shea, K. *Environmental science technology* **2011**, *45*, 2293–2300.

(8) Huang, W.; Cheng, B.-L.; Cheng, Y.-L. *J. Hazrdous Mater.* **2007**, *141*, 115–122.

(9) Pendleton, P.; Schumann, R.; Wong, S. H. *J. Colloid Interf. Sci.* **2001**, *240*, 1–8.

(10) Botes, D. P.; Wessels, P. L.; Kruger, H.; Runnegar, M. T. C.; Santikorn, S.; Smith, R. J.; Barna, J. C. J.; Williams, D. H. *J. Chem Soc., Perkin Trans.* **1985**, *1*, 2747–2752.

(11) Lanaras, T.; Cook, C. M.; Erikson, J. E.; Meriluoto, M. T. C.; Hotokka, M. *Toxicon* **1991**, *29*, 901–906.

(12) Bagu, J. R.; Sonnicshsen, F. D.; Williams, D. H.; Anderson, R. J.; Sykes, B. D.; Holmes, C. F. . *Nat. Struct. Biol.* **1995**, *2*, 114–116.

(13) No Title http://water.epa.gov/scitech/drinkingwater/dws/ccl/ccl3.cfm.

(14) Han, C.; Doepke, A.; Cho, W.; Likodimos, V.; Cruz, A. A. de la; Back, T.; Heineman, W. R.; Halsall, B.; Shanov, V. N.; Schulz, M. J.; Falaras, P.; Dionysios, D. *Advanced Functional Materials* **2013**, *23*, 1807–1816.

(15) Hoffmann, J. R. H. *water S. A.* **1976**, *2*, 58–60.

(16) Himberg, K.; Keijola, A. M.; Hsvirta, L.; Pyysalo, H.; Sivonen, K. *water res.* **1989**, *29*, 979–984.

(17) Keijola, A. M.; Himberg, K.; Esala, A. L.; Sivonen, K.; Hiisvirta, L. *Toxic Assess.* **1988**, *3*, 643–656.

(18) Govindan, V. . *Asian Environ.* **1985**, *7*, 4.

(19) Qiao, J.; Dong.L; Hu, Y. *Fres. Env. Bull.* **2011**, *20*, 764–772.

(20) Wang, Y.; Zhuo, S.; Yang, Y.; Li, N. *Adv. Mat. Res.* **2013**, *347-353*, 1911–1916.

(21) Pan, G.; Zou, H.; Chen, H.; Yuan, X. *Environmental Pollution* **2006**, *141*, 206–212.

(22) Yan, Q.; Yu, Y.; Feng, W.; Pan, G.; Chen, H.; Chen, J.; Yang, B.; Li, X.; Zhang, X. *Microbial Ecology* **2009**, *58*, 47–55.

(23) Zheng, S.; Yang, Z.; Jo, D. H.; Park, Y. H. *water res.* **2004**, *38*, 2315–2322.

(24) Kinzell, L. H.; McKenzie, R. M.; Oslo, B. A.; Kirsch, D. G.; Shull, L. R. *Environmental science technology* **1979**, *13*, 416–423.

(25) Edgehill, R. U.; Finn, R. F. *Eur. J Appl. Microbiol. Biotechnol.* **1982**, *16*, 179–184.

(26) Gonzalez, F. J.; Hu, W. . *Appl. Microbiol. Biotechnol.* **1991**, *35*, 100–104.

(27) Pignatello, J. J.; Martinson, M. M.; Steiert, J. G.; Carison, R. E.; Crawford, R. L. *Applied and environmental microbiology* **1983**, *46*, 1024–1033.

(28) Etzel, J. E.; Kirsch, E. J. *Dev. Ind. Microbiol.* **1975**, *16*, 287–295.

(29) Melin, S. E.; Ferguson, J. F.; Puhakka, J. A. *Appl. Microbiol. Biotechnol.* **1997**, *47*, 675–682.

(30) Jarvinen, K. T.; Puhakka, J. A. *Envirn. Technol.* **1994**, *15*, 823–832.

(31) Jorgensen, O. N. *Chem. Geol.* **2002**, *184*, 359–370.

(32) Gong, R.; Guo, P.; Chen, J.; Huang, F. *Environmental Engineering Science* **2009**, *26*, 1561–1566.

(33) Staples, C. A.; Dorn, P. B.; Klecka, G. M.; O'Block, S. T.; Harris, L. R. *Chemosphere* **1998**, *36*, 2149.

(34) *Update on Bisphenol A for Use in Food Contact Applications U.S. Food and Drug Administration January 2010*; 2010; pp. 1–7.

(35) Naficy, S.; Razal, J. M.; Spinks, G. M.; Wallace, G. G. *Sensors and Actuators A Physical* **2009**, *155*, 120–124.

(36) Finkenstadt, V. L.; Millane, R. P. *Macromolecules* **1998**, *31*, 7776–7783.

(37) Cai, J. I. E.; Liu, Y.; Zhang, L. *J. Pol. Sci. B. Pol. Phys.* **2006**, 3093–3101.

(38) Fink, H. P.; Weigel, P.; Purz, H. J.; Ganster, J. *Progress in Polymer Science* **2001**, *26*, 1473–1524.

(39) Miao, J.; Zhang, F.; Takieddin, M.; Mousa, S.; Linhardt, R. J. *Langmuir* **2012**, *28*, 4396–4403.

(40) McCarthy, S. J.; Gregory, K. W.; Morgan, J. W. Tissue dressing assemblies systems, and methods formed from hydrophilic polymer sponge structures such as chitosan. WO 062896, 2005.

(41) El-Mekawy, A.; Hudson, S.; El-Baz, A.; Hamza, H.; El-Halafawy, K. *J Appl Pol Sci* **2010**, *116*, 3489–3496.

(42) Sandoval, M.; Albornoz, C.; Muñoz, S.; Fica, M.; García-Huidobro, I.; Mertens, R.; Hasson, A. *Journal of drugs in dermatology JDD* **2011**, *10*, 75–79.

(43) Pinkert, A.; Marsh, K. N.; Pang, S.; Staiger, M. P. *Chemical reviews* **2009**, *109*, 6712–6728.

(44) Tran, C. D.; De Paoli Lacerda, S. H. *Analytical chemistry* **2002**, *74*, 5337–5341.

(45) Han, X.; Armstrong, D. W. *Accounts of chemical research* **2007**, *40*, 1079–1086.

(46) Tran, C. D. In *ACS Symbosium Series*; 2010; pp. 35–54.

(47) Welton, T. *Chemical Reviews* **1999**, *99*, 2071–2083.

(48) Wasserscheid, P.; Welton, T. *Ionic Liquids in synthesis*; Wiley-VCH: Weinheim, 2003.

(49) Soukup-Hein, R. J.; Warnke, M. M.; Armstrong, D. W. *Ann. Rev. Anal. Chem* **2009**, *2*, 145–168.

(50) Ho, Y. .; McKay, G. *Wat. Res.* **2000**, *34*, 735–742.

(51) Kumar, K. V.; Sivanesan, S. *Journal of Hazardous Materials* **2006**, *136*, 721–726.

(52) Li, Q.; Sun, L.; Zhang, Y.; Qian, Y.; Zhai, J. *Desalination* **2011**, *266*, 188–194.

(53) Chowdhury, Shamik Chakraborty, S.; Saha, P. *Colloids and Surfaces B: Biointerfaces* **2011**, *84*, 520–527.

(54) Chakraborty, S.; Chowdhury, S.; Das Saha, P. *Carbohydrate Polymers* **2011**, *86*, 1533–1541.

(55) Weber, W. J.; Morris, J. C. *Journal of the sanitary engineering division, ASCE* **1963**, *89*, 31–39.

(56) Gu, W.; Sun, C.; Liu, Q.; Cui, H. *Transactions of Nonferrous Metals Society of China* **2009**, *19*, s845–s850.

(57) Langmuir, I. *Journal of American Chemical Society* **1916**, *38*, 2221–2295.

(58) Freundlich, H. M. F. *Journal of Physical Chemistry* **1906**, 385–471.

(59) Dubinin, M. M.; Radushkevich, L. V *Proc. Acad. Sci. USSR Phys. Chem. Sect.* **1947**, *55*, 331–337.

(60) Dubinin, M. M. *Chem. Rev.* **1960**, *60*, 235–266.

(61) Deng, Y.; Qi, D.; Deng, C.; Zhang, X.; Zhao, D. *Journal of the American Chemical Society* **2008**, *130*, 28–9.

(62) Gao, Y.; Gao, N.; Gu, J.; Shen, Y.; Wang, S. *Water Environ. Res.* **2012**, *84*, 562–568.

(63) Chen, H.; Lu, X.; Deng, C.; Yan, X. *J. Phys. Chem. C* **2009**, *113*, 21068–21073.

(64) Morri, R. J.; Williams, D. E.; Luu, H. A.; Holmes, C. F.; Andersen, R. J.; Calvert, S. E. *Toxicon official journal of the International Society on Toxinology* **2000**, *38*, 303–308.

(65) Yan, H.; Gong, A.; He, H.; Zhou, J.; Wei, Y.; Lv, L. *Chemosphere* **2006**, *62*, 142–148.

(66) Lee, J.; Walker, H. W. *Environmental science technology* **2006**, *42*, 7336–7342.

(67) Pyo, D.; Moon, D. *Bull. Korean Chem. Soc.* **2005**, *26*, 2089–2092.

(68) Mao, Y.; Hu, H.; Yan, Y. *Journal of Environmental Sciences* **2011**, *23*, 1104–1112.

(69) Caira, M. R. *Curr. Org. Chem.* **2011**, *15*, 815–830.

(70) Caira, M. R.; Bettinetti, G.; Sorenti, M.; Catenacci, L.; Cruickshank, D.; Davies, K. *Chem. Commun* **2007**, 1221–1223.

(71) Hamai, S. *Bull. Chem. Soc. Jpn* **1992**, *65*, 2323.

(72) Leyva, E.; Moctezuma, E.; Strouse, J.; Ia-, M. A. G. **2001**, 41–46.

(73) Rekharsky, M. V.; Inoue, Y. *Chemical reviews* **1998**, *98*, 1875–1918.

(74) Politi, M. J.; Tran, C. D.; Gao, G.-H. *The Journal of Physical Chemistry* **1995**, *99*, 14137–14141.

(75) Bertrand, G. L.; Faulkner, J. R.; Han, S. M.; Armstrong, D. W. *J. Phys. Chem.* **1989**, *93*.

(76) Narita, M.; Mima, S.; Ogawa, N.; Hamada, F. *Analytical sciences : the international journal of the Japan Society for Analytical Chemistry* **2001**, *17*, 379–85.

(77) Chelli, S.; Majdoub, M.; Jouini, M.; Aeiyach, S. *J. Phys. Org. Chem* **2007**, *20*, 30–43.

(78) Kitano, H.; Endo, H.; Gemmei-Ide, M.; Kyogoku, M. *Journal of Inclusion Phenomena* **2003**, *47*, 83–90.

(79) Katritzky, A. R.; Fara, D. C.; Yang, H.; Karelson, M.; Suzuki, T.; Solov'ev, V. P.; Varnek, A. *Journal of chemical information and computer sciences* **2003**, *44*, 529–41.

(80) Kundu, S.; Gupta, A. K. *Chem. Eng. J.* **2006**, *122*, 96–106.

Chapter 4. BIOMEDICAL APPLICATIONS OF POLYSACCHARIDE COMPOSITE MATERIALS: DRUG DELIVERY SYSTEMS CHIRAL SEPARATIONS AND ENCAPSULATION OF FULLERINE DERIVATIVES

4.1. Background

4.1.1. Drug Delivery Vehicles

Significant medical advances have occurred in the area of controlled drug delivery systems. Some of the dosage forms being considered as controlled drug release vehicles include pellets.[1–4] The purpose of the controlled drug release vehicle will be to maintain the drug concentration in the target for as long as possible. The release vehicle should be able to exert control on the drug release rate for a certain period of time.[5]

There are varied physical and chemical properties that influence drug release from different formulations. The release patterns include those that release the drug at a slow zero or first order rate. Some formulations provide an initial rapid dose, followed by slow zero or first order release.[6] There are a number of kinetic models which are used to describe the overall release of drug from the dosage form. These are useful in reducing the necessity for bio-studies each time a new formulation is created. The methods used to investigate kinetics of drug release can be classified into three categories. These are: 1) Statistical methods, 2) Model dependent methods and 3) model independent methods.[6]

Model dependent methods are based on mathematical functions which describe the drug release profile. Some of the models commonly used to describe drug release include the zero order, first order, Higuchi and Korsmeyer-Peppas (Power Law) models.[6]

Zero order kinetics

The zero order model can be described by the equation:

$$\frac{Mt}{M\infty} = Kt$$

The pharmaceutical dosage form that follows this release profile release the same amount of drug per unit time and is the ideal method of drug release to achieve a pharmacological prolonged action.[7]

First order release

This model can be described by the equation:

$$\ln\left(1 - \frac{Mt}{M\infty}\right) = -Kt$$

Higuchi model

This was the first mathematical model that was aimed at describing drug release from a matrix system:

$$\left(\frac{Mt}{M\infty}\right)^2 = Kt$$

This model has been derived from Fick's first law of diffusion and is suited for the modeling of drug release from a homogeneous planar matrix.

Korsmeyer-Peppas model

This is sometimes referred to as the Power Law model:

$$\frac{Mt}{M\infty} = Kt^n$$

This model can be used to study the drug release mechanism by analyzing the release exponent, n. According to this equation if n ≤ 0.45 the Fickian mechanism, for 0.5≤ n ≤0.8 the Non-Fickian and if 0.8≤ n ≤1 a zero-order mechanism is governing the drug release from the film matrix.[8–10] In all these equations, $\frac{Mt}{M\infty}$ is the fraction of drug released at time, t, K is the release rate constant for the particular model and in the case of the Korsmeyer-Peppas model, n is the release exponent.

As described earlier in Chapter 1 and 2 Cellulose (CEL) is the most abundant natural material. It is made up of glucose units joined together by β (1-4) glycosidic linkages. Cellulose is biodegradable, renewable and has excelled mechanical and rheological properties. These properties make it attractive for use in various technological applications. Chitosan (CS) is a deacetylation product of the naturally abundant chitin. Chitosan has attracted a lot of interest as a biomedical material because of its good biocompatibility and its application in drug delivery has been reported.[4,11] Wool keratin (KER) is a kind of unbranched protein which exhibits a stable three-dimensional conformation. This conformation is maintained by a range of non-covalent interactions which include electrostatic forces, hydrogen bonds, hydrophobic forces and covalent interactions (disulfide bonds), in addition to the peptide bonds between individual amino acids.[12]

In this study, film compositions of [CS+CEL] and [CS+KER] made by processing the materials in 1-butyl-3-methylimidazoiulm chloride [$BMIm^+Cl^-$] ionic liquid were investigated as possible controlled drug releasing vehicles. Ciprofloxacin (cipro) [1-

cyclopropyl-6-fluoro-1,4-dihydro-4-oxo-7-(piperazinyl) quinolone-3-carboxylic acid] was used as the model drug molecule (Structure shown in Scheme 4.2). Cipro is a synthetic fluoroquinolone derivative which has been shown to have broad spectrum activity against many pathogenic bacteria. This bactericidal action comes from interference with the enzyme DNA gyrase which is required for the synthesis of bacterial DNA.

4.2. Preparation of Cipro-doped Composites for drug release studies

The synthesis of the various cipro-doped films is shown in Scheme 4.1 below:

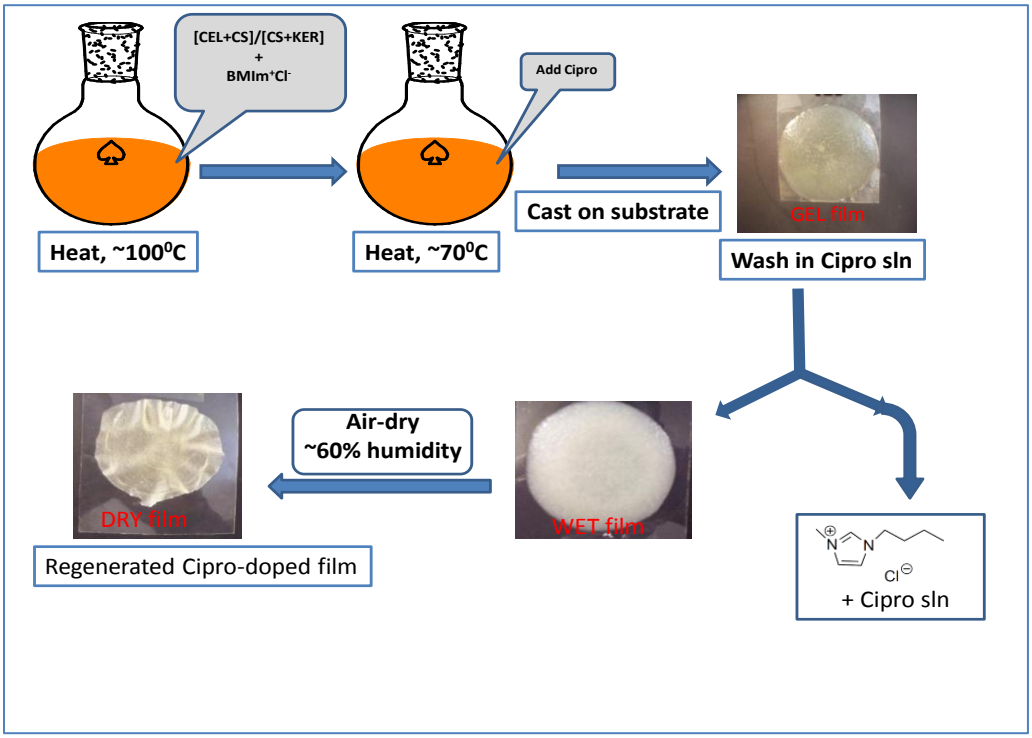

Scheme 4.1: Preparation procedure for cipro-doped polysaccharide composite films.

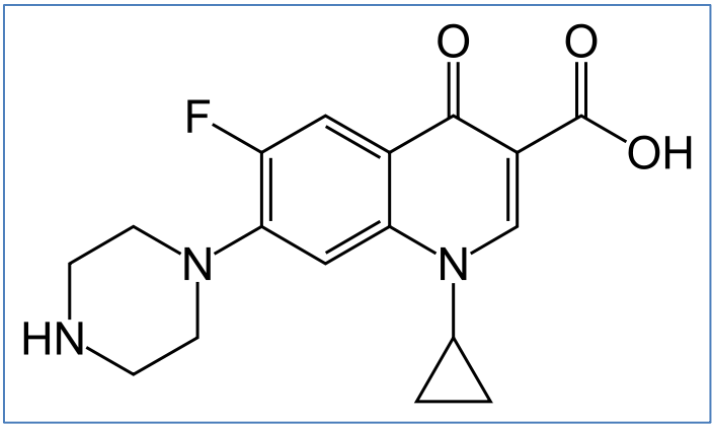

Scheme 4.2: Structure of the drug used (Ciprofloxacin)

In the preparation of [CS+CEL] composite films, cellulose (CEL) was dissolved first followed by chitosan (CS) and for the [CS+KER] composite films, CS was dissolved first followed by keratin (KER). Similar to the procedure described in Chapter 2 for the preparation of [CEL+CS] composites, CEL, CS and KER were added in 1% w/w portions until the desired concentration was reached. The wool KER utilized in these experiments is the raw sheep wool obtained from a local farm. The KER was cleaned by an acetone/ethanol mixture solvent system prior to the dissolution experiments.[12] Briefly, the wool KER was loaded into a Soxhlet extraction thimble, and was washed in a Soxhlet extractor using a 1:1 acetone/ethanol mixture for 48 hrs. After 48 hrs, the KER was rinsed thoroughly with de-ionized water and they were dried at 100^0C. The clean, dry KER fibers were cut into very small pieces using a scissors prior to the dissolution experiments. Cipro was only added after the complete dissolution of the polymers. Dissolution of the polymers was performed at about 100^oC. After complete dissolution of the polymers, the temperature was reduced to about 70^oC before adding Cipro. This was done to minimize any chances of thermal decomposition of the Cipro compound. The UV

spectrum of a Cipro solution stirred at 70°C for 2 hrs was compared to that of a freshly prepared Cipro solution. As illustrated in Figure 4.1 below, the two spectra were not significantly different and hence 70°C was determined to be a safe temperature for the dissolution of the Cipro. After reducing the temperature to 70°C, an appropriated amount of Cipro was added such its final concentration in the dried composite film will be 0.5% w/w. Stirring was continued at 70°C for a further 2 hrs after which the samples were cast onto PTFE molds on Mylar substrates and allowed to gel at room temperature overnight.

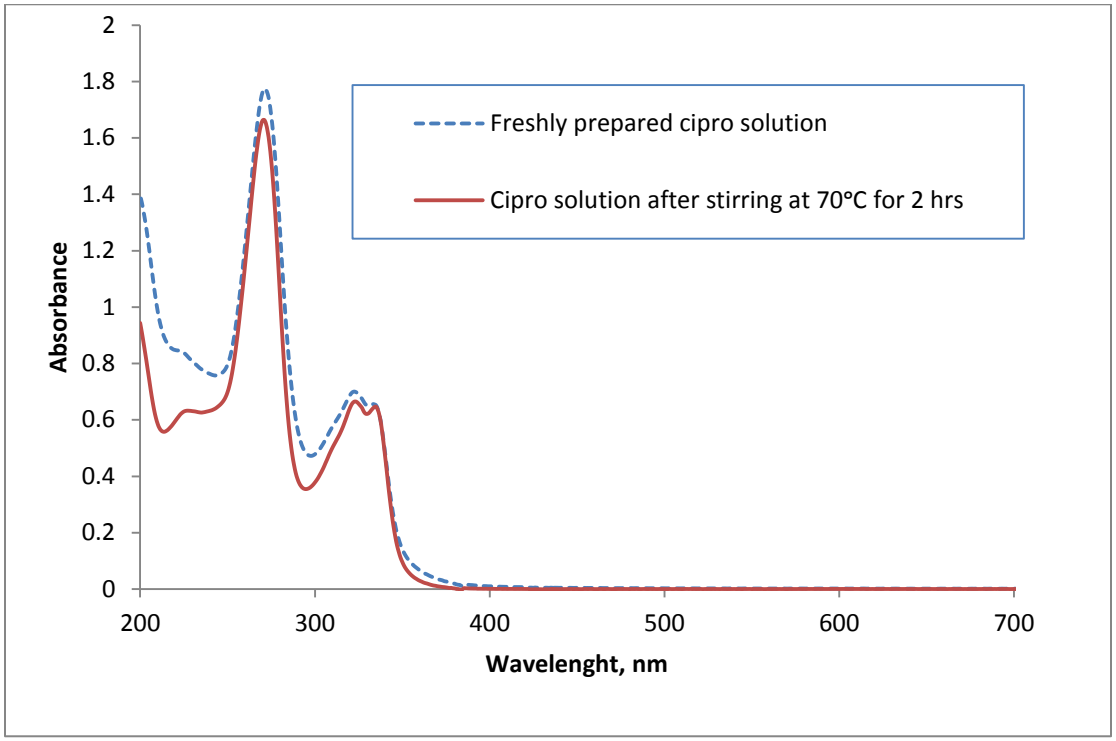

Figure 4.1: Comparison of the UV absorption spectra of a freshly prepared Cipro solution and one that was stirred at 70°C for 2 hrs.

Similar to the preparation of [CEL+CS] composites described earlier, the [$BMIm^+Cl^-$] was removed by washing the composites in water. However, since Cipro is soluble in water too, the GEL films were washed in saturated solution of Cipro. The saturated solution was made by stirring 0.1g of Cipro in 1L of water for at least 2 hrs before filtering. The filtered solution was then used to wash the films. The samples were washed over a period of 72 hrs and the washing solution was replaced with fresh saturated Cipro solution every 24 hrs. After 72 hrs, the resultant wet films were dried in the humidity controlled chamber. Generally, drying time was about 3 – 5 days depending on the thickness of the films.

Table 4.1: Formulation of [CS+CEL] and [CS+KER] cipro-doped composites.

Composition in Ionic Liquid			**Final Film Composition**	
%CS	**%CEL or %KER**		**%CS**	**%CEL or %KER**
4.0	0.0		100.0	0.0
3.5	0.5		87.5	12.5
3.0	1.0		75.0	25.0
2.5	1.5		62.5	37.5
2.0	2.0		50.0	50.0
1.5	2.5		37.5	62.5
1.0	3.0		25.0	75.0
0.5	3.5		12.5	87.5
0.0	4.0		0.0	100.0

Different [CS+CEL] and [CS+KER] composites were prepared according the formulations shown in Table 4.1. above. This formulation involved blending different amounts of CS and CEL or KER in the [$BMIm^+Cl^-$] ionic liquid but maintaining the total concentration of the polymers in the ionic liquid at 4%. In all these film compositions, the Cipro level was maintained at 0.5% by weight of the polymers thus ensuring that the concentration of Cipro in all the dry films was the same.

The Cipro release kinetics of the various films was investigated by fluorimetric measurement of the amount of Cipro released in 0.001M phosphate buffer, pH 7.2 as a function of time. The fluorescence of the sample was measured after 5, 10, 20, 30, 40, 50, 60 minutes and every hr after that for 8 hours. The final measurement was done at 24 hrs after starting the experiment. This 24 hr point measurement was taken as the final Cipro released at equilibrium. Each sample was measured in triplicates. The fitting of the data to four different kinetic models was checked using PSI Plot data analysis software.

4.3. Drug releasing behavior of [CS+CEL] and [CS+KER] composites

The excitation and emission fluorescence spectra of different forms of cipro are shown in Figure 4.2 below.

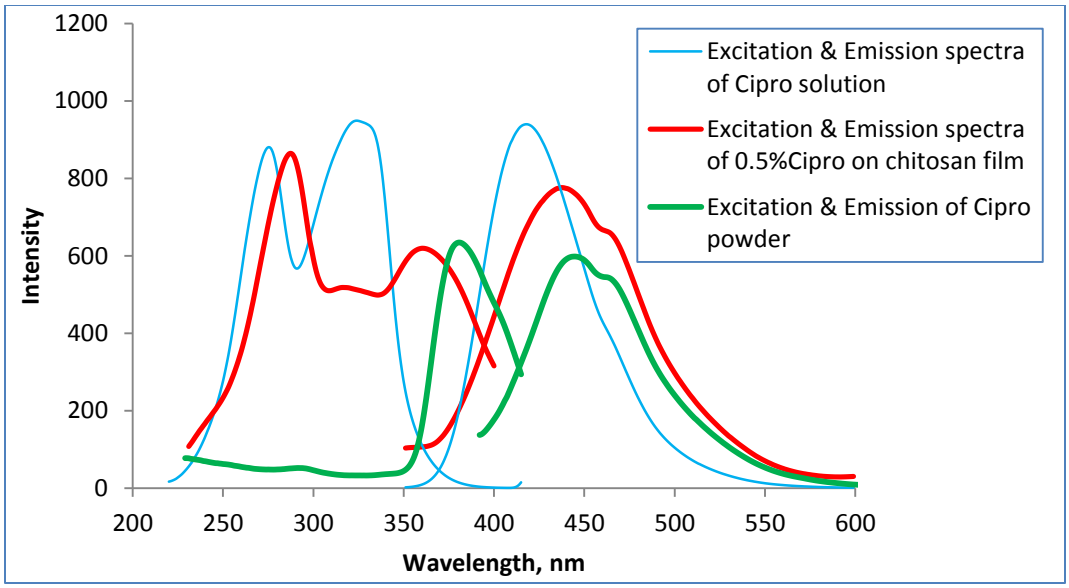

Figure 4.2: Excitation and emission fluorescence spectra of different forms of ciprofloxacin.

The spectra in light blue are for a solution of Cipro in phosphate buffer (pH 7.2) and shown in red are the spectra of a 100%CS film that has been doped with 0.5% w/w Cipro. The excitation and emission spectra of pure Cipro powder were also measured and are shown in green. Fluorescence of a Cipro-doped chitosan film was measured by holding a small piece of the film 45^{o} to the incident beam. Cipro powder was measured by pressing the powder into a pellet and also measuring at 45^{o} to the incident beam. The predominant species of Cipro present is dependent on the media, particularly the pH.[13] There are several protonated species of Cipro, depending on the pH and each of these species has a slightly different fluorescence maximum. Yang et al. reported that the emission wavelength of Cipro is blue shifted with increasing pH.[13] The presence of different predominant species of cipro in solution and solid (100%CS film and cipro powder) could be the reason why the fluorescence spectra in Figure 4.12 are blue shifted.

However, the results in Figure 4.2 clearly indicate that cipro-doped chitosan films were successfully made as indicated by the cipro emission spectrum observed on the 0.5%Cipro 100%CS film. Table 4.2 shows the fluorescence excitation and emission maxima for the different Cipro samples that were measured.

Table 4.2: Excitation and emission maximum for the different forms of cipro measured.

Sample	Excitation λ		Emission λ
Cipro solution	275nm	324nm	418nm
0.5% Cipro in 100CS film	287nm	360nm	438nm
Cipro powder		381nm	445nm

Composite materials were made by blending chitosan (CS) with either cellulose (CEL) or keratin (KER). The amount of cellulose in the blends was varied from 0% to about 100%. Similarly, the amount of keratin was varied from 0% to 87.5%. It was not possible to obtain a film out of 100% KER sample using the method as described above. The material would disintegrate during the washing step (a different regeneration solvent would have to be used instead of water). All the different blend composites were doped with Cipro at the same 0.5% w/w level. The reason making the composite films with varying CEL and KER compositions is to study if the drug releasing properties of these composites can be "tuned" by changing the composition. It is hoped that results of such a study can be used in formulating optimum drug delivery systems.

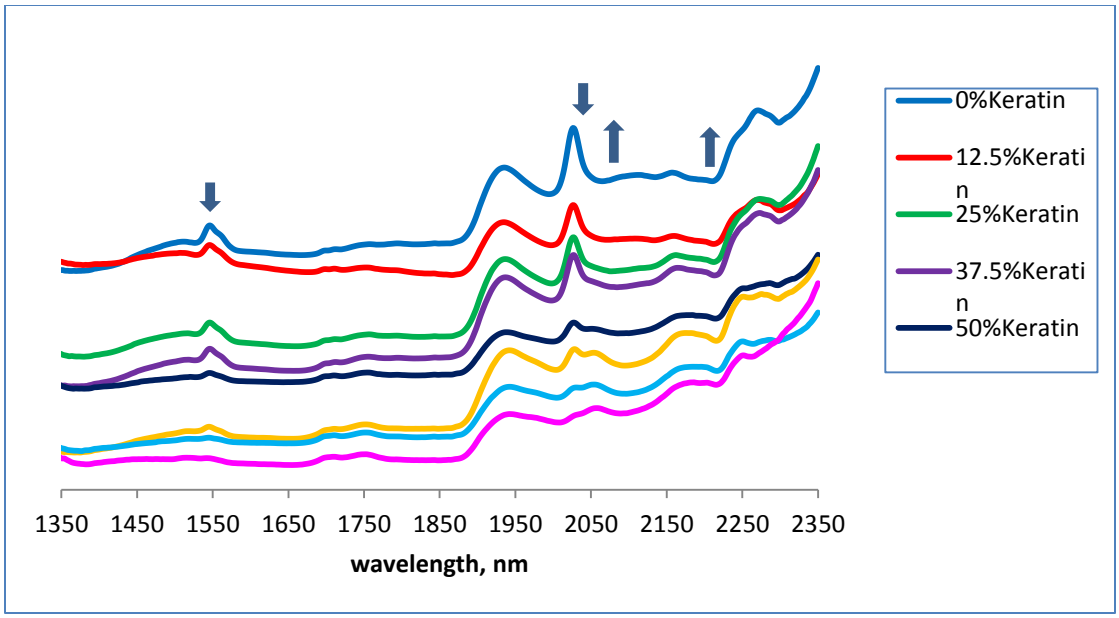

Figure 4.3A: NIR absorption spectra of different chitosan/keratin composite materials.

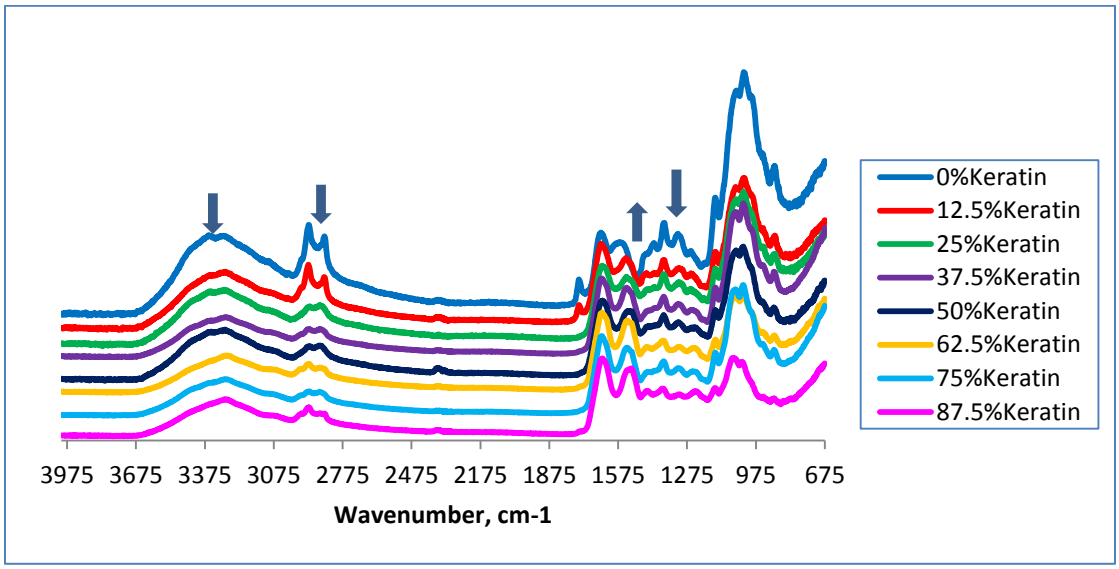

Figure 4.3B: FT-IR absorption spectra of different chitosan/keratin composite materials.

The different [CS+KER] composite materials were analyzed by both NIR and FT-IR spectroscopy. Figure 4.3A shows the changes that occur in the NIR spectra of the composite films as the keratin content is changed. The arrows in the figure indicate some of the spectral changes observed for the different compositions. Similarly, Figure 4.3B shows the spectral changes for the same samples as observed by FT-IR spectroscopy. These results confirm that different film compositions were successfully made by processing CS and KER in [$BMIm^{+}Cl^{-}$] ionic liquid.

As shown in Figure 4.2, the fluorescence emission spectrum of a 100%CS composite film containing 0.5% Cipro has an emission band around 438 nm, which could be attributed to the Cipro. Efforts were made to confirm the presence of Cipro in the composite films by FT-IR spectroscopy. Figure 4.4 shows the structure of Cipro and its FT-IR spectrum is shown in Figure 4.5A together with that of 100%CS film and 100%CS film containing 0.5% Cipro. In the FT-IR spectra of Cipro, characteristic peaks are found around 3000-2950 cm^{-1} represented alkene and aromatic C-H stretching, mainly υ = C-H.[14] The peak between 1650 and 1600 cm^{-1} can be assigned to quinolones.[14] The band from 1450 to 1400 cm^{-1} represented υ = C-O and at 1300 to 1250 cm^{-1}can be assigned to bending vibration of O-H group which proved the presence of carboxylic acid. A strong absorption peak between 1050 and 1000 $cm^{-1}$was assigned to the C-F group.[14] Since the concentration of Cipro in the composite films is relatively low (0.5%), not all these cipro FT-IR absorption bands were observed in the FT-IR spectrum of a Cipro containing composite (Figure 4.5A). However, a closer view of the 1220 cm^{-1} to 1800 cm^{-1} region (Figure 4.5B) shows that there are some clear differences between the FT-IR spectra of a Cipro-doped CS film and a CS film without Cipro. Some subtle peaks appear in the FT-

IR spectrum of the Cipro-doped CS film around 1634 cm^{-1}, 1459 cm^{-1}, 1309 cm^{-1} and 1303 cm^{-1}. As described above, these indicator bands can be assigned to the functional groups in Cipro and their presence in the Cipro-doped CS film can be taken as confirmation for the presence of Cipro in the composite materials.

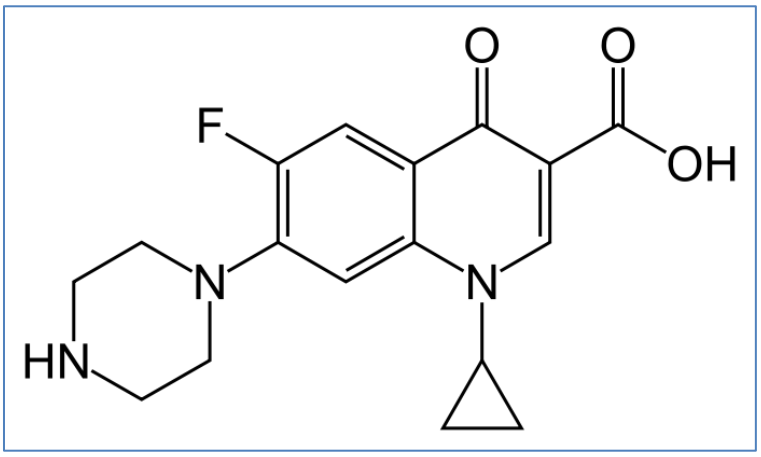

Figure 4.4: Structure of Cipro.

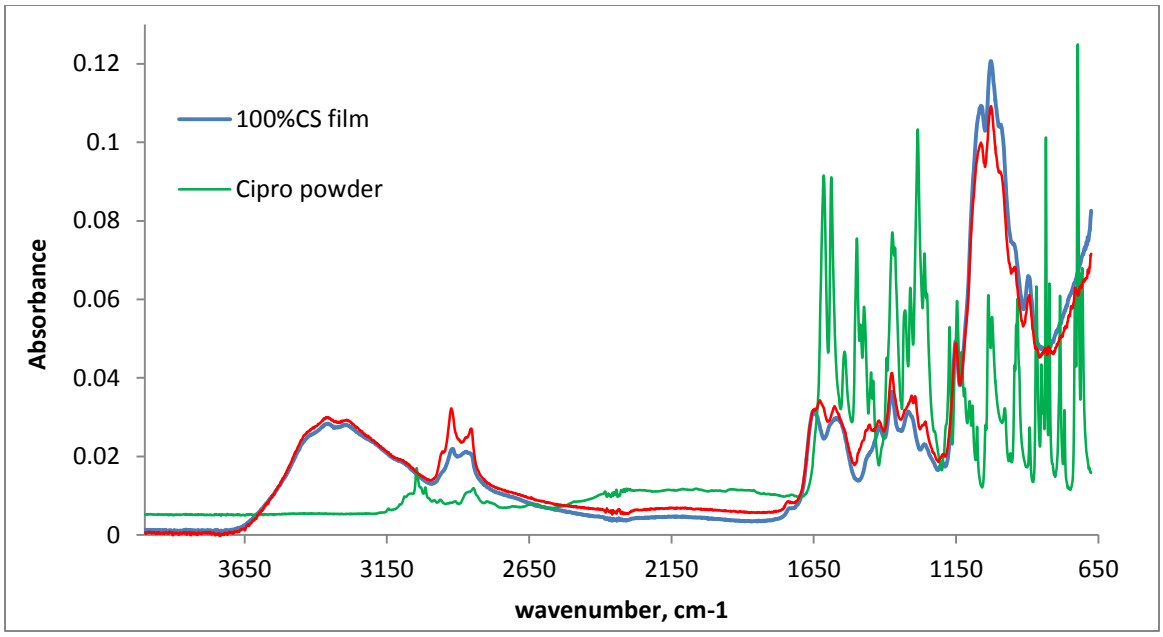

Figure 4.5A: FT-IR spectra showing the successful incorporation of Cipro into a 100%CS film

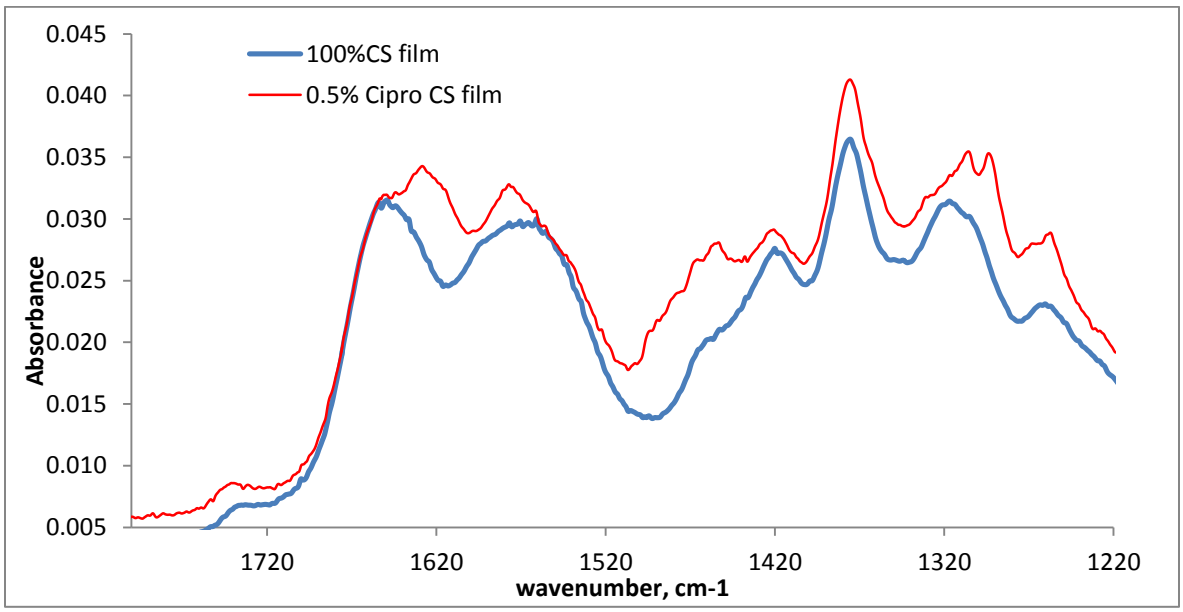

Figure 4.5B: FT-IR spectra showing the successful incorporation of Cipro into a 100%CS film

Having successfully made different film composites as confirmed by NIR and FT-IR spectroscopy and successfully doping these different films with 0.5% Cipro as confirmed by fluorescence emission and FT-IR spectroscopy, the release kinetics of the films were measured by following the amount of Cipro released into aqueous solution buffered at the physiological pH of 7.2 (phosphate buffer) as a function of time. The release profiles obtained for some of the [CS+CEL] composite films and some [CS+KER] composite films plotted for the first 4 hours are shown in Figure 4.36A and Figure 4.6B respectively. As illustrated in these two figures, most of the film composites show release saturation after about 2 hours. The results shown in Figure 4.6A suggest that there seem to be very little differences in the release profiles for the different [CS+CEL] composite films shown here. In contrast, the results in Figure 4.36B indicate a significant difference in the release profiles of the different [CS+KER] film compositions, particularly between the pure chitosan film (100%CS) and the other three composite films. It can be seen from Figure 4.36B that the release of Cipro from a 100%CS film seems to be rapid, reaching above 80% in the first 30 minutes. The release from the [CS+KER] composite films however, seem to be slower, reaching 80% after about 2 hrs. These results indicate that indeed the drug releasing properties of the [CS+KER] composite films can be tuned by varying the amount of KER in the composite films. Such information can be very useful in optimizing the development of effective drug carrier systems.

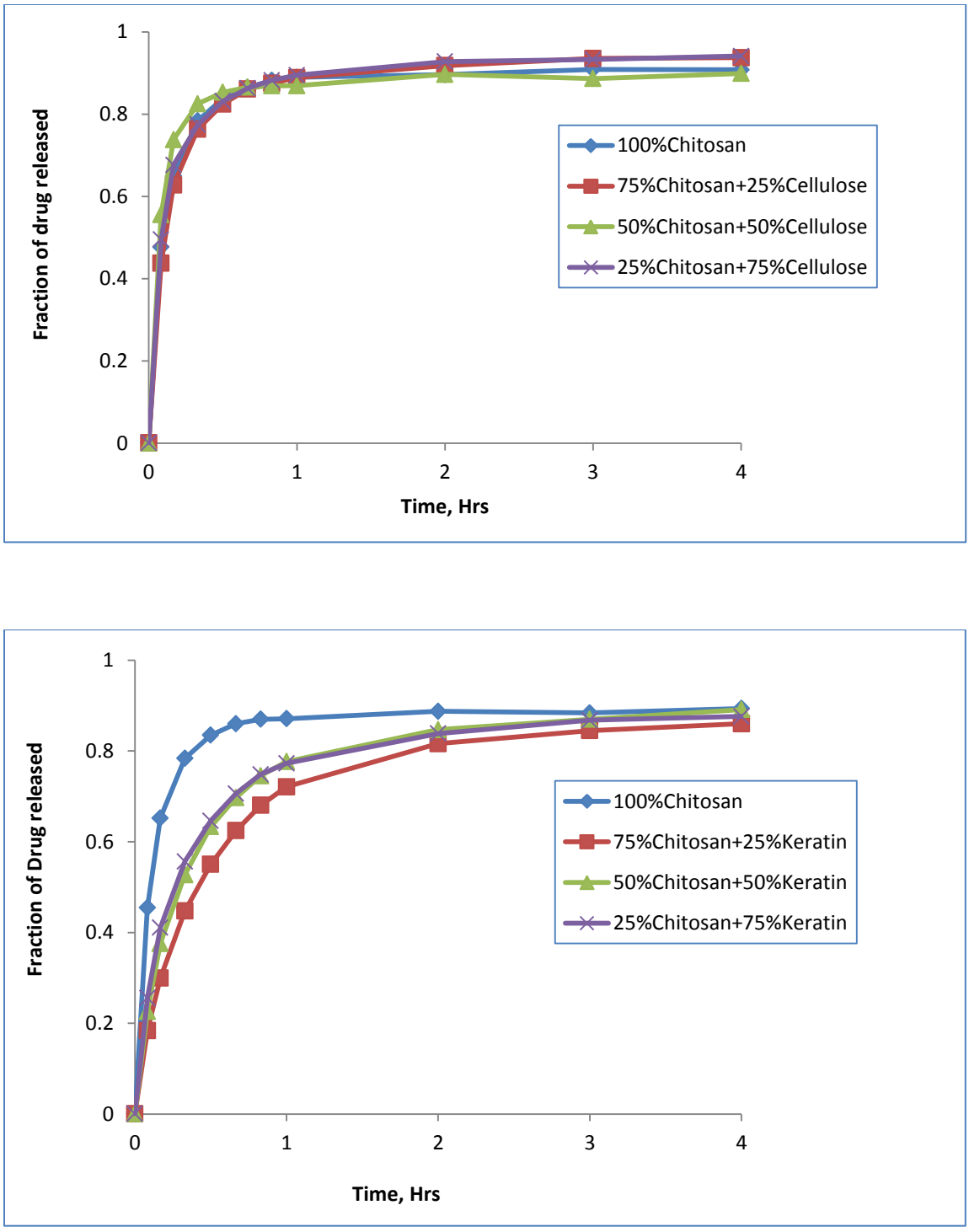

Figure 4.6: Cipro release profiles for different [CS+CEL] (top) [CS+KER] (bottom) composite films.

In order to get more information and understanding on the release mechanism of the composite films, the amount of Cipro released from these different film compositions was measured and the data for each film composition was fitted to 4 different kinetic models. The kinetic models used in this study are:

1) Zero order model
2) First order model
3) Higuchi model
4) Korsmeyer-Peppas (Power Law) model.

The results obtained after fitting the release data for the initial 1 hr period to these models are shown in Tables 4.3A – 4.3D. The data was fitted for the initial 1 hr release period because according to the derivation of the power law model, Fickian diffusional release from a thin film is characterized by an initial $t^{1/2}$ time dependence of the drug released. This short-time approximation is valid for the first 60% of the total released drug (i.e., $M_t/M_\infty \leq 0.6$).[8–10] Comparison of the fitting of the experimental data to the theoretical models is shown in Figure 4.7A (1^{st} order) and 4.7B (power law) for the [CS+KER] composites. The good fit of the data to the power law model is clearly illustrated in Figure 4.7B The release rate constant, k, is shown together with the correlation coefficient, r^2, and the Model Selection Criteria (M.S.C) for the first three models, while the release exponent, n, is also shown for the Kosrmeyer-Peppas (Power Law) model. Based on the correlation coefficient of fitting, r^2, and the M.S.C, the results in Tables 4.3A – 4.3D indicate that the Cipro release profiles of [CS+CEL] and [CS+KER] composite films are best described by the Korsmeyer-Peppas (power law) model (model has the highest r^2 and M.S.C values. The M.S.C takes into account the

number of parameters in each model and allows a better comparison of models with different parameters. The 1st order model also showed good correlation, even though it wasn't as good as the power law model. The zero order model had the least r^2 and M.S.C fitting values, indicating that the release of cipro from these composites does not follow the zero order model. One characteristic of zero order release kinetics is that the amount of drug released throughout the test period should be constant. However, the results in Figure 4.6A and 4.6B, show that the amount of cipro released from the films is actually decreasing with time, which explains why the release observed here does not fit the zero order model. Further analysis of the data was performed only for the first order and Korsmeyer-Peppas models, which showed better fitting to the data.

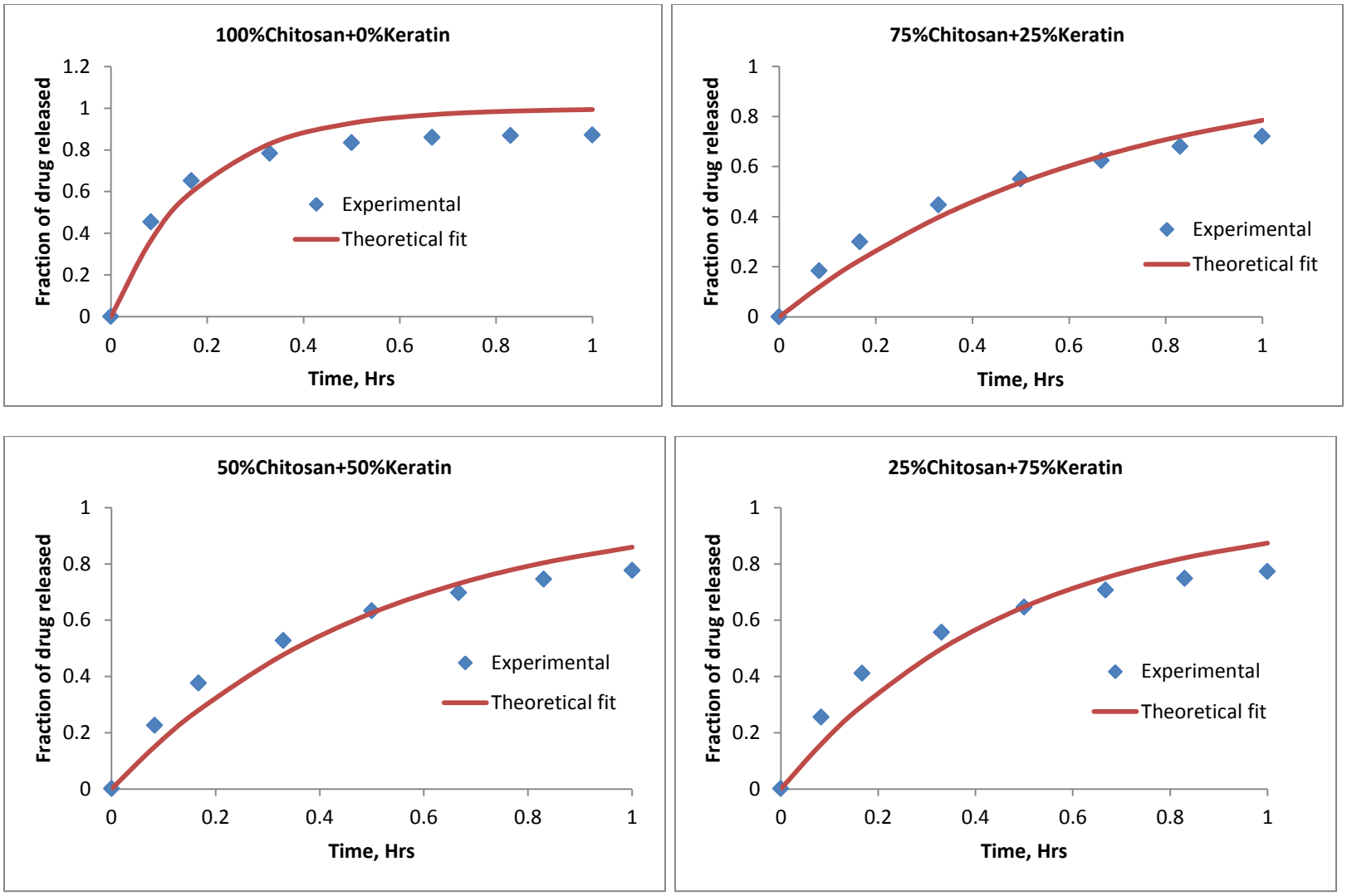

Figure 4.7A: Experimental vs. theoretical fit for the first order model

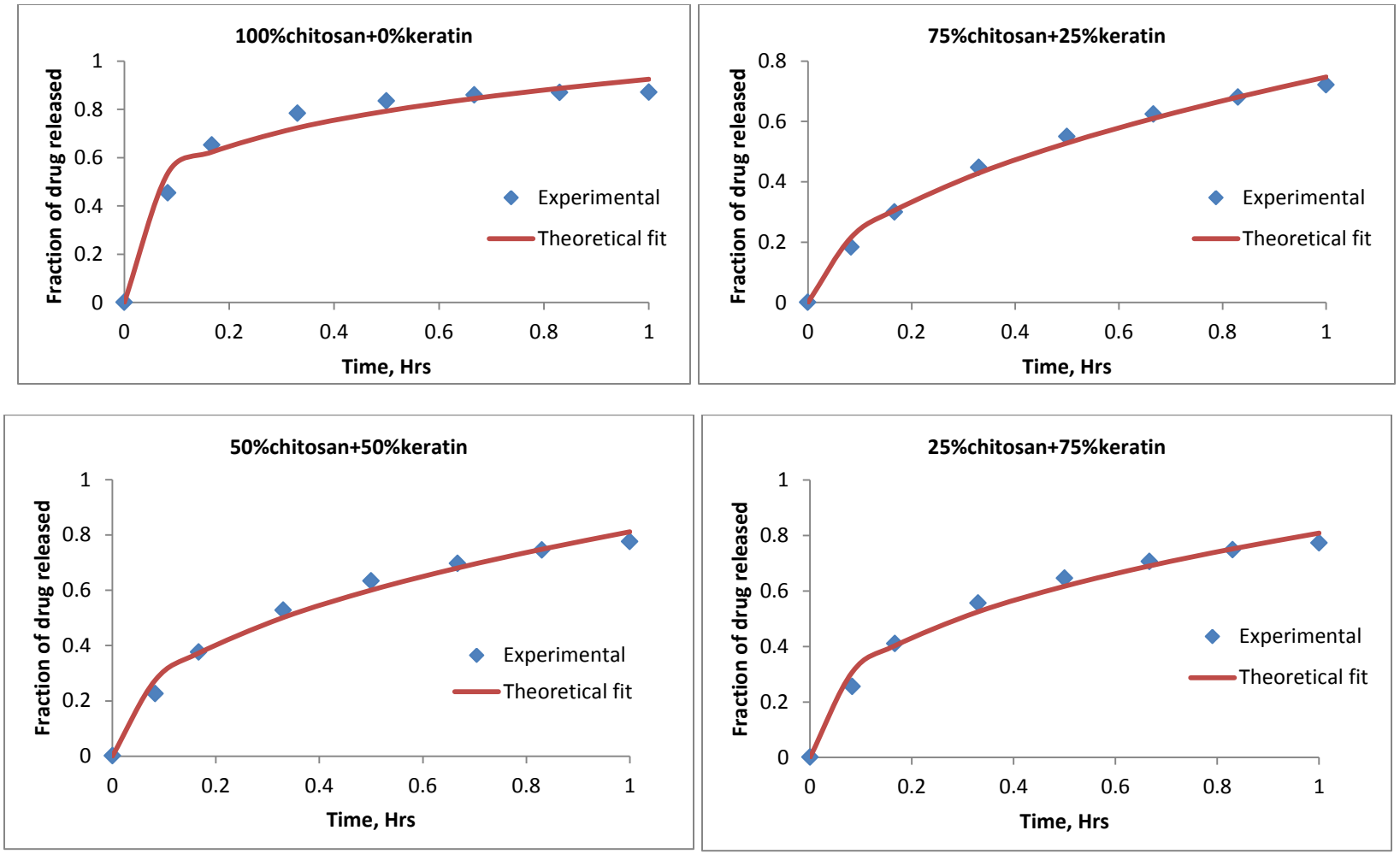

Figure 4.7B: Experimental vs. theoretical plots for the power law model

Table 4.3A: Cipro release parameters for the zero order model

Zero Order Model						
% CS	**[CS+CEL]**			**[CS+KER]**		
100.0	**k**	**R^2**	**MSC**	**k**	**R^2**	**MSC**
87.5	1.20	0.6864	-0.64	1.21	0.7271	-0.50
75.0	1.18	0.8088	-0.14	0.87	0.9505	1.27
62.5	1.22	0.7722	-0.33	1.05	0.8742	0.28
50.0	1.20	0.7055	-0.57	0.96	0.9260	0.87
37.5	1.21	0.7911	-0.22	1.09	0.8611	0.15
25.0	1.20	0.7768	-0.29	0.97	0.9065	0.62
12.5	1.24	0.7491	-0.42	0.91	0.9275	0.87
0.0	1.00	0.8114	-0.14			

Table 4.3B: Cipro release parameters for the first order model

First Order Model						
	[CS+CEL]			[CS+KER]		
% CS	**k**	**R^2**	**MSC**	**k**	**R^2**	**MSC**
100.0	5.48	0.9832	2.12	5.52	0.9825	2.12
87.5	8.46	0.9808	1.68	7.44	0.9841	1.99
75.0	4.96	0.9833	2.29	1.54	0.9909	3.00
62.5	6.54	0.9856	2.23	2.69	0.9757	2.00
50.0	7.69	0.9820	1.81	1.97	0.9871	2.66
37.5	6.02	0.9856	2.33	3.13	0.9749	1.95
25.0	6.22	0.9819	2.12	2.10	0.9799	2.24
12.5	7.40	0.9883	2.38	1.73	0.9834	2.40
0.0	2.62	0.9361	1.04			

Table 4.3C: Cipro release parameters for the higuchi model

Higuchi Model						
	[CS+CEL]			[CS+KER]		
% Chitosan	**k**	**R^2**	**MSC**	**k**	**R^2**	**MSC**
100.0	1.07	0.9280	1.23	1.06	0.9181	1.22
87.5	1.10	0.8584	0.54	1.10	0.8873	0.77
75.0	1.06	0.9396	1.45	0.75	0.9969	4.82
62.5	1.10	0.9162	1.11	0.93	0.9739	2.34
50.0	1.09	0.8726	0.67	0.84	0.9921	3.79
37.5	1.08	0.9273	1.32	0.97	0.9682	2.08
25.0	1.08	0.9180	1.19	0.85	0.9859	3.18
12.5	1.12	0.9019	0.93	0.79	0.9928	3.87
0.0	0.89	0.9410	1.46			

Table 4.3D: Cipro release parameters for the power law model

Power Law								
	[CS+CEL]				[CS+KER]			
% CS	**k**	**n**	**R^2**	**MSC**	**k**	**n**	**R^2**	**MSC**
100.0	0.93	0.22	0.9917	3.62	0.92	0.22	0.9872	3.20
87.5	0.90	0.12	0.9926	3.66	0.93	0.16	0.9901	3.46
75.0	0.93	0.25	0.9906	3.53	0.75	0.50	0.9970	4.63
62.5	0.94	0.20	0.9935	3.86	0.86	0.33	0.9929	3.75
50.0	0.91	0.15	0.9896	3.41	0.81	0.43	0.9947	4.04
37.5	0.94	0.23	0.9931	3.85	0.88	0.30	0.9949	4.09
25.0	0.93	0.21	0.9932	3.89	0.81	0.39	0.9941	3.94
12.5	0.95	0.18	0.9911	3.54	0.76	0.43	0.9955	4.23
0.0	0.79	0.24	0.9924	3.71				

Figure 4.8 is a comparison of the 1st order release rate constants for the [CS+CEL] and [CS+KER] composite films. The rate constant is plotted as a function of CS concentration for both composites. As illustrated in Figure 4.8, while the release rate constant for [CS+CEL] composite films is not changing significantly as CS concentration is reduced, the release rate for the [CS+KER] films is clearly decreasing with CS concentration to about 50%CS. Further decrease in CS content beyond 50% does not cause result in any further decrease of the rate constant. Also shown in Figure 4.8 is the variation of the release rate constant for the power law model. As was observed for the

first order model, the release rate constant for this model also show a similar trend, where it decreases with an increase in KER content for the [CS+KER] composite films. However, the rate constant does not change for the [CS+CEL] composite films.

The variation of the release exponent (n), for the power law model, which characterizes the release mechanism for the different films is shown in Figure 4.9. According to this model, if $n \leq 0.45$ it is the Fickian mechanism, $0.5 \leq n \leq 0.8$ Non-Fickian mechanism and if $0.8 \leq n \leq 1.0$ a zero order mechanism governing the drug release from the film matrix.[4] Except for the [75%CS+25%KER] composition which had $n = 0.50$, all the other film compositions have $n \leq 0.45$, meaning drug release from these films is governed by the Fickian mechanism. The results in Figure 4.9 demonstrate that the drug release kinetics and indeed the mechanism of release can be tuned by varying the composition of the films.

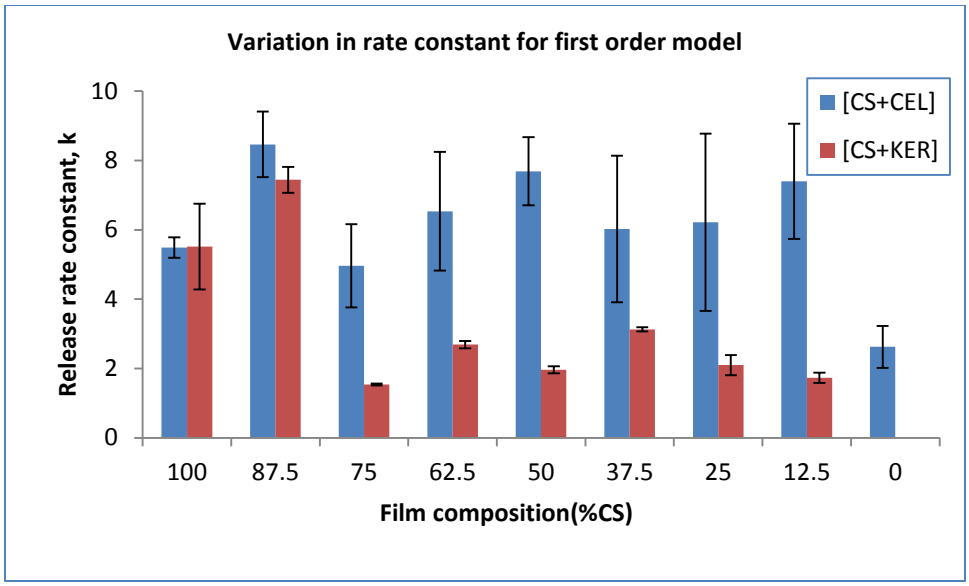

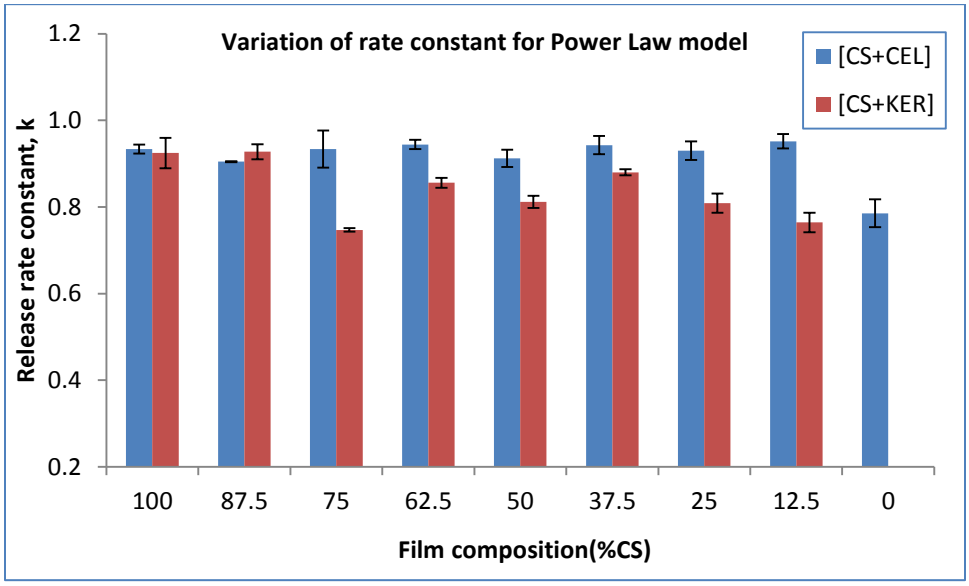

Figure 4.8: Variation of the release rate constant for the first order (top) and power law (bottom)

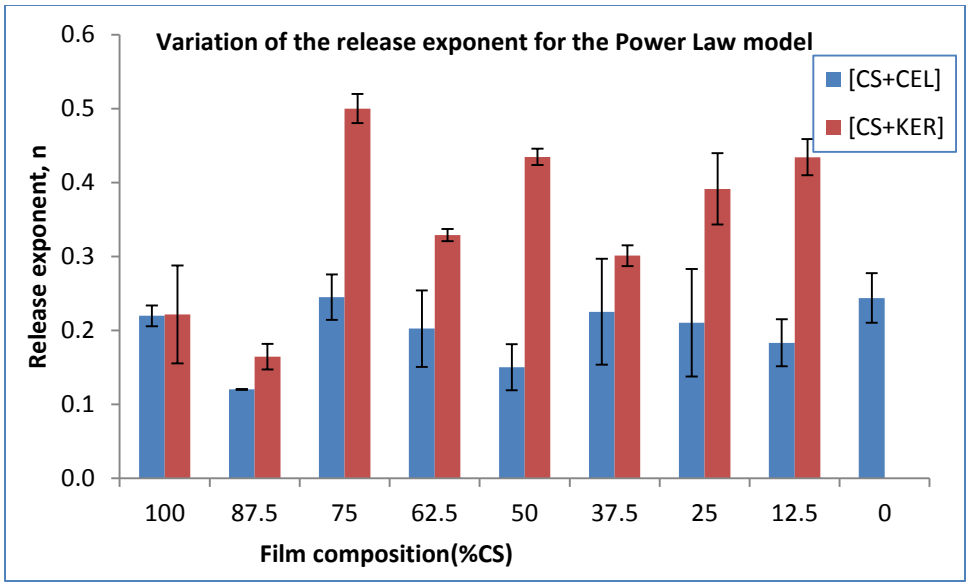

Figure 4.9: Comparison of the release exponent for the [CS+CEL] and [CS+KER] composite films

Chitosan/cellulose and chitosan/keratin composite films which can be used as controlled drug release systems, were successfully prepared by processing the biopolymers in [$BMIm^{+}Cl^{-}$] ionic liquid. The composition of the different film composites was confirmed by both NIR and FT-IR spectroscopy. The presence of the cipro drug in the films was confirmed by direct fluorimetric and FT-IR measurement of the films.

The release kinetics from different formulations of [CS+CEL] composite films indicated that a simple variation in the composition of such composite films may not be enough to give any significant change in the release kinetics. However, results from for the [CS+KER] composite films showed that the release properties of these films can be "tuned" by systematic variation of the film composition. An increase in the KER content

was found to decrease the release rate constant. This is probably because keratin has a high degree of functionality which acts as retention sites for the drug molecule.

Based on the Korsmeyer-Peppas equation, with the exception of [75%CS+25%KER] composition which had n = 0.50, all the other film compositions had $n \leq 0.45$, meaning drug release from these films is governed by the Fickian mechanism.

4.4. Chiral separations using polysaccharide composite materials

Chirality is a phenomenon of great biological and chemical importance. Under many circumstances, only one enantiomer could meet specific needs while the other one possess less or even negative effect. This justifies the need for enantiomeric separation. Most active pharmaceutical ingredients (API) are chiral in nature and the US food and drug administration (FDA) requires detailed analysis of pure active pharmaceutical ingredients (APIs).[15] As a result, chiral separation has become an increasingly important downstream process in the pharmaceutical industry. Current technologies used to produce pure enantiomers include asymmetric synthesis, high performance liquid chromatography (HPLC),[16] capillary electrophoresis (CE)[17] and preferential crystallization.[18] Membrane separation can provide a more promising solution for the production of pure enantiomers than the current technologies because it is more cost effective, amenable to continuous operation and is more easily scaled up.[15,19–21]

The [CEL+CS], [CEL+TCD] and [CS+TCD] composite materials were investigated for their ability to resolve racemic mixtures of amino acids. Preliminary results of this investigation are discussed below.

4.4.1. Materials and Methods

The polysaccharide composite materials used are those described in Chapter 2. D- and L-enantiomers (99%) of Tryptophan (Trp), Tyrosine (Tyr), Histidine (His) and Phenylalanine (Phe) were obtained from Alfa Aesar. Experiments with racemic mixtures were done on a Shimadzu LC-20AT prominence Liquid Chromatograph equipped with a SPD-20A prominence UV/Vis detector. Separation was done using an Astec Chirobiotic TAG column. The mobile phase for Trp, Tyr and Phe was 60:40 methanol/water with 1.0mL/min flow rate while His was separated using 30:70 ethanol/water in 160mM sodium phosphate buffer adjusted to pH 4.5. Flow rate for His was also 1.0mL/min. Trp and Tyr were detected at 275nm while His and Phe were detected at 205nm. Any experiments with optically active (pure enantiomers) samples were carried out on a Perkin Elmer Lambda 35 UV/VIS spectrometer.

For the enantiomeric resolution experiments, about 0.3g of the dry composite material was placed in a sample vial. 30mL of $1.0x10^{-3}$M DL racemic solution of the amino acid was added (concentration of both the D and the L enantiomers in this solution was $5.0x10^{-4}$M). The vials were tightly closed and agitated on a mechanical shaker at room temperature. At specific time intervals, 20µL solutions were withdrawn and injected into the HPLC for analysis.

4.4.2. Enantiomeric resolution of amino acids using polysaccharide composite materials

Typical HPLC chromatograms for the analysis of racemic mixtures of different amino acids by 6 different composites are shown in Figure 4.10A (Trp), 4.10B (Tyr) and 4.10C (His). As expected, the HPLC chromatograms contain two bands, with the band for the L enantiomer indicated by an arrow. It can be seen from the results in Figure 4.10 that the intensity of the two HPLC bands was found to decrease with time. However, as indicated by the arrow in Figure 4.10, the intensity of the L enantiomer decreases faster than that of the D enantiomer. For some composites, especially the 100%CS composite, the HPLC band for the L enantiomer decreases and disappears completely while the HPLC band for the D enantiomer had only changed slightly. These results clearly indicate that when the composite materials were kept in racemic solutions of the amino acids, the enantiomeric composition of the solutions was changing, with the concentration of the L enantiomer getting less and less with time. This seems to suggest that the composite materials are selectively favoring the adsorption of the L enantiomer to the D enantiomer.

From these HPLC results, the amount of each enantiomer that has been adsorbed onto the composite material can be calculated using the following mass balance equation:

$$q_t = \left(\frac{C_i - C_t}{m}\right) V$$

where q_t (mg/g) is the amount adsorbed at any given time, t, C_i and C_t (mg/L) are the initial and prevailing solution concentration at time, t, respectively. V (L) is the volume of the solution and m (g) is the weight of the composite film material. Typical results for the adsorption of D and L His form a racemic mixture by a 100%CS composite material are shown in Figure 4.11. Figure 4.11A is a depiction of the change in solution concentration with time calculated from the HPLC results and Figure 4.11B shows the amount of each enantiomer that has been adsorbed at different time intervals. As illustrated, the solution concentration of L His was found to decrease much faster than that of the D enantiomer. This translates to higher adsorbed L amount as shown in Figure 4.11B. The results suggest that for this 100%CS composite material, the racemic solution is resolved into a solution of D His after about 120 hrs.

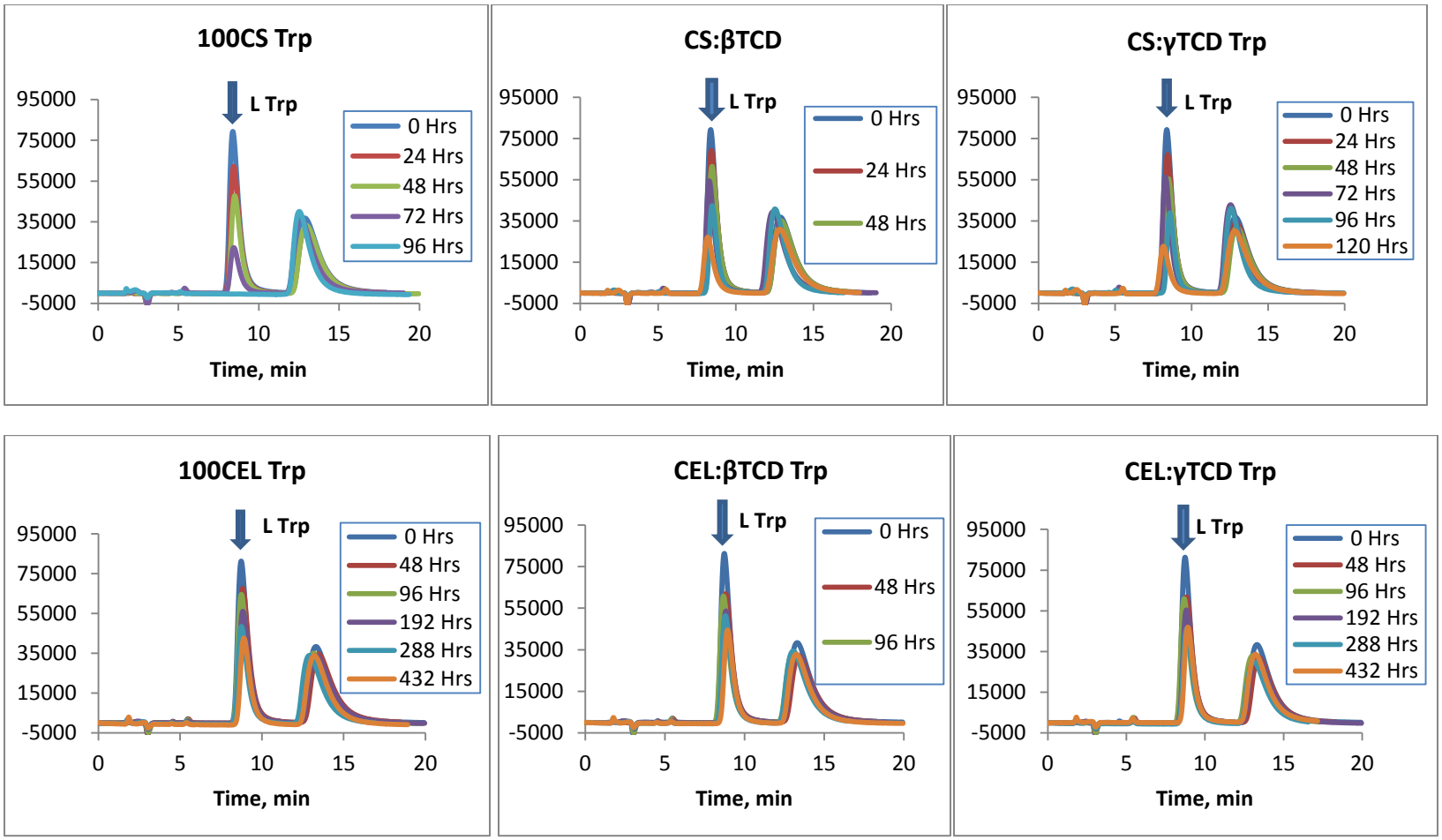

Figure 4.10A: HPLC chromatograms for the sorption of D and L Trp on to 6 different composites.

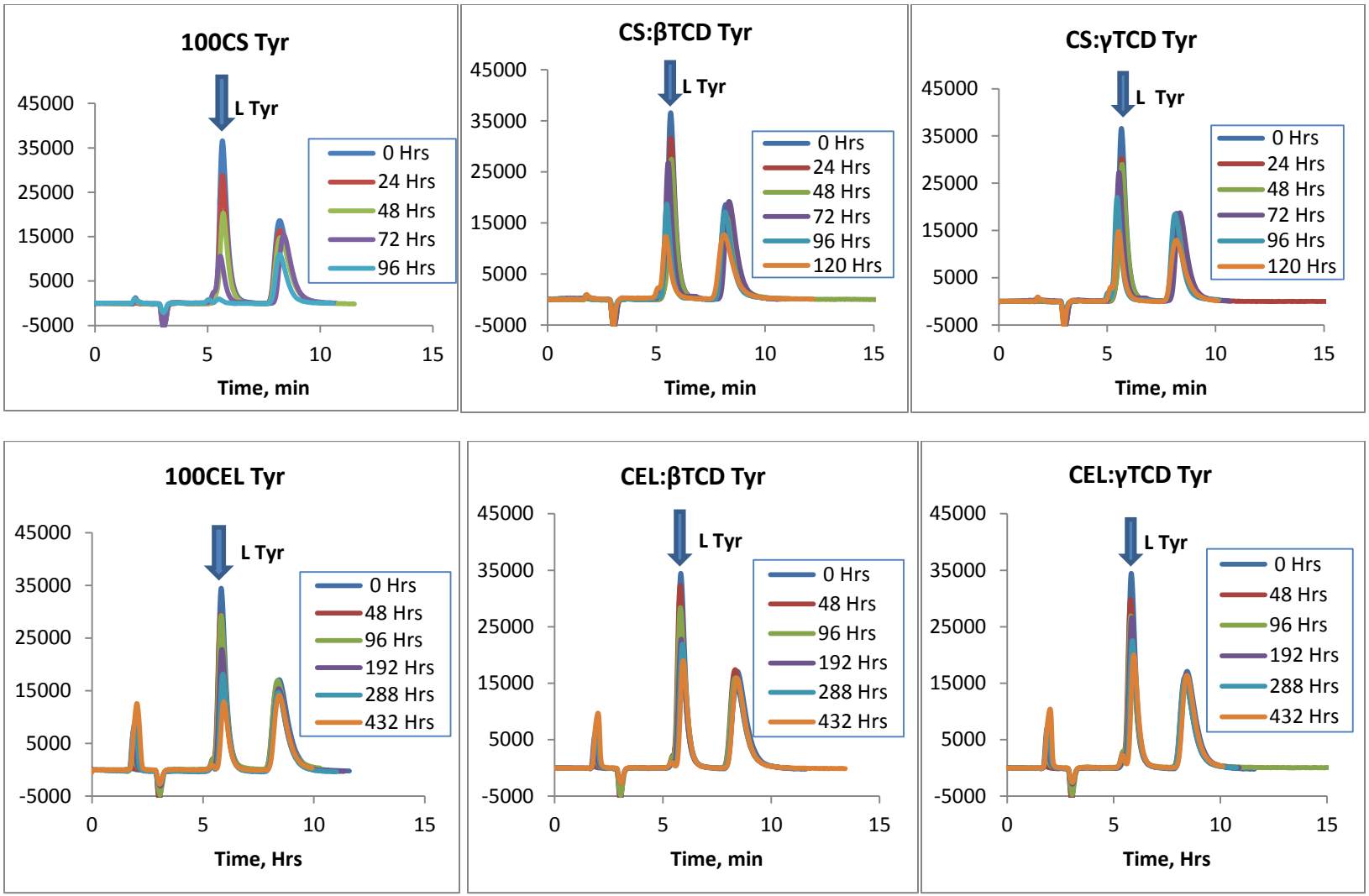

Figure 4.10B: HPLC chromatograms for the sorption of D and L Tyr on to 6 different composites.

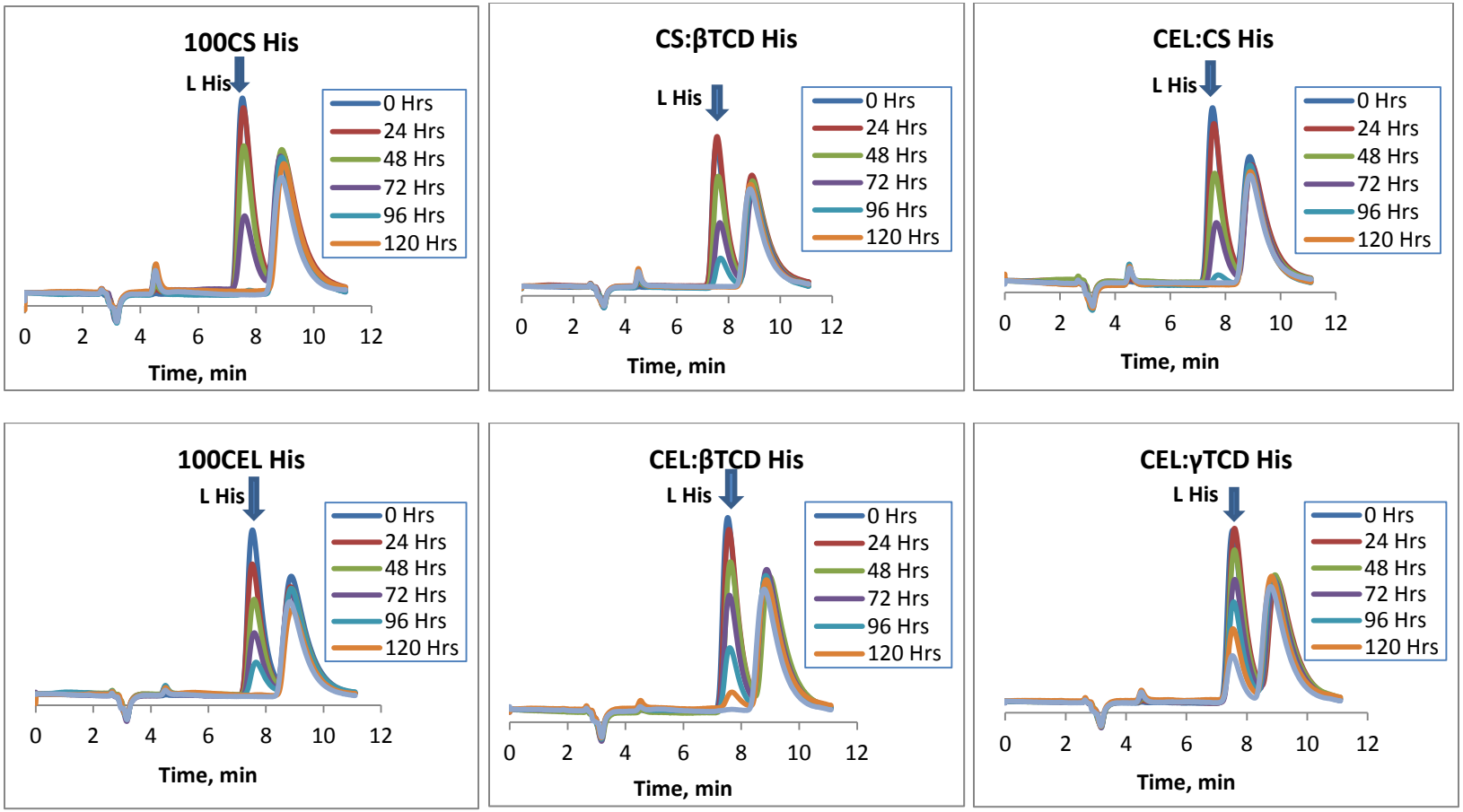

Figure 4.10C: HPLC chromatograms for the sorption of D and L His on to 6 different composites.

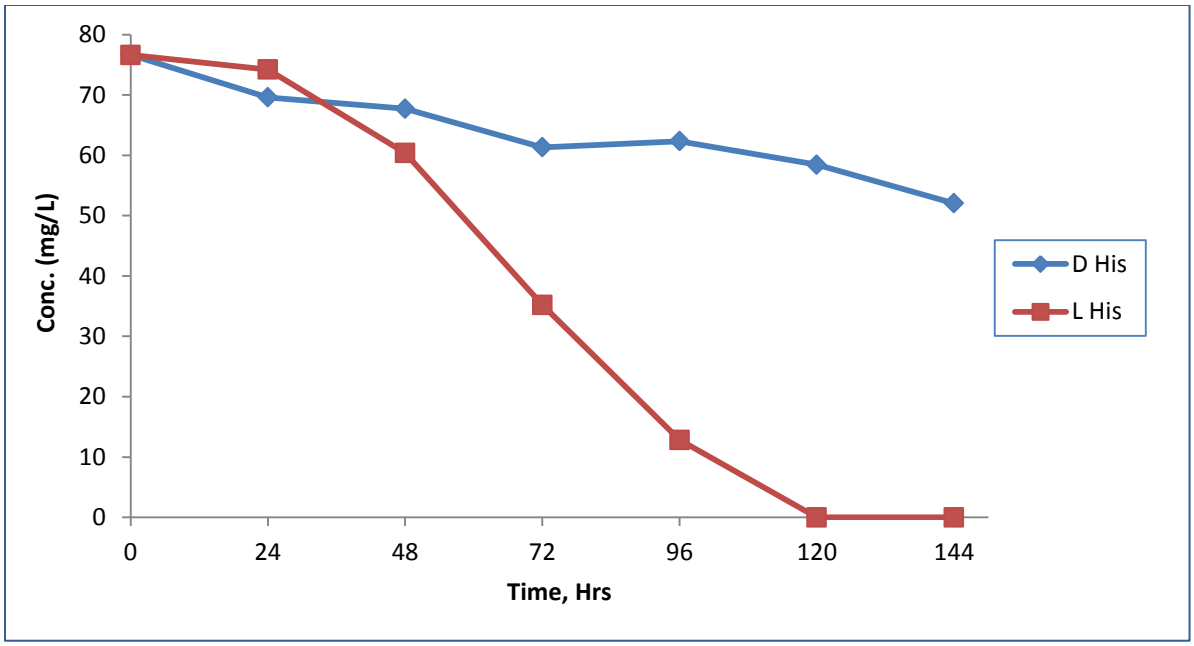

Figure 4.11A: Change in solution concentration with time for a His racemic solution with a 100%CS composite material

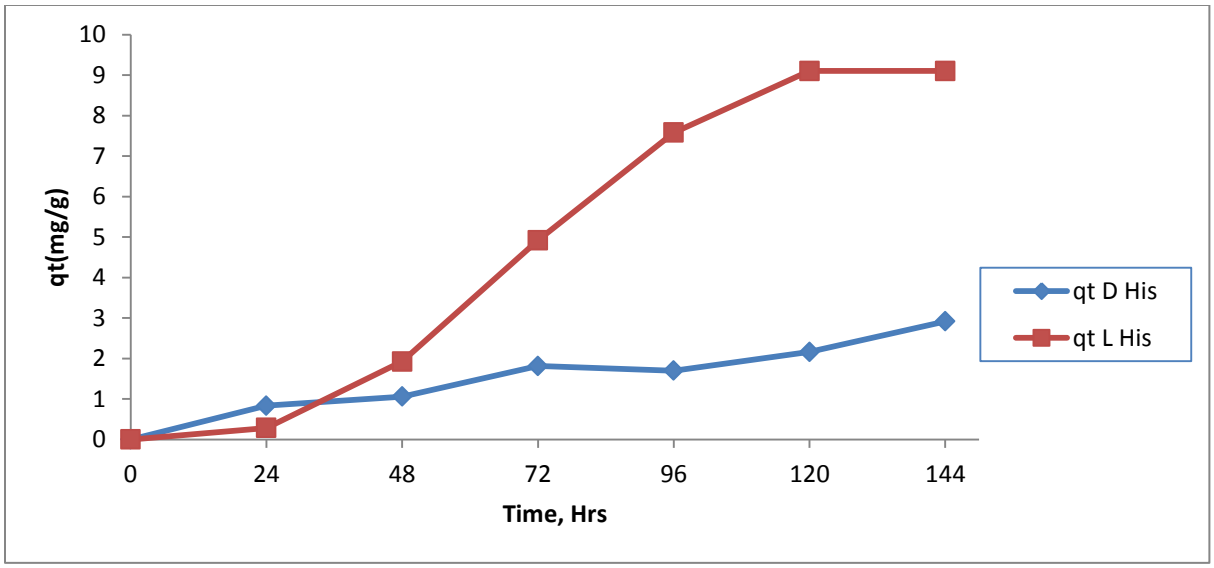

Figure 4.11B: Typical adsorption profiles for the adsorption of D and L His from a racemic mixture by a 100%CS composite material calculated using results in Figure 4.11A and equation 4.1

An attempt was made to describe the observed results in terms of kinetic resolution of the two enantiomers. This was done by fitting the results (qt vs. t) to the pseudo 1st order and pseudo 2nd order models, similar to what was described for the adsorption of pollutants. However, as shown in Table 4.4A (for Trp) and 4.4B (for Tyr), the data does not appear to follow either the pseudo 1st order or the pseudo 2nd order models. The correlation coefficients for these two models are not very good and some of the errors of fitting observed on the rate constant (k) were too high to be used for comparison purposes.

To gain more insight into the adsorption of the D and L enantiomers by the composite materials, the adsorption of optically active (pure enantiomers) D and L enantiomers was measured. The experimental set and conditions (mass of film and

volume of solution) was the same as that of the racemic mixture. The concentration of the optically active solutions used for this experiment was $5x10^{-4}$M. This concentration is the same as that of the individual enantiomers used for the racemic experiment described above. Also, since these were solutions of pure enantiomers, the residual concentration in solution at specific time intervals was determined by UV absorption measurements. After each measurement, the solution was returned to the sample vial to minimize volume changes during the course of the experiment.

The results obtained from one such experiment, for the adsorption of Tyr and His enantiomers by a 100%CS composite material are plotted together with the HPLC results for the racemic experiment in Figure 4.12A (for Tyr) and 4.12B (for His). The concentration of each enantiomer at the beginning of the experiment is indicated in square brackets in the figure. It can be observed from these two figures that the adsorption profiles for the racemic mixture and the optically active samples are not the same. For Tyr, the adsorption from the racemic mixture is higher than the adsorption of the corresponding enantiomer in the optically active sample.

Table 4.4A: First and second order rate constants for Trp on different samples.

		1st order			2nd order		
Sample	**Enantiomer**	**K (Hr^{-1})**	**Error**	**r^2**	**K (g/mg Hr)**	**Error**	**r^2**
100CS	D Trp	0.0006	0.0027	0.0116	0.4247	5.0150	0.1016
	L Trp	0.0181	0.0036	0.8935	0.0000	0.0001	0.0610
CS:βTCD	D Trp	0.0042	0.0033	0.2871	0.3561	1.9850	0.6157
	L Trp	0.0135	0.0017	0.9386	0.0000	0.0000	0.0520
CS:γTCD	D Trp	0.0043	0.0278	0.0060	0.0023	0.0929	0.0006
	L Trp	0.0121	0.0018	0.9173	0.0004	0.0004	0.3705
CEL:CS	D Trp	0.0052	0.0021	0.2714	0.0150	0.0120	0.7327
	L Trp	0.0094	0.0006	0.9860	0.0000	0.0000	0.0721
100CEL	D Trp	0.0042	0.0028	0.3553	0.0056	0.0035	0.6991
	L Trp	0.0059	0.0004	0.9665	0.0001	0.0001	0.5382
CEL:βTCD	D Trp	0.0037	0.0074	0.0588	0.0135	0.0109	0.8884
	L Trp	0.0065	0.0009	0.8814	0.0027	0.0008	0.9365
CEL:γTCD	D Trp	0.0005	0.0027	0.0067	0.0048	0.0043	0.6256
	L Trp	0.0042	0.0016	0.5742	0.0019	0.0007	0.8662

Table 4.4.B: First and second order rate constants for Tyr on different samples.

		1st order			2nd order		
Sample	**Enantiomer**	**K (Hr^{-1})**	**Error**	**r^2**	**K (g/mg Hr)**	**Error**	**r^2**
100CS	D Tyr	0.0088	0.0015	0.8791	0.0002	0.0003	0.1751
	L Tyr	0.0217	0.0035	0.9267	0.0001	0.0001	0.5903
CS:βTCD	D Tyr	0.0054	0.0041	0.3667	1.1364	17.3072	0.9130
	L Tyr	0.0093	0.0009	0.9706	0.0026	0.0018	0.7311
CS:γTCD	D Tyr	0.0068	0.0036	0.5496	0.0053	0.0043	0.5625
	L Tyr	0.0084	0.0008	0.9732	0.0001	0.0001	0.1544
CEL:CS	D Tyr	0.0043	0.0005	0.9095	0.0001	0.0001	0.2520
	L Tyr	0.0103	0.0008	0.9779	0.0006	0.0001	0.9501
100CEL	D Tyr	0.0026	0.0008	0.6479	0.0014	0.0009	0.4883
	L Tyr	0.0045	0.0004	0.9432	0.0001	0.0001	0.2819
CEL:βTCD	D Tyr	0.0031	0.0012	0.5432	0.0024	0.0014	0.5926
	L Tyr	0.0050	0.0003	0.9681	0.0002	0.0001	0.4701
CEL:γTCD	D Tyr	0.0022	0.0009	0.4589	0.0037	0.0045	0.3104
	L Tyr	0.0042	0.0004	0.9294	0.0003	0.0001	0.5693

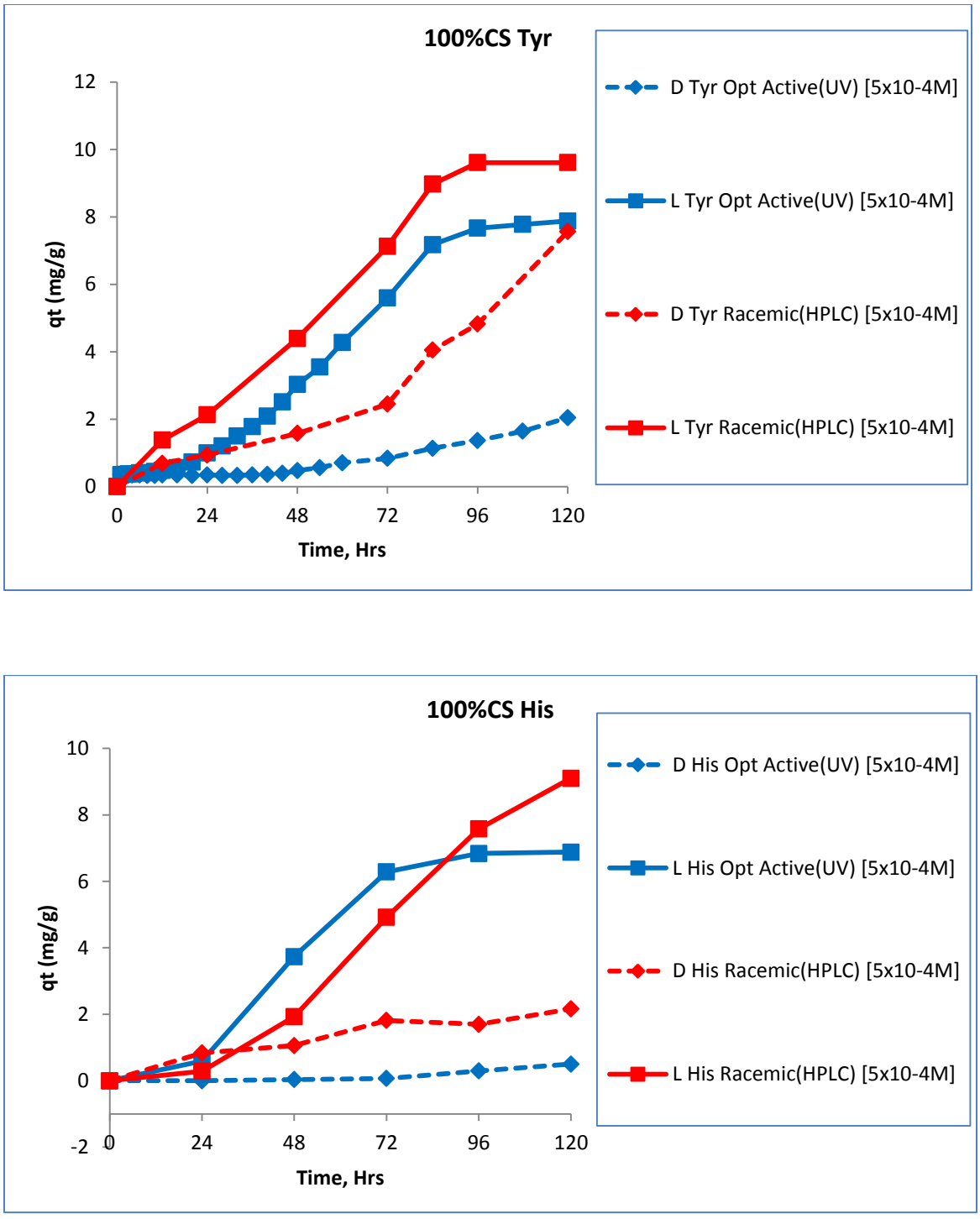

Figure 4.12: Sorption profiles of Tyr (top) and His (bottom) enantiomers by 100%CS composite material from optically active (Blue) and racemic (red) solutions.

Adsorption of His enantiomers follows a similar trend, except for the adsorption of L His from the racemic mixture which only becomes higher than the corresponding enantiomer from optically active sample after about 96 hrs. The reasons for this behavior are not yet clear at the moment but the higher total concentration ($1x10^{-3}$M) prevailing in the racemic mixture could be one of the sources of this difference. Competition between the D and L enantiomers for available adsorption sites in the racemic mixture could also potentially result in different adsorption kinetics and mechanism.

Further experiments were carried out in an effort to understand the mechanism of adsorption taking place in these solutions. Specifically, a solution containing twice as much L enantiomer as D enantiomer (i.e. $6.67x10^{-3}$M L and $3.33x10^{-3}$M D) was measured and analyzed by HPLC (green plots). The total concentration of this solution was kept the same as that used for the racemic solution, i.e., $1x10^{-3}$M. Also measured (by UV) was a solution of $1x10^{-3}$M pure L enantiomer (pink plots). Finally, measurements were also done with $1x10^{-3}$M DL racemic solution (purple plots). This last measurement was done by UV and is assumed to give the total amount of D and L adsorbed. The results are shown in Figure 3.13A (for Tyr) and Figure 3.13B (for His). The results for the adsorption of Tyr by 100%CS composite material (Figure 4.13A) showed some interesting features where $1x10^{-3}$M pure L (pink plot) had the highest adsorption profile. Interestingly, the adsorption profile of $1x10^{-3}$M DL racemic solution (purple plot) was just about half of what was observed for the $1x10^{-3}$M pure L solution. Since the total concentration of these two solutions are the same, the result seem to suggest that in the racemic mixture, the adsorption seem to exclusively favor the L enantiomer, hence half the adsorbed amount, than the D enantiomer. These results are in agreement with what

was observed with the HPLC chromatograms where the intensity of the HPLC band for the L enantiomer was observed to decrease much faster than that of the D enantiomer. However, the results for the adsorption of His enantiomers by the same composite material does not show a similar trend to that described for Tyr. For this amino acid, even though the sorption profile of $1x10^{-3}$M DL racemic is still about half that of $1x10^{-3}$M pure L enantiomer, both of these sorption profiles were unexpectedly lower. The results for the sorption of Tyr and His enantiomers by the rest of the composite materials are shown in Figure 4.14 (for Tyr) and Figure 4.15 (for His). While the adsorption of Tyr by the CS composites has a somewhat similar trend, adsorption by the CEL composites does not seem to have any kind of trend.

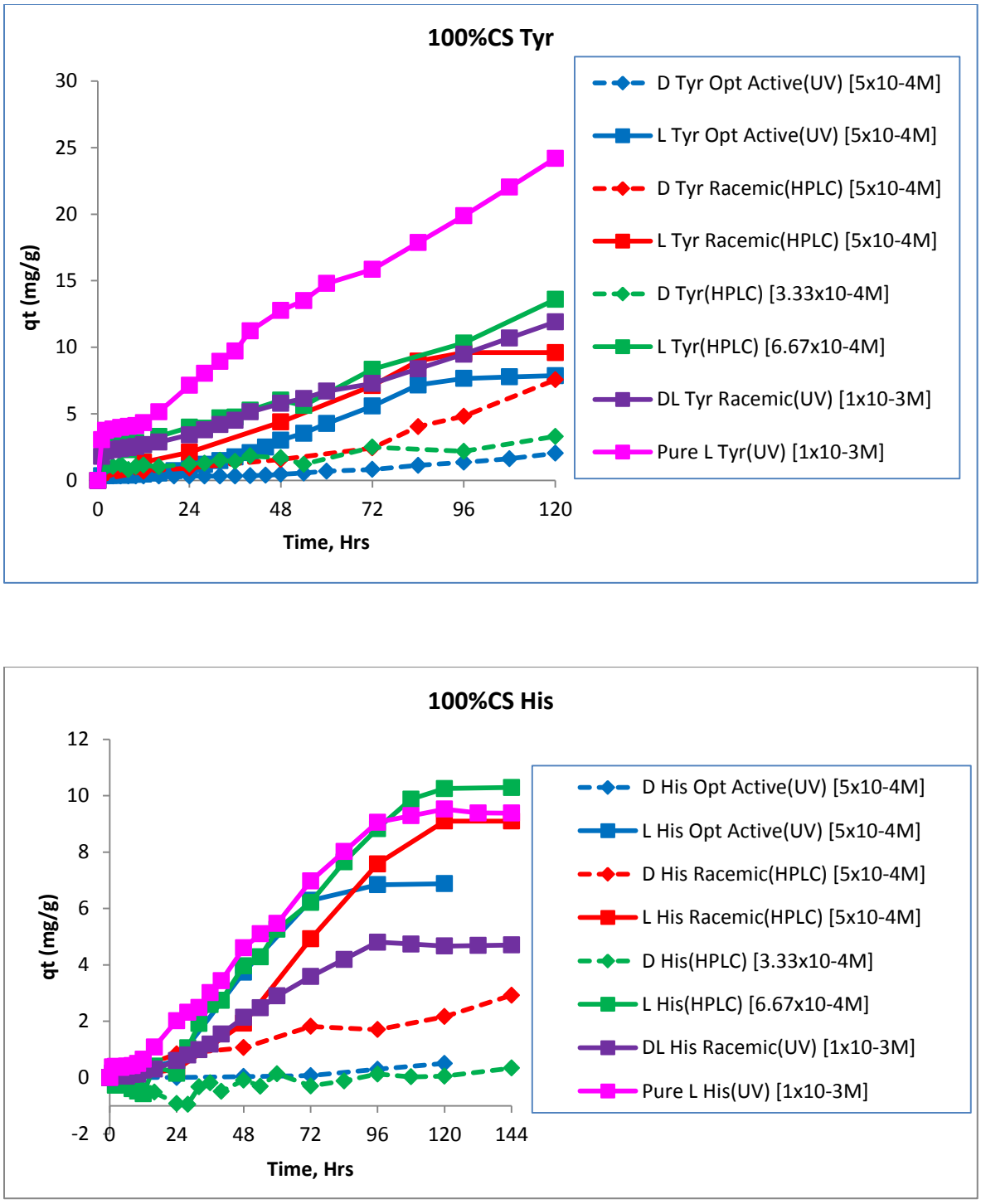

Figure 4.13: Sorption profiles of Tyr (top) and His (bottom) enantiomers by 100%CS composite material from different solutions.

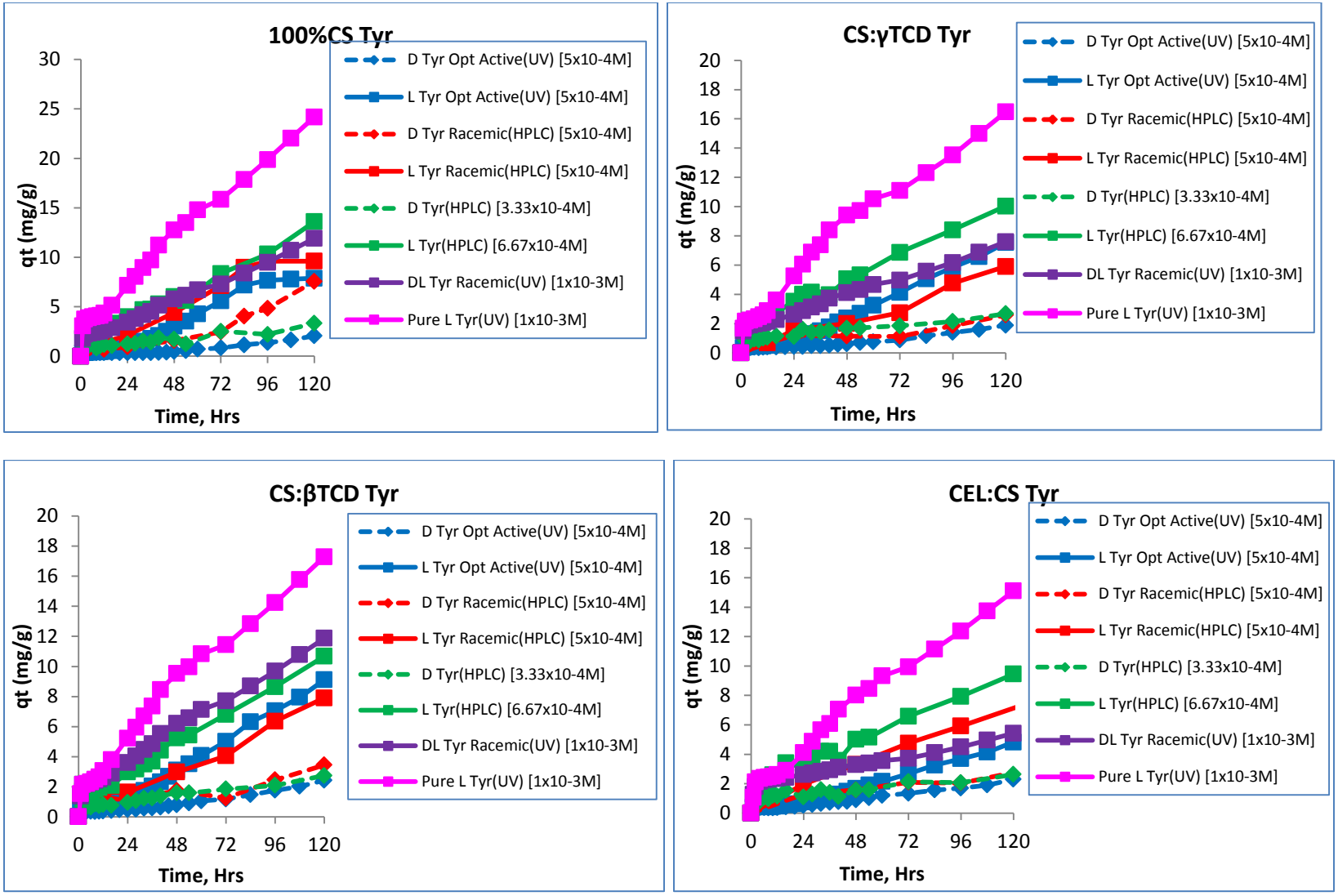

Figure 4.14: Sorption profiles of different solutions of Tyr enantiomers by different composite materials

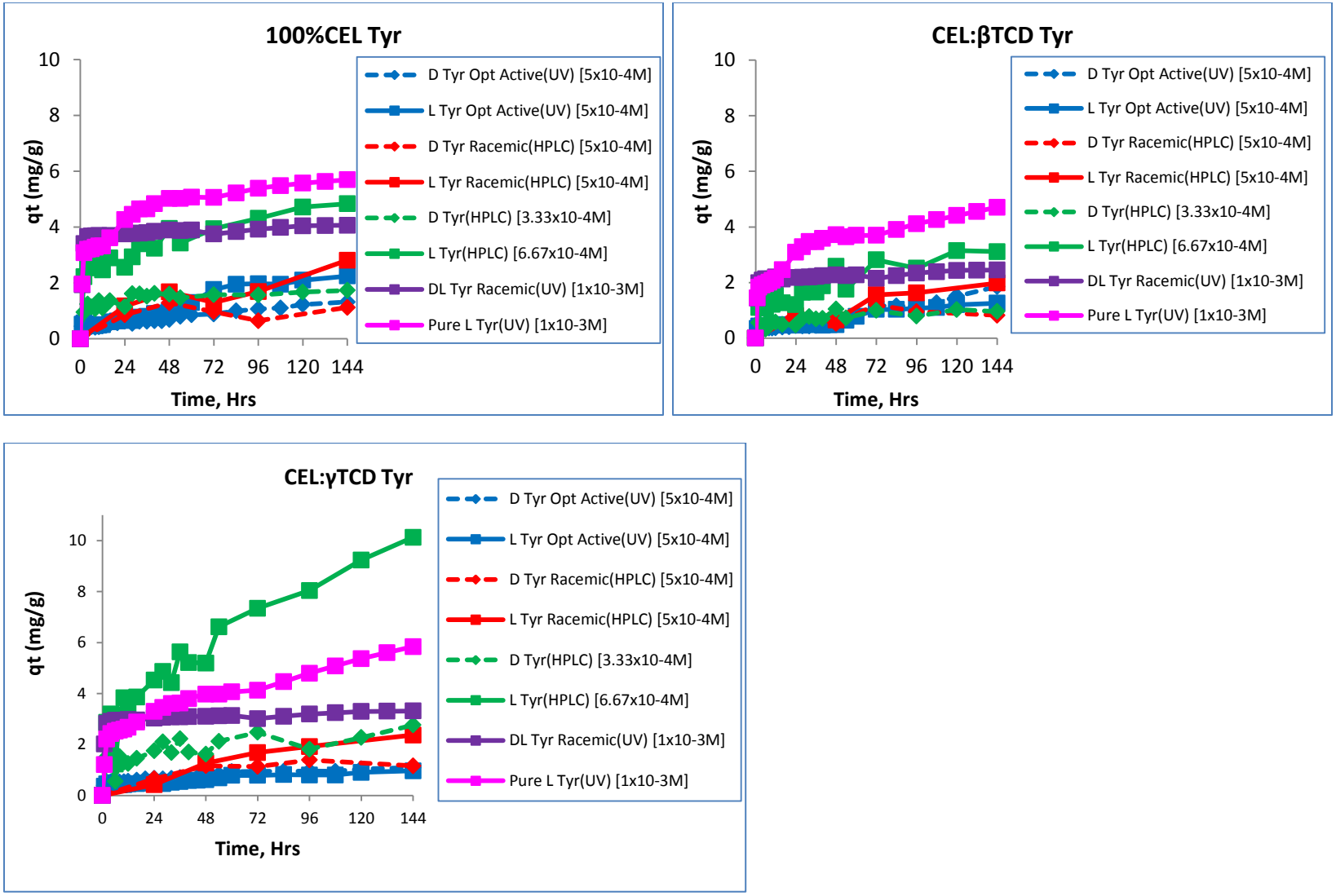

Figure 4.14: Sorption profiles of different solutions of Tyr enantiomers by different composite materials

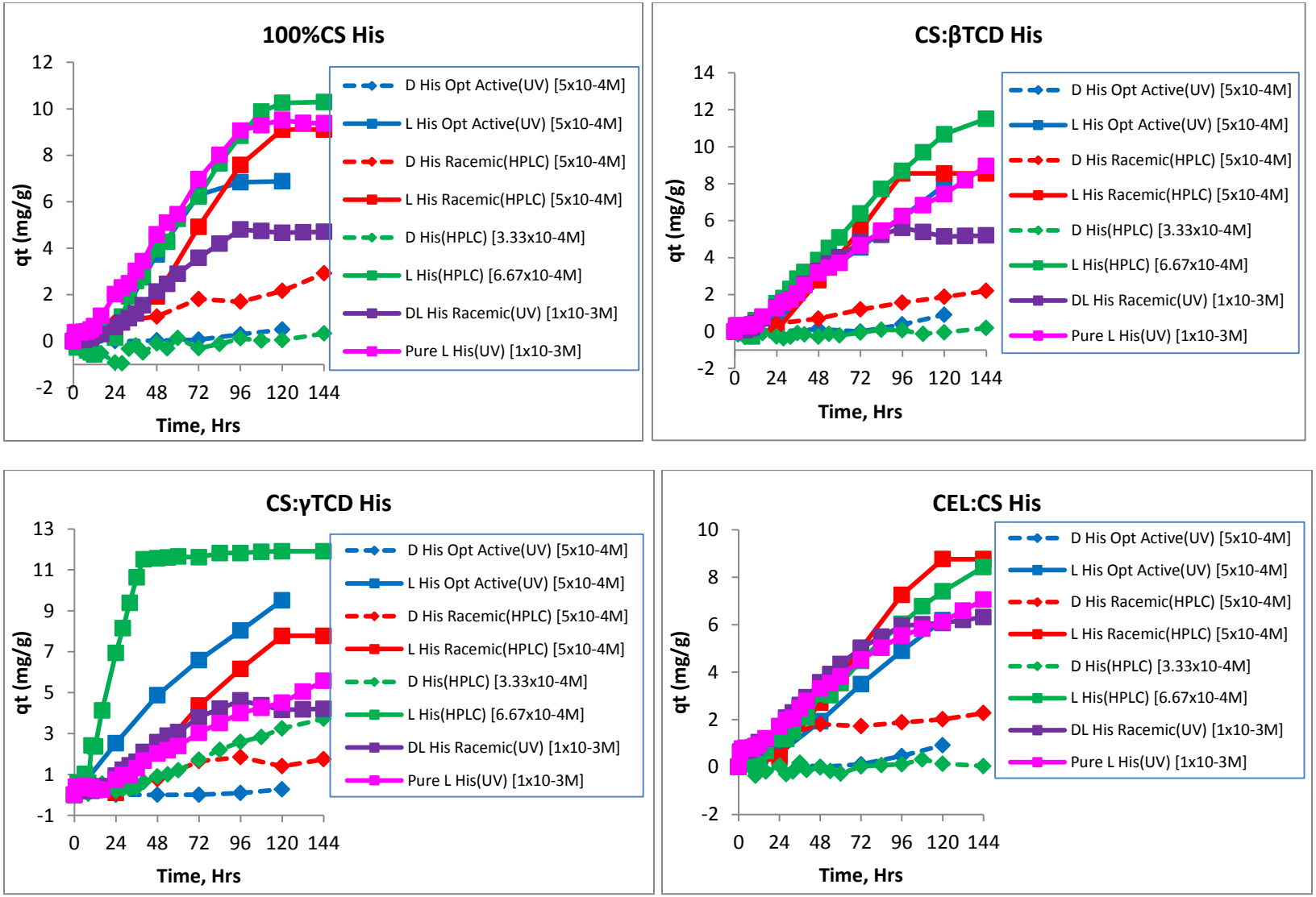

Figure 4.15: Sorption profiles of different solutions of His enantiomers by different composite materials

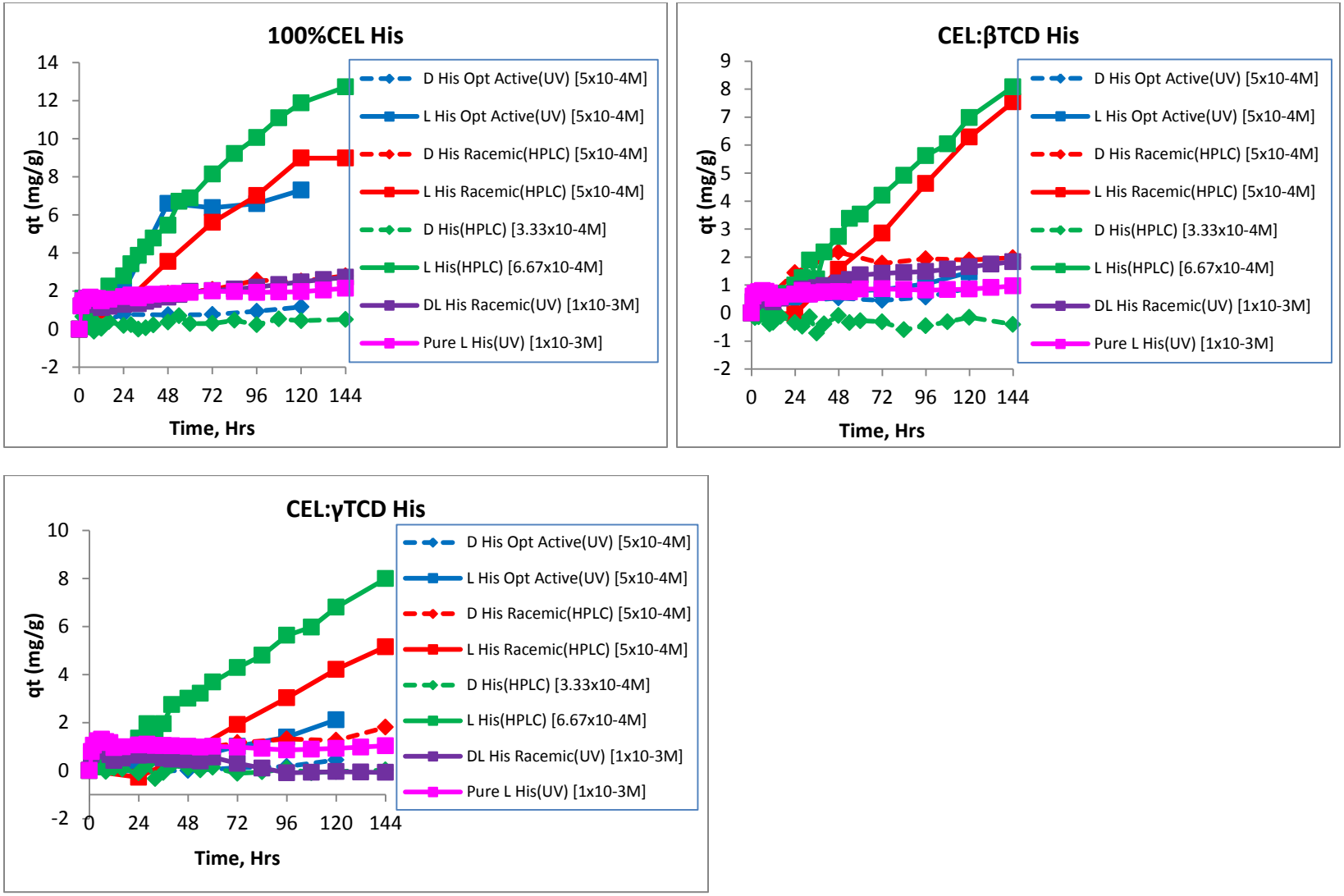

Figure 4.15: Sorption profiles of different solutions of His enantiomers by different composite materials

The intraparticle diffusion model plots are for the adsorption of Tyr enantiomers by the various composite materials are shown in Figure 4.16. The intraparticle parameters obtained from the different experiments are shown in the table immediately below each graph. As illustrated in this figure, there seem to be two distinct linear regions in these plots. There is an initial slow adsorption in the first 16 hrs followed by a more rapid adsorption from about 24 hrs to about 120 hrs. As will be expected, the adsorption of the L enantiomer has a larger slope (k_i2) than that of the D enantiomer, which is an indication of the faster rate at which the L enantiomer is being adsorbed. The fact that there are two linear regions in these plots is an indication that intraparticle diffusion is not the sole mechanism governing the sorption of the enantiomers. There is some other mechanism that is also involved in the sorption of the enantiomers in addition to the diffusion of the enantiomers in to the film matrix.

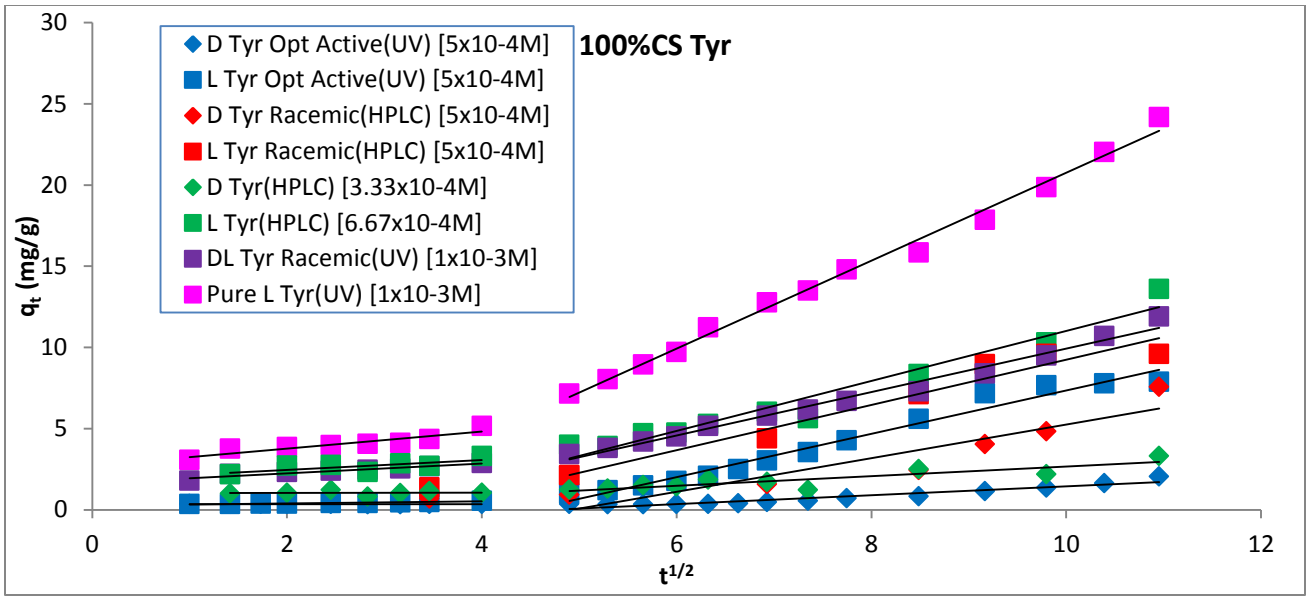

100CS						
	k_{i1}	Error	R^2	k_{i2}	Error	R^2
D Tyr Opt Active(UV) [5x10^{-4}M]	-	-	-	0.274	0.025	0.9086
L Tyr Opt Active(UV) [5x10^{-4}M]	0.051	0.007	0.9093	1.338	0.065	0.9722
D Tyr Racemic(HPLC) [5x10^{-4}M]	-	-	-	1.037	0.222	0.8455
L Tyr Racemic(HPLC) [5x10^{-4}M]	-	-	-	1.585	0.130	0.9803
D Tyr(HPLC) [3.33x10^{-4}M]	0.017	0.090	0.0092	0.295	0.056	0.7739
L Tyr(HPLC) [6.67x10^{-4}M]	0.191	0.147	0.2970	1.541	0.120	0.9539
DL Tyr Racemic(UV) [1x10^{-3}M]	0.220	0.020	0.9678	1.337	0.051	0.9841
Pure L Tyr(UV) [1x10^{-3}M]	0.262	0.036	0.9314	2.708	0.066	0.9935

Figure 4.16A: Intraparticle diffusion model plot and parameters for Tyr

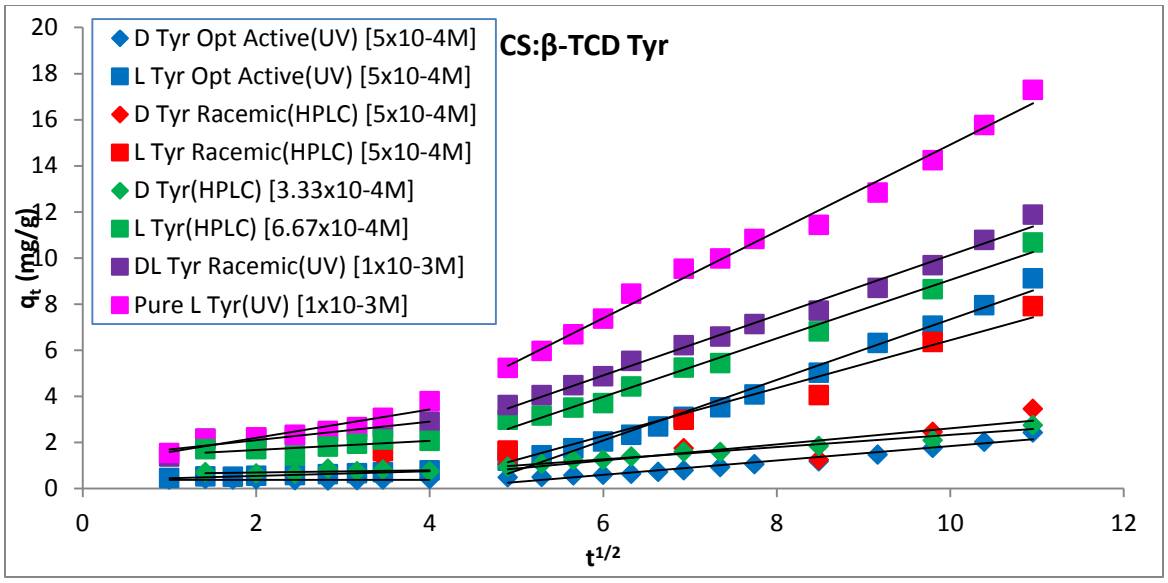

CS:β-TCD						
	k_{i1}	Error	R^2	k_{i2}	Error	R^2
D Tyr Opt Active(UV) [5x10^{-4}M]	-	-	-	0.310	0.020	0.9505
L Tyr Opt Active(UV) [5x10^{-4}M]	0.092	0.011	0.9374	1.315	0.044	0.9870
D Tyr Racemic(HPLC) [5x10^{-4}M]	-	-	-	0.350	0.124	0.7273
L Tyr Racemic(HPLC) [5x10^{-4}M]	-	-	-	1.037	0.134	0.9525
D Tyr(HPLC) [3.33x10^{-4}M]	0.070	0.045	0.3796	0.266	0.017	0.9697
L Tyr(HPLC) [6.67x10^{-4}M]	0.199	0.119	0.4103	1.267	0.046	0.9895
DL Tyr Racemic(UV) [1x10^{-3}M]	0.234	0.028	0.9454	1.304	0.036	0.9916
Pure L Tyr(UV) [1x10^{-3}M]	0.408	0.089	0.8387	1.882	0.053	0.9914

Figure 4.16B: Intraparticle diffusion model plot and parameters for Tyr

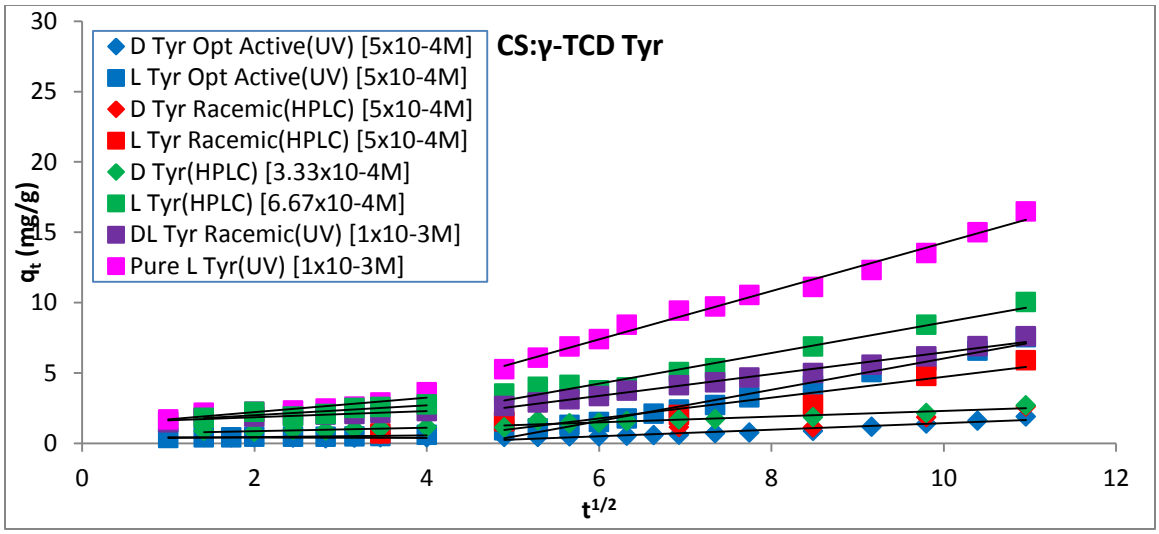

CS:γ-TCD						
	k_{i1}	Error	R^2	k_{i2}	Error	R^2
D Tyr Opt Active(UV) [5x10^{-4}M]	-	-	-	0.234	0.019	0.9266
L Tyr Opt Active(UV) [5x10^{-4}M]	0.038	0.007	0.8491	1.114	0.041	0.9842
D Tyr Racemic(HPLC) [5x10^{-4}M]	-	-	-	0.215	0.093	0.6419
L Tyr Racemic(HPLC) [5x10^{-4}M]	-	-	-	0.739	0.151	0.8889
D Tyr(HPLC) [3.33x10^{-4}M]	0.105	0.036	0.6820	0.205	0.024	0.9005
L Tyr(HPLC) [6.67x10^{-4}M]	0.332	0.125	0.6391	1.090	0.074	0.9648
DL Tyr Racemic(UV) [1x10^{-3}M]	0.154	0.007	0.9910	0.775	0.027	0.9867
Pure L Tyr(UV) [1x10^{-3}M]	0.325	0.062	0.8718	1.714	0.055	0.9889

Figure 4.16C: Intraparticle diffusion model plot and parameters for Tyr

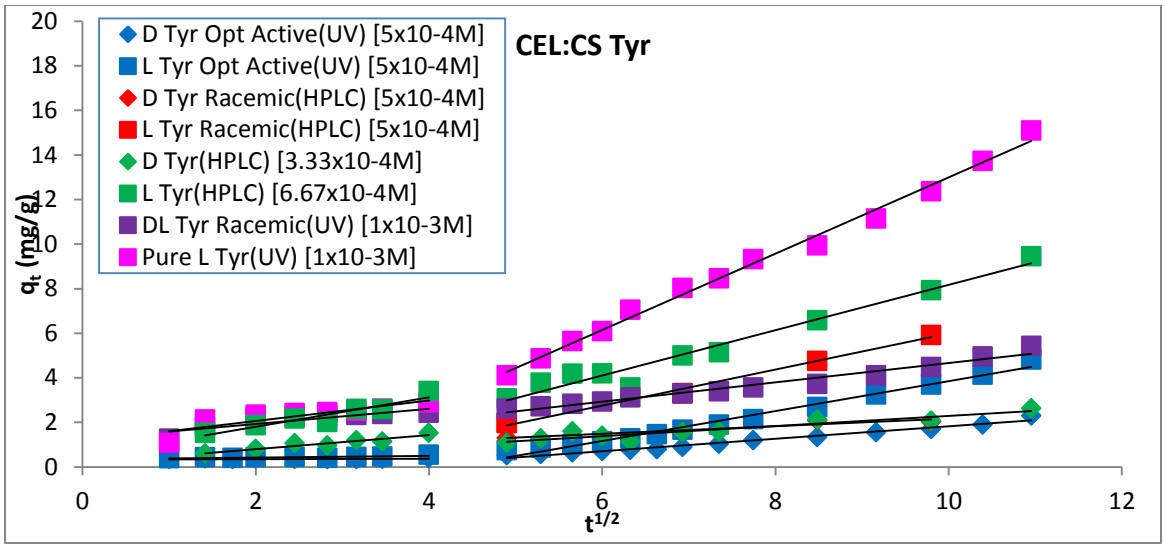

CEL:CS						
	k_{i1}	Error	R^2	k_{i2}	Error	R^2
D Tyr Opt Active(UV) [5x10^{-4}M]	-	-	-	0.279	0.012	0.9769
L Tyr Opt Active(UV) [5x10^{-4}M]	0.014	0.008	0.3749	0.669	0.025	0.9833
D Tyr Racemic(HPLC) [5x10^{-4}M]	-	-	-	0.172	0.042	0.8916
L Tyr Racemic(HPLC) [5x10^{-4}M]	-	-	-	0.810	0.047	0.9933
D Tyr(HPLC) [3.33x10^{-4}M]	0.269	0.056	0.8518	0.229	0.031	0.8697
L Tyr(HPLC) [6.67x10^{-4}M]	0.518	0.094	0.8845	1.017	0.068	0.9658
DL Tyr Racemic(UV) [1x10^{-3}M]	0.253	0.055	0.8411	0.434	0.025	0.9641
Pure L Tyr(UV) [1x10^{-3}M]	0.216	0.023	0.9547	1.711	0.043	0.9931

Figure 4.16D: Intraparticle diffusion model plot and parameters for Tyr

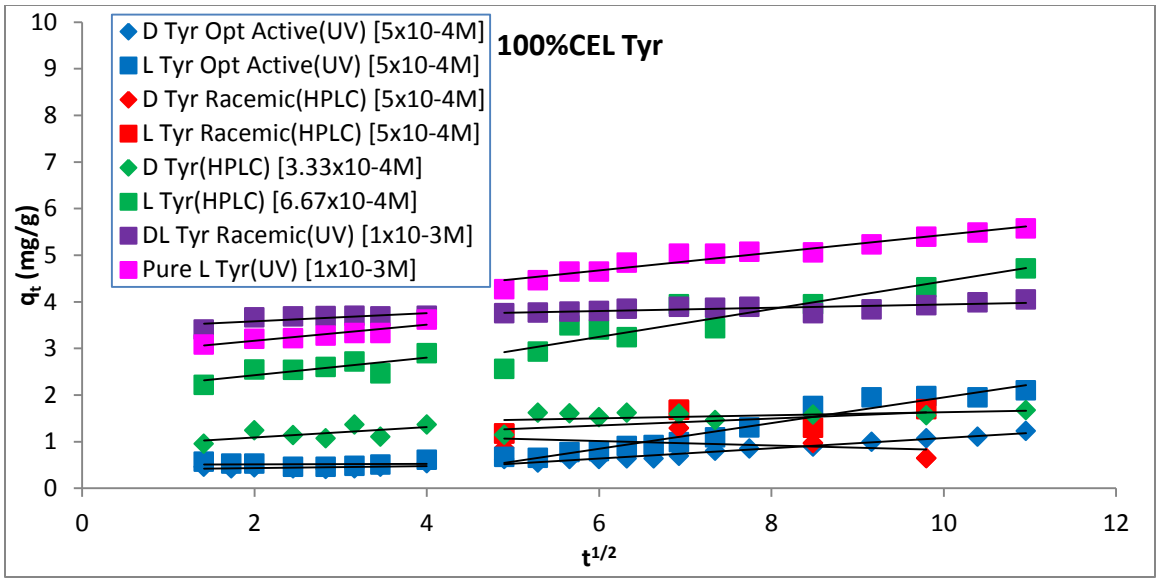

100CEL						
	k_{i1}	Error	R^2	k_{i2}	Error	R^2
D Tyr Opt Active(UV) [5x10^{-4}M]	-	-	-	0.109	0.006	0.9616
L Tyr Opt Active(UV) [5x10^{-4}M]	-	-	-	0.276	0.018	0.9495
D Tyr Racemic(HPLC) [5x10^{-4}M]	-	-	-	-0.048	0.083	0.1438
L Tyr Racemic(HPLC) [5x10^{-4}M]	-	-	-	0.074	0.072	0.3482
D Tyr(HPLC) [3.33x10^{-4}M]	0.083	0.084	0.1986	0.033	0.024	0.1974
L Tyr(HPLC) [6.67x10^{-4}M]	0.144	0.083	0.4311	0.298	0.043	0.8584
DL Tyr Racemic(UV) [1x10^{-3}M]	0.117	0.047	0.6042	0.036	0.008	0.6297
Pure L Tyr(UV) [1x10^{-3}M]	0.129	0.016	0.9580	0.191	0.015	0.9382

Figure 4.16E: Intraparticle diffusion model plot and parameters for Tyr

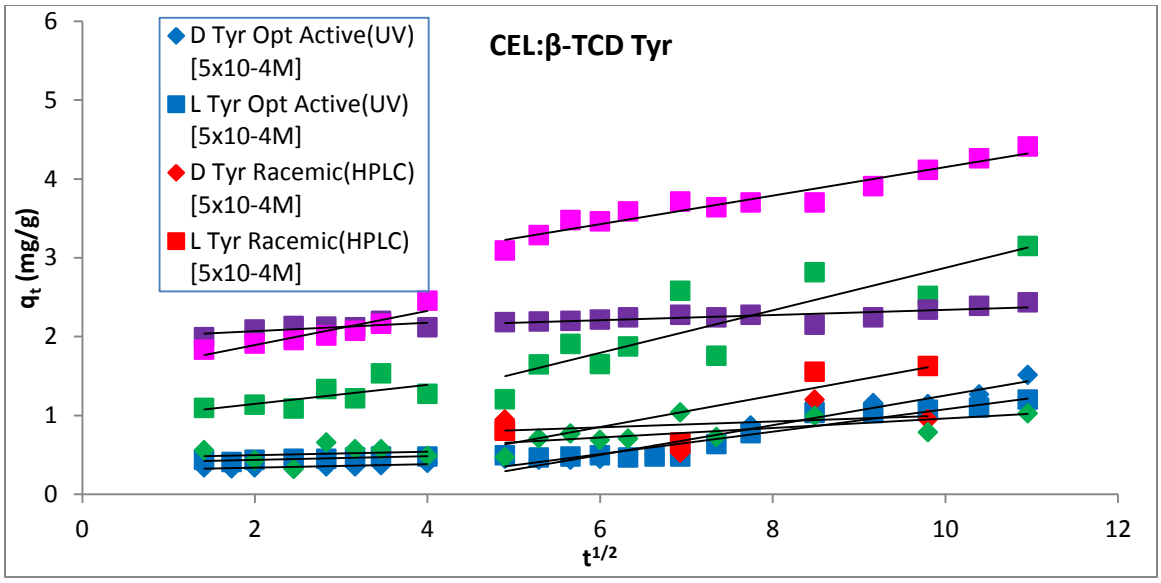

CEL:β-TCD						
	k_{i1}	Error	R^2	k_{i2}	Error	R^2
D Tyr Opt Active(UV) [$5x10^{-4}$M]	0.015	0.004	0.7594	0.189	0.015	0.9285
L Tyr Opt Active(UV) [$5x10^{-4}$M]	0.026	0.007	0.7539	0.142	0.014	0.8988
D Tyr Racemic(HPLC) [$5x10^{-4}$M]	-	-	-	0.038	0.090	0.0809
L Tyr Racemic(HPLC) [$5x10^{-4}$M]	-	-	-	0.200	0.091	0.7067
D Tyr(HPLC) [$3.33x10^{-4}$M]	0.049	0.076	0.0930	0.061	0.023	0.4562
L Tyr(HPLC) [$6.67x10^{-4}$M]	0.179	0.071	0.6142	0.269	0.053	0.7631
DL Tyr Racemic(UV) [$1x10^{-3}$M]	0.081	0.019	0.8225	0.033	0.008	0.6195
Pure L Tyr(UV) [$1x10^{-3}$M]	0.151	0.014	0.9665	0.181	0.014	0.9355

Figure 4.16F: Intraparticle diffusion model plot and parameters for Tyr

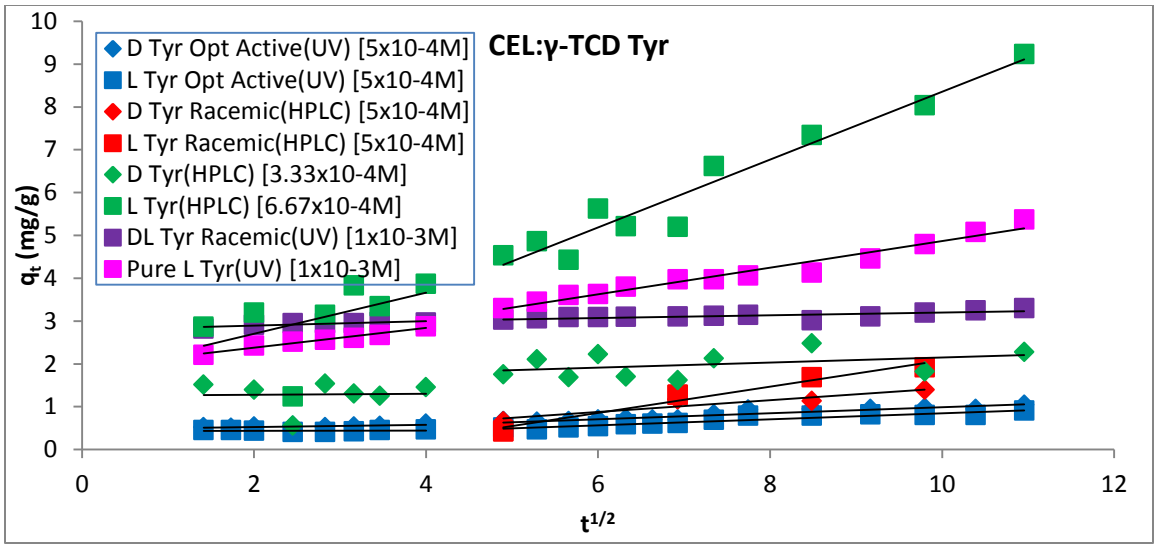

CEL:γ-TCD						
	k_{i1}	Error	R^2	k_{i2}	Error	R^2
D Tyr Opt Active(UV) [5x10^{-4}M]	0.014	0.008	0.3678	0.070	0.007	0.8825
L Tyr Opt Active(UV) [5x10^{-4}M]	-	-	-	0.070	0.007	0.9065
D Tyr Racemic(HPLC) [5x10^{-4}M]	-	-	-	0.137	0.038	0.8678
L Tyr Racemic(HPLC) [5x10^{-4}M]	-	-	-	0.307	0.039	0.9686
D Tyr(HPLC) [3.33x10^{-4}M]	-	-	-	0.059	0.048	0.1578
L Tyr(HPLC) [6.67x10^{-4}M]	0.376	0.554	0.1030	0.793	0.068	0.9449
DL Tyr Racemic(UV) [1x10^{-3}M]	0.066	0.014	0.8417	0.031	0.007	0.6155
Pure L Tyr(UV) [1x10^{-3}M]	0.209	0.024	0.9486	0.310	0.018	0.9629

Figure 4.16G: Intraparticle diffusion model plot and parameters for Tyr

Another experiment was carried out with the aim of checking for and analyzing the desorption profiles that might have been obtained for the different enantiomers. For this experiment, the composite materials that were used for the adsorption of Tyr $1x10^{-3}$M racemic samples were used. To check the desorption, the composite materials were taken out of Tyr solution at the end of the adsorption experiment, quickly blotted with a filter paper, and placed in vials containing 30 mL of de-ionized water. The sample vials were sealed and agitated on a mechanical shaker at room temperature. At specific time intervals, 20µL aliquots were withdrawn and injected into the HPLC. Figure 4.17 below shows the HPLC chromatograms for this release experiment measured at 2 hr and 24 hr time periods for 4 different composites. The HPLC chromatogram of a Tyr standard solution is included in each figure for reference. As illustrated, there were no HPLC bands for either the L or D enantiomer even after 24 hrs with the composites in water.

The sorption selectivity for the racemic mixtures of the different amino acids was calculated according to the following equation:[20]

$$Sorption\ selectivity\ (\alpha) = \frac{(C_{Li} - C_{Lf})/C_{Lf}}{(C_{Di} - C_{Df})/C_{Df}}$$

Where C_{Li} and C_{Lf} denote the initial and final L concentration and C_{Di} and C_{Df} is the initial and final D concentration respectively. The selectivity was calculated for the HPLC experiments with $1x10^{-3}$M racemic solutions. The 96 hr time period was chosen for this calculation as this was generally the amount of time it took for the HPLC band of the L enantiomer to disappear for the 100%CS composite material. The results are plotted together with the amount of each enantiomer adsorbed at this time point in Figure 4.18. For Tyr and Trp, selectivity was higher for the CS composite materials than for the CEL

composite materials with 100%CS giving the highest selectivity. The sorption selectivity for both CS and CEL composite materials was found to decrease when α-, β- or γ-TCD was incorporated into these composites. Wang et al.[20] observed a similar trend for Trp when native β-CD was incorporated into CS membranes. They attributed this to the fact that the chiral environment of CS may have been effective in distinguishing between the D and L enantiomers while the β-CD was less selective due to host/guest complex formation with the amino acid molecules.[20] While there is some increased selectivity for Phe and His with CS:β-TCD and CS:γ-TCD composite materials compared to the 100%CS composite, the results do not seem to be consistent enough to be conclusively attributed to the TCDs in these composites.

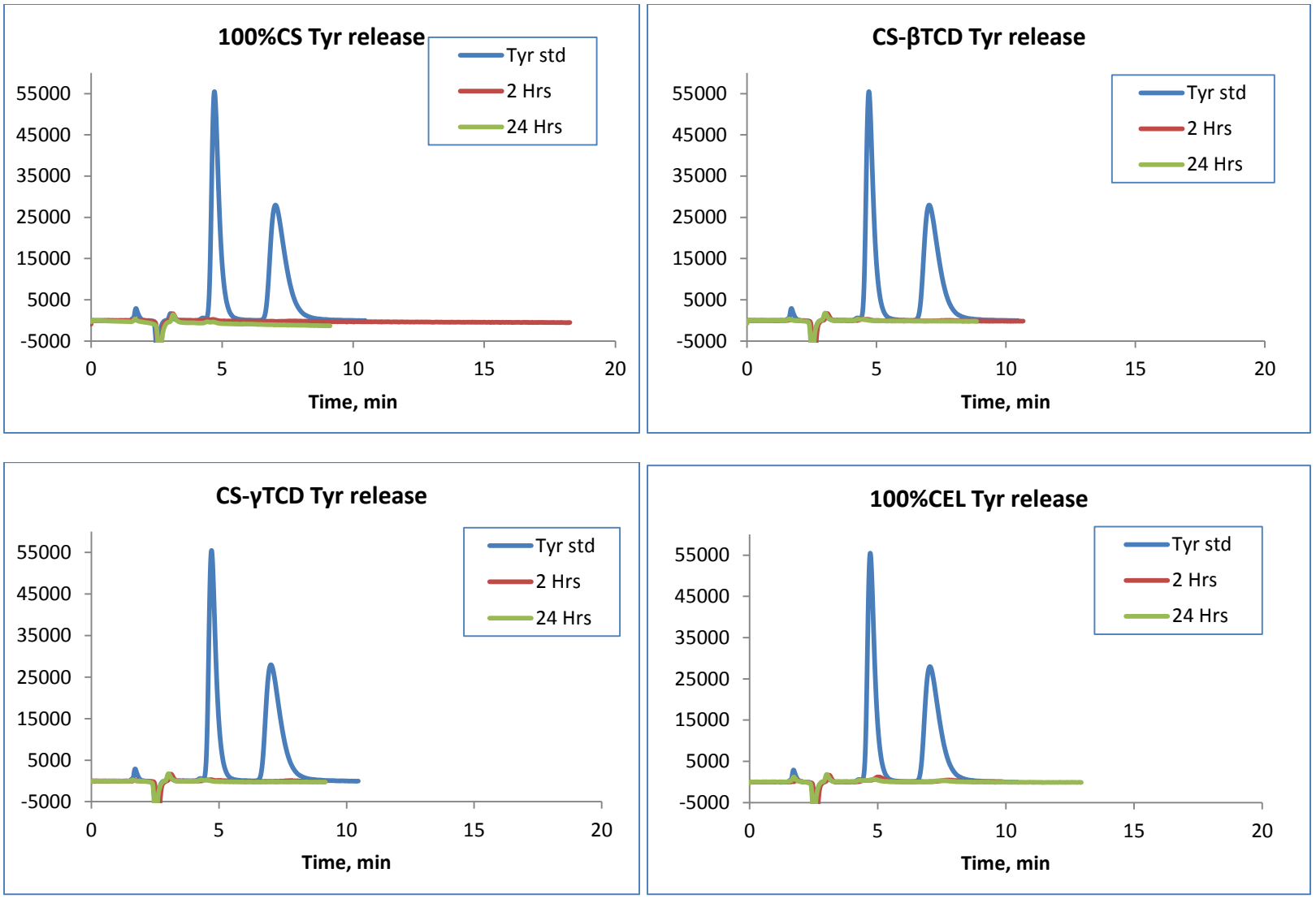

Figure 4.17: HPLC chromatograms showing no release of Tyr enantiomers from 4 different composites.

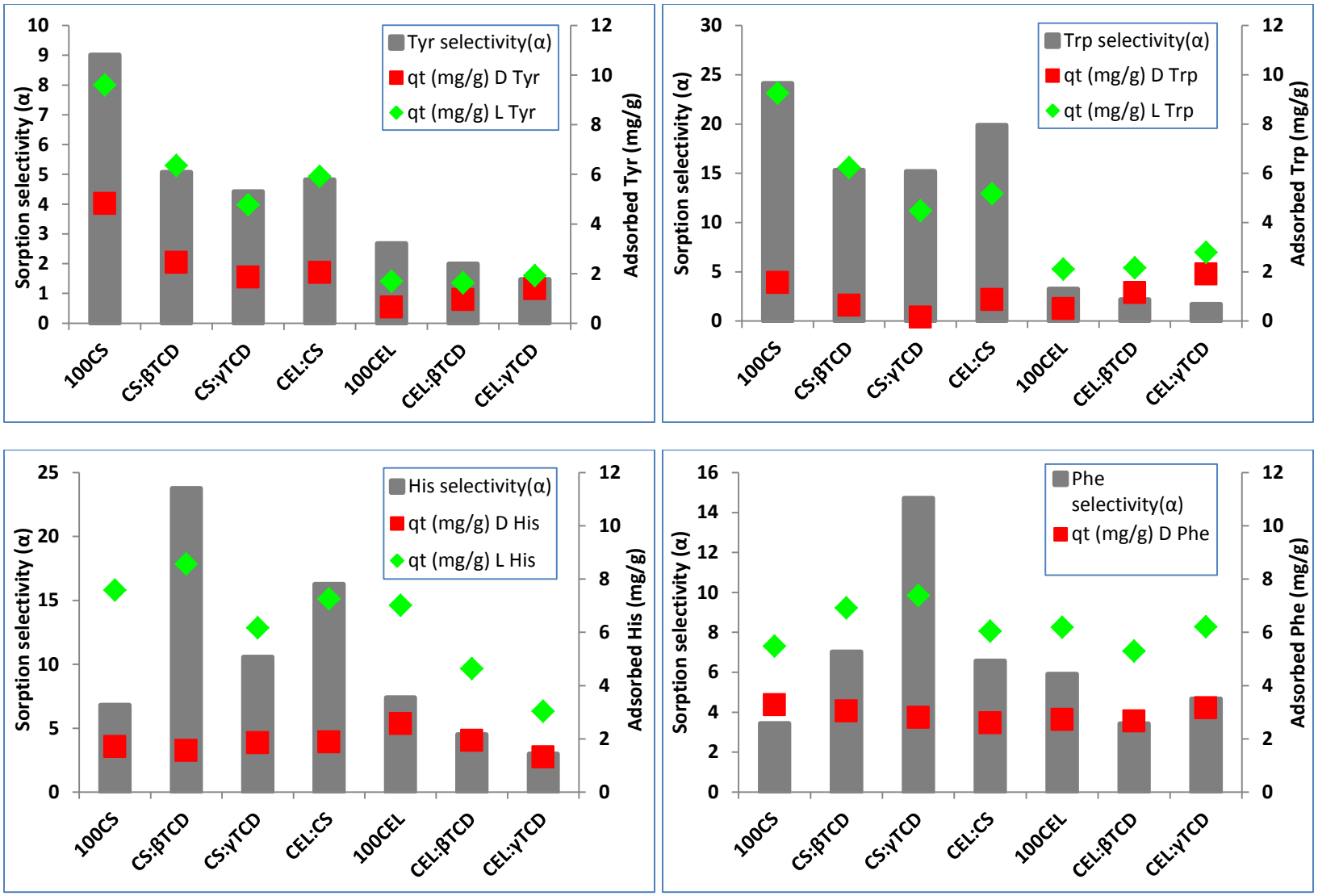

Figure 4.18: Comparison of the selectivity of the different composite materials with the 4 amino acids studied

In summary, the polysaccharide composite materials developed here have shown promising potential application in chiral separations. Preliminary results with 4 different amino acids show that racemic mixtures can potentially be resolved by selective adsorption of the L enantiomer in about 96 to 120 hrs for the 100%CS composite material. The mechanism of the selective adsorption is still not clear at this point as attempts to use pseudo 1st order and pseudo 2nd order models were not successful. CS composites alone seem to have better selectivity for Trp and Tyr than the TCD-doped composites.

4.5. Encapsulation of fullerene derivatives into polysaccharide composite materials

A fullerene is any molecule composed entirely of carbon, in the form of a hollow sphere, ellipsoid or tube. Spherical fullerenes are also called buckyballs, and the cylindrical ones are called carbon nanotubes or buckytubes. Fullerenes are similar in structure to graphite, which is composed of stacked graphene sheets of linked hexagonal rings; but they may also contain pentagonal (or sometimes heptagonal) rings.

In recent years, the chemical and physical properties of fullerenes have been a hot topic in the field of research and development, and are likely to continue to be for a long time. In April 2003, fullerenes were under study for potential medicinal use: binding specific antibiotics to the structure to target resistant bacteria and even target certain cancer cells such as melanoma. The October 2005 issue of *Chemistry & Biology* contains an article describing the use of fullerenes as light-activated antimicrobial agents.[22]

Mashino et al. reported on the antibacterial and antiproliferative activity of cationic fullerene derivatives.[23] Aoshima et al. evaluated the antimicrobial activity of fullerenes and their hydroxylated derivatives.[24] Nakamura and Mashino reported on the biological activity of water soluble fullerene derivatives while an interesting study on the antibacterial activity of cyclodextrins against Bacillus strain has been reported.[25,26] In the field of nanotechnology, heat resistance and superconductivity are some of the more heavily studied properties.

Due to its interesting properties and potential for application in various commercial and medical devices, fullerene derivatives were doped into our polysaccharide composite materials. Two types of fullerene derivatives were used in this study; polyhydroxy fullerene and N-ethyl polyamino fullerene. The structures of these two derivatives are shown in Figure 4.19 below:

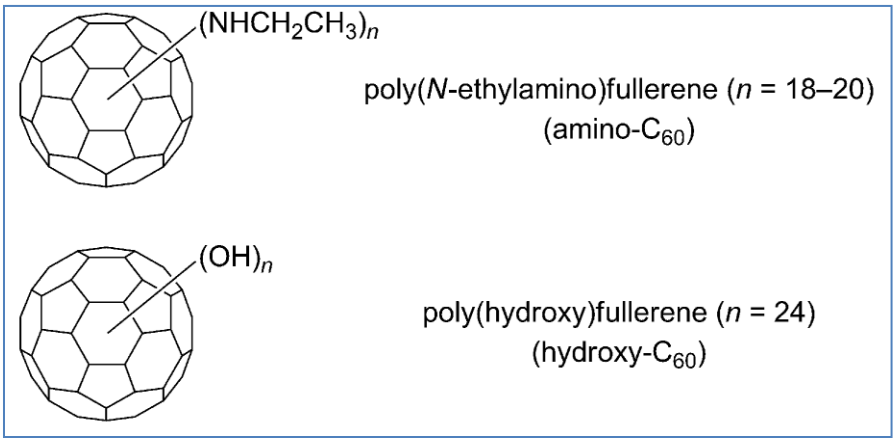

Figure 4.19: Structures of the fullerene derivatives used.

The synthesis and characterization of the polysaccharide composites used in this study is described in detail in Chapter 2. After preparing the composites as described in Chapter 2, the fullerene derivatives were encapsulated into 100%CEL, 100%CS, [CEL:γ-TCD] and [CS:γ-TCD] composites by adsorption from an aqueous solution of the respective derivative. Adsorption procedure used for the fullerene derivatives is similar to that described in Chapter 3 for pollutants, with the exception that for the fullerene derivative, aqueous solutions of approximately 1.0 x 10^{-4}M were used. The results of the adsorption process by the different composites are shown in Figure 4.20. The pseudo second order fitting parameters for this adsorption process are shown in Table 4.5. It is clear from the results in Figure 4.20 and Table 4.5 that for all composites the amount of Polyhydroxy fullerene adsorbed is higher than the corresponding N-ethyl polyamino fullerene amount at this particular concentration (~1.0x10^{-4}M).

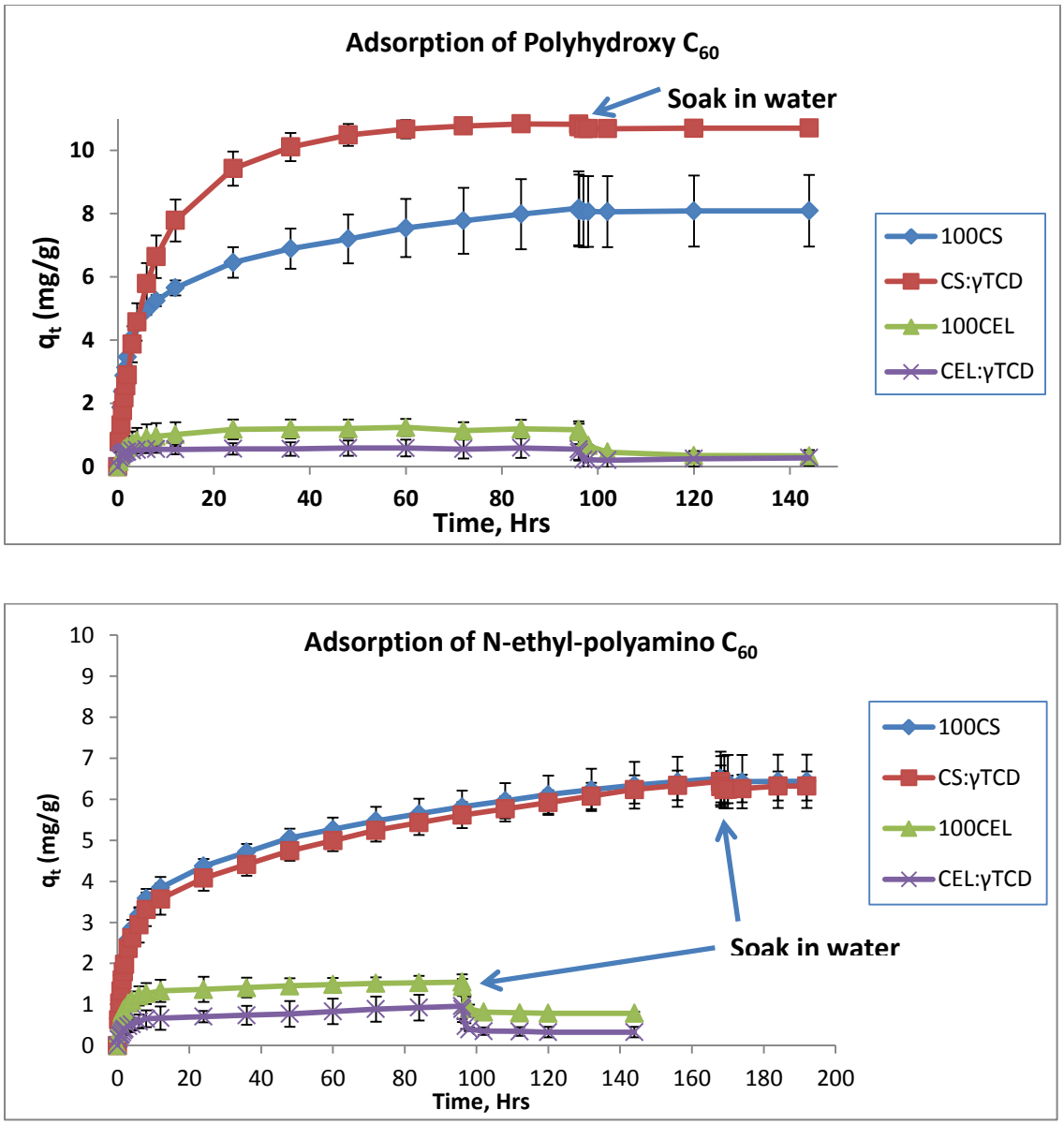

Figure 4.20: Adsorption of Polyhydroxy fullerene (top) and N-ethyl polyamino fullerene by 4 different composites.

Table 4.5: Pseudo second order sorption parameters for the adsorption of fullerene derivatives by 4 different composites.

	Pseudo-second order sorption parameters													
		Polyhydroxy fullerene							N-ethyl-polyamino fullerene					
	q_e, expt (mg/g)	q_e (mg/g)	Error	k (g/mg Hr^{-1})	Error	R^2	M.S.C	q_e, expt (mg/g)	q_e (mg/g)	Error	K (g/mg Hr^{-1})	Error	R^2	M.S.C
100%CS	8.17	8.21	1.20	0.036	0.016	0.9969	5.6	6.51	6.51	0.58	0.022	0.004	0.9942	5.1
50:50 CS:γ-TCD	10.83	11.58	0.07	0.016	0.003	0.9997	8.1	6.44	6.40	0.31	0.019	0.001	0.9914	4.6
100%CEL	1.24	1.21	0.26	0.535	0.288	0.9981	6.1	1.54	1.55	0.18	0.348	0.005	0.9987	6.7
50:50 CEL:γ-TCD	0.59	0.57	0.32	0.849	0.262	0.9924	5.0	0.96	0.94	0.33	0.301	0.142	0.9882	4.2

Another interesting feature that is illustrated in Figure 4.20 is that when the composites were soaked in water after the adsorption experiment, both the polyhydroxy fullerene and the N-ethyl polyamino fullerene were easily washed off from the CEL and the [CEL:γ-TCD] composites. However, these fullerene derivatives could not be washed off the CS and [CS:γ-TCD] composites.

Further analysis of the adsorption of the polyhydroxy fullerene and the N-ethyl polyamino by the 4 different composites was done using the Intraparticle diffusion model. The results are shown in Figure 4.20A (for 100%CS and [CS:γ-TCD]) and Figure 4.21B (for 100%CEL and [CEL:γ-TCD]). The intraparticle diffusion model fitting parameters are shown in Table 4.6. As illustrated, the adsorption profiles for these 2 fullerene derivatives by the 4 composites can be divided into approximately 2 regions. There is an initial rapid adsorption, followed by a gradual slower adsorption. The fact that there are multi-linear regions in the Intraparticle diffusion profiles for these composites is indicative of several adsorption mechanisms taking place.

Thermodynamic isotherm experiments were carried out for the 100%CS and [CS:γ-TCD] composite materials using procedures described in Chapter 3 for chlorophenols. The thermodynamic sorption isotherm parameters are shown Figure 4.22 and in Table 4.7. The results indicate that these 2 composites have relatively high sorption capacities for both derivatives. As expected, the [CS:γ-TCD] composite showed higher capacity than the 100CS for the 2 derivatives. While the q_{max} for N- ethyl polyamino fullerene is higher than that of polyhydroxy fullerene for 100%CS composite, the qmax for the 2 derivatives for the [CS:γ-TCD] composite are almost the same.

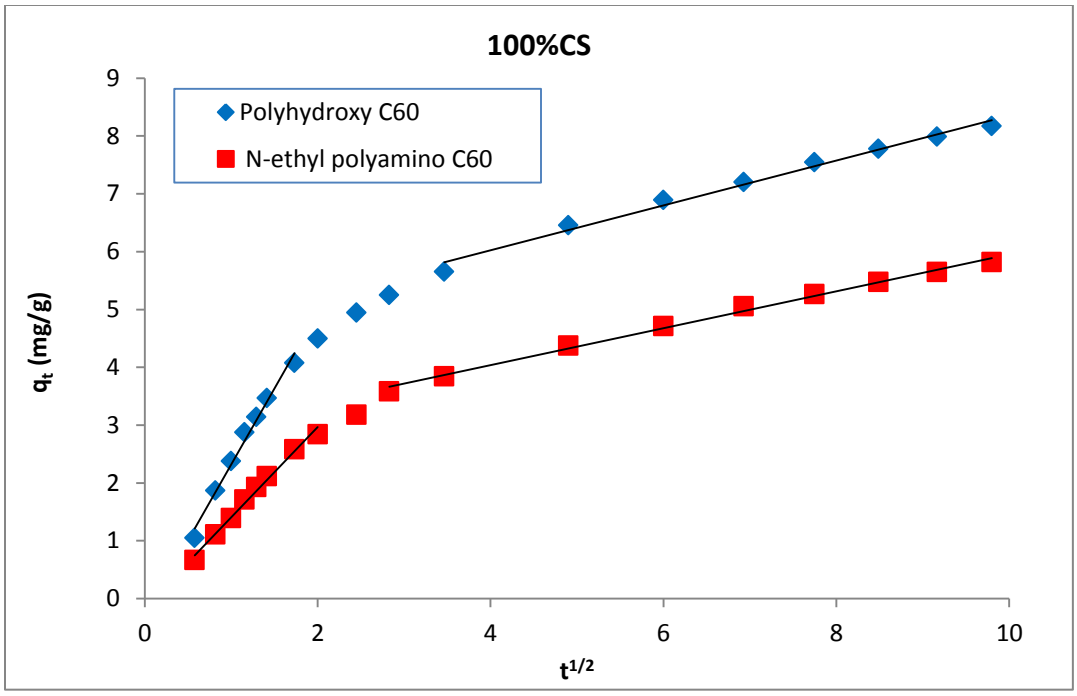

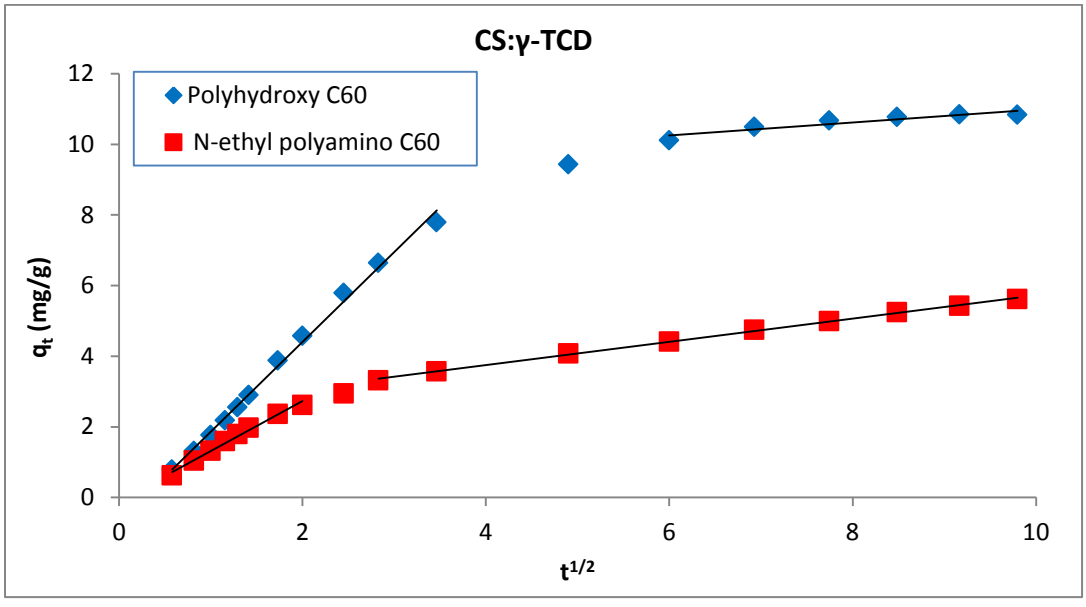

Figure 4.21: Intraparticle diffusion plots for 100%CS(top) and [CS:γ-TCD] composites for the sorption of fullerene derivatives.

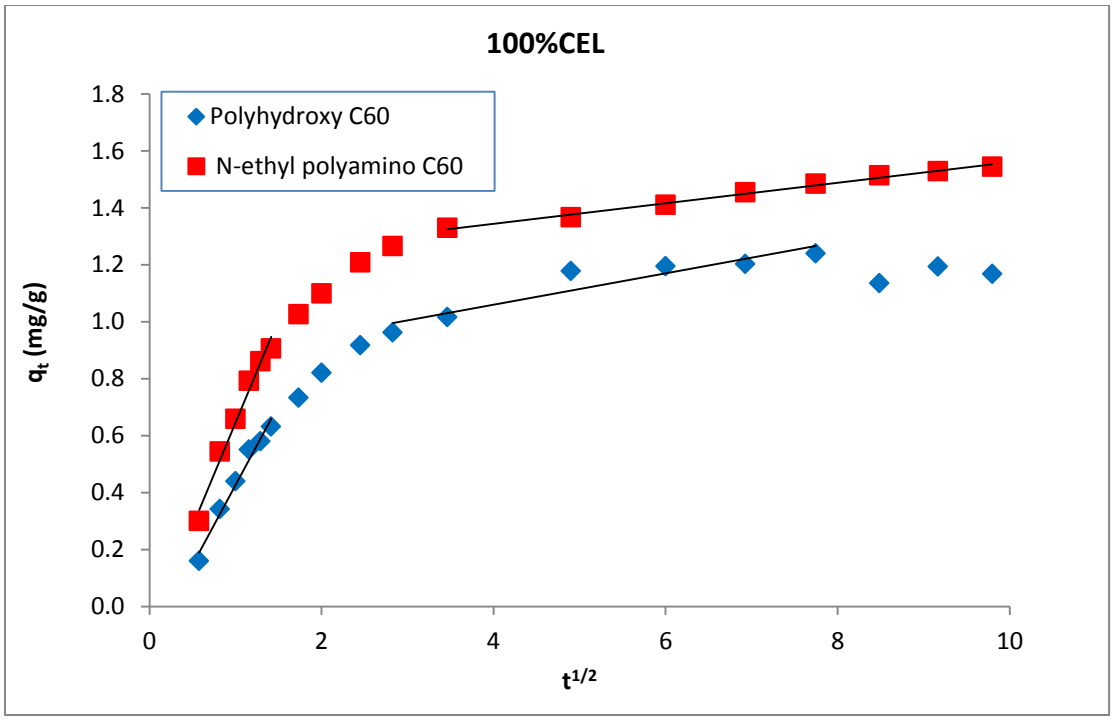

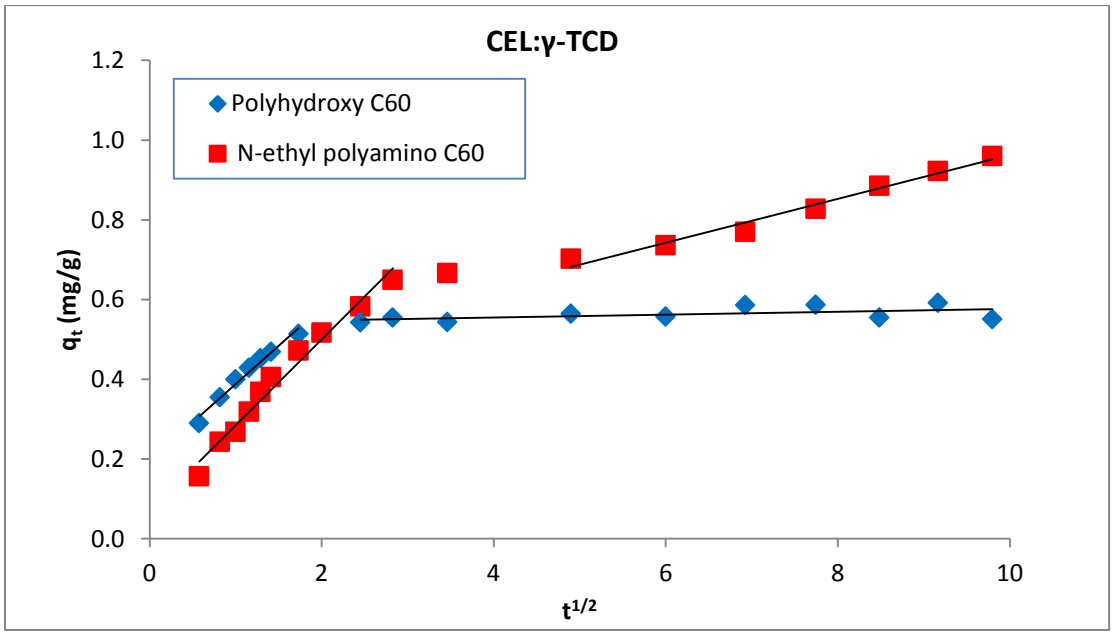

Figure 4.22: Intraparticle diffusion plots for 100%CEL(top) and [CEL:γ-TCD] composites for the sorption of fullerene derivatives

Table 4.6: Intraparticle diffusion parameters for the sorption of the fullerene derivatives by 4 different composites.

	Polyhydroxy C_{60}						N-ethyl polyamino C_{60}					
	k_{i1}	Error	R^2	k_{i2}	Error	R^2	k_{i1}	Error	R^2	k_{i2}	Error	R^2
100CS	2.628	0.141	0.9857	0.388	0.017	0.9880	1.557	0.063	0.9902	0.319	0.009	0.9950
CS:γTCD	2.541	0.060	0.9950	0.185	0.037	0.8656	1.416	0.062	0.9888	0.329	0.004	0.9987
100CEL	0.563	0.043	0.9771	0.055	0.010	0.8806	0.726	0.053	0.9792	0.036	0.001	0.9922
CEL:γTCD	0.192	0.014	0.9745	0.004	0.002	0.2759	0.215	0.012	0.9766	0.055	0.004	0.9776

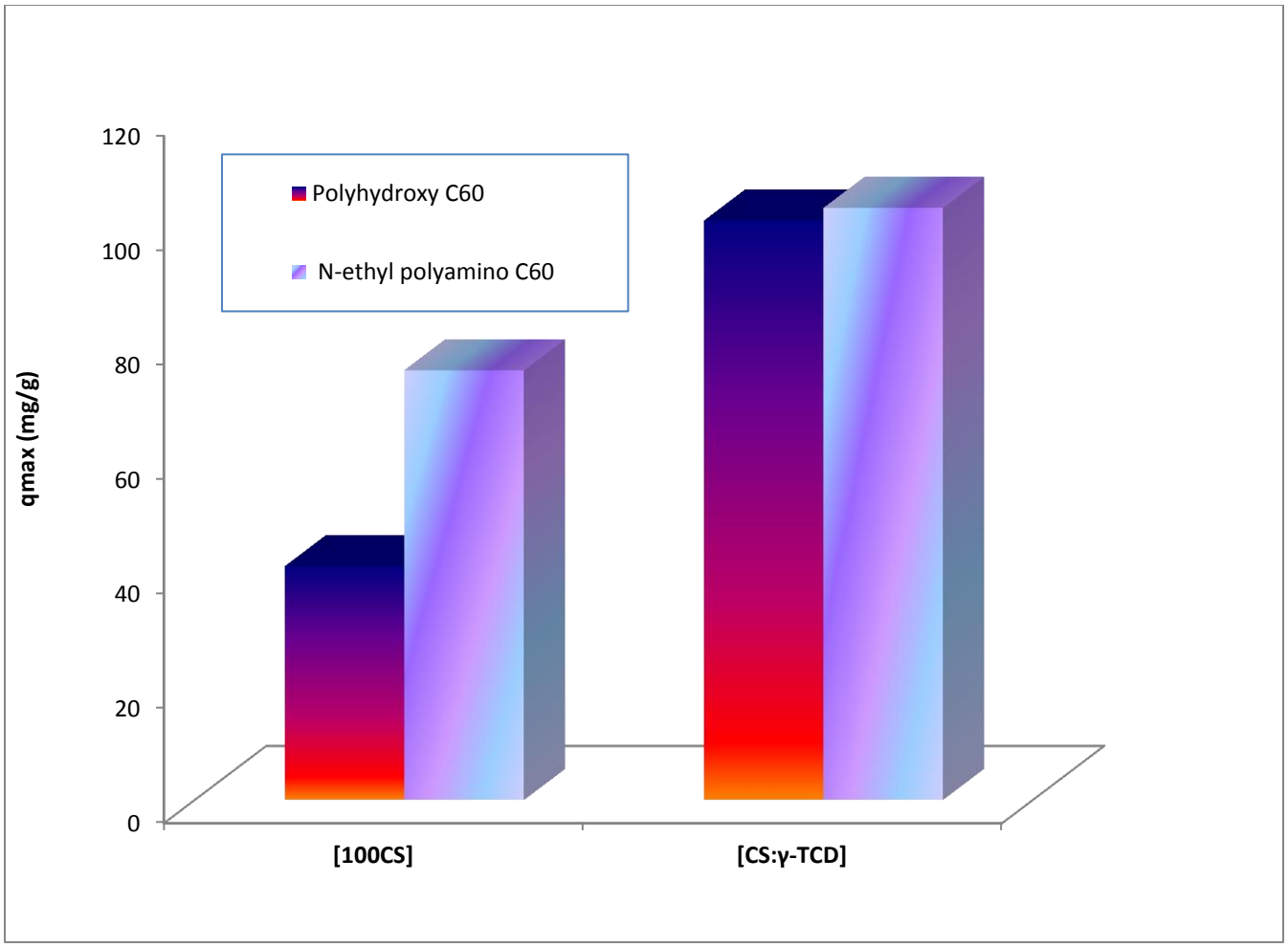

Figure 4.23: Comparison of qmax values from the langmuir fit

Table 4.7: Thermodynamic isotherms parameters

100%CS										
	Langmuir Isotherm parameters			**Freundlich isotherm parameters**			**D-R isotherm parameters**			
	q_{max} (mg/g)	**k_L (L/mg)**	**R^2**	**n**	**k_F (mg/g)(L/mg)$^{1/n}$**	**R^2**	**q_{max} (mg/g)**	**β (mmol^{2}J^{-2})**	**E (kJ/mol)**	**R^2**
Polyhydroxy C_{60}	40.8	0.0062	0.9618	2.9	3.26955	0.9926	34.8	0.0035	12.0	0.8074
N-ethyl polyamino C_{60}	75.1	0.0008	0.9911	1.5	0.34349	0.9852	33.9	0.0130	6.2	0.9212
	CS:γ-TCD: Polyhydroxy C60 Isotherms									
	Langmuir Isotherm parameters			**Freundlich isotherm parameters**			**D-R isotherm parameters**			
	q_{max} (mg/g)	**k_L (L/mg)**	**R^2**	**n**	**k_F (mg/g)(L/mg)$^{1/n}$**	**R^2**	**q_{max} (mg/g)**	**β (mmol^{2}J^{-2})**	**E (kJ/mol)**	**R^2**
Polyhydroxy C_{60}	101.2	0.0005	0.9833	1.4	0.22988	0.9891	44.0	0.0429	3.4	0.9661
N-ethyl polyamino C_{60}	103.4	0.0006	0.9918	1.4	0.28141	0.9901	45.9	0.0281	4.2	0.9598

From the fitting to Dubinin–Radushkevich isotherm model, the mean free energy E values of the sorption process per mole of fullerene derivative are all lower than 8k J/mol except for the sorption of polyhydroxy fullerene onto 100%CS which is about 12 kL/mol. However, the fitting of this sample was not as good as for the rest of the samples as indicated by the lower correlation coefficient. The low mean free energy values suggest adsorption by physisorption, which is rather unexpected especially for the γ-TCD containing composites.

The results presented above show that it is possible to incorporated fullerene derivatives into our polysaccharide composite materials. While the fullerene derivatives were observed to wash off CEL and [CEL+γ-TCD] composites, they were observed to remain encapsulated in CS and [CS+γ-TCD] composites upon washing in water. It is anticipated that the unique properties of the fullerenes will stay intact in the composites hence conferring some chemical and electronic properties that otherwise are not present in our polysaccharide composites.

Taken together, the results of the controlled drug release using ciprofloxacin as a model drug compound and the enantioselectivity observed with Tyr, Trp, His and Phe demonstrate the possible wide applicability of our polysaccharide composite materials. The ready availability of the starting materials, their recyclable synthesis using a single solvent, their improved mechanical and rheological properties achieved by adding cellulose and the wide applicability including pollutant adsorption, controlled drug release systems and enantioselectivity demonstrated here makes them attractive alternatives to synthetic polymers. The ability to encapsulate fullerene derivatives into our composite materials is expected to confer some extra and unique chemical and

electronic properties that otherwise are not present in our polysaccharide composites. These possibilities including antimicrobial studies are already being investigated.

4.6. References

(1) Hosney, E. A.; El-Mahrouk, G. M.; Al-Angary, A. *Drug Dev. Ind. Pharm.* **1994**, *20*, 1085–1091.

(2) Saettone, M. F.; Perini, G.; Rijli, P.; Rodriguez, L.; Cini, M. *Int. J. Pharm.* **1995**, *126*, 83–88.

(3) Sonaglio, D.; Bataille, B.; Ortigosa, C.; Jacob, M. *Int. J. Pharm.* **1995**, *125*, 53–60.

(4) Varshosaz, J.; Tabbakhian, M.; Salmani, Z. *Open Drug De J* **2008**, *2*, 61 – 70.

(5) R, R. J. *Controlled drug delivery*; Lee, V. H. L., Ed.; Marcel Deckker, Inc.: New York, Basel, 1987.

(6) Dash, S.; Murthy, P. N.; Nath, L.; Chowdhury, P. *Acta Poloniae Pharmaceutical-drug Research.* **2010**, *67*, 217–223.

(7) Costa, P.; Manuel, J.; Lobo, S. *European J. of Pharm. Sci.* **2001**, *13*, 123–133.

(8) Ritger, P. L.; Peppas, N. A. *J. Controlled Drug release* **1987**, *5*, 37–42.

(9) Ritger, P. L.; Peppas, N. A. *J. Controlled Drug release* **1987**, *5*, 23–36.

(10) Peppas, N. A.; Sahlin, J. J. *Int'l J. Pharmaceutics* **1989**, *57*, 169–172.

(11) Muzzarelli, R. A. A. *Chitin*; Pergamon: Oxford, UK, 1977.

(12) Xie, H. B.; Li, S. H.; Zhang, S. B. *Green Chem.* **2005**, *7*, 606.

(13) Yang, R.; Fu, Y.; Li, L.; Liu, J. *Spectrochimica Acta Part A.* **2003**, *59*, 2323–2332.

(14) Sahoo, S.; Chakraborti, C. K.; Behera, P. K. *Asian Journal of Pharmaceutical and Clinical Research* **2012**, *5*, 5–10.

(15) Zhou, Z.; Xiao, Y.; Hatton, T. A.; Chung, T.-S. *j. membrane sci.* **2009**, *339*, 21–27.

(16) Ravelet, C.; Peyrin, E. *J. sep. sci.* **2006**, *29*, 1322–1331.

(17) Wistuba, D.; Schurig, V. *J Chromatogr. A.* **2000**, *875*, 255–276.

(18) Li, J. Z.; Grant, D. J. W. *J. pharmaceutical Sci.* **1997**, *86*, 1073–1074.

(19) Xiao, Y. C.; Chung, T. S. *Journal of Membrane Science* **2007**, *290*, 78–85.

(20) Wang, H.-D.; Chu, L.-Y.; Song, H.; Yan, J.-P.; Xie, R.; Yang, M. *j. membrane sci.* **2007**, *297*, 262–270.

(21) Zhou, Z.; Cheng, J.-H.; Chung, T.-S.; Hatton, T. A. *j. membrane sci.* **2012**, *389*, 372–379.

(22) Tegos, G. P.; Demidova, T. N.; Arcila-Lopez, D.; Lee, H.; Wharton, T.; Gali, H.; Hamblin, M. R. *Chemistry & biology* **2005**, *12*, 1127–35.

(23) Mashino, T.; Nishikawa, D.; Takahashi, K.; Usui, N.; Yamori, T.; Seki, M.; Endo, T.; Mochizuki, M. *Bioorganic & Medicinal Chemistry Letters* **2003**, *13*, 4395–4397.

(24) Aoshima, H.; Kokubo, K.; Shirakawa, S.; Ito, M.; Yamana, S.; Oshima, T. *Biocontrol Sci.* **2009**, *14*, 69–72.

(25) Nakamura, S.; Mashino, T. *Journal of Physics: Conference Series* **2009**, *159*, 012003.

(26) Zhang, H.-M.; Li, Z.; Uematsu, K.; Kobayashi, T.; Horikoshi, K. *Archives of microbiology* **2008**, *190*, 605–9.

Chapter 5. APPLICATIONS OF NEAR INFRARED SPECTROSCOPY

5.1. Discriminating pulmonary hypertension caused by monocrotaline toxicity from chronic hypoxia by Near-Infrared spectroscopy and multivariate methods of analysis

5.1.1. Background

Monocrotaline (MCT) produces pulmonary hypertension and right ventricular hypertrophy in rats.[1] MCT is a pyrrolizidine alkaloid and is present in a variety of plant sources including in the seeds of *Crotalaria* species.[2] It has been found that a single intraperitoneal (ip) injection (60-90mg/kg) of MCT in rats leads to a sustained elevation of pulmonary pressure and right ventricular hypertrophy in the subsequent 2 to 3 weeks with clinical features that resemble human idiopathic pulmonary hypertension.[3,4] Generally, it believed that MCT must undergo hepatic metabolism to some reactive metabolites that are subsequently transported to the lungs to induce a pneumotoxic response.[1] MCT appears to require biotransformation in the liver to a reactive species that subsequently circulates to the lungs where it initiates a pneumotoxic process.[5,6] Hepatic metabolites of MCT are still yet to be identified, however, the electrophilic dehydrogenation product monocrotaline pyrrole has been implied for many years to be the ultimate toxin.[7,8] Also, the exact mechanism by which MCT causes pulmonary toxicity is still not completely understood. A technique which can noninvasively detect, identify MCT and all of its intermediate(s) and product(s) during its biochemical transformation processes is therefore required. Near-infrared spectroscopy, with its deep

tissue penetration capability (from Near-IR light) and ability to provide chemical composition and structure in a sample may be able to provide some useful information in the mechanism of MCT toxicity.

The purpose of this study was to determine if it is possible to synergistically combine NIR measurements with multivariate methods of analysis to chemically detect and identify, directly on lung tissues, not only MCT but also any alterations on lung tissues caused by MCT.

5.1.2. Materials and Methods

Samples used were histological slides prepared from lung tissue of rats (Sprague–Dawley and Fawn-Hooded). These samples were prepared at the Clement J. Zablocki VA Medical Center, Milwaukee by Professor Robert C. Molthen. One set of animals was left under normal conditions, another was subjected to chronic hypoxia (CH) and the last set was given a single subcutaneous injection (60mg/kg) of monocrotaline (MCT) and raised in room air. The CH exposure was achieved by housing the animals in chambers maintained at 10% O_2. CH is also known to cause PH, but through significantly different mechanisms than monocrotaline exposure.

All rats also had Partial Left Pulmonary Artery Occlusion (PLPAO) surgery in which the left pulmonary artery is banded at a fixed diameter approximately 1/3 of its normal value. This had the effect of reducing blood flow to the left lung and increasing the flow in the right lung. In one set of animals, PLPAO surgery was done on the third day after exposure to MCT and in another set, it was done three days before MCT exposure. All the studies were done under approval of the Zablocki VA Medical Center

IACUC review board and in compliance with the National Research Council's Guide for the Care and Use of Laboratory Animals.[9]

After 24-days, the rats were anesthetized with sodium pentobarbital (40 mg/kg, imp), heparinized (200 IU/kg) through right ventricular injection and the lungs excised, distended and fixed with a 10% buffered formalin solution. The lungs were then paraffin embedded, 4 um thick sections were prepared on slides and stained with hematoxylin and eosin. The slides were measured without any further treatment. Near-infrared (NIR) spectra were taken on the home-built NIR spectrometer based on an acousto-optic tunable filter. This NIR spectrometer has been described in detail in our previous papers.[13-15] Unless otherwise stated, each spectrum at a single position in a slide was an average of 2000 spectra taken at a 2-nm interval from 1300 to 2100 nm. The absorption of each sample was measured on 6 different locations. Not only did this increased the sample size, but also facilitates determination of variation within a sample. Information on spatial distribution of PH in the sample tissues can be obtained by this procedure.

A total of 180 spectra were obtained for analysis of the right lung. Each of the three groups, normal right lung, CH right lung and MCT right lung had 60 spectra. Out of the 60 spectra of each group, we used 54 spectra to construct the calibration model, with the remaining 6 spectra for unknown. The left side samples had 20 spectra for each group. 16 samples from each group were used for calibration leaving 4 samples for unknown. Since there was no independent validation set in this analysis cross validation method was used. Multivariate analysis was done on the raw spectra without any preprocessing using Unscrambler version 9.2 (Camo ASA), similar to the procedures used in previous publications. [13-15]

5.1.3. NIR and FT-IR spectra of tissue samples

The NIR and FT-IR spectra for normal, CH and MCT treated lung tissue cells are shown in Figure 5.1 and Figure 5.2. In NIR the absorption is very small and the spectra for the three different samples look very similar. It will be very difficult to distinguish these three samples just by inspecting their NIR spectra.

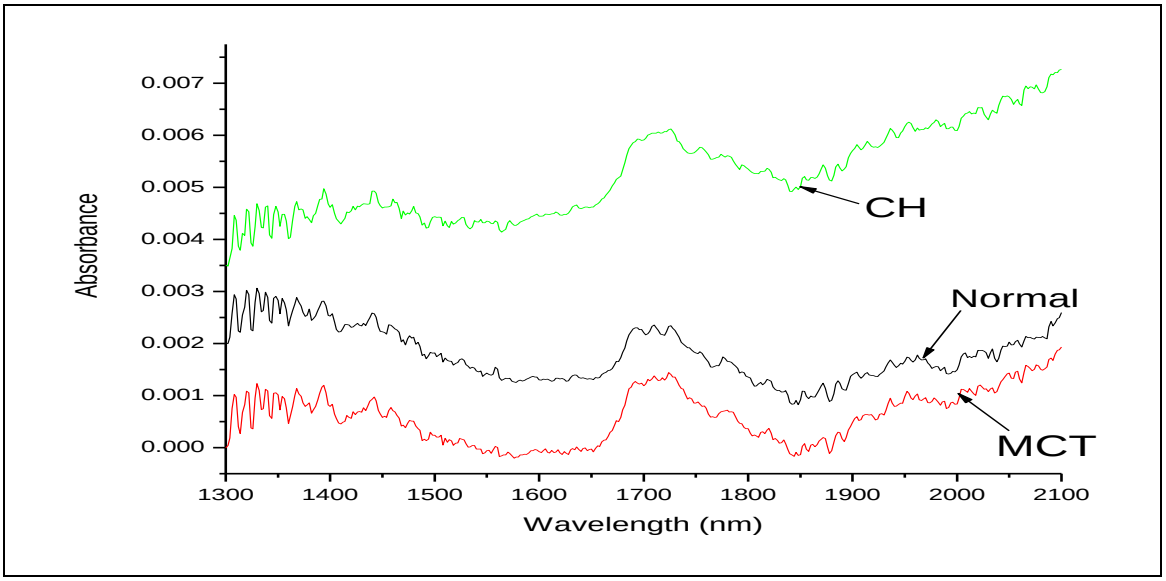

Figure 5.1: NIR spectra for normal, CH and MCT treated lung tissue

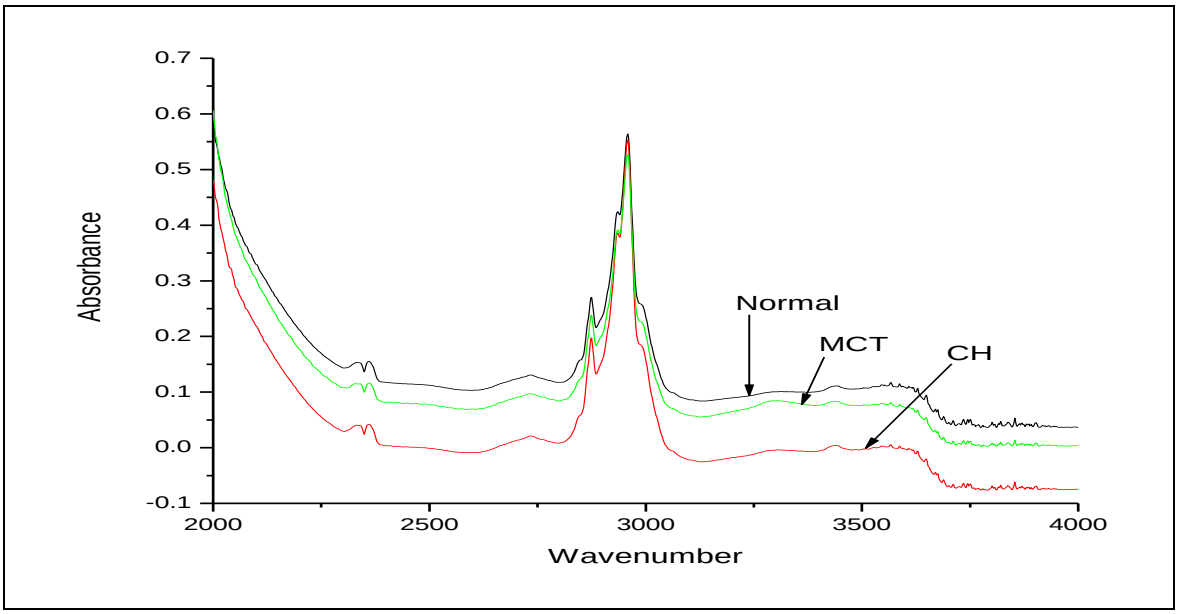

Figure 5.2: FT-IR spectra for normal, CH and MCT treated lung tissue

Similarly, the FT-IR spectra of the three samples also look too similar to classify the samples just by visual inspection. There are differences in these spectra however small, which can be found at many different wavelengths. It is these kinds of differences which are well suited for multivariate analysis by chemometric techniques such as Principal Component Analysis (PCA) and Partial Least Squares (PLS). By applying these techniques to the NIR and FT-IR data, it should therefore be possible to distinguish the different kinds of tissue cells in Pulmonary Hypertension.

5.1.4. Principal Component Analysis

Principal Component Method of Analysis is very useful when studying the relationship between samples and variables. Principal component analysis is a variable reduction procedure. It is useful when data has been obtained on a number of variables (possibly a large number of variables), and it is believed that there is some redundancy in those variables. In this case, redundancy means that some of the variables are correlated with one another, possibly because they are measuring the same construct. Because of this redundancy, it should be possible to reduce the observed variables into a smaller number of artificial variables (called principal components, PCs) that will account for most of the variance in the observed variables. The variables in this case are the NIR or FT-IR absorbances of the different samples. A PCA model was therefore used to determine if there is any systematic variation in the different types of lung tissue samples based on their NIR spectral data. A total of 108 NIR spectra were used for this model, 36 spectra for each sample type; normal, CH and MCT. The first task was to study the variation between the different groups; that is whether the samples can be separated into their respective groups.

All the sample types were from the right side of the lung. Figure 5.3A shows the 3D scores plot obtained from this model for the first three components; i.e., (principal components) PCs 1, 2 and 3. Scores plot describe the data structure in terms of sample patterns, it can therefore be used to study differences and similarities among samples.[16] As illustrated, the samples are not randomly scattered. Rather they systematically fall into 3 nearly distinct groups corresponding to the sample types. The normal samples are

relatively well separated from the other two groups. This distinction is clearly illustrated in Figure 5.3B which is a line plot of the sample scores along PC 3. It can be seen from Figure 5.3B that along this PC, most normal samples have positives scores while the CH and MCT samples have negative scores. This clearly indicates that PCA can distinguish normal samples from PH samples. However some degree of overlap was observed between the CH and MCT samples. This is expected since both of these sample groups have pulmonary hypertension, only to a different degree. The results clearly demonstrate that different lung tissue samples can be classified into their respective groups by use of the PCA method to analyze their NIR spectra.

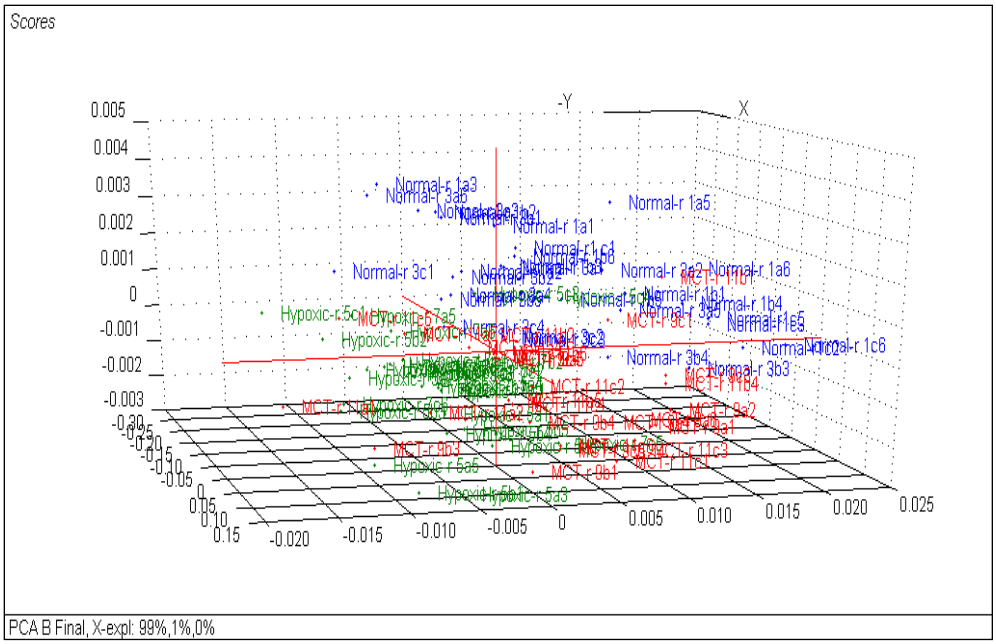

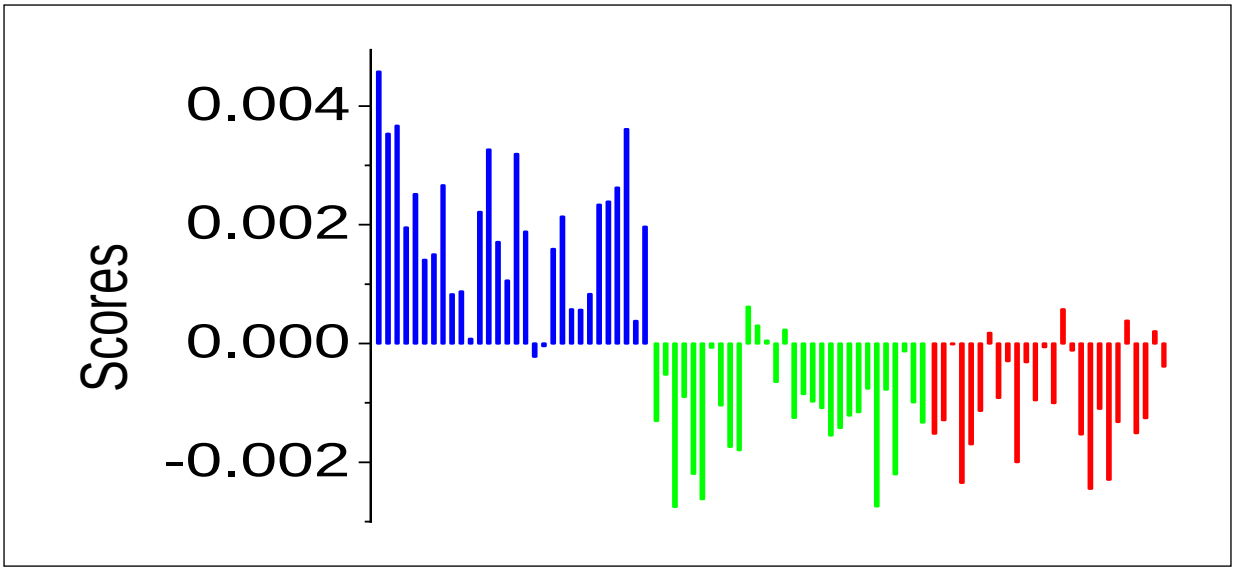

Figure 5.3: PCA 3D scores plot (top) and line plot of the sample scores along PC3 (bottom). In both graphs, normal samples are in blue, CH in green and MCT in red.

The PCA loadings form this model were used to gain insight into the variables (i.e., spectral range) that are contributing most to the observed differences. This was accomplished by performing a PCA analysis on each sample group separately. Such treatment allows the comparison of the PC loading spectra of the different sample types which, in turn, make it possible to determine how and in which spectral range they are different. PCA loadings describe the data structure in terms of variable correlations. Each variable has a loading on each PC, and this reflects how much that variable contributes to that PC.

The PCA spectral loadings for the first 3 components for the analysis of each sample group are shown in Figure 5.4. The loading spectra show that the greatest variation in the loadings for the different samples occurs in the region 1600 nm to 1800 nm. This could be the most important spectral region in describing the variation of the three sample types. There is no single PC where all the loading spectra for the three sample types are all different. However, the CH loading spectrum is clearly different from the loading spectra of normal and MCT samples for PC 2 while the MCT loading spectrum is clearly different from those of normal and CH for PC 3. These results seem to suggest that CH samples can be distinguished from the others using PC 2 while MCT samples can be distinguished from the others along PC 3.

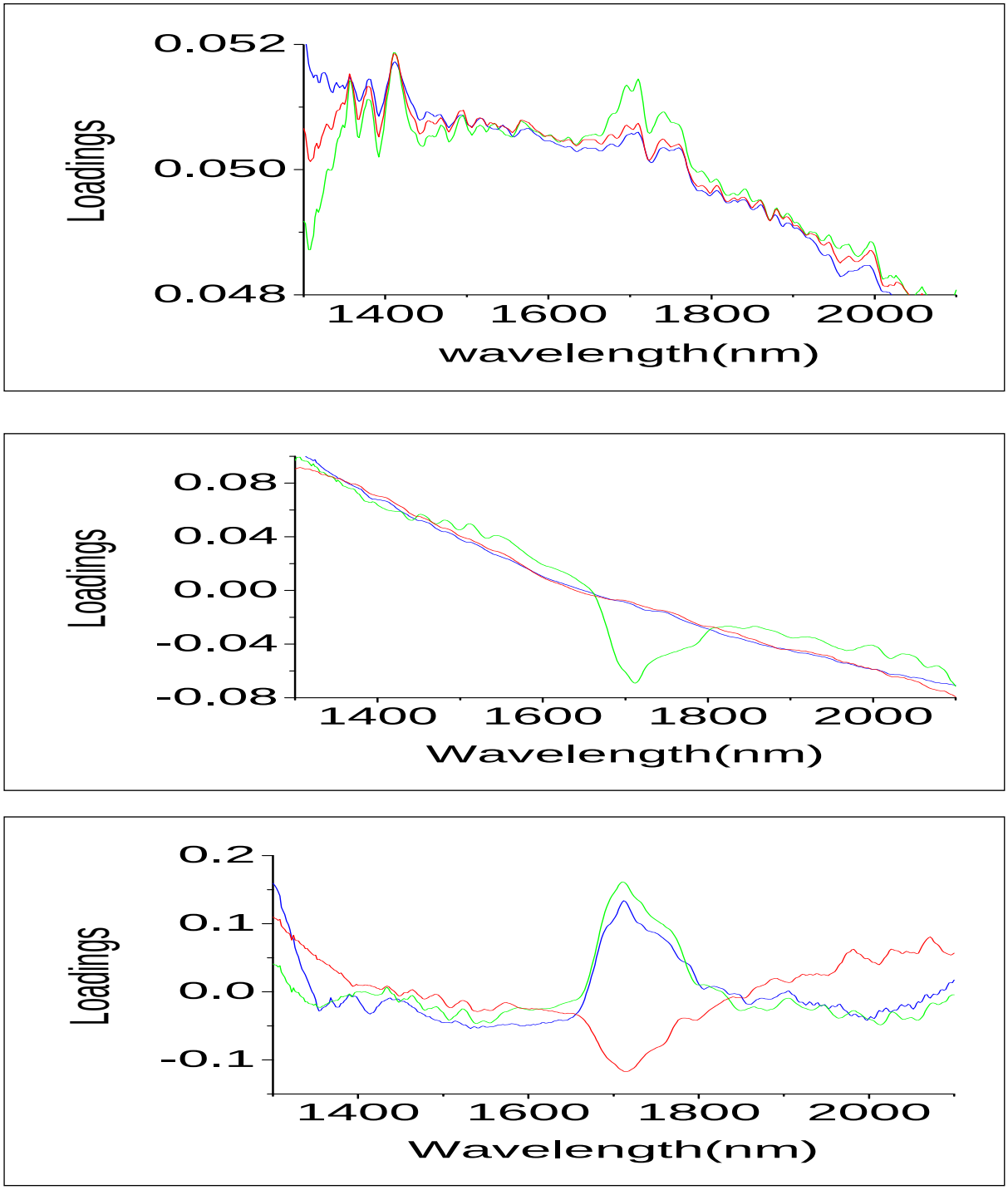

Figure 5.4: PCA Loading spectra for PC1 (top), PC2 (middle) and PC3 (bottom). Normal (blue), CH (green) and MCT (red)

These results indicate that CH produced some alterations in the lungs which can be best represented by PC 2 while the alterations of MCT are represented by PC 3. The results also seem to imply that the two conditions, CH and monocrotaline treatment, produce somewhat different chemical transformations in the tissues samples. However, the exact nature of these different chemical alterations cannot be deduced from the set of experiments and data used in this study.

5.1.5. Analysis by Partial Least Squares Regression

In addition to the PCA method described above, PLS method was also used to make models that could be used for prediction of unknown samples. While both methods are designed to extract useful information from NIR spectra of the lung tissue samples they are not the same, and each method has its own advantages. Specifically, the PCA method is performed on the X data matrix without looking at the correlation between the X and Y variables. It is therefore best at studying sample patterns and correlations between samples and variables as illustrated by the discussion and results in the previous section.

PLS on the other hand models both the X and Y data matrices simultaneously to find the latent variables in X that will predict the latent variables in Y the best. PLS is therefore a method of constructing predictive models when the goal is not necessarily on trying to understand the underlying relationships between samples and variables or just among variables, but just to make prediction of the Y variables from the X variables. Since PLS is essentially a regression technique, it was used for predicting unknown sample sets into their respective groups. The information obtained from PCA and PLS

was highly complementary; with PCA being highly useful in understanding the sample – variable relationships among normal, hypoxic and MCT sample groups while PLS was useful in predicting unknown samples into their respective groups. PLS-LDA (Linear Discrimination Analysis) method was used for the analysis of the samples. In this method, the samples are essentially classified into their respective groups before performing the PLS model. Samples were classified by assigning them a value of 1 for the group to which they belong and a value of 0 for the other groups. Since there are three groups, this classification will result in a sample having 3 Y values which allows the use of the PLS 2 method. PLS 2 is different from PLS 1 because at least two Y-variables are used in the former, whereas only one Y-variable is used in the latter.

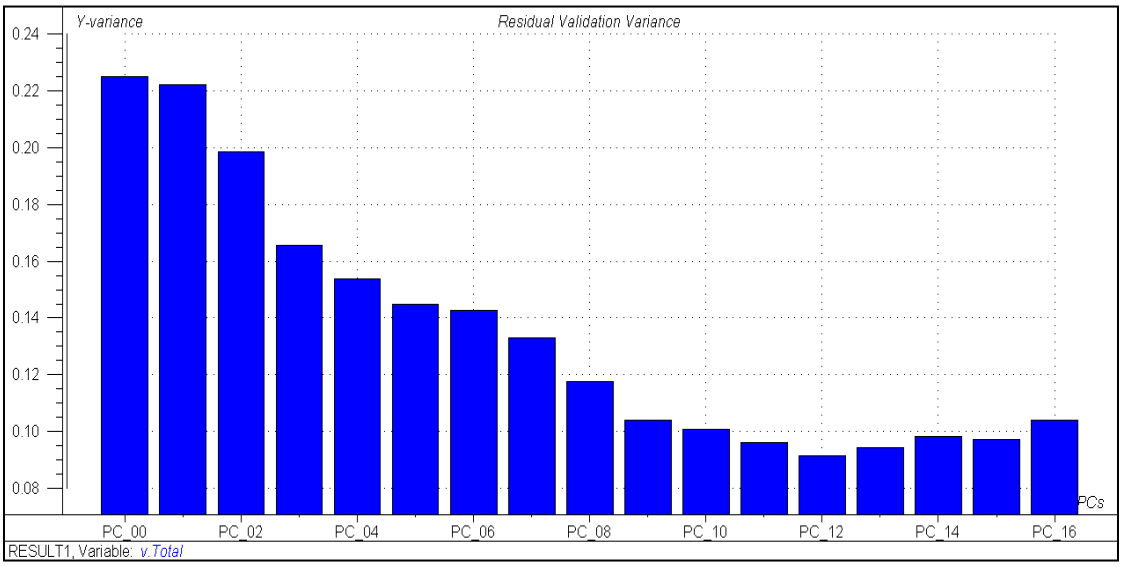

Figure 5.5: Residual validation variance plot from the PLS analysis of NIR spectra

The residual validation variance plot for the PLS model is shown in Figure 5.5. This shows the amount of variation that the model is able to explain. The y-axis in Figure 5.5 shows the variance that is still yet to be explained by the model. In PLS and other multivariate techniques, variation in a given data set is explained by Principal Components (PCs). Components are usually taken to represent sample constituents. However, in their broadest sense, components must be understood to be synonymous with sources of variation. Any independent source of variation will be represented by a component. Even variation due to things like instrument drift or due to different sample cells will constitute components in multivariate data. The components are constructed on a rank by rank basis where the first principal component is designed to span the greatest amount of variation in the data set. The next component spans the greatest amount of variation which was not span by the previous component. Each successive component continue to span the greatest amount of variation left out by the preceding components. This process is continued until all the components have been identified. All the components are made orthogonal to each other. It is clear therefore that each successive component will explain lesser and lesser variation. It is therefore the first few components which contain the greatest amount of information in the data and this is why the components in a residual validation variance plot, represented by bars in Figure 5.5, always decrease with each successive component. The first bar (PC 0) shows the total amount of variation that must be explained. Successive bars (PCs) show the variance that is still to be explained after each PC, hence the name "residual variance". The variation explained by each component will continue to decrease until all the components which contain useful information have been identified. Any increase in the residual variance in

latter PCs is due to over fitting, when the PCs begin to model noise. The actual number of PCs which must be used for any model can be taken to be all those PCs up to the point when residual variance stops decreasing. In the above model, the residual variance decreases up to PC 12, hence this model has 12 components. Any prediction or classification will be based on at most 12 PCs.

It can be seen from figure 5.5 that the greatest decrease in residual validation variance is observed with PC 2 and PC 3. This means that these two PCs can be used to account for a great deal of the variation in the samples that were used to make this model. The clustering of the samples into their respective groups can be studied by looking at the scores plot from this model. On a scores plot, similar samples will appear or cluster together. Since PCs 2 and 3 explains a great deal amount of the variation, a 3D score plot was made with for PC 1, PC 2 and PC 3.In the score plot, shown in Figure 5.6, the samples were separated into three clusters, and, as expected, these clusters correspond to the three different types of lung tissue, namely: normal, MCT and CH. This is similar to the clusters observed with PCA. While there are some overlap of a few samples, the fact that the samples were separated into three corresponding clusters clearly indicate that multivariate analysis of NIR spectra is effective in distinguishing closely related samples such as normal, MCT and CH. Both MCT and CH conditions cause hypertension but it is more in MCT treated samples where lesions are observed. It is quite possible therefore that MCT and CH cells are chemically similar to some extent hence the observed overlap. Overlap with the normal samples is due to any other natural similarities found in tissue cells, especially when they are from the same organ, like these lung cells.

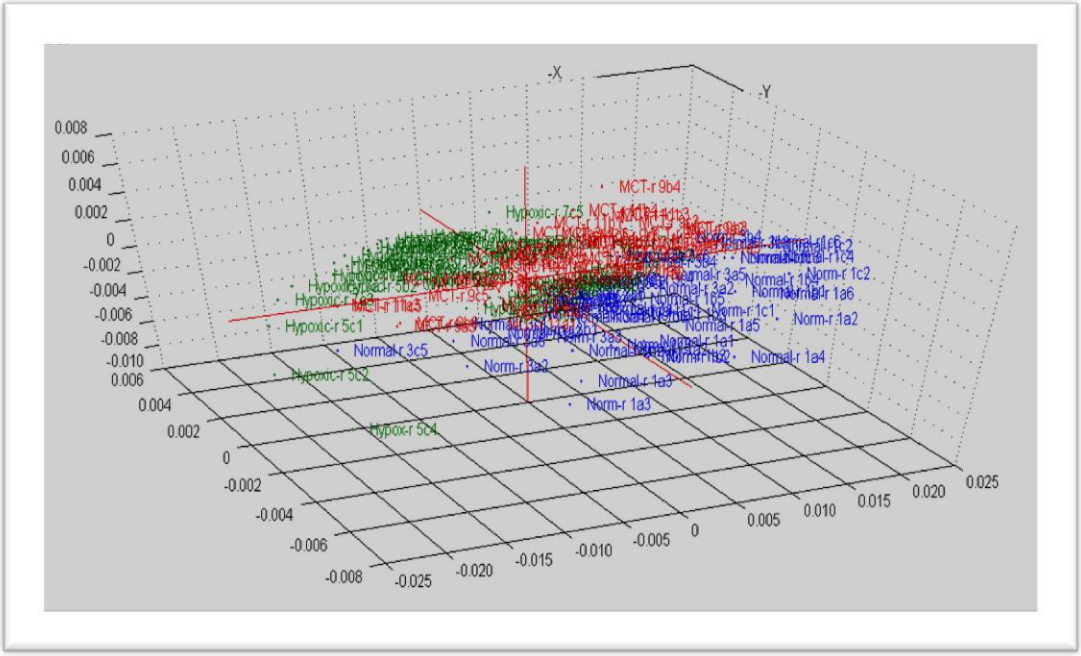

Figure 5.6: Scores plot obtained using PLS 2 –LDA method

As already explained, the axes in the above scores plot are PC1, PC 2 and PC3. It will be informative if we can determine the physical meaning of these PCs. Unfortunately, with the spectral information available now, we can only state that each of these PCs represents a single source of independent variation among the samples. It is not possible to determine the physical nature of these variations except noting that the MCT and CH conditions seem to produce alteration in the tissue such that their NIR signatures are different from normal cells. However. looking at the 3D scores plot, it is clear that by using NIR measurements and chemometric techniques, we are able to distinguish normal, MCT and CH tissue cells on this sample map.

5.1.6. Prediction of unknown samples using PLS Models

Partial Least squares in latent variables (PLS), just like PCA is a factor based multivariate technique but goes further than PCA in that PLS finds factors for both the spectral and the concentration data sets. So PLS is really a regression technique in which we can use the spectral data to predict the concentration data of samples. So by making PLS models using NIR and FT-IR data, it should be possible to predict whether a sample is normal, MCT or CH.

To be able to make PLS models, a second set of variables (the Y-variables) is needed in addition to the spectral data (the X-variables). Since we are studying pulmonary hypertension, the different samples were assigned an arbitrary value of hypertension ranging from 0 up to 1, with 0 being the least value of hypertension and 1 being the highest. Since the greatest amount of hypertension is induced by MCT, all MCT samples were assigned a hypertension value of 1 and the normal samples were assigned 0 since no hypertension is expected in any normal tissue cells. CH samples, which are known to be hypertensive and which are likely to be chemically similar to MCT samples were assigned a hypertension value of 0.6.

It should be noted however that while this assignment of the Y-variables is true in principle, it makes the model very rigid. While it is true that the MCT samples have the highest amount of hypertension, it might not be very correct to assume that they are all 1 or to say all normal samples have a hypertension value of 0. There surely should be some amount of variation, however small, within each group. Our models have not been able to capture this variation. However, this is almost certainly the only information which we

truly know about the samples and by using a large calibration set, it is hoped that good predictions will be obtained.

The first PLS model was made with NIR spectra measured from 1300nm to 2100nm. The calibration set contained about 54 samples for each of the 3 groups i.e. normal, MCT and CH. The calibration results from this model are shown below.

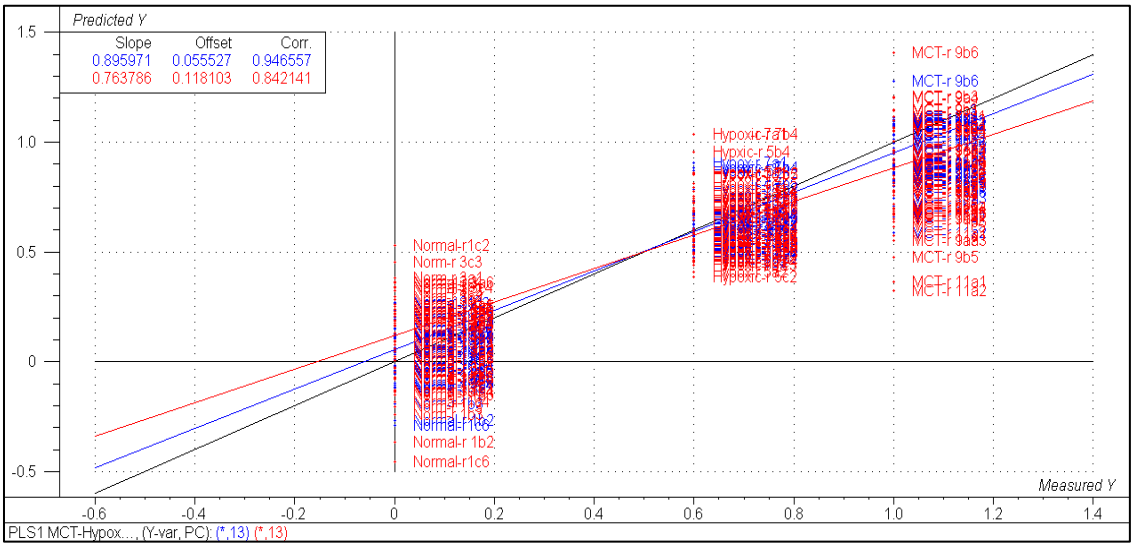

Figure 5.7: Predicted versus measured plot for the NIR PLS model. Black line is target line, blue and red line are calibration and validation curves, respectively.

The black trend line is the target line, the blue is the calibration curve and the red is the validation curve. The validation used in this and all the other models is the full cross validation method. Cross validation was used since there was not enough samples to make an independent validation set. Cross validation is performed by calculating a calibration matrix using all of the calibration samples except one (leave 1 out). The

calibration matrix is then used to predict the concentration of the components in the sample that was left out. The sum-squared errors between the expected and predicted concentrations for this sample are calculated. The procedure is repeated leaving out a different sample until all the samples have been computed.

The NIR model shown in Figure 5.7 has a calibration correlation coefficient of about 0.95. This is fairly high considering the rigidity of our model in terms of the Y-variables and also considering that each slide had to be measured on 6 locations. Just as was observed with the scores plot, there is a considerable amount of overlap in terms of the predicted values (Y-axis) between the CH and MCT samples. The normal samples are better separated from the rest. Also the variation within each group which has not been captured by our model is evident here. The validation correlation coefficient is 0.84. The models were refined by removing outliers and any X-variables (wavelengths) which had relatively small regression coefficients.

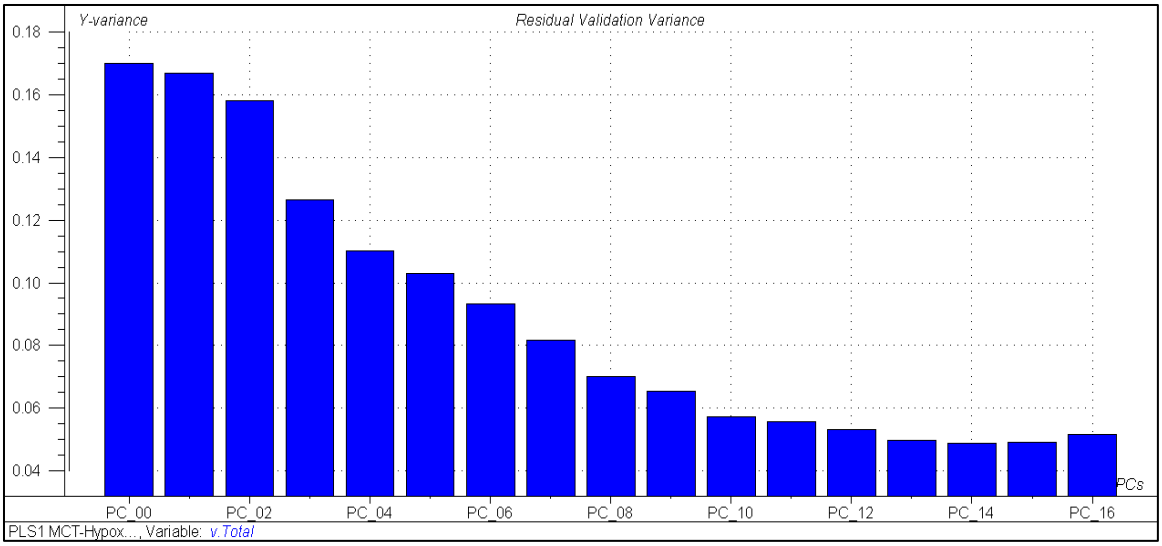

Figure 5.8: PLS1 Residual Validation Variance of the NIR model

The residual validation variance plot for the NIR model is shown in Figure 5.8. As illustrated, the residual validation variance decreases up to PC 13. As explained earlier, this suggest that 13 PCs are required to account for all the variation in the samples. As a result, prediction of unknown samples was done with 13 PCs. There is a larger decrease in residual variance on PC 3, which was also observed with PLS-LDA model (Figure 5.5). This suggests that this PC contains a significant amount of information which can be used to explain the variation in normal, CH and MCT treated samples.

The above model was used to predict a set of normal, CH and MCT samples measured in the same NIR region. The set contained 18 samples, 6 from each group. The prediction results with their deviation is shown in Figure 5.9 below.

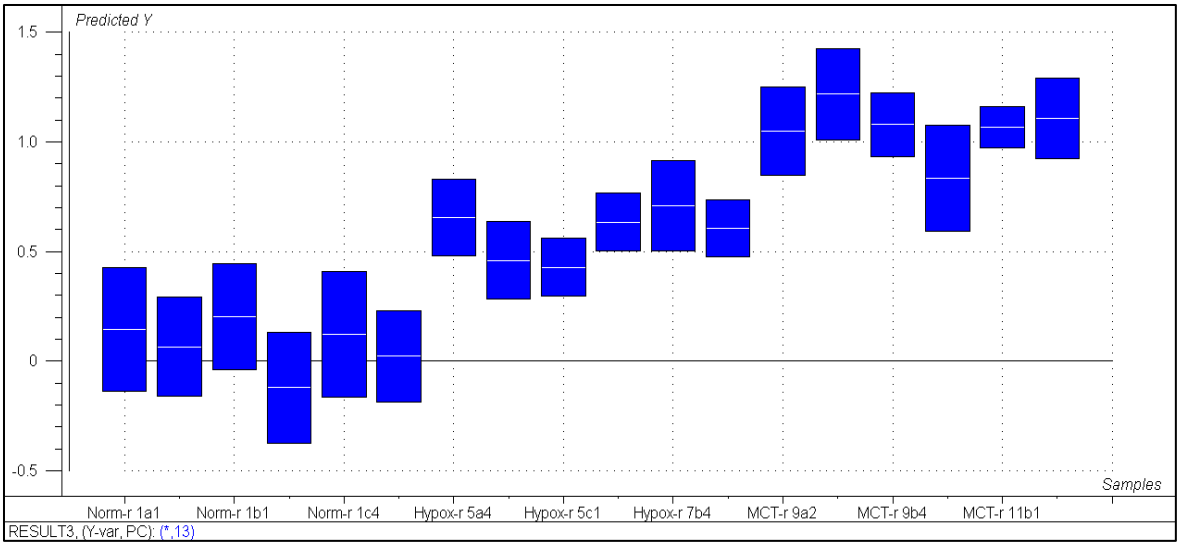

Figure 5.9: Prediction of a set of 'unknowns' with the NIR model

In making the model, all MCT samples were assigned a hypertension value of 1, normal samples were assigned 0 and CH samples were given 0.6. So any sample predicted to be around these values is taken to be belonging to these respective groups. The actual sample groups are indicated below each prediction result along the x axis. The first 6 samples were all normal samples, second 6 were CH and last 6 were MCT samples. As can be seen from Figure 5.7, all normal samples are predicted to be close to 0, the hypoxic samples also appear around 0.6 and the MCT samples are around 1.

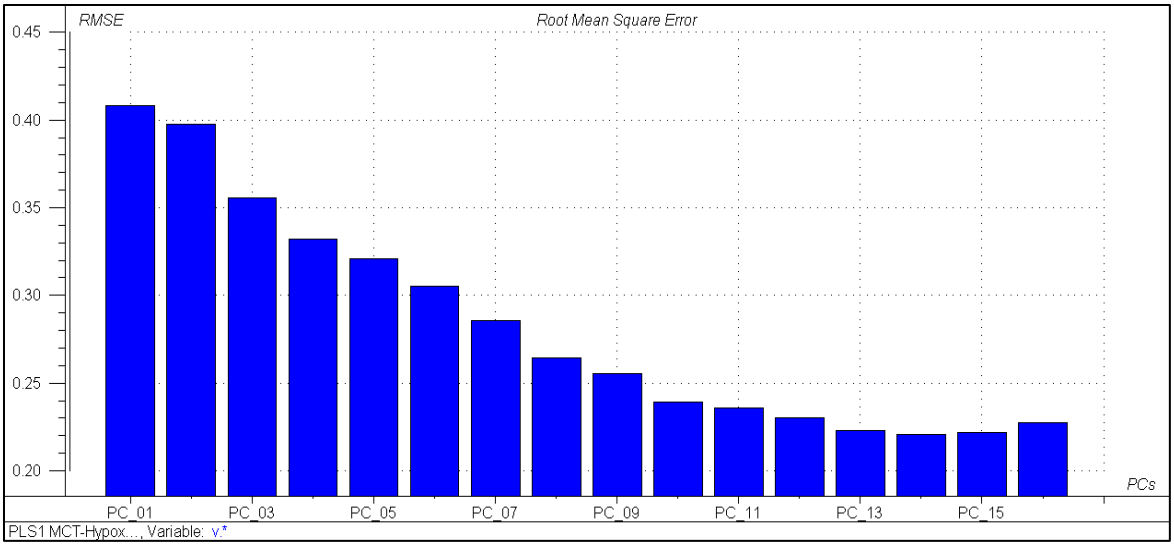

Figure 5.10: Root Mean Square Error of Prediction for the NIR Model

Figure 5.10 shows the Root Mean Square Error of Prediction (RMSEP) for the NIR model. The RMSEP is shown for each component (PC) and it decreases with the components because each successive PC explains less and less variation and hence the error also decreases. Just like the residual variance, the error also decreases up to PC 13, which is the number of components the model requires to explain the variation in the samples. The average RMSEP for this model with 13 PCs is 0.296. The results in Figure 5.9 show that it is possible to distinguish normal cells, CH and MCT treated cells using NIR measurements. Using this model, it was possible to correctly predict most of the unknown samples. Of course the results show that the samples do not all lay in a perfect line at the expected value. This will be expected since there should be some degree of chemical variation in any given tissue sample.

5.1.7. Prediction with the FT-IR Model

Another model was made using the same samples but the measurements were done on a FT-IR spectrophotometer from 4000 cm^{-1} to 2000 cm^{-1}. Since the samples were histological slides stained on glass measurements could not be done below 2000 cm^{-1} because of intense absorption which is most likely due to the glass. The predicted vs. measured plot of the FT-IR model is shown below.

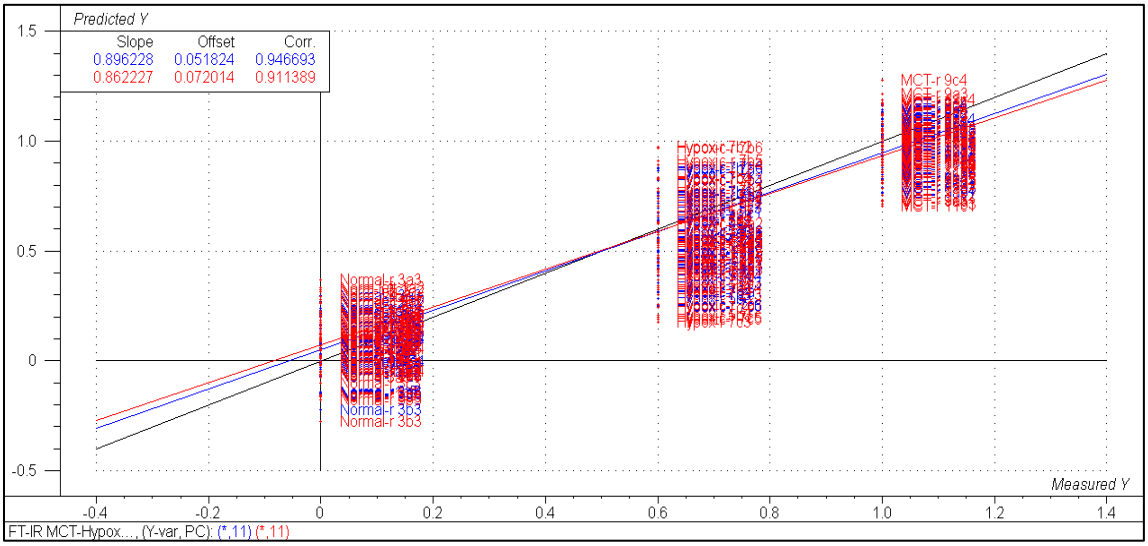

Figure 5.11: Predicted vs. Measured plot for the FT-IR model. Black- target line, blue- calibration curve and red- validation curve.

It can be seen from Figure 5.11 above that the calibration correlation coefficient is high and is the same as for the NIR model (0.95). However, the validation correlation coefficient in this model is much higher (0.91) than in the NIR model (0.84). This seems to suggest that the FT-IR model is more effective in modeling the variation found in the normal, CH and MCT treated tissue cells. The residual variance of this model, shown in Figure 5.12 below, shows a decrease in the residual variance up to PC 11. Each PC seems to be explaining just about an equal amount of variation, unlike in the NIR model where some PCs explained a greater amount of variation than others.

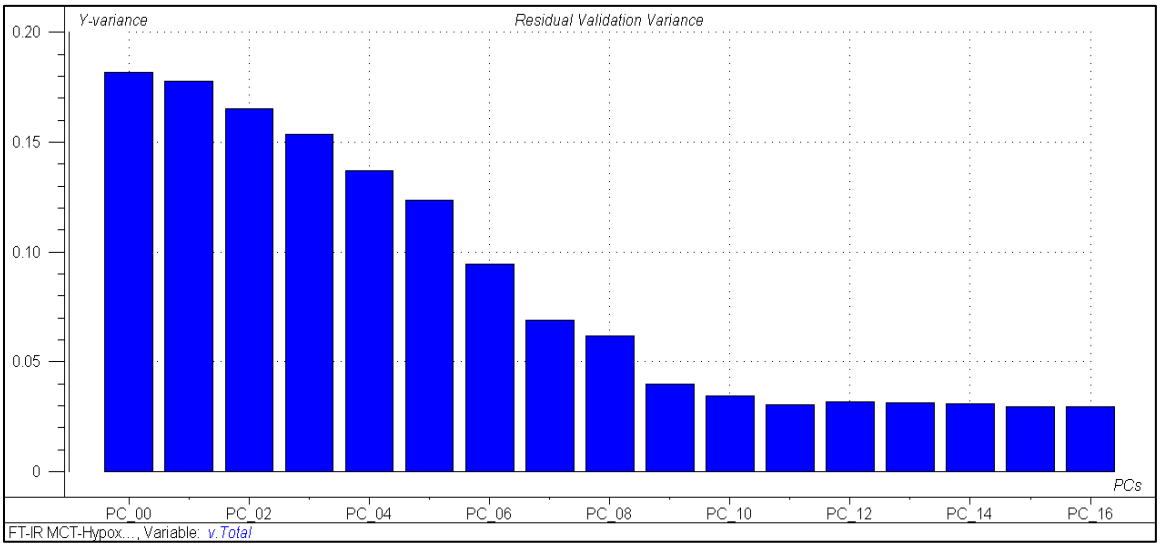

Figure 5.12: Residual Validation variance of the FT-IR model.

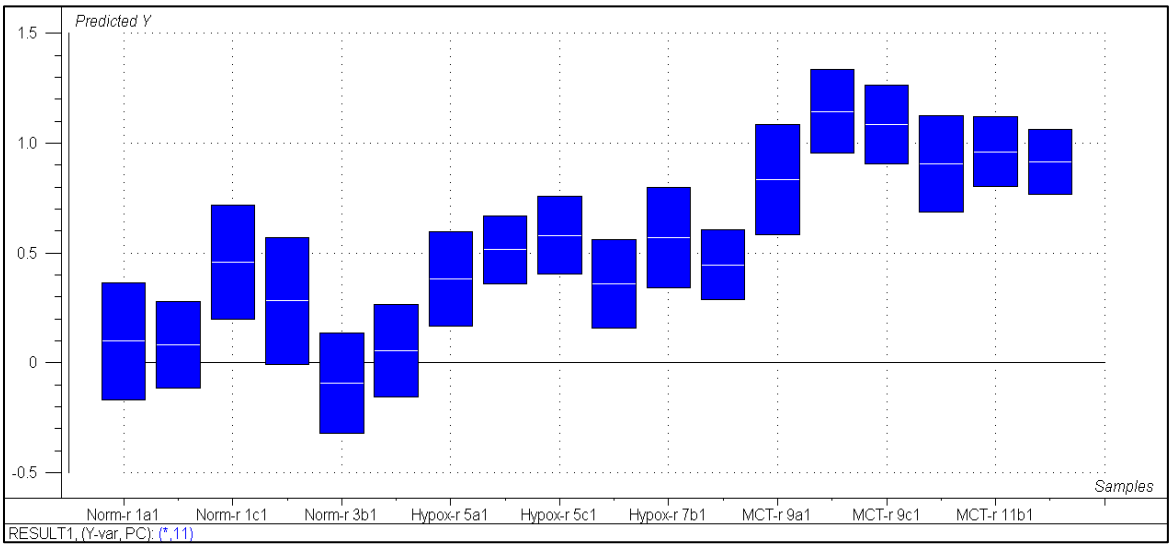

Figure 5.13: Predicted with deviation for the FT-IR model.

The FT-IR model was used to predict the same set of unknown samples used for the NIR model. The results of prediction are shown in Figure 5.13. Just like with the NIR model, it is possible to predict almost all of the samples into their respective groups. However, due to the overlap between these groups of samples, some samples which are expected to belong to a particular group appear slightly different. This could be an indication that tissue cells, especially cells from unhealthy organs, are not chemically homogeneous. For example if a sample is hypertensive due to MCT treatment, it does not necessarily result in all the tissue cells being bad or sick. There are some locations within the tissue that remain good or some that are affected to a lesser extent than others. The normal samples that appear slightly above the normal level could really be just outliers resulting from the many measurements that were done on a single slide. It is possible that on measuring

multiple times on a single slide, there are chances that one can measure an area which is not a true representative of the whole sample, and the result is that this measurement will appear different from the others.

The FT-IR model was shown to have better correlation than the NIR model. However, as illustrated by Figures 5.9 and 5.13,the prediction with the FT-IR model is not as good as that of the NIR model. RMSEP for FT-IR model was found to be 0.302 compared to 0.296 for the NIR model. This could be explained by understanding both the calibration and prediction steps in PLS. As explained earlier, calibration is done on a rank by rank basis. This means regression coefficients for the spectral data are calculated for each component. The prediction step is also done on a rank by rank basis using pairs of spectral and concentration factors or components. The projection of the unknown spectra onto the individual components is calculated and the overall projection is obtained by summing the contributions of the individual components. It therefore should follow that when the individual components do not explain much of the variation as in FT-IR model (Figure 5.12), the prediction will not be as good. The individual components in the FT-IR model do not contain as much information as those of the NIR model even though the total explained variance is larger for the FT-IR model. The better prediction of NIR comes therefore from the fact that there are components which contain much information that explains much of the variation in the samples. FT-IR does not have such individual PCs with a lot of information about the differences in the samples.

5.1.8. Analysis of the Left side samples

The samples used to make all the models discussed above and the models that will follow were made from rat (Sprague-Dawley) lungs which had been subjected to normal, CH and MCT conditions. In addition to this, the animals also had Partial Left Pulmonary Occlusion (PLPAO) surgery done on them. This surgery had the effect of reducing blood flow to the left lung while increasing blood flow in the right lung. The right lungs, which received increased blood flow, have been observed to have increased structural changes reflecting Pulmonary Vascular Remodeling (PVREM) which is associated with hypertension. On the other hand, structural changes were reduced in the left lungs that had reduced blood flow.

NIR and FT-IR analysis was applied to see if the right lung can be distinguished from the left lung by analyzing the spectral data of these samples. The NIR and FT-IR models as described in the previous sections could not be used to predict the left side samples because these samples were not part of the calibration of these models. So new models were made from the NIR and FT-IR measurements but including the left side samples. To simplify the models, the hypoxic samples were left out of the new models. Just as in the first models, the normal right side samples and the MCT right side samples were assigned hypertension values of 0 and 1 respectively. The normal left side samples were also assigned 0 because these animals were not subjected to any hypertensive condition. The MCT left side samples are known to have reduced blood flow and hence reduced PVREM. These were therefore assigned an intermediate hypertension value of 0.5. The calibration results of the two models are shown in Figure 5.14 and 5.15 below.

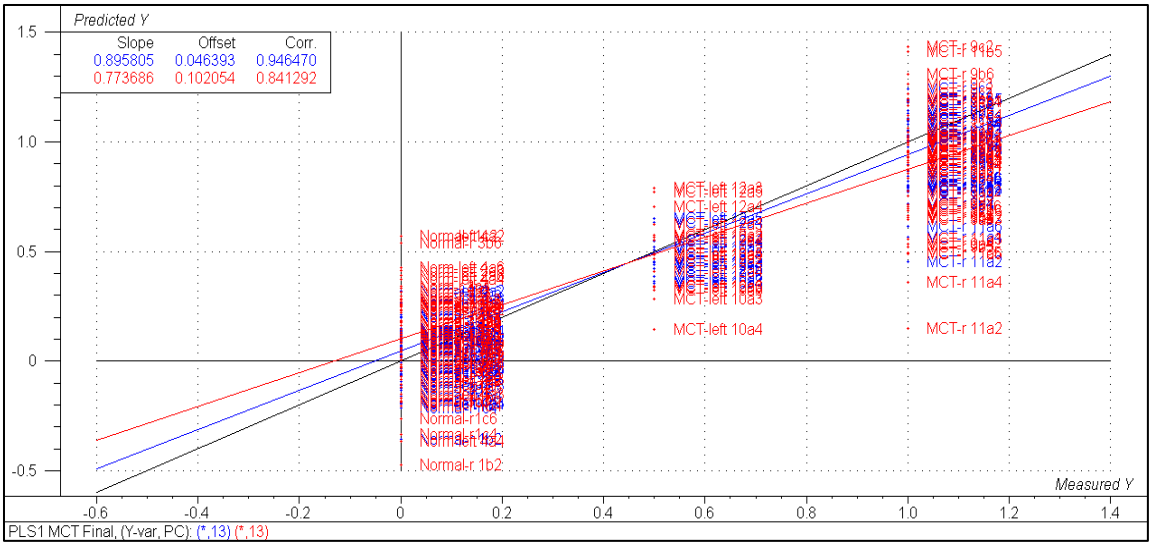

Figure 5.14: Predicted vs. Measured for the NIR MCT model

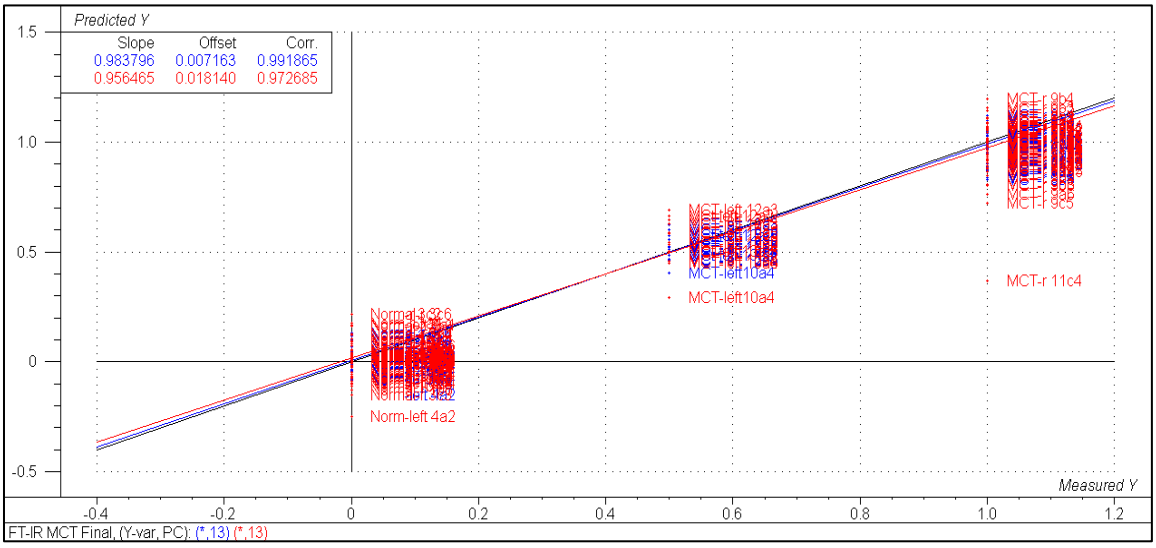

Figure 5.15: Predicted vs. Measured for the FT-IR MCT model

Figures 5.14 and 5.15 show the NIR and FT-IR calibration models that include the left side samples respectively. Calibration correlation coefficients are high for both the NIR and FT-IR models. Just as the case in the previous models, the FT-IR model has a superior validation correlation coefficient (0.97) compared to the NIR model (0.84). The Root Mean Square Error of Prediction for the FT-IR model was 0.276 while that of the NIR model was 0.483. The variation within each group is significantly smaller in the FT-IR model than in the NIR model, and as a result the prediction of the FT-IR model is better for these samples than with the NIR model. It could be because the absorption of the samples in NIR was very small as compared to IR hence it was difficult for the model to clearly distinguish closely related samples.

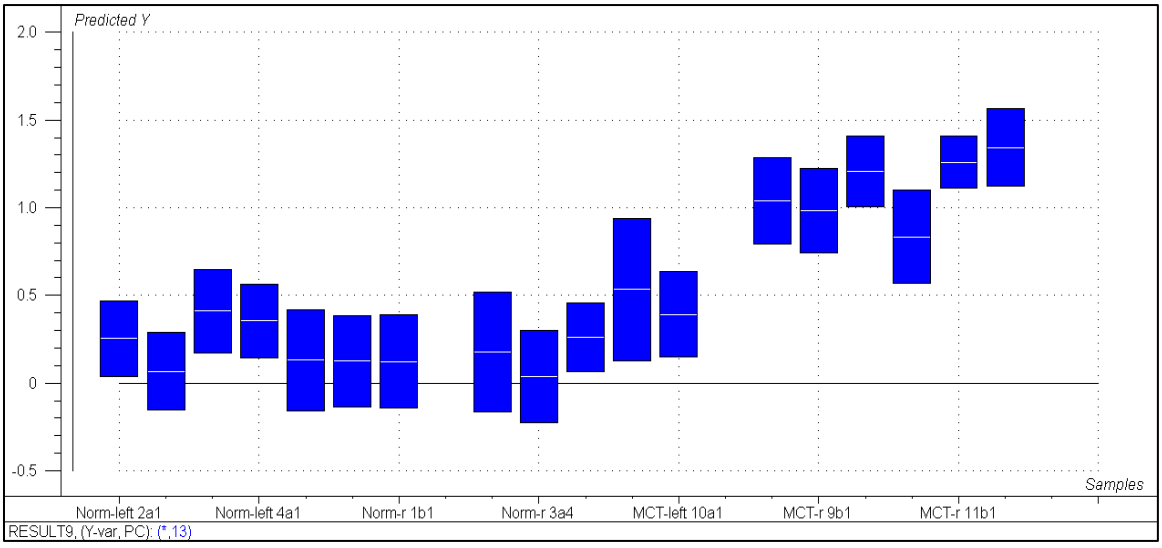

Figure 5.16: Prediction of the MCT left side samples with the NIR model.

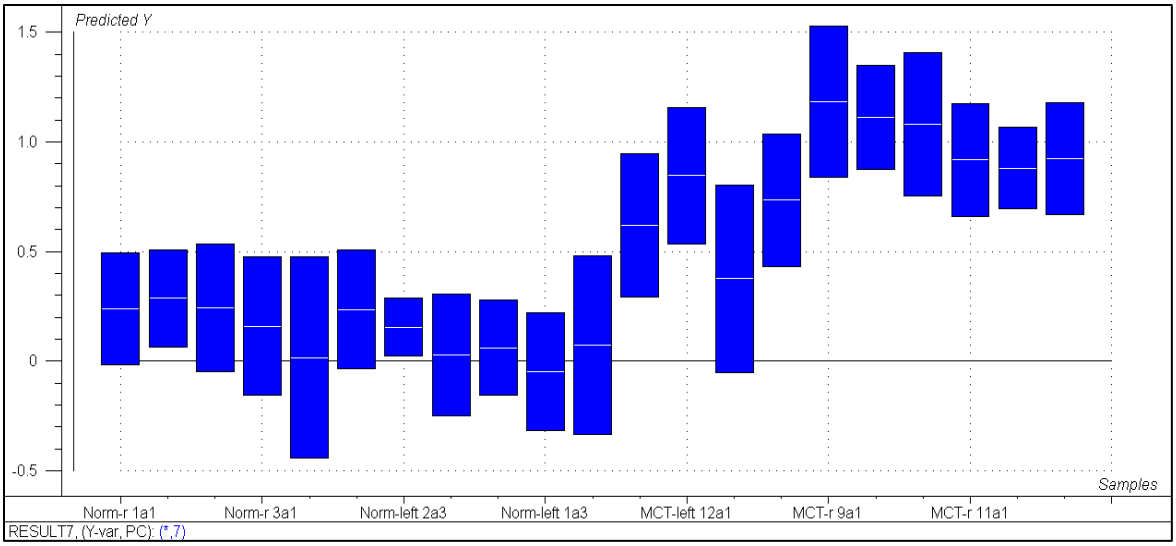

Figure 5.17: Prediction of the MCT left side samples with the FT-IR model.

The results of prediction with the two models are shown in Figure 5.16 and 5.17. Both the NIR and FT-IR models show the same trend, that the left side samples are not as bad as the right side samples. The left side samples still shows some signs of hypertension because even though the blood flow was reduced, metabolites of MCT can still get to this side of the lung because the blood flow was not completely blocked. The FT-IR model is particularly good in predicting the left side samples. Figure 5.16 and figure 5.17 show the normal left side samples appearing just like the normal right side samples. This will be expected since these samples were not exposed to any hypertensive conditions. This shows again that it is possible to distinguish normal (healthy) tissue cells from sick (unhealthy) cells using NIR and FT-IR in conjunction with chemometric methods of analysis.

5.1.9. Pre-PLPAO samples

For all the results described above, the animals had Partial Left Pulmonary Artery Occlusion (PLPAO) surgery done on them first, and then on the third day they were exposed to the different conditions, which are normal, CH and MCT. From the MCT model with the left side samples, we have seen that decreased blood flow to the left side reduces the extent of hypertension which occurred in the cells. It will be interesting to see if there is going to be any significant change in the effect of surgery, if it is done a few days after exposure to the different conditions. So instead of doing the surgery first, the rats were subjected to normal, CH and MCT conditions and on the third day the rats had PLPAO surgery done on them. The experiment was continued as before and both NIR and FT-IR models were created for these samples. Sample types, pre-PLPAO and post-PLPAO were included in the model.

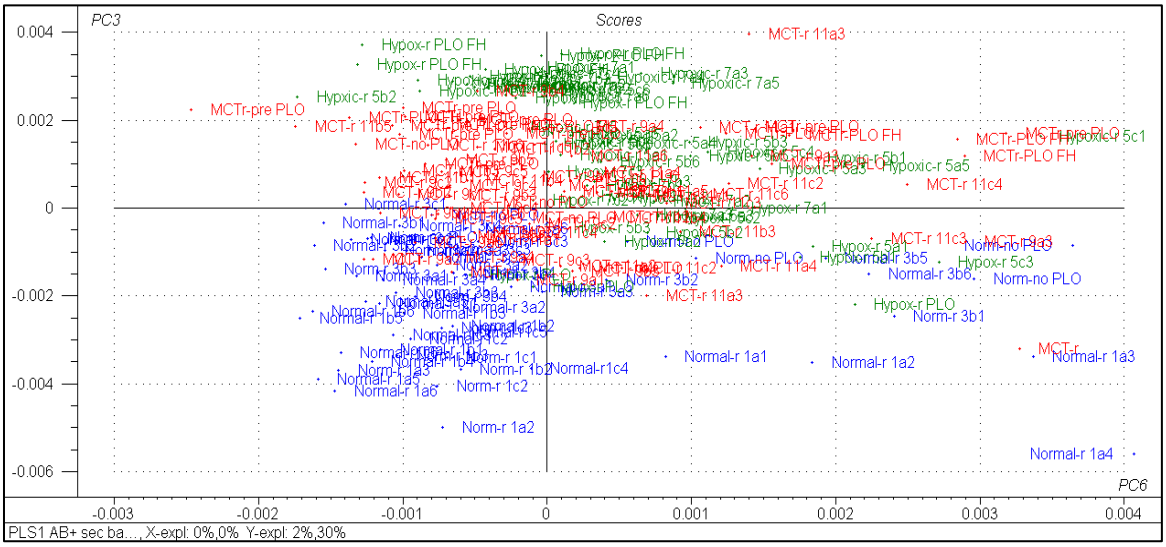

Figure 5.18: Scores plot for the NIR model

Figure 5.18 shows the scores plot of the NIR model that includes the pre-PLPAO MCT samples. As we move up PC 3 on the left part of the map, we can clearly see the separation of the three groups of samples. We encounter normal samples first, followed by MCT samples and finally hypoxic samples. This PC can be said to contain most of the information that has to do with the difference among the three groups of samples. On the right side of the map, there is greater overlap among the samples especially the MCT and CH samples. This is not much surprising especially the overlap between MCT and CH because these samples could be chemically similar. And again like in the previous NIR models, the greatest separation is in the direction of PC 3, which might imply that it is this PC that carries most of the information that explains the chemical differences found in normal, CH and MCT samples. It should also be noted that there is no clear systematic separation of the pre-PLPAO MCT samples from the rest of the MCT samples on this scores plot. This is an indication that there is no much difference between pre-PLPAO and post-PLPAO surgery in the MCT samples.

The NIR model had a calibration correlation coefficient of 0.89 and the validation coefficient was 0.77. The RMSEP for this model is 0.232. This model was used to predict the pre-PLPAO and post-PLPAO MCT samples. The results of which are shown in Figure 5.19 below.

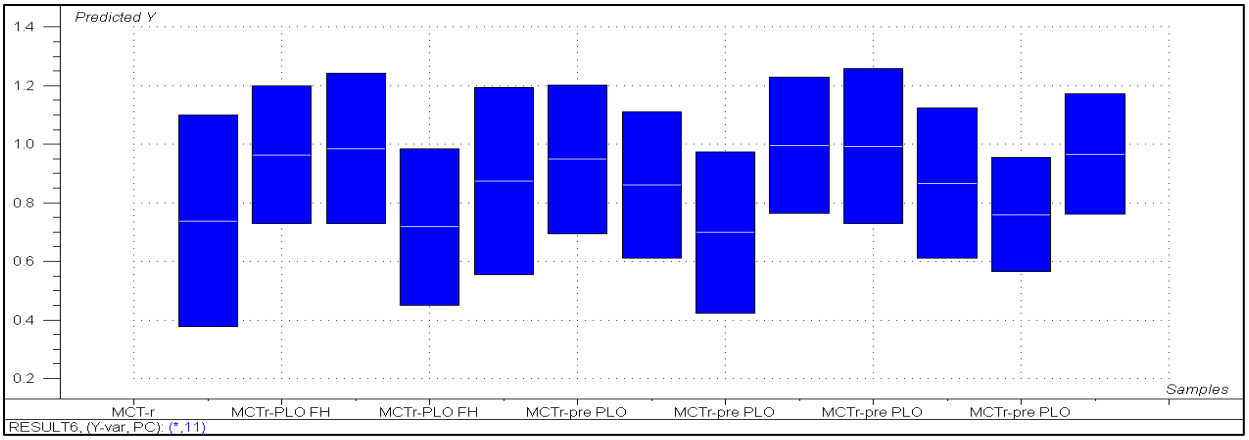

Figure 5.19: Prediction of pre-PLPAO and post-PLPAO MCT right side samples with NIR model.

Most of the samples appear close to 1 which is expected of MCT samples. The first 5 samples in Figure 5.19 had surgery before exposure to the different conditions (post-PLPAO), and the remainder of the samples had surgery on the 3rd day of exposure (pre-PLPAO). As can be seen, there isn't any significant difference between these samples. This shows that pre-PLPAO and post-PLPAO will basically lead to the same amount of hypertension and they are chemically indistinguishable too. Four of the post-PLPAO samples were from rats of a different species (Fawn Hooded) and it shows here that there is no difference in the way these animals respond to the different conditions.

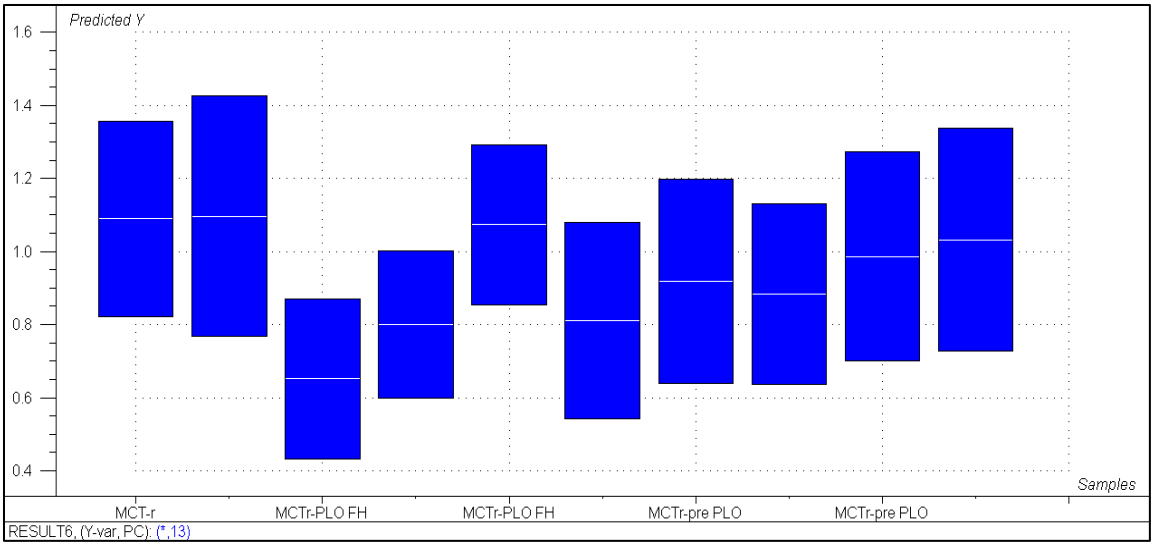

Figure 5.20: Prediction of pre-PLPAO and post-PLPAO MCT right side samples with the FT-IR model

An FT-IR model was created and used to predict the same sample used above for the NIR model. The results of prediction are shown in Figure 5.20. Similar to the NIR model, most samples appear around 1 in the FT-IR model and there is not much difference between the post-PLPAO samples and the pre-PLPAO samples. The pre and post-PLPAO MCT left side samples were also predicted using the FT-IR model, and the results are shown in Figure 5.21.

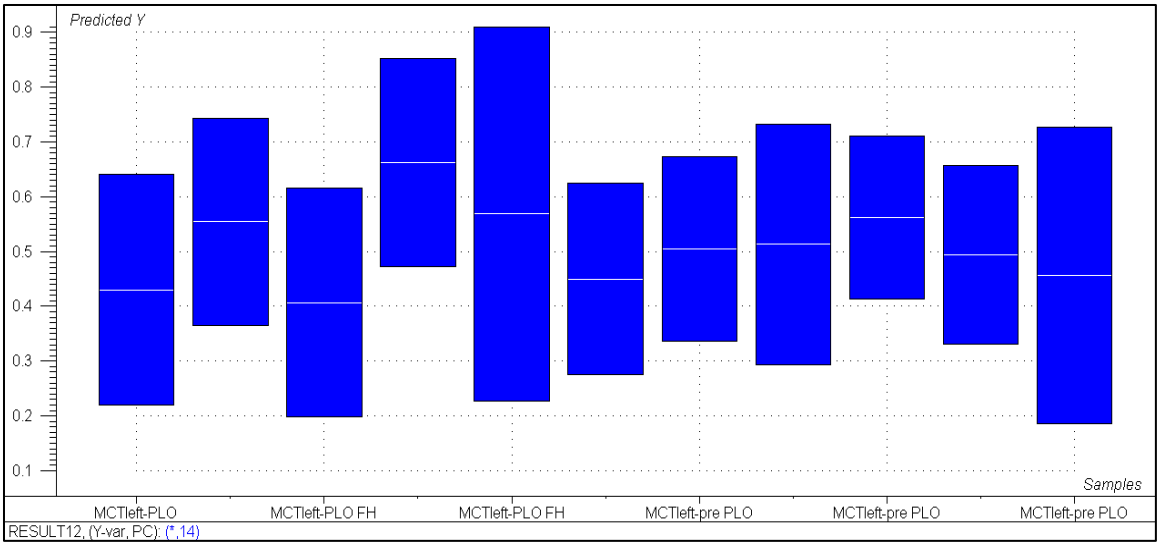

Figure 5.21: Prediction of PLPAO MCT left side samples using the FT-IR model.

As illustrated, most of the samples lay around 0.5. This is what is expected of the left side samples since there is decreased blood flow to this side of the lung as a result of the PLPAO surgery. This is another indication that indeed the PLPAO surgery mitigates the PVREM that is caused by hypertensive conditions. Another important observation that is made from Figure 5.21 is that there seem not to be any significant difference between the pre-PLPAO and post-PLPAO samples. This is in agreement with observation made with the MCT right side samples described above.

In summary, multivariate analysis of NIR and IR spectral data was able to distinguish between normal and hypertensive tissue cells. The normal, hypoxic and MCT samples were clearly separated on PLS scores plots. Using NIR and FT-IR PLS models, it was possible to successfully predict normal, hypoxic and MCT samples into their respective groups. In addition, NIR and FT-IR PLS models were able to distinguish MCT left side samples which received low blood flow, from MCT right side samples which

had high blood flow, thereby confirming that PLPAO surgery mitigates PVREM in lungs. Both NIR and FT-IR PLS models showed that PLPAO surgery before and after exposure to different hypertensive conditions will generally lead to the same amount of hypertension in the animals.

5.2. Determination of Chemical Homogeneity of Polymeric Nanocomposite Materials by Near-Infrared Multispectral Imaging Microscopy

5.2.1. Background

Multispectral Imaging Microscopy

A multispectral imaging spectrometer is an instrument that is able to simultaneously record spectral and spatial information about a sample.[10–14] Unlike conventional imaging techniques, which rely on recording a single image using either single or multiwavelength light for illumination, the multispectral imaging technique records a series of several thousand images, each image at a specific wavelength (spectra of images). That is, it measures absorption spectra of a sample not at a single position, as is the case for a conventional spectrophotometer, but simultaneously at many different positions within a sample (by using a focal plane array detector rather than a single channel detector).[10–14] Chemical composition and structure at different positions within a sample can be elucidated from such images. A novel near-infrared multispectral imaging (NIR-MSI) microscope that employs an acousto-optic tunable filter (AOTF) for rapid spectral tuning and a microscope for higher spatial resolution was previously developed in our lab.[11–13,15,16] This NIR-MSI system was used in the current studies to determine chemical homogeneity of polymeric composite materials.

5.2.2. Materials and Methods

The NIR images were measured using a NIR microscope imaging system that is based on an acousto-optic tunable filter with a liquid N_2 cooled, 320x256 pixel indium antimonide (InSb) focal plane array camera (Santa Barbara Focal Plane, Goleta, CA) as the detector. This system has a resolution of about 0.93μm. Polyethylene (PE) polymer films to which undecenoic acid (a C-11 carboxylic acid) intercalated Mg-AL Layered Double Hydroxide (LDH) has been added were used as the samples. These samples had a loading of about 20% w/w of the LDH. Images of the samples at different locations were recorded using the NIR microscope imaging system in the region 1400 nm up to 2600 nm at 2 nm intervals with 1ms exposure time. Since the polymer films were relatively thin, the measurements were easily done in the transmission mode.

NIR spectra for the samples were calculated from these images for this entire range using an in-house programme. ImageJ was used to calculate the absorption images at the wavelengths of interest. 3D surface plots at these wavelengths were also calculated using ImageJ. Some of the results were further analyzed using MATLAB software package.

5.2.3. Chemical inhomogeneity of polymeric composite materials

Figure 5.22 shows the NIR absorption spectra of polyethylene (PE) films to which different amounts (% w/w) of the Magnesium-Aluminum Layered Double Hydroxide (Mg-Al LDH) intercalated by undecenoic acid (a C-11 carboxylic acid) has been added. This LDH was added to improve the flame retardant properties of the polyethylene. The

NIR spectrum of a pure polyethylene film is also shown in the same figure. It is evident from this figure that the broad absorption band observed around 1950 nm is due to the added LDH, and the absorption increases linearly with the amount of LDH added. This linear relationship is clearly illustrated in Figure 5.23. The absorption band at around 1758nm is due to the polyethylene substrate and as expected, it does not change significantly for the different composites as PE is the major constituent of these composites.

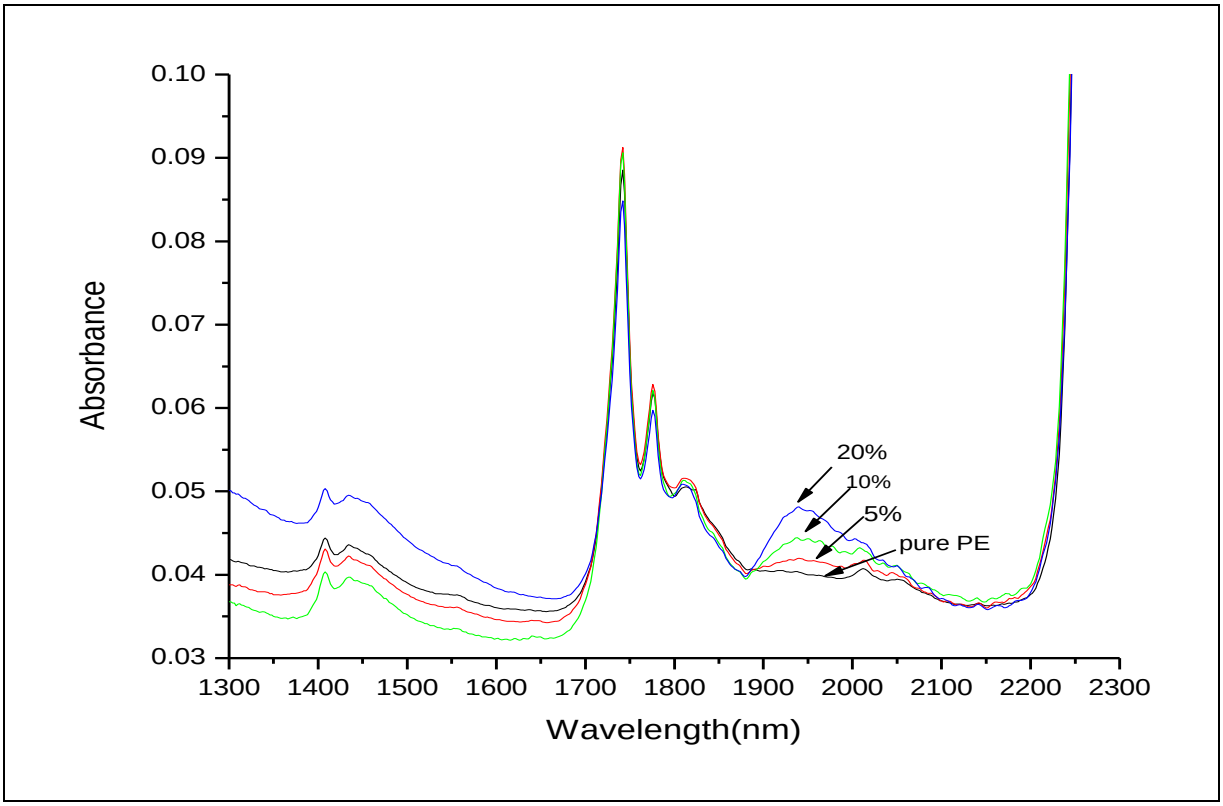

Figure 5.22: NIR absorption spectra of PE films loaded with different amounts of Mg-Al LDH

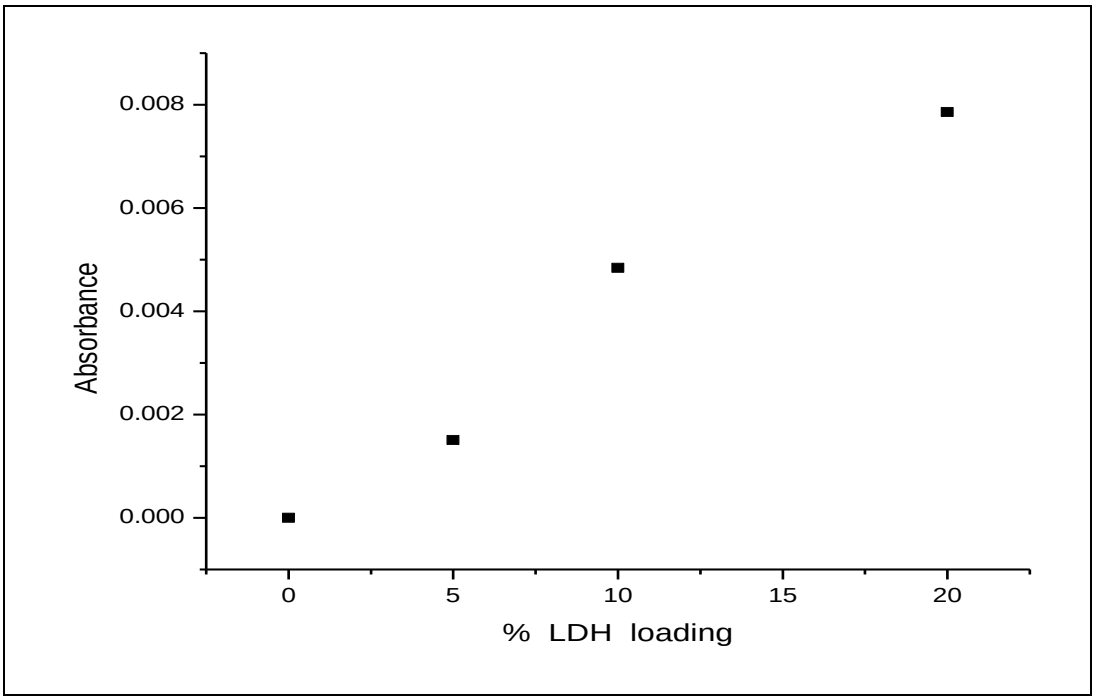

Figure 5.23: Absorbance of PE films with different amounts of Mg-Al LDH at 1950nm.

Based on the results in Figures 5.22 and 5.23, it should be possible to use NIR absorption measurements for both qualitative and quantitative analysis of chemical compounds in the polymer films. Ultimately therefore, if the NIR image of the 'doped' polymer film at 1950nm is obtained, the absorbancies at different pixels in the image should correspond to the amount of the chemical species being measured at that wavelength, at different locations of the sampled area. This means NIR micro spectroscopy can be used as a tool to quickly identify and even quantify small isolated contaminants or localized areas on a large sample. By studying the absorption pattern in the image, information can be obtained about the dispersion or the distribution of the additive in the polymer film. This ultimately leads to information about the heterogeneity of the polymer film.

To gain an insight into the dispersion of the undecenoic acid intercalated Mg-Al LDH flame retardant in polymer films, the NIR imaging system was used to record images in the region 1400 nm to 2600 nm. Figure 5.24 shows the NIR spectrum of a polymer film with 20% by weight of the LDH, calculated from the images obtained by this system. This spectrum is similar to the one obtained with the conventional NIR spectrophotometer which is shown in Figure 5.22. The other bands observed at around 1758 nm and 2316 nm are due to the PE substrate.

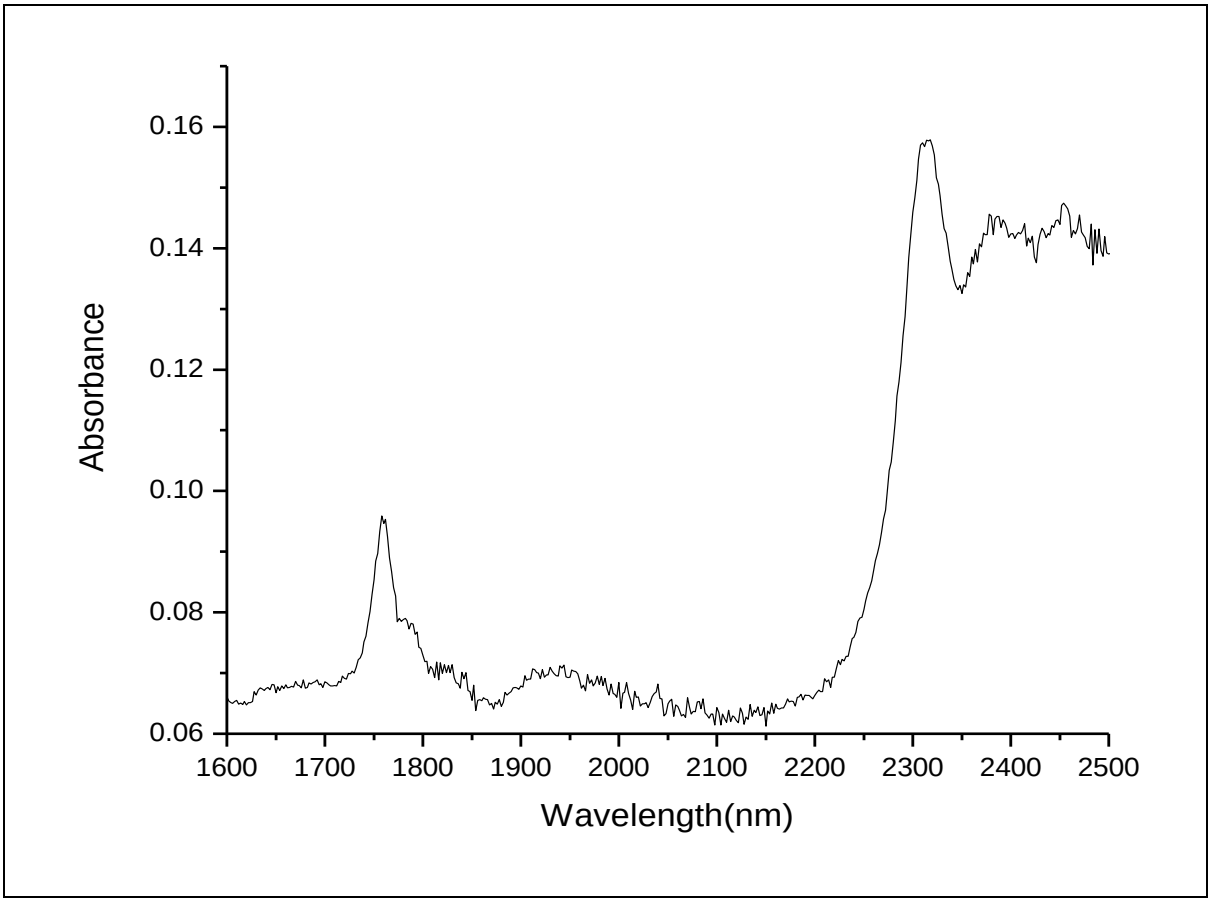

Figure 5.24: Absorption spectrum of a 20% sample calculated from the images measured on the NIR microscope imaging system.

Having established from figure 5.22 that the C-11 carboxylic acid intercalated LDH is responsible for the absorption band observed at 1950nm, absorption images were calculated at this wavelength. Different absorbancies at different pixels would mean different concentration of the LDH additive at different sample locations, which ultimately means inhomogeneity in the sample. However, considering the Beer's Law:

$$A = \varepsilon bC \quad (5.1)$$

where A is the absorbance, ε is the molar absorptivity, b is sample thickness and C is the concentration, it means that in addition to the amount of the LDH additive at any given location, the absorbance is also affected by the molar absorptivity of the species being measured and also the sample thickness. Since only the LDH additive absorbs at the wavelength being used (1950nm), ε is the same for each pixel and hence is a constant in equation 5.1. However producing films with uniform thickness is not easily achievable. As a result it is necessary in the analysis of these NIR images to take into account the possibility of having different film thickness at different locations of the polymer in the image area. A simple method was devised for the elimination of the effect of film thickness in the calculation of the final absorption images.

This method is based on taking the absorbance ratio at two different wavelengths. The first wavelength is the wavelength of maximum absorption of the LDH additive ($\lambda_{additive}$) and the second wavelength is for the absorption of the polymer substrate

($\lambda_{substrate}$). Based on the spectrum in Figure 5.24, 1950nm was chosen as $\lambda_{additive}$ while $\lambda_{substrate}$ was chosen to be 2316nm. Taking the absorbance ratio at the two wavelengths:

$$\frac{A_{\lambda additive}}{A_{\lambda substrate}} = \frac{\varepsilon_{additive} b_{additive} C_{additive}}{\varepsilon_{substrate} b_{substrate} C_{substrate}} \quad (5.2)$$

If it is assumed that for these relatively thin films, at any given location, the additive spans the whole z-axis (thickness) of the film, it means $b_{additive}$ and $b_{substrate}$ are equal. Hence equation 5.2 reduces to:

$$\frac{A_{\lambda additive}}{A_{\lambda substrate}} = \frac{\varepsilon_{additive} C_{additive}}{\varepsilon_{substrate} C_{substrate}} \quad (5.3)$$

Realizing that $\varepsilon_{additive}$ and $\varepsilon_{substrate}$ are constants for the additive and substrate respectively, equation 5.3 is further reduced to equation 5.4 below:

$$\frac{A_{\lambda additive}}{A_{\lambda substrate}} = K\frac{C_{additive}}{C_{substrate}} \quad (5.4)$$

Where *K* is just the ratio of the molar absorptivities for the additive and substrate. The implication of equation 5.4 is that taking the ratio of two images at $\lambda_{additive}$ and $\lambda_{substrate}$ gives the relative ratio of the additive to the polymer substrate at any given location of the polymer film in the image.

Figures 5.25A shows images taken at different sample positions for a polyethylene film to loaded with 20% by Mg-Al LDH. The images show the relative ratio of the LDH additive to the polymer substrate at each location (given by x-y coordinates) as calculated according to equation 4 above. Different values are plotted as different colors according to the scale on the color bar shown on the right of each image. The results show that the ratio ranges between 0.25 (green color) up to 0.55 (blue color). This

implies that the additive is not uniformly distributed or dispersed in the polymer. Clearly, there are some areas where there is high concentration of the LDH additive which appear blue as compared to most of the area which appears green. This kind of heterogeneous distribution of the LDH additive within the polymeric phase is important because it directly influences the physical and chemical properties of the material. The extent of this heterogeneity is also somewhat different for different locations on the film.

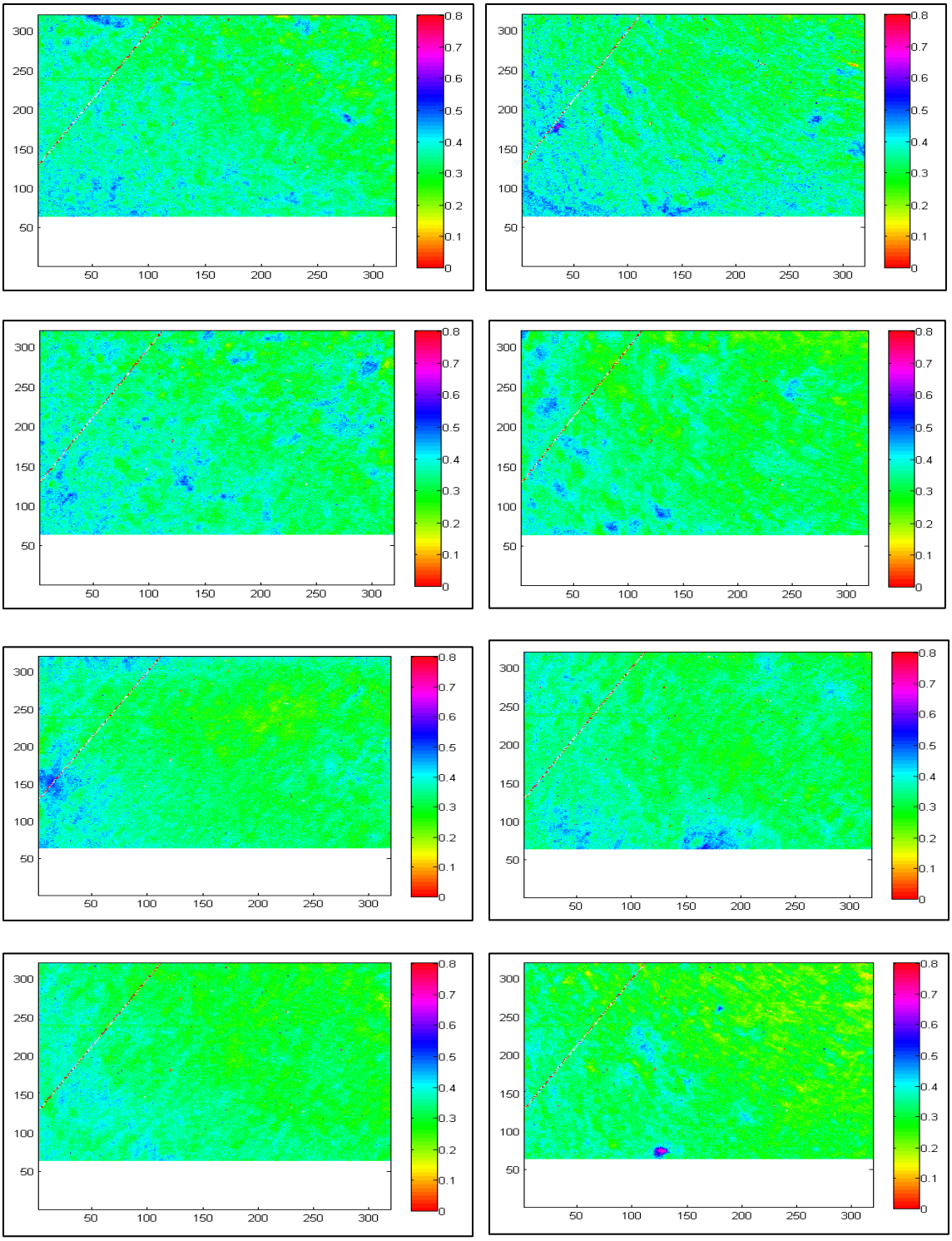

Figure 5.25: Distribution of the relative ratio of LDH additive to polymer substrate (scaled by a factor K = λadditive/λsubstrate) in 20% LDH films

As illustrated in Figure 5.25, there are some areas which show less heterogeneity as compared to the distribution pattern shown in Figure 5.25. Due to this inhomogeneity, chemical and physical properties of such a material would not be expected to be uniform and would therefore affect its usefulness in such fields as engineering.

Figure 5.26A and 5.26B show the 3D absorption surface plots for the polymer substrate at 1758 nm (top plot) compared to the distribution of the additive as calculated according to equation 4 (bottom plot). In both figures, the 3D plots for the polymer substrate at 1758 nm shows much less inhomogeneity when compared to the corresponding 3D plots for the additive. In these 3D plots, sample locations with higher absorbance (and hence higher concentration) will appear as peaks or 'mountains'. The number and size of peaks and 'mountains' in the 3D plots show the extent of heterogeneity of the material. For both figures shown in Figure 5.26, the number of peaks and 'mountains' are markedly less and lower for the polymer substrate than for the LDH additive. Some sharp peaks which appear in the 3D plots for the polymer substrate are a result of bad pixels of the camera. Nevertheless, the 3D plots at the absorption wavelength for the polymer substrate are mostly smooth whereas those of the additive have numerous spiky peaks indicating that indeed the LDH additive is not homogeneously distributed in the polymer film.

The distribution of any chemical species in a polymeric material will depend on such factors as diffusion, permeability, nature of the polymer and compatibility with the

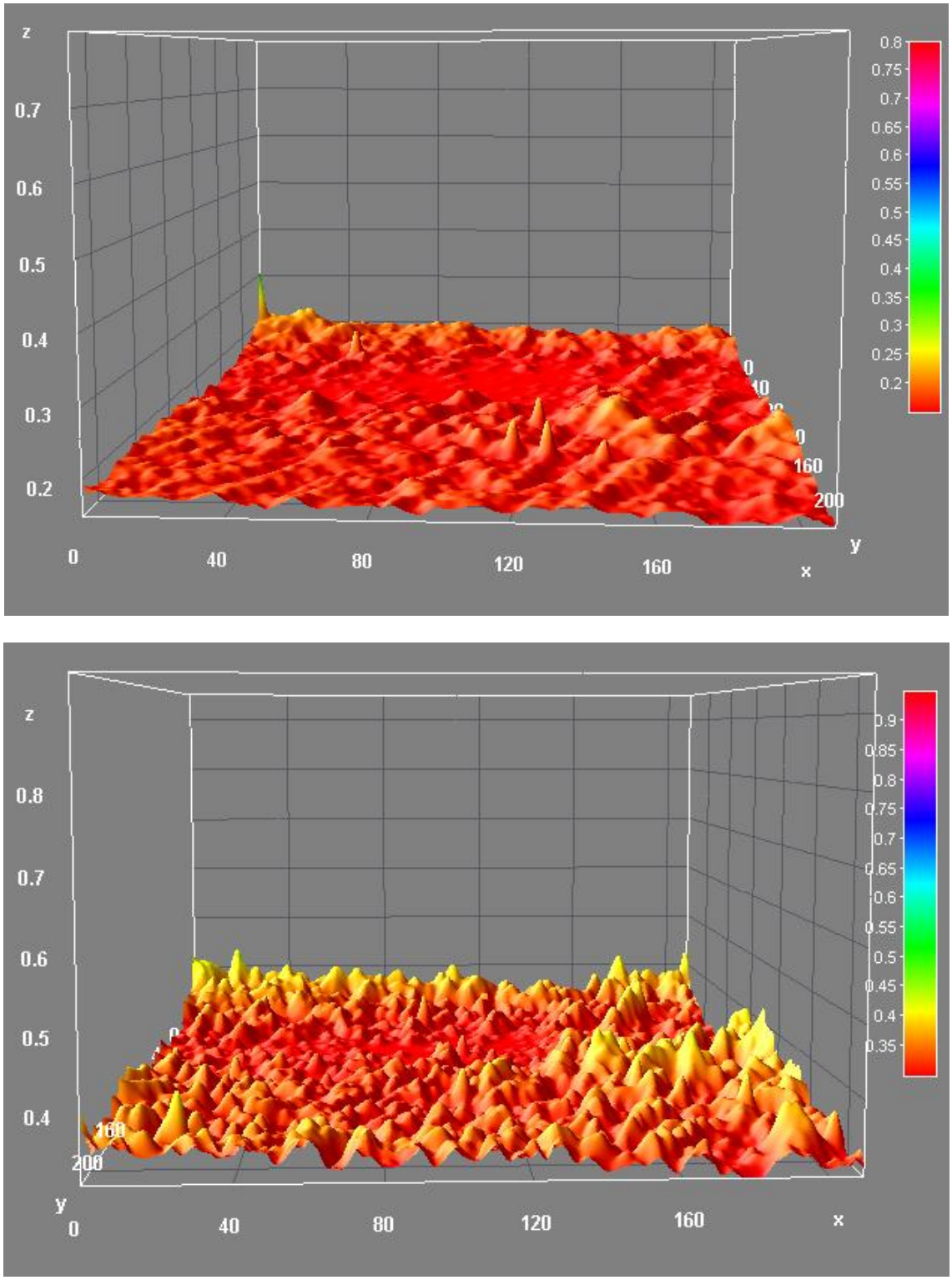

Figure 5.26A: 3D surface plots for the polymer film at 1758 nm (top) and for the image showing the distribution of the additive at 1950 nm (bottom).

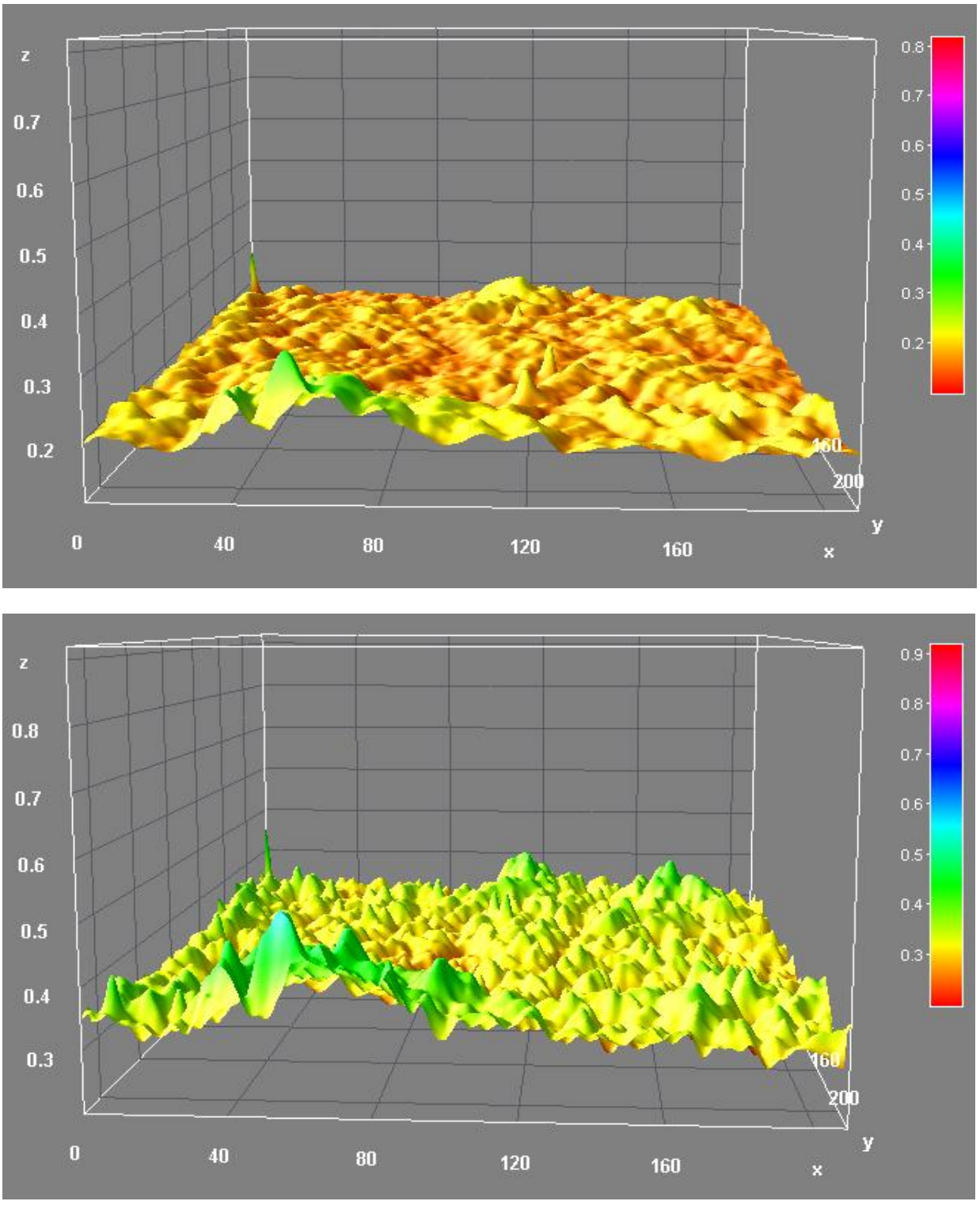

Figure 5.26B: 3D surface plots for the polymer film at 1758 nm (top) and for the image showing the distribution of the additive at 1950 nm (bottom).

polymer. Generally, a hydrophilic inorganic additive such as a LDH is thermodynamically incompatible with a more apolar organic polymer phase. As a result, it means it is difficult in practice to manufacture a polymer in which an additive is evenly dispersed throughout the material. This could be one of the major contributors to the heterogeneity that was observed here. If a polymer substrate consist of both crystalline and amorphous regions, the additive is likely to be more concentrated in the amorphous regions leading to inhomogeneous distribution of the additive. More homogeneous distributions can be achieved if both the permeability of the polymer and the diffusion of the additive in the polymer are high. Inhomogeneity can also be a result of incomplete mixing of the additive and the polymer during blending at sample preparation stage.

Simple absorption images were also calculated for the 20% LDH PE film. From these absorption images, 3-D surface plots of absorbance at 1950 nm of the sample as a function of its dimension can be obtained. The result is shown in Figure 5.27A where units for x, y and z axes of the plot are pixel, pixel and absorbance at 1950 nm, respectively with one pixel corresponding to 0.93 μm, and the color of the plot denotes different absorbance at 1950 nm with scale shown in upper right-hand. For comparison, 3-D plot of a sample of pure PE polymer sample taken at the absorption of the C-H group at 1750 nm is also shown in Figure 5.27B. As described above, absorbance at 1950 nm of doped PE sample is related to concentration of added LDH whereas absorbance at 1750 nm of pure PE sample corresponds to its concentration or rather its thickness. As illustrated, the 3-D image shown in Figure 5.27B is not smooth but has some contours which indicate that the PE film does not have the same microscopic thickness over its entire surface. This is hardly surprising considering the fact that the film was prepared

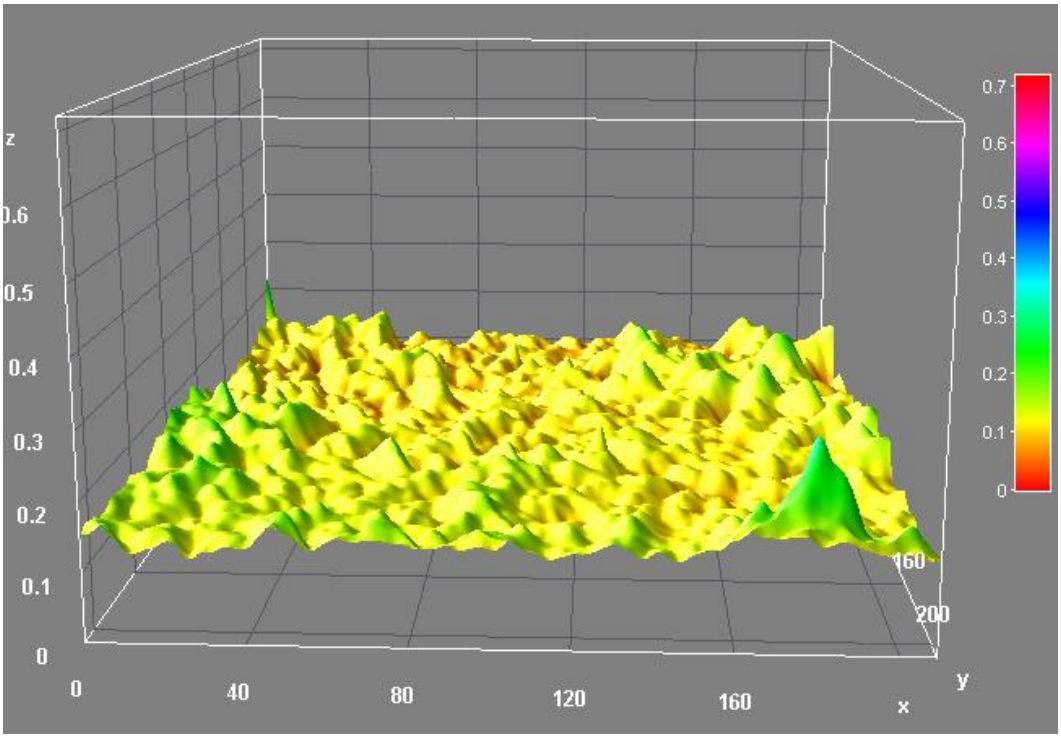

A

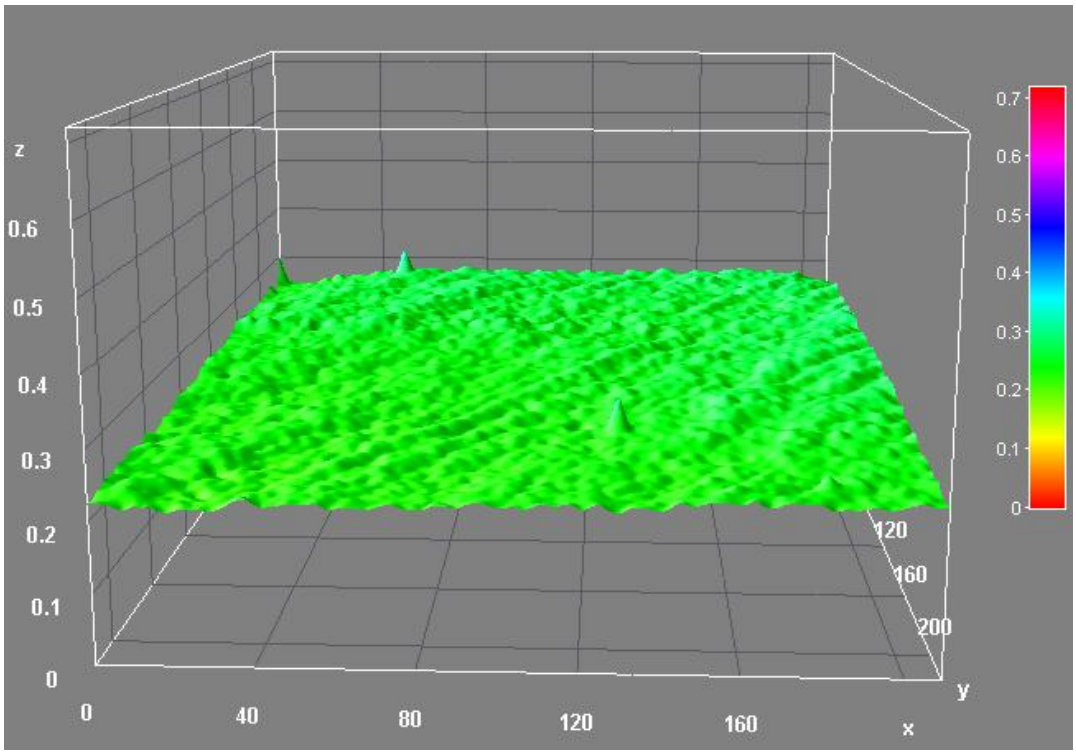

B

Figure 5.27: 3-D absorption images taken at (A) 1950 nm of a polyethylene sample doped with 20% MgAl-C11LDH, and (B) at 1750 nm of pure PE film. Units for x,y and z axes are pixel, pixel and absorbance at 1950 nm and 1750 nm, respectively (one pixel corresponds to 0.97µm)

using a mechanical hot plate. Substantial differences in the absorbance at 1950 nm were observed for the PE sample doped with 20% LDH. Because the absorbance differences observed here is much larger than those observed for PE sample at 1750 nm, they cannot be account solely due to the difference in the thickness of the sample. Rather they are due mainly to the differences in distribution of added LDH compound. That is added LDH is not homogeneously distributed over the entire the PE polymer film.

5.2.4. Chemical inhomogeneity of polysaccharide composite materials

The NIR-MIS was used to study the chemical distribution in a [CEL+CS] composite film. This polysaccharide composite film was prepared according to procedures described in Chapter 2. As described above, studying absorption images at specific wavelength is susceptible to errors arising from differences in film thickness at different sample locations. This is even more complex in the case of two polymers mixed together. As a result, a different approach was used to visualize the chemical distribution of the compounds in the cellulose and chitosan composite materials.

In this new approach, chemical composition was visualized by studying the absorption spectra as a function of sample location. This means the absorption at each wavelength is plotted for each pixel along an axis on the image. It is anticipated that by looking at the whole spectrum, more information will be obtained from the sample than just looking at the absorption at a specific wavelength. Figure 5.28 is one such plot of a cellulose/chitosan composite sample.

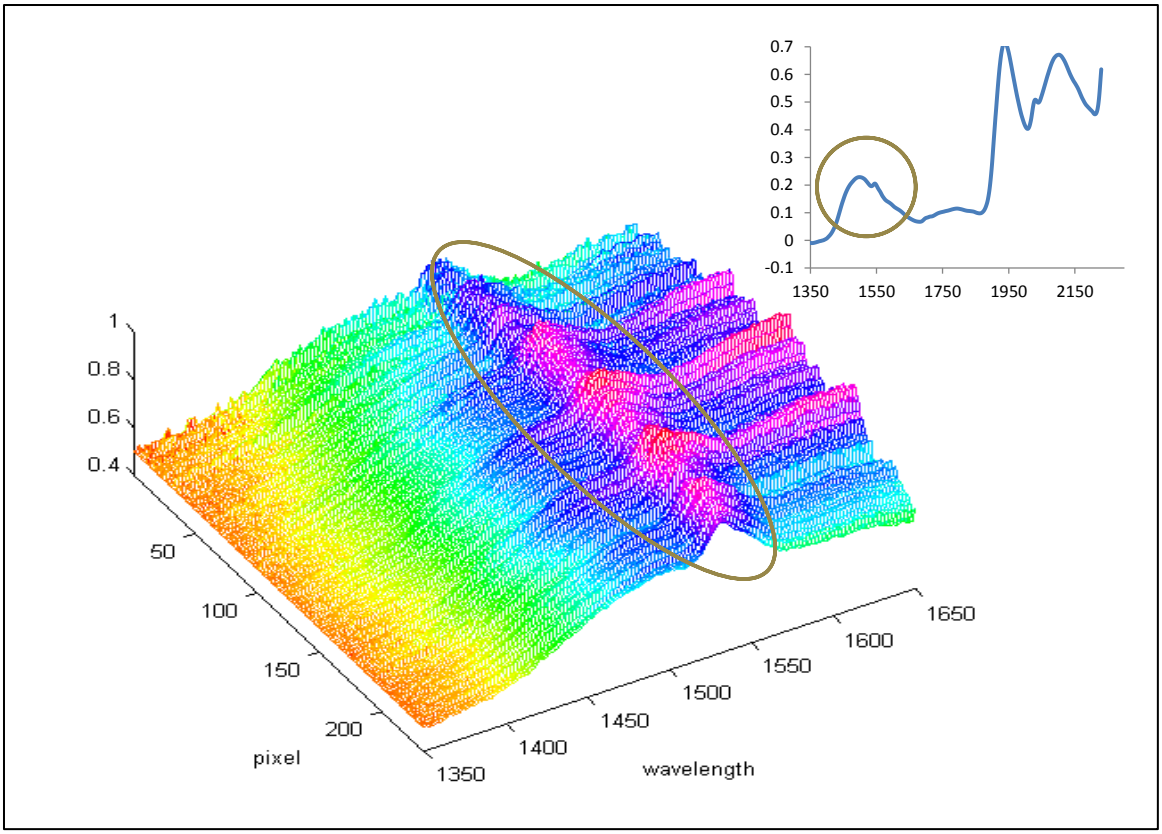

Figure 5.28: NIR absorption spectra at different locations for a [CEL+CS] composite film

The absorption band that appears around 1500 nm is mainly due to OH of both chitosan and cellulose. The NH band of chitosan appears as a shoulder on this same OH band such that the two bands appear merged together in the above plot. However, there are areas where this band appears to be broader than in most areas. This is an indication that the NH band of chitosan is more intense in that area of the sample. Therefore, it seems that chitosan is not uniformly distributed in the sample. However, this chemical inhomogeneity is not so much since for those areas that are different, the absorption band is only slightly broader than in most areas.

In summary, we have demonstrated for the first time that the NIR-MSI microscope can be successfully used to determine microscopic concentration distribution of LDH compound added to a polymer film. Use of LDHs with nonpolar polymers such as poly(ethylene) is known to be a challenging system for obtaining good nanodispersion.[17] Having the ability to monitor dispersion (chemical homogeneity) on the micron length scale will provide an excellent complement to other methods of characterization. NIR-MSI offers the possibility of examining more chemically complex systems, such as those containing mixtures of additives.

5.3. References

(1) Pan, L. C.; Wilson, D. W.; Lame, M. W.; Jones, A. D.; Segal, H. J. *toxicology and applied pharmacology* **1993**, *118*, 87–97.

(2) Smith, L. W.; Culvenor, C. C. J. *J. Nat. Prod* **1981**, *44*, 129–152.

(3) Kay, J. M.; Kean, P. M.; Suyama, K. L.; Gauthier, D. *Thorax* **1982**, *37*, 88–96.

(4) Ghodsi, F.; Will, J. A. *Am. J. physiol.* **1981**, *240*, H149–H155.

(5) Mattocks, A. R.; Bird, I. *Chem. Biol. Interact.* **1983**, *43*, 209–222.

(6) Mattocks, A. R.; White, I. N. H. *Chem. Biol. Interact.* **1971**, *3*, 383–396.

(7) Mattocks, A. R. *nature* **1968**, *217*, 723–728.

(8) Butler, W. H.; Mattocks, A. R.; Barnes, J. M. *J. Pathol.* **1970**, *100*, 169–175.

(9) *Guide for the care and use of laboratory*; National academic press: Washington, D.C., 1996.

(10) Morris, M. D. *Microscopic and Spectroscopic Imaging of the Chemical State*; Marcel Deckker, Inc.: New York, 1993.

(11) Tran, C. D. *J. Near-Infrared Spectrosc* **2000**, *8*, 87–89.

(12) Tran, C. D. *Fresenius J. Anal. Chem.* **2001**, *369*, 313–319.

(13) Tran, C. D. *Appl. Specrosc. Rev.* **2003**, *38*, 133–153.

(14) Tran, C. D. *Analytical Letters* **2005**, *38*, 735–752.

(15) Fischer, M.; Tran, C. D. *Analytical chemistry 71*, 953–959.

(16) Gustafson, S. B.; Fulkerson, P.; Bildfell, R.; Aguilera, L.; Hazzard, T. M. *Prehospital emergency care official journal of the National Association of EMS Physicians and the National Association of State EMS Directors* **2006**, *11*, 172–178.

(17) Nyambo, C.; Wilkie, C. A.; Wang, D. *Polym. Adv. Technol.* **2009**, *20*, 332–340.